Single Molecule Analysis of DNA Electrophoresis in Microdevices

by

Greg C. Randall

Submitted to the Department of Chemical Engineering
in partial fulfillment of the requirements for the degree of

Doctor of Philosophy

at the

MASSACHUSETTS INSTITUTE OF TECHNOLOGY
[February 2006]
January 2006

Author ....
Department of Chemical Engineering
January 10, 2006

Certified by ....
Patrick S. Doyle
Doherty Assistant Professor of Chemical Engineering
Thesis Supervisor

Accepted by ....
William M. Deen
Professor of Chemical Engineering
Chairman, Committee for Graduate Students

Single Molecule Analysis of DNA Electrophoresis in Microdevices

by

Greg C. Randall

Submitted to the Department of Chemical Engineering
on January 10, 2006, in partial fulfillment of the
requirements for the degree of
Doctor of Philosophy

Abstract

Given that current electrophoresis technology is inadequate for mapping large O[100 kilobasepair] DNA, several promising lab-on-chip designs for DNA mapping have been recently proposed that require either 1) a DNA molecule negotiating an obstacle course in a microchannel or 2) stretching a DNA molecule for linear analysis. The goal of this research is to experimentally probe the fundamental physics that underlie these DNA mapping designs. Furthermore, we present a continuous stretching process that offers significant improvement over results in literature. In general, the governing physics is complex due to the confinement of the microchannel, the coiled-nature of long DNA molecules, and the induced electric field gradients from obstacles and changes in channel dimensions.

Using single DNA fluorescence microscopy, we have investigated many of the governing physical mechanisms at play in these gene mapping microfluidic devices. For example, we have determined transport coefficients for DNA in a confined channel and performed an analysis of hydrodynamic background flows in these thin channels. We have also performed a systematic study of the impact and unhooking dynamics of a DNA molecule driven into a small stationary post. Furthermore, we have thoroughly investigated DNA stretching in electric field gradients created by a contraction and a large insulating obstacle. Just as a flow gradient stretches a polymer, an electric field gradient can stretch a charged polymer like DNA. Because electric field gradients have no local rotational components, a charged polymer will experience purely extensional deformation. This is true even near surfaces, unlike the cyclic extension-compression dynamics characteristic in shear flows.

A recurring theme is this work is the notion of configuration effects, or "molecular individualism", a term coined by DeGennes eight years ago to denote the sensitive dependence of a single polymer's deformation dynamics to its initial configuration. New mapping designs often require or force DNA to strongly deform and we see molecular individualism arise when studying phenomena central to these mapping designs, *e.g.* DNA colliding into stationary posts or DNA stretching in electric field gradients. Molecular individualism counteracts mapping and other potential engineering applications that might require uniform behavior of all DNA molecules. However, our results show that molecular individualism can be bypassed by pre-configuring the DNA configurational distribution before strong deformation. The main impact of these findings will be to foster the design of custom unit operations in biomolecule microfluidic processes, *e.g.* for DNA mapping applications and beyond.

Thesis Supervisor: Patrick S. Doyle
Title: Doherty Assistant Professor of Chemical Engineering

Acknowledgments

I feel that a Ph. D. thesis is both a pursuit to solve interesting and unsolved problems and equally, a learning experience. There are many people whom I would like to acknowledge and thank for offering their help and support.

I would like to thank my advisor Prof. Pat Doyle for allowing me the freedom to explore the variety of ideas and topics covered in this thesis, as well as other subjects not presented here. Furthermore, he was a great balance for me, someone who always pressed me to seek a valid explanation for some of my more instinctive ideas. I would also like to thank my thesis committee of Profs. Greg Rutledge and Gareth McKinley for helpful questions and great suggestions for the path this research took.

I also wish to thank past and present members of Doyle group: Thierry Savin, Patrick Underhill, Ramin Haghgooie, Dhananjaya Dendukuri, Anthony Balducci, Dan Pregibon, Malancha Gupta, Kelly Shultz, and Ju Min Kim. Many members in the group are often helpful for troubleshooting or modeling and I am lucky to have had them to bounce ideas off of. In particular, I thank Pat Underhill for many helpful discussions of different modeling ideas in this thesis. He has a keen sense for mathematical modeling and his arguments can truly be taken as fact. I'd like to thank Anthony Balducci who also works on DNA experiments. We often compared notes on experimental techniques, experimental design, and theoretical scalings. I thank Malancha Gupta (DNA diffusion in confinement) and Kelly Shultz (DNA migration in porous UV polymerized gels) who validated and/or performed some of the experiments that I report. I'd like to thank Dhananjaya Dendukuri and Dan Pregibon for help with my gel experiments (Chapter 8). Their expertise was invaluable to troubleshoot experimental problems. Thanks go out to Dhananjaya Dendukuri and Ramin Haghgooie for SEM work. I thank Ju Min Kim for performing finite element calculations for the electric field in a hyperbolic contraction and recently, performing some bead-spring simulations to mimic my experiments. I also thank Ramin Haghgooie, Thierry Savin, and Pat Underhill for tremendous support for computing issues. I thank Kurt Broderick and Gwen Donahue at the MTL microfabrication lab at MIT for their help in the photolithography steps to construct microchannels.

I am grateful to other professors at MIT who helped answer difficult questions that arose in this research. Not only did Prof. Martin Bazant teach an extremely interesting class that I took (18.366), he was also very helpful in interpreting some nonlinear electrophoresis observations that we stumbled upon (not presented here). Furthermore, I thank Prof. Vladimir Entov for a helpful discussion on the similarity of modeling permeation driven flows in PDMS with large-scale potential flow of oil through cracks in rocks.

I would like to thank the many friends I have made at MIT and in particular those that started with me back in the Fall semester of September 2000. My "homework group" of Steve Fox, Kathryn Miller, Evan Piland, and Fred Bernadin truly made 1^{st} semester much more enjoyable. I am thankful for meeting the likes of Kyle Jensen, Brian Baynes, Greg Zugates, Joe Moritz, Mike Raab, Jeremy Johnson, Prem Pavoor, and Mike Berg. This cast of characters, who always made for a truly enjoyable end of the week TG, are sure to succeed in their respective career paths. I am also grateful for everyone I've met playing ChemE sports and other activities.

Finally I thank my family for being there for me, literally. I am from the Boston area and it was

nice to have them close by, especially during difficult times over the last 5 years. Though my career path may often seem "off the beaten path", they are proud of me and truly support this and future endeavors. For all this, I am thankful.

This research was funded by National Science Foundation CAREER Grant No. CTS-0239012 and U.S. Genomics (Woburn, MA).

Contents

List of Figures

List of Tables

Chapter 1

Introduction

1.1 Motivation: DNA mapping

Recent advances in gene therapy and crime investigation have spurred a demand for rapid "gene mapping" of large (kbp-Mbp, bp=basepair) DNA molecules. As opposed to DNA sequencing, these applications rely on a very low resolution view of a DNA's genetic code [2]. Current sequencing technology calls for cutting DNA strands at known locations and then determining the resulting length distributions by a *DNA separation process.* DNA separations are generally performed by electrophoresis where negatively charged DNA molecules are driven through a "specialized" channel by an electric field. In an empty channel, the velocity of each DNA molecule is independent of its size. Therefore, "specialized" physical barriers (gels, polymers, etc.) are added to these channels that cause different length DNA molecules to move at different average velocities to achieve a size-separation.

Current state-of-the-art capillary and gel electrophoresis sequencing processes are not suitable for size separation of the large DNA fragments ideal for gene mapping. In addition to the practical issues of long separation times, clogging, and irreversibly immobilized DNA strands, gel pores are too small to separate large DNA; the length dependence of the reptation sieving mechanism saturates at O[10 kbp] DNA lengths [3]. Furthermore, loading the specialized polymer and gel networks is not an easily automated process. Clearly, current DNA mapping technology is not optimized and it cannot meet the growing demand for DNA analysis. In September 2004 there were over 500,000 DNA samples backlogged and waiting for analysis in US crime labs [4]. The demand grows when one considers potential medical diagnostic tests that could be performed to check for genetic diseases.

In order to meet the growing demand for DNA mapping applications, it would be preferable to map large O[Mbp] pieces of DNA in a "Lab-on-Chip" [5] device that can be easily automated and run in parallel. Several promising Lab-on-Chip designs for DNA mapping have been recently proposed in proof-of-principle studies. These novel mapping schemes for large DNA can be grouped into two broad classes: *obstacle course separations* and *DNA stretching devices.*

1.1.1 Obstacle course separations

Obstacle course mapping devices continue along the lines of current sequencing technologies and take advantage of a size-dependent mechanism to separate polydisperse DNA samples into monodisperse electrophoresis bands. However, the DNA to be separated are ideally much larger than the sizes used in modern electrophoresis sequencing devices, so the size-dependent phenomena can be induced by changes in the microchannel geometry (*e.g.*, by adding physical barriers). We review some of the proposed channel geometries here. We concentrate on pore devices, hooking collision devices, diffusion arrays, and entropic traps.

An ideal DNA mapping device would be able to quickly distinguish between different sized O[kbp-Mbp] DNA. The performance of a separation device can be evaluated in terms of two parameters: the *average mobility in the obstacle course* $\langle\mu\rangle$, and the *dispersion coefficient* $D^\star$ which tells how a band of monodisperse molecules will broaden in time. Often the DNA's average mobility through the obstacle course is given in terms of a power law exponent φ where $\langle\mu\rangle \sim L^{\varphi}$. The separation *resolution* between two DNA sizes is determined by these two parameters and the total separation time. Quantitatively speaking, resolution is the time lag between the two monodisperse bands divided by the average width of the bands. An ideal separation has a high mobility differential for different length DNA ($\varphi \gg 1$) and $D^\star \sim 0$, so that resolution > 1. When the resolution ≤ 1 for two different size DNA, "poor" separation is achieved. It is also helpful from an engineering perspective to have a large $\langle\mu\rangle$ so that a fast separation is obtainable.

Pore devices: Volkmuth and Austin tried to develop a way to perform DNA electrophoresis in a synthetic lattice of microfabricated obstacles [6, 7]. Their intent was to bypass the main limitation (pore size) of gel electrophoresis by custom microfabrication of obstacle courses with larger pores. Using microlithographic techniques, they constructed a dense mesh of small obstacles in a microchannel (1 μm cylindrical obstacles with 2 μm center-to-center spacing). Initial separation attempts with the microchannels were not successful due to an observed hooking mechanism that arose occasionally when a DNA molecule collided with and hooked around an obstacle. This hooking mechanism turned out to be a good separation mechanism itself (discussed below), however others continued to pursue the pore lattices with larger obstacles and/or tighter pores (Fig. 1-1 (a)). Inatomi *et al.* constructed tightly spaced 15 μm PDMS obstacles inside a microchannel to yield O[μm] pores. They were able to discern differences in average mobility between λ DNA and T4 DNA, however the resolution was poor. Similar experiments were done in channels filled with ~30 nm nanoparticles [8, 9]. These 1-4 min separations yielded a power-law separation exponent of $\varphi = -1$ [8] for separation of O[0.1-1 kbp] DNA. However, the separation resolution is poor for sizes over 1 kbp, likely due to the small pore size.

Hooking collision devices: The hooking collisions observed by Volkmuth and Austin led to high dispersion in their intended pore separation. However they noted that the unhooking mechanism is itself strongly length dependent and thus could lead to size-separation in a less dense obstacle course (Fig. 1-1 (b)). This was tested with simulations [1, 10–13] and later proved with experiments [14]. Doyle *et al.* [14] used magnetic colloids that self-assemble into columns in the presence of a magnetic field to serve the same purpose as the Volkmuth and Austin's custom microfabricated obstacles. Comparing the 48.5 (λ) and 145.5 (3λ) kbp bands, Doyle *et al.* report a resolution value of 3.3 after 30 min, and analysis of their data gives $\varphi \sim 0.3$. Single post array arguments suggest $\langle\mu\rangle \sim 1 - L^{3/2} f(\Delta x_{obs})$, where $f(\Delta x_{obs})$ is a function of the obstacle course geometry [12].

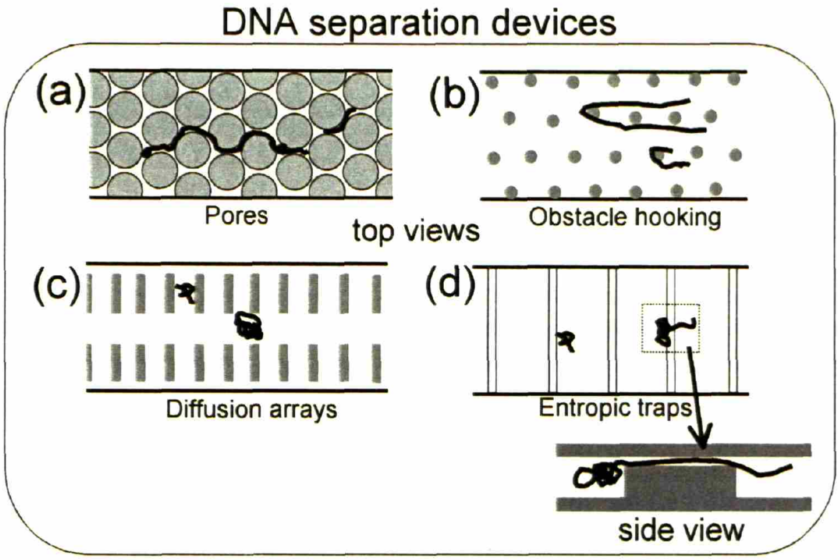

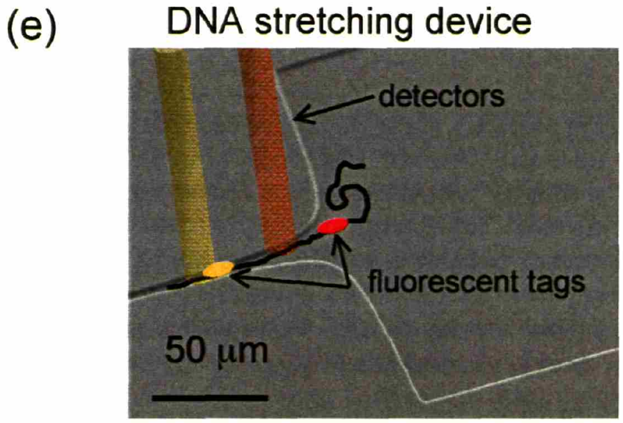

Figure 1-1: Schematics of obstacle courses for DNA mapping. (a) Pore devices (b) Obstacle hooking devices (c) Diffusion arrays and (d) Entropic traps. In (a) and (b) smaller DNA move faster than larger DNA, whereas in (c) and (d) larger DNA move faster than smaller DNA. (e) Schematic of a DLA stretching device. Fluorescent probes are specifically attached to target genes, the DNA molecules are stretched in the contraction, and detectors read the probe signals continuously.

Patel and Shaqfeh [15] simulated DNA moving through two different random dilute post arrays and reported $\varphi \sim 0.1$ in the 100 kbp size range, however it is not clear if they optimized the obstacle geometry. Minc *et al.* [16] were able to continue collision array experiments at higher fields and in more dense arrays and still were able to separate λ, 2λ, and T4 DNA with resolutions between 1-2. Though the observed power law scaling is low, the main advantage of using hooking collisions is that the collision hold-up time t_H is highly length dependent ($t_H \sim L^{3/2}$), and it is likely to work for very large DNA O[Mbp].

Other induced hairpin hook obstacle designs can be employed to lead to very fast separations. By using a pulsed alternating electric field aligned diagonally across the obstacle course, Bakajin *et al.* [17] were able to separate λ DNA (48.5 kbp) from T4 DNA (169 kbp) in only 10 s with a resolution of 2. Like the hairpin hooking event, the size-dependent mechanism in this study was the disengagement time of a DNA molecule pinned at an obstacle. They predict a scaling of $\langle\mu\rangle \sim 1 - (L/L^*)$ where L^* is an upper critical cut-off length, above which a molecule will not disengage from an obstacle. The results presented were for T4 DNA close to L^*, so T4 molecules were the largest possible DNA molecules that could be separated in this device at those operating conditions. Nevertheless, this device does show the ability to achieve a high-resolution binary separation and the alternating field frequency could possibly be adjusted to refine its separation performance and ability to separate multiple DNA lengths.

The main result from these hooking separation studies is that the resulting separation efficiency depends strongly on the obstacle disengagement time, collision probability, and obstacle course layout. In order to optimize the obstacle layout and separation conditions, these single obstacle collision events should be investigated.

Diffusion arrays: Duke and Austin envisioned [18] and then succeeded to drive molecules through a micromachined lattice of large obstacles, using the length dependence of *lateral diffusivity* as the separation mechanism [19]. A similar technique was proposed by Baba *et al.* [20] (Fig. 1-1) (c). DNA move down a channel with large obstacles oriented against the field direction. Large DNA are more likely to remain in the main "aisle" while smaller DNA are more likely to diffuse into the stagnant regions between obstacles. Hence larger DNA move through the obstacle course quicker than smaller DNA. Duke and Austin's diffusion array operates with this principle, however the obstacle geometry creates a lateral separation [19]. One problem associated with this device is that diffusion coefficients are considered weak functions of contour length, $D \sim L^{-0.6}$, which leads to poor resolution. More importantly, this method is especially difficult for large DNA fragments because they tend to collide with the obstacles and form hairpin hooks described above.

Entropic traps: Craighead and Han [21] employed nanotechnology techniques to fabricate a device of entropic traps to separate DNA (Fig. 1-1 (d)). Their device consists of alternating troughs (1.5-3 μm deep) and narrow slits (75-100 nm) which are smaller than the radius of gyration of kb-size DNA. A trap's function is to detain electrophoresing DNA at the entrance of a narrow slit until the chain can realign and pass through the slit. The separation mechanism is a combination of passage through an entropic barrier [21] and a diffusion array [22]. Large DNA move faster than small DNA because 1) they have more contour in contact with the narrow slit and 2) they are less likely to diffuse into the low field strength regions near the bottom of the trough after moving through a slit. Han and Craighead show that they are able to separate T2 DNA (164 kbp) from T7 DNA (37.9 kbp) in times ranging from 15-30 minutes with resolution ~ 2, though results show significant dispersion and secondary peaks for intermediate sizes. Furthermore, an interesting phenomenon occurs when the size of the slit increases; the mobility trend reverses and smaller DNA begin to move faster through the device than larger DNA [23, 24]. This mobility trend reversal is attributed to long DNA deforming in the field gradients caused by the gaps. The deformation pulls the DNA's center of mass out of the main channel toward the low fields in the trenches so that on average, the long DNA move slower [24].

Summary: In all of these separation devices, it is apparent that the issues of DNA confinement, hooking collisions, and deformation in electric field gradients are important to understand to better design optimum Lab-on-Chip mapping processes. We will choose to study the unhooking separation mechanism in detail, because out of the proposed mechanisms, it is best suited for future O[Mbp] separations DNA.

1.1.2 DNA stretching devices

DNA separations extract genetic information indirectly, *i.e.* the resulting gene maps depend on the obtained length distributions and the enzymatic cutting steps. Direct mapping techniques are more desirable than indirect methods because they eliminate many pre-treatment and post-processing mapping steps. However, genetic information is inherently difficult to extract directly from DNA molecules because, in the size range of O[10 kbp] and above, they adopt "random coil" configurations. Thus, if certain gene locations can be tagged with a fluorescent probe, a detection device cannot accurately determine the linear distance between the respective genes along the DNA backbone. The coil must first be unraveled and stretched [25, 26]. A *direct linear analysis* (DLA) gene mapping method involves binding known-sequence markers along the strand of DNA, flowing the DNA through a contraction so flow gradients cause it to stretch, and then directly measuring the distance between these markers on the linear stretched molecule in-line (Fig. 1-1 (c)) [25–27]. The performance of a DLA device relies on the ability to *completely* and *uniformly* stretch nearly all DNA in a sample ensemble. Previous experimental studies have been able to stretch some DNA completely by flowing DNA solutions through contractions [26, 27]. However the resulting stretching distribution is fairly broad, typical of polymer deformation in extensional flows at finite strain. It would be desirable to design a stretching device to improve this stretching efficiency.

1.1.3 Conclusion

With all of these inventive new ways to map DNA, there is a wealth of fundamental single DNA physics to study to help improve their design. For example, how does DNA deform in the electric field gradients induced by these obstacles and changes in channel dimensions? Or, how does the unhooking time of DNA entangled on an obstacle depend on its size and other experimental variables? Or, how does confinement affect a single DNA molecule's motion and conformation? This thesis will attempt to answer some of these questions.

1.2 Objectives

The goal of this research is to experimentally probe the fundamental physics that underlies the two broad classes of electrophoretic gene mapping techniques: obstacle course separations and DNA stretching. In general, the governing physics is complex due to background hydrodynamic flows, the confinement of the microchannel, the coiled-nature of the long-DNA molecules, and the induced electric field gradients from obstacles and changes in channel dimensions. Our focus will be on DNA deformation in electric field gradients and the single obstacle unhooking problem. For our experiments, we use soft lithography to construct thin PDMS (polydimethylsiloxane) microchannels with custom geometry, and fluorescence microscopy to track single molecules of DNA in these devices. The main topics of study are:

- Background flows in PDMS microchannels
- DNA dynamics in confinement
- DNA deformation in electric field gradients
- Collision of a DNA molecule with a post

By building on these fundamental studies, we also propose a new electrophoresis design for a DNA stretching DLA mapping device which can completely and uniformly stretch DNA molecules at finite "electrophoretic strain".

1.3 Overview of results

In Chapter 2, we present a background of polymer physics, electrophoresis, and deformation. Our goal here is to provide the very general foundation of the important physics that we expect to be important in our experiments. Chapter 3 details our experimental methods and procedures. We provide an introduction to single molecule fluorescence microscopy followed by a description of our analytical methods and detailed experimental procedures.

In Chapter 4 we discuss background hydrodynamic flows that often arise in these PDMS microchannels. These flows can potentially bias our experimental results so it is crucial that we understand and eliminate them. Chapter 5 details our first work with DNA to experimentally determine how polymer dynamics (diffusion coefficient D and relaxation time τ) are affected by confinement on the order of the radius of gyration R_g. The confined DNA diffusion coefficient is helpful to model dispersion and trajectory-dependent passage times, whereas the confined relaxation time is the central parameter for modeling deformation and relaxation processes in these microdevices. In Chapter 6 we address DNA in *electric field gradients*, which is important because all gene mapping devices under consideration require obstacles or channel constrictions and therefore introduce the DNA molecule to electric field gradients during electrophoresis. We look at two experimental electrophoresis case studies: DNA deformation at a stagnation point of a large cylinder and

DNA deformation in a hyperbolic contraction. In Chapter 7, we study the electrophoretic collision of a DNA molecule with a *small obstacle*, applicable to the popular hooking DNA separation mechanism. Using microscopy and automated tracking and collision time algorithms, we are able to directly determine both the probability of forming a hooked configuration and the probability distribution of unhooking times on microfabricated obstacles. Chapter 8 is an experimental study of a novel application derived from discoveries in previous chapters. Here we propose and experiment with a microchannel design that completely and uniformly stretches DNA molecules at finite electrophoretic strain. The device exploits principles of electrophoretic deformation, molecular individualism, and entropic extension in confinement. Chapter 9 summarizes our conclusions and outlook for future research in this area.

Chapter 2

Background Science

This chapter reviews some of the background science central to studying single molecule DNA physics in complex microfluidic electrophoresis devices. In this discussion, we will assume general knowledge of statistical mechanics, fluid mechanics, and electrodynamics. Specifically we will introduce:

2.1 Polymer statistical mechanics

2.2 Electrophoresis

2.3 Polymer deformation

2.4 Summary

In each section, we will provide a brief review of the material for the unfamiliar reader. Whenever possible, we will introduce topics from very general first steps, set up the problem, and then quote important results. We will also then directly relate the introduced topics specifically to the physics of DNA.

It is most important to stress that the DNA molecules we study are long, flexible, negatively charged molecules. The subjects reviewed here will help us understand both why DNA has these physical characteristics and consequently, what physics to expect in complex electrophoresis microchannels.

2.1 Polymer statistical mechanics

Long DNA molecules are polymers, *i.e.* "large" molecules made up of smaller repeating units. DNA is a linear polymer, meaning that its chemical backbone structure is continuous and without branches. DNA is found in cells in a compact complex with many proteins; the most abundant proteins are histones which DNA wraps around [28]. DNA analysis is often performed after these

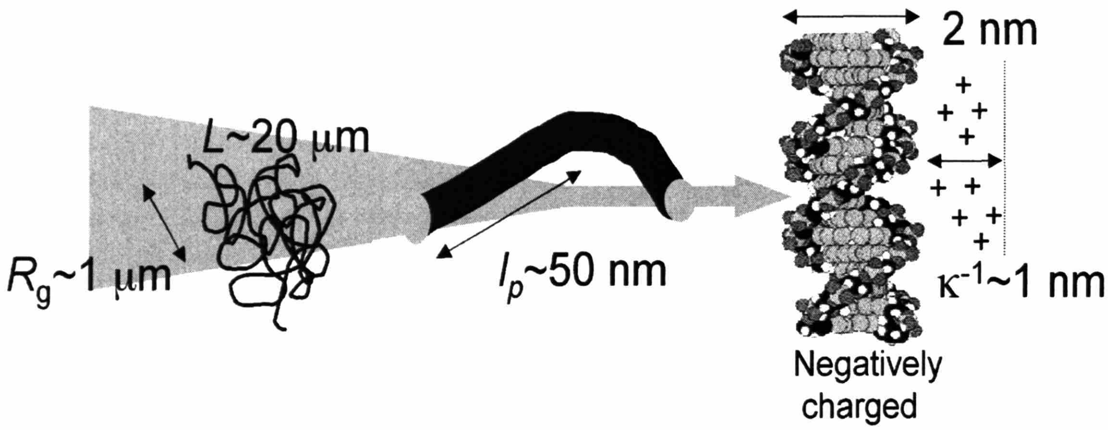

Figure 2-1: Length scales of a DNA molecule. O[kbp-Mbp] DNA have a coil dimension of ~ 1 μm. At the persistence length scale of DNA ($\sim$ 50 nm) DNA looks like a thin rod. The double-helix atomic structure and electrical double layer are apparent at the nanometer scale. Double helix structure taken from http://cs.felk.cvut.cz/ xobitko/ga/dna.html.

proteins are removed, which is why we will only consider DNA free of proteins in this work. DNA differs from common linear industrial polymers like polystyrene because 1) it has a *sequence*, or a non-repeating pattern of chemical monomers ("nucleotides" G, A, T, C) and 2) it is *double-stranded*, meaning that bases of one strand are hydrogen-bonded to complementary bases on another strand to make basepairs (bp), *e.g.* AT or GC. The two strands assemble into the famous "double helix" structure (Fig. 2-1). Despite these differences, a long DNA molecule's configuration and dynamics can still be modeled with classical polymer models because the four nucleotides are chemically very similar so that the *physical* properties of DNA generally do not depend strongly on its basepair sequence. The main consequence of these differences between DNA and common industrial polymers is that DNA is much stiffer. The stiffness is characterized by a characteristic length scale (l_p) at which the polymer appears straight. We will elaborate on this flexibility length scale below, but we should note that for DNA, this length scale is much larger (O[100 nm]) than it is for common polymers (O[1 nm]) because of DNA's double stranded backbone. Hence, DNA is a model polymer because its "random coil" dimension (R_g, described below) is routinely large enough to be studied with optical microscopy, yet still small enough that its configuration undergoes significant thermal fluctuations. When stretched out, a long DNA's contour length L is much longer than its coil size. Figure 2-1 shows the important length scales of DNA (specifically for O[kbp-Mbp] sizes that we are interested in), from R_g to l_p to the double-helix diameter of $\sim$ 2 nm. In order to quantitatively model the statistics of a single DNA's configuration in aqueous solutions, we turn to polymer statistical mechanics. We will be able to derive equilibrium properties of a DNA's configuration by examining moments of its end-to-end vector distribution $P(\mathbf{R})$, whereas we will extract dynamic properties of the configuration by the time correlation functions of the center of mass and the end-to-end vector.

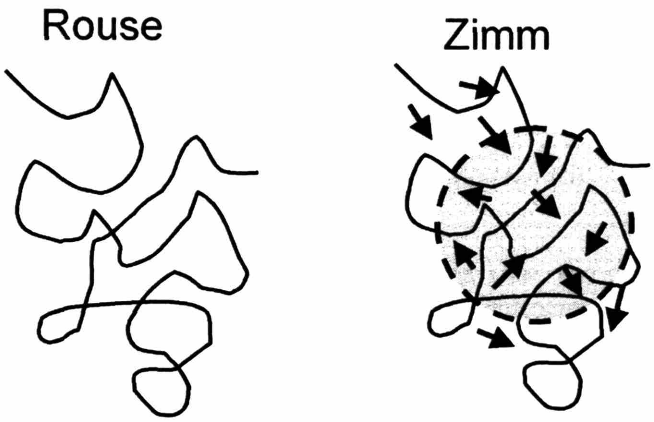

Figure 2-4: Schematics of a Rouse polymer (no hydrodynamic interactions) and a Zimm polymer with hydrodynamic interactions. The dashed circle implies that the Zimm polymer entrains solvent and its drag scales like a R_g-sized sphere.

Zimm Model: Including hydrodynamic interactions in the polymer dynamics model amounts to adding a perturbation fluid velocity at "bead" n from point forces due to the movement of all other $m \neq n$ "beads" of the chain. Consequently the Eq. 2.14 becomes:

$$\frac{\partial \mathbf{x}_n(t)}{\partial t} = \sum_m \mathbf{H}_{nm} \cdot \left(\frac{3kT}{l_k^2} \frac{\partial^2 \mathbf{x}_m(t)}{\partial m^2} + \mathbf{f}_m \right) \tag{2.20}$$

where $\mathbf{H}_{nm}$ is a version of the Oseen tensor [34, 66]:

$$\begin{aligned} \mathbf{H}_{nn} &= \boldsymbol{\delta}/\zeta_n \\ \mathbf{H}_{nm} &= \frac{1}{8\pi\eta|\mathbf{x}_{nm}|} \left(\frac{\mathbf{x}_{nm}\mathbf{x}_{nm}}{|\mathbf{x}_{nm}|^2} + \boldsymbol{\delta} \right), \qquad n \neq m \\ \mathbf{x}_{nm} &\equiv \mathbf{x}_n - \mathbf{x}_m \end{aligned} \tag{2.21}$$

Note that n and m mean "bead n" and "bead m" and despite notation similarities, $\mathbf{H}_{nm}$ is not at all related to the effective Hamiltonian H. To simplify the analysis of this n-body dynamical equation, Zimm [34, 67] used a preaveraging approximation, which approximates $\mathbf{H}_{nm}$ by its average for an *equilibrium distribution*:

$$\mathbf{H}_{nm} \rightarrow \langle \mathbf{H}_{nm} \rangle = \frac{1}{Z} \int \mathcal{D}\mathbf{R}(s) \mathbf{H}_{nm} P[\mathbf{R}(s)] \tag{2.22}$$

Using the approximation of Eq. 2.22, it is possible to obtain normal mode correlation functions as where $H_0[\mathbf{R}(s)]$ accounts for a potential resulting from chain connectivity and $H_{\text{int}}[\mathbf{R}(s)]$ includes any other potential energy, *e.g.* external field potentials, bending potentials, excluded volume interactions, etc. Following Boltzmann statistics, the configurational partition function is [29, 35]:

$$Z(N) = \int \mathcal{D}\mathbf{R}(s) \exp\left(-\frac{H[\mathbf{R(s)}]}{kT}\right) \tag{2.2}$$

where $H[\mathbf{R(s)}]$ is the effective Hamiltonian for the configuration and $\exp(-H[\mathbf{R(s)}]/kT)$ is the Boltzmann factor. The notation $\int \mathcal{D}\mathbf{R}(s)$ means a functional integral over all space curves or "paths" ($\int \mathcal{D}\mathbf{R}(s) \sim \int d\mathbf{x}_0 d\mathbf{x}_1 \ldots d\mathbf{x}_N$). From the formalism of statistical mechanics, the partition function is used to determine the expected probability of an observable. The probability distribution of a given configuration $P[\mathbf{R}(s)]$ is:

$$P[\mathbf{R}(s)] = \frac{1}{Z} \exp\left(-\frac{H[\mathbf{R}(s)]}{kT}\right) \tag{2.3}$$

One of the primary objectives of polymer statistical mechanical calculations is to determine the characteristic size of the polymer, and hence we can consider subsets of the configurational distribution. Specifically we investigate the distribution of the end-to-end vector $\mathbf{R}$. The probability distribution of a given end-to-end vector $P(\mathbf{R})$ is:

$$P(\mathbf{R}) = \frac{1}{Z} \int \mathcal{D}\mathbf{R}(s) \exp\left(-\frac{H[\mathbf{R}(s)]}{kT}\right) \delta\left(\mathbf{x}_N - \mathbf{R}\right) \tag{2.4}$$

Note that the integral in Eq. 2.4 is exactly the Euclidean (or "imaginary time") quantum mechanical path integral [36]. Equation 2.4 solves a diffusion equation and can be generally solved with Green's function techniques [36]. Hence the configuration of a Gaussian thread resembles the trajectory of a Brownian particle.

Gaussian polymer: freely jointed chain: The well-known potential energy, and hence the effective Hamiltonian, of a Gaussian thread is $H \equiv H_0[\mathbf{R}(s)] = \frac{3kT}{2l_k} \int_0^L ds (\frac{d\mathbf{R}(s)}{ds})^2$ [29, 34, 35]. Applying Eq. 2.4 with $H = H_0$ and taking the $N \gg 1$ limit gives the expected Gaussian distribution of the end-to-end vector [29, 34, 35]:

$$P(\mathbf{R}) = \left(\frac{3}{2\pi l_k^2 N}\right)^{3/2} \exp\left(\frac{-3\mathbf{R}^2}{2Nl_k^2}\right) \tag{2.5}$$

Note that the Gaussian distribution allows for infinitely long polymer configurations, which obviously is not true for a real polymer with finite N. However it is a sufficiently good configuration model for many polymers near equilibrium. With the moments ($\langle \mathbf{R}^n \rangle = \int d\mathbf{R}\mathbf{R}^n P(\mathbf{R})$) of the distribution function $P(\mathbf{R})$ we can determine the observable size of a typical polymer. Because $\langle \mathbf{R} \rangle = 0$, a Gaussian polymer's ends are most likely to be found at the same coordinates. The second moment, $\langle \mathbf{R}^2 \rangle = Nl_k^2$, gives the simplest measure of the characteristic size of a polymer coil. Note that this characteristic size $\langle \mathbf{R}^2 \rangle^{1/2} = N^{1/2} l_k$ is generally much smaller than the contour length of the molecule ($L = Nl_k$) because $N \gg 1$.

Another frequently used expression for the characteristic size of a polymer coil is the radius of gyration R_g, defined as $R_g^2 = \frac{1}{N} \sum_{n=0}^{N} \langle (\mathbf{x}_n - \mathbf{x}_{\text{com}})^2 \rangle$ where $\mathbf{x}_{\text{com}}$ is the center-of-mass position of the polymer. This is used particularly in the experimental community because it is difficult to observe the polymer's endpoints whereas it is possible to extract R_g measurements from light scattering [34, 35] and even fluorescence microscopy experiments [37]. For a Gaussian coil, $R_g^2 = \frac{1}{6} Nl_k^2$, which gives the characteristic size $\sim 40\%$ smaller than $\langle \mathbf{R}^2 \rangle$. The radius of gyration distribution function has been analyzed by Fixman [38] and later asymptotically solved by Fujita and Norisuye [39].

Freely jointed chain with interactions: Though the Gaussian chain model can mimic some dilute polymer solution equilibrium behavior, often it is too simple (as in the case of DNA). More detail is required to model the polymer's configurational potential energy. Next we consider a polymer thread model with additional potentials or interactions, *i.e.* $H_{\text{int}} \neq 0$ in Eq. 2.1. $H[\mathbf{R}(s)]$ can more generally be written as [29, 40]:

$$
\begin{aligned}
H[\mathbf{R(s)}] = & \int_0^L ds \frac{3}{2} \left| \frac{d\mathbf{R}(s)}{ds} \right|^2 + \int_0^L ds U_1[\mathbf{R(s)}] \\
& + \frac{1}{2!} \int_0^L ds ds' U_2[\mathbf{R}(s), \mathbf{R}(s')] + \frac{1}{3!} \int_0^L ds ds' ds'' U_3[\mathbf{R}(s), \mathbf{R}(s'), \mathbf{R}(s'')] + \ldots
\end{aligned}
\tag{2.6}
$$

where the first term is the potential of the Gaussian thread (accounting for connectivity of the chain), and U_n, $n = 1, 2, 3 \ldots$ are n-body interaction potentials for $\mathbf{R}(s)$. Actually, given our convention that the contour variable has units of length, the U_n potentials are actually potentials per unit length, area, volume, etc. Note that the factorial prefactors prevent overcounting identical n-body interactions. Typical 1-body interactions include external potentials and bending potentials (which we will see arise when considering DNA). A common 2-body interaction is the self-avoidance hard wall potential between two monomers. Adding interaction potentials will generally break the Gaussian distribution properties of the polymer end-to-end configuration. Additionally, any $n > 1$ -body interactions break the Markov chain properties and require many-body techniques such as field theory to make analytical progress.

1-body interactions: We consider two common 1-body potentials: an external hard wall (*i.e.* "a polymer in a box") and a bending potential. For a polymer in a slit confined in the z-direction:

$$
U_1 = \begin{cases} \infty & \text{for } |z| > L_{\text{box}}/2 \\ 0 & \text{for } -L_{\text{box}}/2 < z < L_{\text{box}}/2 \end{cases}
$$

Substituting this into Eqs. 2.6 and 2.4 and solving with a Green's function technique yields [34, p. 19]:

$$P(\mathbf{R}, N) \sim G_z(z_o, z_N, N) \exp\left(\frac{-3(x_0 - x_N)^2}{2Nl_k^2}\right) \exp\left(\frac{-3(y_0 - y_N)^2}{2Nl_k^2}\right) \tag{2.7}$$

where:

$$G_z(z_o, z_N, N) = \frac{2}{L_{\text{box}}} \sum_{p=1}^{\infty} \sin\left(\frac{p\pi z_0}{L_{\text{box}}}\right) \sin\left(\frac{p\pi z_N}{L_{\text{box}}}\right) \exp\left(-p^2\pi^2 N l_k^2 / 6L_{\text{box}}^2\right) \tag{2.8}$$

The main point to take away here is that the distributions of end-to-end displacement in the x- and y-directions are still Gaussian. Therefore, for a confined Gaussain chain, only the confined dimension shrinks. Obviously at some level of confinement, excluded volume will come into play and begin to affect unconfined dimensions of the chain.

The other 1-body potential we consider here is a bending potential. For common industrial polymers, the flexibility length scale is generally not much more than an order of magnitude greater than the backbone bond lengths. However, in certain polymers like DNA, the flexibility length scale can be more than 2 orders of magnitude larger than the bond rotation length scale. Consequently, we associate a bending potential energy to the conformation:

$$U_1 = \frac{\kappa^2}{2}\left|\frac{d^2\mathbf{R}(s)}{ds^2}\right|^2$$

where κ^2 is the bending modulus. It is also standard to apply a finite extensibility constraint $\left|\frac{d\mathbf{R}(s)}{ds}\right|^2 = 1$, which is to say that the tangent vector is a unit vector so that $\int_{s=0}^{s=L} \frac{d\mathbf{R}(s)}{ds} ds = L$. This polymer model with a bending potential and finite extensibility is called the *worm-like chain.* Much analytical work has been performed to compute configurational statics for the worm-like chain [29, 35, 41, 42], though the details are not required for this work. It is sufficient for us to consider the general properties of large worm-like chains, as these results apply closely to the DNA to be studied. The second moment of a worm-like chain is:

$$\langle \mathbf{R}^2 \rangle = 2Ll_p - 2l_p^2[1 - \exp(-L/l_p)] \tag{2.9}$$

where $l_p = \kappa^2/(kT)$ is the persistence length, a correlation length for the end-to-end vector along $\mathbf{R}(s)$. When $L/l_p \gg 1$, $\langle \mathbf{R}^2 \rangle = 2Ll_p$ and we recover the Gaussian $\langle \mathbf{R}^2 \rangle \sim N$ scaling. Using $L = Nl_k$ (where l_k is the Kuhn length), we see that substituting $l_p = l_k/2$ gives the exact second moment for a Gaussian chain. Consequently, the static configuration of a long worm-like chain with a persistence length l_p can be thought of as a Gaussian chain with $l_k = 2l_p$ and $L = Nl_k = 2Nl_p$. DNA's persistence length has been experimentally measured to be $l_p \sim 50$ nm at high ionic strength (O[0.1 M]) [43]. More details of the worm-like chain are found in Refs. [29, 35, 42].

Though the static properties of a long worm-like chain are basically rescaled versions of a Gaussian thread, a worm-like chain behaves much differently under an applied force. Stretching forces are generally applied to tethered polymers one of two ways: 1) from a constant pulling force on the free end or 2) from a constant background flow or field [44]. Note that the second situation is much more complex than the first due to coupled elastic and hydrodynamic effects which result in a non-uniform tension distribution in the chain. DNA extension in a constant background flow or field has been studied experimentally [45, 46] and analytically [44, 47–51]. The results confirm 1) tension is non-uniform along the stretched polymer's backbone, 2) the polymer is not free-draining, even when highly extended, and 3) the fractional extension results show universal behavior when plotted against the function $\eta v L^{\gamma}$ where $0.54 < \gamma < 0.75$ [45, 52]. This is the type of extension we may expect in DNA-obstacle hooking collisions.

Pulling the chain at its ends isolates the thermodynamic elasticity from hydrodynamics. Constant tension stretching is effectively adding another 1-body interaction to the polymer model, so it has been studied for both a freely jointed chain and a worm-like chain [44, 53]. The force-extension of a freely jointed chain obeys the inverse Langevin function (Eq. 2.10), a general result for the effect of an orienting field on anything with dipole symmetry [53].

$$\frac{f_{FJC} l_k}{kT} = \mathcal{L}^{-1}\left(\frac{x_{\text{ex}}}{L}\right), \quad \mathcal{L}(x) = \coth(x) - 1/x \tag{2.10}$$

However a worm-like chain displays different force-extension behavior. A useful approximate interpolation formula was presented by Marko and Siggia [44]:

$$\frac{f_{WLC} l_p}{kT} = \frac{x_{\text{ex}}}{L} - \frac{1}{4} + \frac{1}{4(1 - x_{\text{ex}}/L)^2} \tag{2.11}$$

Figure 2-3 shows a comparison of the two laws using $l_k = 2l_p$. Note specifically that they show different high-extension behavior. DNA's elasticity has been experimentally proven to nicely fit the worm-like chain force-extension curve (Eq. 2.11) [54, 55]. A force on the order of 1 pN is required to stretch DNA to nearly its entire contour length.

n-body interactions: field theory: Calculations with pair potentials (U_2) or higher-body potentials require a true n-body treatment. One can see the difficulty dealing with $n >$ 1-body interactions in Eq. 2.6, as these interactions require nested integrals that break the local Markov property of the chain. These interactions are *non-local* meaning that effects from distant regions (far away in s to be precise) of the polymer configuration can affect the behavior of any other piece of the polymer. An elegant method to treat these n-body interactions, as first shown by Edwards [56] who considered the excluded volume pair potential, is to introduce a fluctuating field that acts to localize all non-local interactions. Briefly, this is possible because no interactions explicitly depend on the parametrization $n = s/l_k$ and it is possible to examine a coarse-grained version of the problem where n-body interactions depend on the local monomer density $\rho(\mathbf{x}) = (1/l_k) \int_0^L ds \delta(\mathbf{x} - \mathbf{R}(s))$ [29, 36, 40, 57, 58].

As mentioned above, self avoidance is a 2-body interaction. The hard wall interaction potential that dictates that two monomers cannot occupy the same coordinates is:

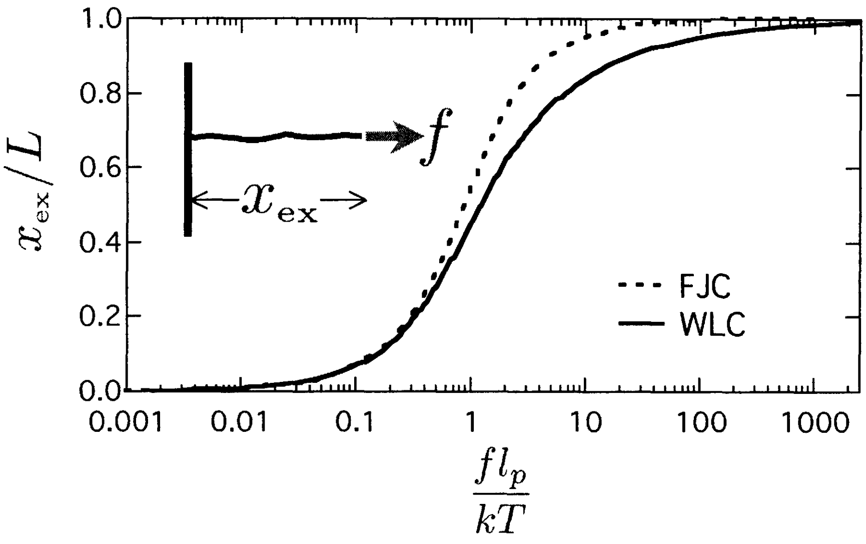

Figure 2-3: Polymer force-extension curves for a freely jointed chain (FJC) and a worm-like chain (WLC) using $l_k = 2l_p$.

$$U_2 = \frac{VkT}{l_k^2}\delta\Big(\mathbf{R}(s) - \mathbf{R}(s')\Big) \tag{2.12}$$

where V is the excluded volume which has units of volume and the delta function (from its normalization convention) implies units of inverse volume. Using the potential of Eq. 2.12, the interacting field theory for a self avoiding polymer becomes equivalent to the well-known ϕ^4 theory of condensed matter physics and quantum field theory [40, 59]. The primary effect of self-avoidance is that the scaling law for the second moment of the end-to-end vector $\langle \mathbf{R}^2 \rangle$ (measures characteristic coil size) changes:

$$\langle \mathbf{R}^2 \rangle \sim N^{2\nu} l_k^2 \tag{2.13}$$

where $\nu \simeq 3/(d+2)$ and $d \leq 4$ is the dimension of space [36, Sec. 15.9]. In 3 dimensions, $\langle \mathbf{R}^2 \rangle^{1/2} \sim N^{\nu} l_k$ where $\nu \approx 3/5$. To be exact, renormalization group methods have shown $\nu = 0.589$ [60]. Hence, self-avoiding polymer coils have an expanded configuration compared to Gaussian coils. The importance of self-avoidance depends critically on the monomer-solvent interaction. For "good solvents," the polymer configurational statistics are best modeled with a self-avoiding interaction. The self-avoidance interaction and polymer-solvent interaction exactly cancel in "theta solvents", whereas "poor solvents" have an attractive interaction between monomers that dominate self-avoidance. Moderate pH buffers like TBE are good solvents for DNA [61]

The equilibrium effects of other 2-body interactions like long-range Coulombic potentials have also been investigated [40, 62]. Although DNA is charged, as we will explain in Section 2.2, Coulombic interactions are short range for DNA in aqueous solutions, though they may affect the persistence length [43, 62].

2.1.2 Dynamic behavior of polymers

The previous sections addressed models for static properties of a polymer's configuration using equilibrium statistical mechanics. However, DNA dynamical properties will also be important in our study of how DNA moves and deforms during electrophoresis. Specifically, we will see that center of mass motion can be described in terms of a diffusivity $D = kT/\zeta$ (where ζ is the DNA's drag coefficient) and polymer deformation can be analyzed in terms of a spectrum of relaxation times τ_p. Obtaining these parameters requires a balance of the major forces on the appropriate molecular scale. We will see that collective effects from intra-chain hydrodynamic interactions are considered important because of their slow decay with distance.

Rouse model: The simplest model of polymer dynamics, known as the *Rouse model* [34, 63], considers the motion of a "phantom" Gaussian chain without any intra-chain hydrodynamic interactions. By "phantom" we mean that the polymer does not have self-avoiding interactions and can therefore have pieces crossing and occupying the same coordinates. Neglecting hydrodynamic interactions amounts to assuming the motion of one piece of the chain does not cause a disturbance flow in the solvent that affects the motion of any other piece of the chain. By balancing the drag force, the force from connectivity, and the Brownian force from the solvent, and then taking the continuous limit, one arrives at the Langevin equation for a Rouse polymer:

$$\zeta_n \frac{\partial \mathbf{x}_n(t)}{\partial t} = \frac{3kT}{l_k^2} \frac{\partial^2 \mathbf{x}_n(t)}{\partial n^2} + \mathbf{f}_n \tag{2.14}$$

where ζ_n is the drag coefficient of a Kuhn monomer and $\mathbf{f}_n$ is the Brownian force with moments satisfying the fluctuation-dissipation theorem [34]. Though the Rouse model does adopt the continuous chain limit, it is useful to retain the discrete notation for the contour length variable $s = nl_k$. Consequently, we can look at Eq. 2.14 as a system of n coupled oscillators with thermal fluctuations. Notice the time-dependent behavior of one monomer n depends on other monomers through the second derivative term. A useful method to solve such an equation is to adopt *normal coordinates* [34, p. 94, Appendix 4.II]. Analogous to a Fourier transform, this amounts to a coordinate change that decouples the motion of oscillator modes. By choosing normal coordinates $\mathbf{X}_p \equiv 1/N \int_0^N dn\ \cos(pn\pi/N)\mathbf{x}_n(t)$ with $p = 0, 1, 2 \ldots$, Eq. 2.14 transforms to:

$$\zeta_p \frac{\partial \mathbf{X}_p}{\partial t} = -k_p \mathbf{X}_p + \mathbf{f}_p \tag{2.15}$$

where:

$$\begin{aligned} \zeta_0 = N\zeta_n \quad \& \quad \zeta_p &= 2N\zeta_n \quad \text{for } p = 1, 2, \ldots \\ k_p &= \frac{6\pi^2 kT}{Nl_k^2} p^2 \quad \text{for } p = 0, 1, 2, \ldots \end{aligned} \tag{2.16}$$

Since the motion of each $\mathbf{X}_p$ is independent of all other $\mathbf{X}_p$, the dynamical motion of the polymer has been converted into independent modes. Generally speaking, $\mathbf{X}_0$ is the center of mass of the polymer and $\mathbf{X}_p$ (for $p > 0$) represents the local motion of a chain with N/p segments [34]. Dynamic properties are computed from time correlation functions. Reference [34, Ch. 4] provides the details of these time correlation calculations.

Using the calculated time correlation functions and the inverse transform $\mathbf{X}_p \rightarrow \mathbf{x}_n$, one can show that the mean square displacement of the center of mass ($\mathbf{x}_{com}$) is then:

$$\langle (\mathbf{x}_{com}(t) - \mathbf{x}_{com}(0))^2 \rangle = \frac{6kT}{N\zeta_n} t \tag{2.17}$$

The polymer's diffusion coefficient is therefore $D = kT/(N\zeta_n)$. Note that the total drag for a Rouse polymer scales linearly with N ($\zeta = N\zeta_n$).

Similarly, the time correlation function for the end-to-end vector can be computed:

$$\langle \mathbf{R}(t) \cdot \mathbf{R}(0) \rangle = Nl_k^2 \sum_{p,odd} \frac{8}{p^2\pi^2} \exp(-tp^2/\tau_1) \tag{2.18}$$

where $\tau_1 = \zeta_n N^2 l_k^2/(3\pi^2 kT)$ is called the longest relaxation time of the polymer, and we see that this time correlation function is described by a series of modes τ_p where $\tau_p = \tau_1/p^2$. The longest relaxation time governs the long-time dynamics of end-to-end vector relaxation; it is essentially a characteristic rotational time for the polymer's configuration. We distinguish τ_1 from the longest stress relaxation time τ, which is the characteristic time for a stretched polymer to relax back to an equilibrium coil. Stress relaxation modes τ_P can be computed with the Rouse model and assuming linear elasticity for small deformation. The result is that these characteristic times are related by a factor of 2 ($\tau_P = \tau_p/2$) [64, 65]. We will generally only be concerned with the longest stress relaxation time ($P = 1$) which is:

$$\tau = \zeta_n N^2 l_k^2/(6\pi^2 kT) \tag{2.19}$$

Note that $D \sim N^{-1}$ and $\tau \sim N^2$ for the Rouse model. These scalings *do not* reproduce experimental results. The main deficiency of the Rouse model is the neglect of hydrodynamic interactions, which as we show here, shifts these scalings.

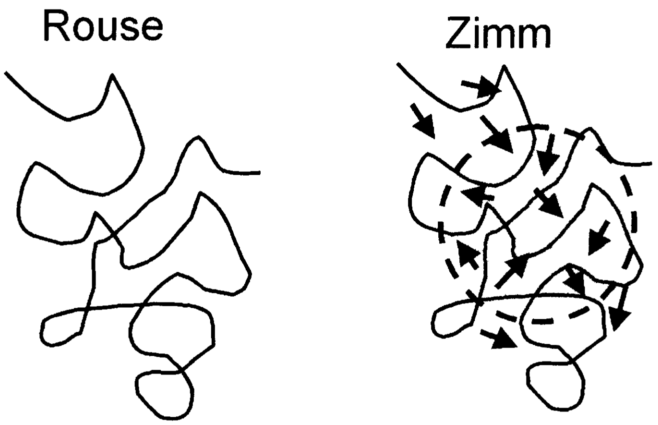

Figure 2-4: Schematics of a Rouse polymer (no hydrodynamic interactions) and a Zimm polymer with hydrodynamic interactions. The dashed circle implies that the Zimm polymer entrains solvent and its drag scales like a R_g-sized sphere.

Zimm Model: Including hydrodynamic interactions in the polymer dynamics model amounts to adding a perturbation fluid velocity at "bead" n from point forces due to the movement of all other $m \neq n$ "beads" of the chain. Consequently the Eq. 2.14 becomes:

$$\frac{\partial \mathbf{x}_n(t)}{\partial t} = \sum_m \mathbf{H}_{nm} \cdot \left(\frac{3kT}{l_k^2} \frac{\partial^2 \mathbf{x}_m(t)}{\partial m^2} + \mathbf{f}_m \right) \tag{2.20}$$

where $\mathbf{H}_{nm}$ is a version of the Oseen tensor [34, 66]:

$$\begin{aligned} \mathbf{H}_{nn} &= \boldsymbol{\delta}/\zeta_n \\ \mathbf{H}_{nm} &= \frac{1}{8\pi\eta|\mathbf{x}_{nm}|} \left(\frac{\mathbf{x}_{nm}\mathbf{x}_{nm}}{|\mathbf{x}_{nm}|^2} + \boldsymbol{\delta} \right), \qquad n \neq m \\ \mathbf{x}_{nm} &\equiv \mathbf{x}_n - \mathbf{x}_m \end{aligned} \tag{2.21}$$

Note that n and m mean "bead n" and "bead m" and despite notation similarities, $\mathbf{H}_{nm}$ is not at all related to the effective Hamiltonian H. To simplify the analysis of this n-body dynamical equation, Zimm [34, 67] used a preaveraging approximation, which approximates $\mathbf{H}_{nm}$ by its average for an *equilibrium distribution*:

$$\mathbf{H}_{nm} \to \langle \mathbf{H}_{nm} \rangle = \frac{1}{Z} \int \mathcal{D}\mathbf{R}(s) \mathbf{H}_{nm} P[\mathbf{R}(s)] \tag{2.22}$$

Using the approximation of Eq. 2.22, it is possible to obtain normal mode correlation functions as outlined for the Rouse model. The details are found in Ref. [34, Sec. 4.2]. The important results are that:

$$\begin{aligned} D &= 0.196\frac{kT}{\eta N^{1/2} l_k} \quad \text{and} \\ \tau_1 &= 0.325\frac{\eta N^{3/2} l_k^3}{kT} \end{aligned} \tag{2.23}$$

The Zimm model results for $D \sim N^{-1/2}$ and $\tau \sim N^{3/2}$ have been confirmed experimentally in theta solvents. For polymers in a good solvent like DNA in a TBE buffer, we can also compute Rouse and Zimm dynamic parameters by including excluded volume in the preaveraging steps. The main results, either using a linearization approximation [34] or renormalization group theory [68], indicate a simple re-scaling of the drag length scale so that $D \sim N^{-\nu}$ and $\tau \sim N^{3\nu}$. These are the scalings we expect for a single kbp-Mbp DNA in an unbounded good solvent (like TBE). The diffusivity scaling has been confirmed experimentally [61].

2.1.3 DNA statistical mechanics summary

We have introduced a large amount of general information on how to model a polymer's equilibrium and dynamic properties. It is useful to pause here and gather the important points for studying DNA. Recall the the static properties of DNA in an aqueous solvent can be modeled as a worm-like chain with excluded volume. Thus, for long DNA ($L \gg l_p$), the static configurational properties are the same as a self-avoiding freely jointed chain with $l_k = 2l_p$ where $l_p \sim 50$ nm [43]. However, DNA's force-extension behavior obeys the worm-like chain result, which scales differently with fractional extension than a freely jointed chain at high extension. Finally, DNA's dynamic properties in an unbounded fluid follow Zimm scalings (with excluded volume) which includes the effects of averaged intra-chain hydrodynamic interactions on the molecule's drag.

2.2 Electrophoresis

Charged surface physics: When a surface, colloidal object, or solute molecule is placed in a fluid, quite often it will carry an equilibrium charge from ionic reactions with the buffer. In aqueous buffer solutions, the pH will govern the degree of charging. For example, for DNA the pH will dictate how many backbone phosphate group deprotonate to give it a negative charge. When a surface acquires a charge, it induces a local electric field, and at steady state, an induced ion concentration gradient in the surrounding fluid. Determination of these induced effects is important to developing models of how charged objects move in an externally applied electric field.

In order to calculate the induced field and ion concentrations, several approximations are generally made [69]:

- Charge is evenly distributed on the smooth surface of the charged object.
- Ions are treated like point charges.
- The induced electric potential goes to zero far away from the charged object.
- The fluid dielectric constant ϵ_{de} is independent of field strength.

Quite often the charged object is assumed to be much larger than the characteristic distance over which the induced electric potential goes to zero, so that all surfaces reduce to a one-dimensional planar geometry. We will assume this for now but come back to this point when we try to apply the results to DNA electrophoresis. Figure 2-5 (a) shows a schematic of the charged surface with the induced potential and ion concentrations (ignore the velocity field for now).

From Maxwell's equations (Gauss' Law) [70], the electrostatic potential ϕ and induced ion charge distribution (c_i for species i) are related by $\epsilon_{de}\nabla^2\phi = -\sum_i z_i F c_i$, where z_i is the charge of species i and F is Faraday's constant. With the large-object approximation and assuming the ionic concentrations can be described by Boltzmann statistics ($c_i(x) = c_{\text{bulk}}\exp[-z_i F\phi(x)/(RT)]$), the above equation simplifies to the one dimensional Poisson-Boltzmann equation. Because electrokinetic equations can be extremely complex, most analytical calculations are performed with a further approximation that the ionic species are "symmetric", *i.e.* $z_+ = -z_- = z$. This is generally not true, however the following analysis captures the important physical behavior. This simplifies the Poisson-Boltzmann equation to:

$$\frac{d^2\phi}{dx^2} = \frac{2zFc_{\text{bulk}}}{\epsilon_{de}}\sinh\left(\frac{zF\phi(x)}{RT}\right) \tag{2.24}$$

where x is the coordinate perpendicular to the charged surface (extending into the solution) and c_{bulk} is the bulk concentration of the symmetric ions. Using one final approximation that $zF\phi(x) \ll RT$, Eq 2.24 reduces to:

$$\frac{d^2\phi}{dx^2} = \kappa^2\phi(x) \qquad \text{where } \kappa^{-1} = \sqrt{\frac{\epsilon_{de}RT}{2z^2F^2c_{\text{bulk}}}} \tag{2.25}$$

This last approximation, called the Debye-Huckel approximation [69, 71], yields the solution $\phi(x) = \phi(0)\exp(-\kappa x)$ with κ^{-1} known as the Debye length. The Debye length is the characteristic length scale over which the induced electric potential of the charged object decays. Consequently, at distances much larger than the Debye length, charged objects do not attract other charged objects. These DNA experiments occur in buffers that can range from $c_{\text{bulk}} = 0.01$ M to 0.2 M, so consequently $\kappa^{-1} \sim 1 - 3$ nm. Since charge screening occurs over very small distances, distances much smaller than a DNA's persistance length (O[50 nm]), electrostatic potentials will not be important in DNA statistical mechanics or dynamics on the coil length scale. The Debye approximation is not strictly valid for DNA in TBE buffer because $zF\phi(x) \sim RT$. Consequently, Eq. 2.24 can be solved more generally with Gouy-Chapman theory [69, 71]. Nevertheless, despite the linearization and symmetric ion assumptions, the Debye-Huckel solution closely captures the important physics of the screening length scale κ^{-1}.

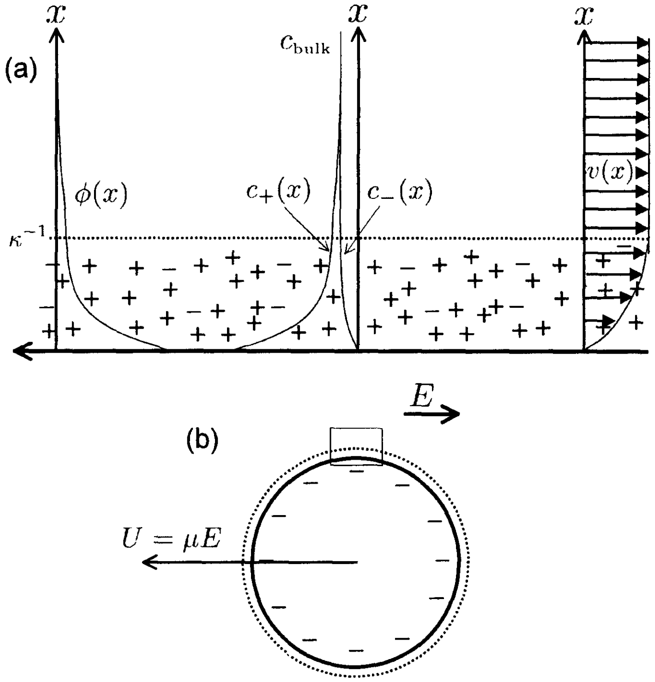

Figure 2-5: Schematic of (a) the double layer and (b) a charged sphere in a uniform external field E. The region of (a) is in the box of (b) (not to scale). Shown in (a) are characteristic profiles for the electric potential ϕ, ion concentrations c_+ and c_-, and fluid velocity v in the sphere's reference frame.

Electrophoretic motion: We have just shown that equilibrium chemistry of ionic groups on a solid surface induces a short ranged electric field and ion concentration gradient. The counter ion concentration rises in this local region whereas the co-ion drops and there is a net charge density in the fluid near the surface. When an external field is applied through the fluid, the surface physics lead to the phenomenon of *electrophoresis.* The charged object will move through the solvent because the fluid near the surface has a net charge and therefore is subject to an electric force that initiates flow. Mathematically the flow comes from an extra term in the Stokes equation for the electrical body force on the fluid[1]. However the external field, ionic current, and induced flow can all affect the local potential and ionic concentrations around the charged object. Consequently, an external electric field leaves us with a highly coupled electrohydrodynamic problem. The derivation of the governing equations and boundary conditions for electrophoresis can be found in many references however, Refs. [72, Sec. 7], [73] and [69, Sec. 4.6] provide very useful details. We will simply set up the general governing equations, quote results, and comment on the appropriate simplifications to decouple the velocity, ionic concentration, and electric fields. Figure 2-5 depicts the problem.

The governing equations are the Nernst-Planck equation for conservation of charge, Gauss' equation for electrostatics, Stokes equation for conservation of momentum, and the continuity equation for conservation of mass. In dimensionless terms they become [72, 73]:

$$\begin{aligned} \frac{\partial \hat{c}_i}{\partial \hat{t}} &= \hat{D}_i \nabla \cdot [\nabla \hat{c}_i + z_i \hat{c}_i \nabla \hat{\phi}] + \text{Pe}\ \nabla \cdot (\hat{c}_i \hat{\mathbf{v}}) \\ \left(\frac{\kappa^{-1}}{L}\right)^2 \nabla^2 \hat{\phi} &= -\sum_i z_i \hat{c}_i \\ \frac{\eta U}{L c_{\text{bulk}} RT} (\nabla^2 \hat{\mathbf{v}} - \nabla \hat{\mathscr{P}}) &= \sum_i z_i \hat{c}_i \nabla \hat{\phi}, \qquad \nabla \cdot \hat{\mathbf{v}} = 0 \end{aligned} \tag{2.26}$$

where terms are non-dimensionalized as:

$$\hat{t} = \frac{tD^*}{L^2}, \quad \hat{D}_i = \frac{D_i}{D^*} \quad \hat{c}_i = \frac{c_i}{c_{\text{bulk}}}, \quad \hat{\phi} = \frac{\phi}{RT/F}, \quad \hat{\mathbf{v}} = \frac{\mathbf{v}}{U}, \quad \hat{\mathscr{P}} = \frac{\mathscr{P} L}{\eta U} \tag{2.27}$$

with Pe $= UL/D^*$, D^* as the effective ion diffusivity ($D^* = 2D^+D^-/(D^+ + D^-)$), U as the characteristic velocity scale (electrophoretic velocity), $\mathscr{P}$ as the dynamic pressure, and all distances non-dimensionalized by the colloid length scale L. Appropriate boundary conditions can be found in Ref. [72] but briefly they include: no slip, no ion flux, and a constant potential at the solid surface, and all variables approach their far-field values at infinity. Note immediately that this set of equations is highly coupled; changes in $\hat{c}_i$, $\hat{\phi}$, $\hat{\mathscr{P}}$, or $\hat{\mathbf{v}}$ will affect all other variables. The grouping of dimensionless parameters multiplying the Laplacian in Stokes equation is a measure of charge convection in the double layer versus charge conduction in the bulk and is generally much less than one for parameters of interest in DNA electrophoesis. Furthermore, the term $(\kappa^{-1}/L)^2$

---

[1] Objects we consider will be "small" so that the Reynolds number will be much less than one. This reduces the non-linear Navier-Stokes equation to the linear Stokes equation [66, Ch. 7].

multiplies the Laplacian in Gauss' equation and we are assuming $\kappa^{-1}/L \ll 1$. In both cases we find a singular perturbation which leads to a boundary layer solution. A boundary-layer analysis of this problem greatly simplifies the solution, but nevertheless, it still remains a complex coupled problem unless more approximate limits are taken. Adding to previous approximations, notably $\kappa^{-1} \ll L$, Smoluchowski derived a simplified solution to Eqs. 2.26 in a realistic limit of low surface (double layer) conduction and Pe $\ll$ 1. The Smoluchowski solution implies $\nabla\hat{\mathscr{P}} = 0$, *i.e.* it considers "pure" electrophoresis without a background pressure drop. Basically, the Smoluchowski solution is valid for a colloid or molecule with a thin double layer and moving slow enough so that its double layer does not polarize. Smoluchowski's solution for the bulk velocity is:

$$\mathbf{v} = -\frac{(\phi_\zeta - \phi(x))\epsilon_{de}\mathbf{E}}{\eta} \tag{2.28}$$

where ϕ_ζ is the zeta potential of the surface, ϵ_{de} is the fluid permittivity, η is the fluid viscosity, and $\mathbf{E}$ is the electric field. The zeta potential and permittivity notation are not standard, but we choose this notation to avoid confusion with drag and strain (used heavily elsewhere). The electrophoretic mobility of the particle in an external electric field is then:

$$\mu = \frac{\phi_\zeta \epsilon_{de}}{\eta} \tag{2.29}$$

Note that this value is solely dependent on solvent parameters and the surface potential and *independent of the object's size.* We will employ the convention of using a minus sign for the mobility if the object is negatively charged ($\phi_\zeta < 0$). DNA is negatively charged so that $\mu\mathbf{E}$, which points in the direction electrophoretic motion, is in the opposite direction of $\mathbf{E}$.

The above analysis is for a "large" colloid with a smooth surface. However O[kbp-Mbp] DNA is best modeled as a long coiled up Gaussian thread with a coil radius of $R_g \sim 1$ μm, persistence length of $l_p \sim 50$ nm and a thread thickness of $d \sim 2$ nm. How does the above analysis pertain to DNA? The clearest description of the mobility of a charged polymer like DNA is given in Ref. [156] using a bead-spring model of the polyelectrolyte. Considering effects from flows, fields, Brownian motion, linear elasticity, and hydrodynamic interactions, the Langevin equation for bead n is:

$$\frac{d\mathbf{x}_n}{dt} = \frac{1}{\zeta_n}[\mathbf{T}(\mathbf{x}_n) + \mathbf{g}(\mathbf{x}_n)] + \mathbf{u}^{\infty}(\mathbf{x}_n) + \mu_n\mathbf{E}(\mathbf{x}_n) + \mathbf{u}_{\text{HI}}(\mathbf{x}_n) \tag{2.30}$$

where ζ_n is the bead drag coefficient, μ_n is the bead mobility, and for the n^{th} bead, $\mathbf{x}_n$ is the position vector, $\mathbf{T}(\mathbf{x}_n)$ is the force due to gradients in tension along the polymer, $\mathbf{g}(\mathbf{x}_n)$ is the Brownian force, $\mathbf{u}^{\infty}(\mathbf{x}_n)$ is the imposed flow field, $\mathbf{E}(\mathbf{x}_n)$ is the imposed electric field, and $\mathbf{u}_{\text{HI}}(\mathbf{x}_n)$ is the induced velocity from hydrodynamic interactions from all other beads of the polyelectrolyte. A general form for $\mathbf{u}_{\text{HI}}(\mathbf{x}_n)$ is [156]:

$$\mathbf{u}_{\mathrm{HI}}(\mathbf{x}_n) = \sum_m \mathbf{H}_{nm}[\mathbf{T}(\mathbf{x}_m) + \mathbf{g}(\mathbf{x}_m)] + \sum_m \mathbf{H}^{\mathrm{EL}}_{nm}[q_m \mathbf{E}(\mathbf{x}_m)] \tag{2.31}$$

where q_m is the charge of the m^{th} bead, $\mathbf{H}_{nm}$ mediates flow disturbances due to non-electric forces from bead m on bead n (which is the Oseen tensor in the far-field limit), and $\mathbf{H}^{\mathrm{EL}}_{nm}$ mediates similar flow disturbances due to electrophoresis of a charged bead. As done for the Rouse and Zimm models, they adopt normal coordinates and solve for normal modes using the pre-averaging approximation for hydrodynamic interactions. In the case of *high-salt concentration* and for a *uniformly charged chain*, the resulting molecular mobility is size-independent and equal to the local mobility μ_n. The size-independent mobility of DNA is the primary reason physical barriers must be incorporated to size-separate DNA. Furthermore, the deformation modes have zero amplitude so that *a uniformly charged chain moves without average deformation* [156]. Can we directly apply the Smoluchowski mobility to equal to DNA mobility? At first glance, the answer is not completely clear. Recall that the bead size must be much greater than κ^{-1} for the Smoluchowski solution (Eq. 2.29) to be valid. Even though R_g and l_p are generally much greater than κ^{-1}, d is about the same as κ^{-1}. Since $l_p \gg \kappa^{-1}$ though, we can still apply Smoluchowski's result to a DNA persistence length moving parallel to the field, which states the mobility is independent of size and shape. Some theoretical work has been done by Stigter [74–76] to compute the mobility differential when a DNA rod is aligned perpendicular versus parallel to the external electric field. The calculated mobility differential is O[1] and no experimental work has confirmed its importance.

All experimental work to date shows that large DNA obeys the linear Smoluchowski scaling at low fields in TBE buffers with μ independent of field strength and size [77]. However, smaller DNA (< 400 bp) and DNA in hybrid asymmetric buffers have shown evidence of non-linear electrokinetic behavior, though these effects are small [77, 78]. For example, the mobility for a 10 bp DNA fragment is only ~ 10 % lower than that of a large coil [77]. Nevertheless, it is unclear if the DNA mobility is exactly the Smoluchowski mobility. For our purposes we can take μ as an experimentally measured constant for a given solvent so that the velocity of all sections of the DNA molecule in a uniform external field is μE.

Non-linear electrophoresis: When the conditions required for the Smoluchowski equation derivation are not met, *i.e.* when high electric fields and velocities exist, nonlinear electrokinetic effects [72, 79–81] arise. Nonlinear electrokinetic effects are forces or flows not directly proportional to $\mathbf{E}$, which result from nonlinear coupling in Eq. 2.26. The two primary nonlinear electrokinetic effects in DC fields are dielectrophoretic forces [70] and induced charge fields and flows [72, 81]. Both of these phenomena result from polarization of the O[nm] electrical double layer around the charged object which in turn results from large ionic currents in the double layer. A polarized object in an electric field gradient experiences a dielectrophoretic force $\mathbf{F}_{\mathrm{DEP}} = \alpha|\mathbf{E}|\nabla\mathbf{E}$, where α may depend on frequency for an AC field, and we have taken the low frequency limit. Furthermore, a polarized double layer has recently been shown in some cases to induce long range ionic concentration gradients *outside of the double layer* [81]. Hence, polarization may induce long range induced electroosmotic flows from diffusiophoresis [82], *i.e.* the flow induced by an ionic species concentration gradient.

These nonlinear effects have not been studied in conjunction with single DNA electrophoresis, but given previous observations of DNA's polarizability and aggregation [83–85], they are bound to

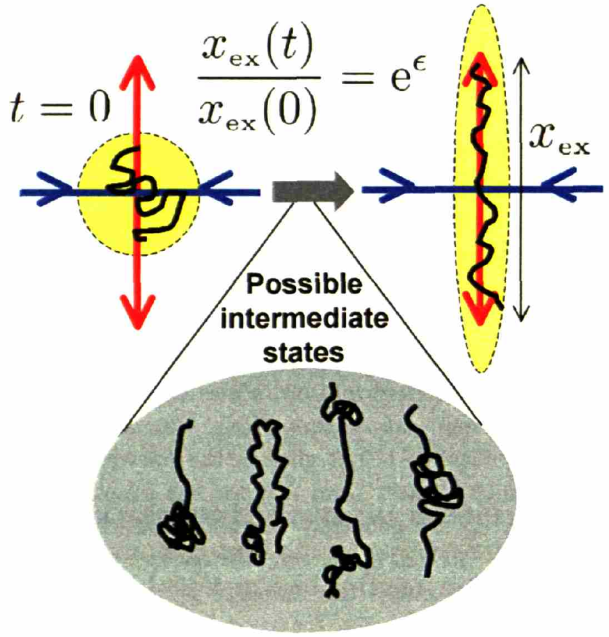

Figure 2-6: Schematic of affine deformation and polymer deformation in extensional flow. The axis of extension is depicted vertically in red and the axis of compression is depicted horizontally in blue. An ideal deformable object (yellow) and a polymer are depicted at $t = 0$ and a later time. In the gray area we show some possible intermediate configurations of the polymer (from left to right: a "half-dumbbell", a "fold", a "dumbbell", and a "coil").

arise at high enough fields O[kV/cm]. The studies in this thesis are generally restricted to low field strengths (O[10-100 V/cm]) where these nonlinearities were not observable, though, based on experimental observations, we do speculate when they might arise in Chapter 8.

2.3 Polymer deformation

In the statistical mechanics section above, we noted that DNA equilibrium configurations expand by excluded volume or by being pulled by an external force. On the other hand, DNA can be dynamically deformed by placing it in a field or flow gradient. Most previous work has addressed polymer and DNA deformation in flow gradients, which we summarize here.

Kinematics: Polymer deformation in hydrodynamic flows ($\mathbf{v} = \mathbf{u}^{\infty}$)[2] has been classified by kinematic models of the gradient in the flow field $\nabla\mathbf{u}^{\infty}$. We gain some physical insight by decomposing the velocity gradient tensor into its symmetric and anti-symmetric parts, *e.g.* $\nabla\mathbf{u}^{\infty} = \mathbf{\Gamma} + \mathbf{\Omega}$, where $\mathbf{\Gamma}$ is the symmetric rate-of-strain tensor and $\mathbf{\Omega}$ is the anti-symmetric vorticity tensor. It

---

[2] We use $\mathbf{u}^{\infty}$ for the background flow in which the polymer is placed, *i.e.* the undisturbed velocity field. In general, polymers will locally perturb $\mathbf{u}^{\infty}$.

can be shown that $\mathbf{\Gamma}$ solely governs the local deformation of fluid elements whereas $\mathbf{\Omega}$ controls the local rotation of fluid elements [66, Ch. 5]. For comparison with electrophoretic stretching, we are primarily concerned with strong deformation and specifically, 2-dimensional (2D) extensional flows with $\mathbf{\Omega} = \mathbf{0}$, though as we review below, researchers have studied DNA deforming in all types of flows. The local deformation in 2D extensional flows can be represented by a 2×2 symmetric matrix with (recalling the properties of symmetric matrices) eigenvalues $\pm\dot{\epsilon}$ and orthogonal eigenvectors $\mathbf{p}_+$ and $\mathbf{p}_-$.

Figure 2-6 shows a schematic of an ideal flexible object (yellow) and a polymer in an extensional flow ($\mathbf{p}_+$ vertically in red and $\mathbf{p}_-$ horizontally in blue) at $t = 0$ and at a later t. When introduced to a 2D extensional flow field, an ideal flexible object will exponentially extend along the axis of extension $\mathbf{p}_+$ and exponentially compress along the axis of compression $\mathbf{p}_-$ at a rate governed by the strain rate $\dot{\epsilon}$. This ideal deformation is known as "affine deformation". Hence, deformation of polymers is analyzed with extension-strain plots where strain ϵ is the accumulated strain rate over a polymer's trajectory $\mathbf{x}(t)$, $\epsilon = \int \dot{\epsilon}[\mathbf{x}(t)]dt$. Most previous work has been for homogeneous extensional flows so that $\epsilon = \dot{\epsilon}t_{\text{res}}$ where t_{res} is the residence time in the flow. An affinely deforming object with initial size x_i will stretch to a length $x_i e^{\epsilon}$ after experiencing a strain of ϵ.

Configurational effect: A flexible polymer in a strong extensional flow may initially deform affinely, but it generally deforms non-ideally because of elasticity and the complexities of a coil configuration [86]. These coil complexities lead to essentially unpredicatable extension dynamics for a single polymer, a phenomenon known as molecular individualism [86, 87]. Molecular individualism can be explained qualitatively by looking at the intermediate polymer states in Fig. 2-6. Depending on the details of the initial configuration, different intermediate states are possible, *e.g.* using the nomenclature of Ref [86], a "half-dumbbell", a "fold", a "dumbbell", or a "coil". These different intermediate states can exhibit drastically different stretching dynamics. For example, a "dumbbell" configuration may initially deform nearly affinely, but a "fold" will only weakly extend until the two ends are separated. Consequently, the path that the stretching molecules take through configurational space sensitively depends on that individual polymer's initial configuration.

Despite molecular individualism, the ensemble average fractional extension shows universal behavior with strain and a dimensionless parameter termed the Deborah number De. De is defined as $\text{De} = \dot{\epsilon}\tau$, and it governs the competition between the diverging fluid elements dragging pieces of the polymer apart and the polymer's elasticity tending to recoil the chain. At a critical Deborah number of $\text{De} = 1/2$, these competing effects exactly cancel and steady state polymer configurations transition from coiled ($\text{De} < 1/2$) to stretched ($\text{De} > 1/2$) [88].

DNA deformation experiments: Because it can be easily visualized and it is generally monodisperse, many DNA experiments have been performed to study polymer deformation in flow gradients. Most important to this thesis are the studies by the Chu group [86, 89, 90] who looked at single DNA molecules deforming in cross-slit planar extensional flow. These experiments, along with Larson's simulations [91], closely investigated molecular individualism and the coil-stretch transition at $\text{De} = 1/2$. The main results from these studies are that 1) molecular individualism causes unpredictable single molecule extension behavior, 2) ensemble average fractional extension shows universal behavior as a function of De, and is independent of De for $\text{De} > 40$, 3) complete extension of all DNA in an ensemble is not achieved until $\epsilon > 10$, and 4) a coil-stretch hysteresis exists at $\text{De}=1/2$. We also note that DNA deformation has also been studied in shear flows [92] and mixed flows [93, 94]. In these flows with rotational components, DNA conformations "tumble", *i.e.* they periodically stretch and compress. Hence, purely extensional flows are desired for stable, strong stretching of a DNA molecule.

2.4 Summary

This Chapter presented a general background of polymer physics and electrophoresis, and in particular, how these subjects apply to our study of DNA. We found that O[kbp-Mbp] DNA in a TBE buffer can be modeled as a worm-like chain with excluded volume interactions. A DNA's dynamic parameters in an unbounded buffer will follow Zimm scalings so that $D \sim N^{-\nu}$ and $\tau_1 \sim N^{3\nu}$ where $\nu \sim 0.6$. Furthermore, the Smoluchowski electrophoresis model was presented and, despite the many approximations, DNA's mobility is expected to obey the Smoluchowski scaling at "normal" conditions, *i.e.* at fields lower than O[kV/cm] and without high concentrations of multi-valent ions. Finally we noted that when placed in an extensional flow, a polymer will strongly stretch, however its dynamics will be highly dependent on its individual initial configuration. In addition to setting the foundation for interpreting our results, we hope this presentation is useful for those wishing to continue research in the area of this thesis.

Chapter 3

Experimental

This chapter details the experimental methods, equipment, and procedures that we use to study single DNA electrophoresis in microchannels. The main experimental techniques covered are single molecule fluorescence microscopy and soft lithography microchannel construction. Additionally, we summarize our methods for data acquisition from experimental data.

3.1 Single molecule analysis of DNA

With current state of the art video microscopy techniques it is possible to directly observe the dynamics of single molecules of DNA. The method to observe single DNA was pioneered by Yanigida [95] and later used to observe DNA dynamics during the course of gel electrophoresis dynamics [96]. It is based on the observation of emitted light from excited fluorescent dyes that are attached homogeneously to the DNA backbone. The underlying approximation is that the observed dye emission intensity is directly proportional to DNA mass. Typical dyes for dsDNA are YOYO and TOTO, which have both a bright characteristic emission when bound to the DNA and a low signal in free solution. In addition to their bound versus unbound signals, these dyes are particularly useful for single DNA studies because they have a strong electrostatic and steric binding affinity to the DNA backbone [97] so that they do not shear off in strong flow [86, 97]. Furthermore, though they slightly decrease a DNA's electrophoretic mobility, they do not alter electrophoretic dynamics or how the mobility scales with the electric field [97]. This, along with visible evidence suggests that the dye binds uniformly along the DNA backbone. However, it is well-known that these dye molecules slightly unwind the double-stranded backbone and therefore increase dsDNA's contour length [97]. Other researchers have found that TOTO-1 increases a DNA's contour length anywhere from 4.1-4.8 Å/dye molecule [45, 98, 99], which for our dye procedure of 4.7 bp/dye would increase

λ DNA's contour length from L=16.3 μm to L=20.5-21.3 μm. Despite this minor issue, TOTO and YOYO dyes are excellent probes for single molecule analysis.

A fluorescent dye is characterized by an adsorption and emission spectrum. Achieving a quality fluorescence image with a high signal to noise ratio relies on 1) the ability to allow the emitted fluorescent light from the dye to pass from the DNA to the camera while simultaneously blocking the excitation light and 2) using a camera with a low inherent noise.

An optical train consisting of a properly chosen excitation, dichroic, and emission filter is able to meet the first requirement (Fig. 3-1 (a)). Figure 3-1 (b) shows the filter transmission spectra of our filter set along with TOTO-1's absorption-emission spectra. In our fluorescence microscopy experiments, we use a Hg-lamp light source (HBO 103, Zeiss) that is first filtered by the excitation filter to ~ 500 nm. The beam is then nearly completely reflected by the dichroic filter towards the microscope (Axiovert 200, Zeiss) objective. The objectives used in our experiments are either 1) 100×, 1.4 numerical aperature (NA) or 2) 63×, 1.4 NA, both oil immersion (Zeiss, Type FF). The beam excites TOTO-1 dye molecules bound to DNA which then emit light at ~ 540 nm. The emitted light then returns through the objective and passes through the dichroic, as 540 nm is in the high transmission portion of its spectrum. The emitted light is then sent to the camera through a final emission filter, which ensures that no stray transmitted excitation light can pass.

The second requirement for a quality fluorescence image depends on the electronics of the camera. A camera (*e.g.* EB-CCD) captures the emitted photons from the dye on a solid state grid which converts photons to electrons [100]. In each pixel of the grid, the electrons build up in a well and then are released in intervals that determine the frame rate. It is this mechanism that determines the quality of the camera. *Blurring* of images can occur when the shutter remains open (collecting photons) while the fluorescent object moves a large distance. The resulting captured image will be a sum of the DNA's history while the shutter is open. *Lag* occurs when the wells of electrons do not completely empty for every interval. This results in ghost images of a moving object. *Blooming* occurs when the electron wells fill and then seep into neighboring pixels. *Interlacing* occurs when the camera is programmed to read the odd and even rows of electron wells *at different times*, usually a half-frame apart. Blurring, lag, blooming, and interlacing are undesirable, since the data of single molecule experiments relies on the ability to distinguish the molecule's actual time-dependent configuration against the background. The main problem for our work was blurring because our non-adjustable 30 frames/s frame rate prevented us from observing high DNA velocities (O[100 μm/s]).

In our experiments, the reflected light from the TOTO dye attached to the DNA backbone is transformed into a bitmap by a Hamamatsu EB-CCD (C7190-20) camera which is equipped with an intensifier and able to record deinterlaced, low-lag, low-blooming images at video rate (30 frames/sec). The camera gain, offset, and intensifier sensitivity can be adjusted to obtain optimal signal to background intensity. We record all experiments on digital video tapes (Sony PDV-124). Important moments from each experiment are then converted to tif movie files by a LG-3 Scientific Frame Grabber (Scion) and NIH Image software. These movies can later be analyzed with custom macros written for NIH Image. The pixelated movies have 8-bit resolution (0-255 in intensity values) and pixel sizes range from 0.14 μm × 0.14 μm for the 100× objective to 0.22 μm × 0.22 μm for the 63× objective. These values were obtained with a microfabricated ruler with 10 μm markings.

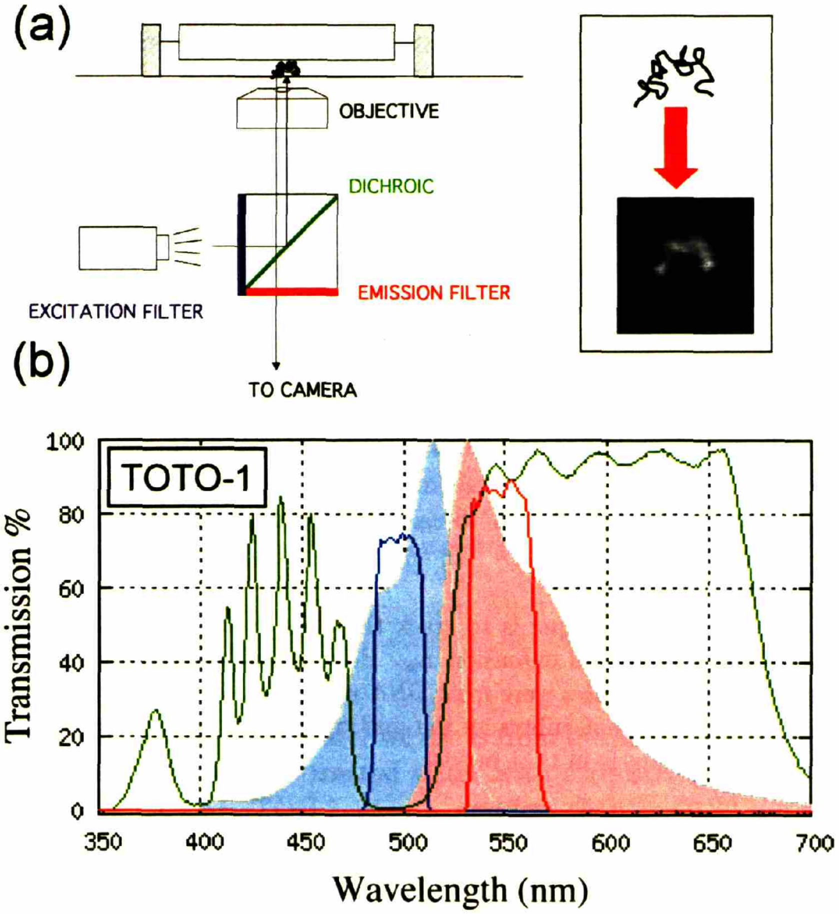

Figure 3-1: (a) Schematic of the microscope optical train along with a sample fluorescence image of a DNA coil. (b) Filter transmission of the optical train (excitation=blue, dichroic=green, emission=red) along with the absorption (shaded light blue) and emission (shaded pink) spectra of TOTO-1 dye bound to dsDNA. Reprinted from www.probes.com.

Researchers such as Chu, Bustamante, Doyle, and Viovy have employed these single molecule observation techniques in order to view the dynamics of individual DNA molecules, *e.g.* see Ref. [101] for a review. These studies are unique because they allow for actual experiments on single molecules instead of averages over a population. They thus deliver polymer physics results that would not be obtainable when working with bulk ensembles of DNA molecules. Furthermore the experiments have direct applications to bioengineering devices, *e.g.* for DNA mapping.

The main experimental hurdle in single molecule DNA fluorescence microscopy is to remove oxygen from the system. Singlet oxygen and oxygen radicals can attack DNA bases to cause damage or strand breaks [102, 103]. Furthermore they foster photobleaching, *i.e.* the intensity of the emitted light from the dye decreases with time. The presence of these reactive oxygen species is magnified in the presence of light, thereby adding difficulty to microscopic observation. Thus, reduction of dissolved oxygen and quenching of reactive oxygen must be performed to obtain decent fluorescence microscopy results. Reactive oxygen scavengers, such as ascorbic acid (Vitamin C) and β-mercaptoethanol can be added to the buffer to provide protection from these harmful effects. More importantly, since it is the source of reactive oxygen species, extreme care must be taken to remove molecular oxygen in preparation of the buffer DNA solutions. Our technique involves initially bubbling argon through the buffer, adding 3-4 % β-mercaptoethanol, and then keeping DNA solutions under a blanket of argon during subsequent processing steps. We also have experimented with enzymatic oxygen scavengers as explained in our procedure section.

3.2 Data analysis

The primary data analysis technique is to track the time evolution of a DNA molecule's center of mass position (x_{com}, y_{com}) and extension x_{ex}. First we filtered out the noise so that the only signals appearing in the movie files were from DNA molecules. A robust noise filter algorithm was developed for the tif movies that subtracts the maximum pixel value from the border of the first frame of a movie from all pixels in that movie.

We have also developed algorithms to compute the DNA's center of mass for every frame of a movie by integrating the position-weighted intensity of a DNA's pixelated image (after noise filtering):

$$(x_{\text{com}}, y_{\text{com}}) = (\sum_i x_i M_i / \sum_i M_i, \sum_i y_i M_i / \sum_i M_i) \tag{3.1}$$

where M_i is the intensity value of pixel i and the sums are over all pixels i in the selected region. In order to perform this calculation, a "region of interest" (ROI) was formed around a single DNA molecule. Once the computer has a center of mass location for a DNA molecule, tracking proceeded as 1) advancing to the next frame, 2) computing the center of mass in the ROI again, 3) moving the ROI so that the DNA is centered in it, and 4) advancing to the next frame, etc. These programs provided a more rigorous way to collect data than previous research methods, which typically employed manual calculation using a cursor. To determine the DNA's extension, we first located the coordinates of the left-most, right-most, top, and bottom pixels of the DNA image with an intensity value of at least 8 (after background filtering). The extension x_{ex} was then defined as the length of the longest line connecting any two of these points. This procedure was automated and worked well for DNA coils or extremely bright images. However, when the DNA was highly stretched, it was preferred to calculate x_{ex} manually with a cursor.

3.3 Procedures

Here we describe some of our experimental protocols we developed.

3.3.1 DNA dye protocol

We employed a few basic protocols for dyeing DNA. We used two methods with ~1 cP buffers that gave similar quality of DNA, however the second method ("new way") gave more robust results because the DNA was handled at a higher concentration so that it was less likely to break. Furthermore, in the second method, we removed ascorbic acid from the formulation which has been shown to form globule-complexes with DNA [104]. We also developed protocols for dyeing DNA at higher viscosity (6 cP and 40 cP listed) by adding sucrose to the formulation. Note: It is important to keep these solutions oxygen-free and away from light. Any step involving DNA is carried out under a small lamp in a dark room and a blanket of Ar is used after waiting steps. These dye procedures were adapted from the work of Perkins [65] and Smith [105].

Required stock solutions

- *MilliQ Ultrapure water (MQ)*: The water we use is from the MilliQ Biocel A10 from Millipore. It provides deionized, filtered, UV treated water with a resistivity of 18.2 MΩ-cm, pyrogen concentration of 0.02 EU/mL, TOC 1-10 ppb, and less than one 0.22 μm particle per mL.

- *5× TBE (0.45 M Tris Borate, 0.01 EDTA)*: This is an asymmetric electrolyte, with pH=8.3 and mostly Tris$^-$ and EDTA^{3-} determining the ionic strength. Using pKa values of Tris=8.3, EDTA=1.7, 2.6, 6.3, and 10.6, and Boric acid=9.2, the ionic strength of TBE buffer is: 0.5×=0.02 M, 2.2×=0.1 M, and 5×=0.17 M. We also have access to 10× TBE which we need for viscosifying procedures.

- *Concentrated DNA (500 μg/mL for λ DNA and 87 μg/mL for T4 DNA)*: We purchase the λ DNA from New England Biolabs and the T4 DNA was donated (phenol extracted in April 2002) by Renaud Falconais from the Viovy Group at Institut Curie in Paris. Both stock solutions were kept at 4°C and when observed had satisfactory (> 60%) monodispersity. Depending on the dye procedure, these stock solutions are further diluted to either 1 or 10 μg/mL in 0.5× TBE for O[6 month] use. The stock solutions are at concentrations greater than the overlap concentration c^* so care must be taken when pipetting to avoid viscoelastic recoil. It is advised to pipette with a cut-tip pipette and then to carefully drag the tip along the stock eppendorf vial as it passes through the meniscus to effectively "cut" the sample loose from the stock solution.

- *1000 μM TOTO-1 dye*: The dye was purchased from Molecular Probes in a solution of DMSO. These dyes become unstable after O[days] in aqueous solutions. Though we never observed this instability, even after storing a 10 μM aqueous dye solution for 3-5 days, whenever we prepared a dye solution, we used it within 12 hours. The stock dye solution is continuously kept at $-20°$C and 10 μL samples are partitioned and kept at 4°C for O[6 month] use. Extreme care must be taken to ensure that the 1000 μM stock solution is well-mixed before partitioning.

- *β-mercaptoethanol*: This scavenger of reactive oxygen performs best when not exposed to air. Consequently, we limit the number of times that the stock container is opened and closed by partitioning smaller ~5 mL aliquots for monthly use. CAUTION: Hazardous chemical.

- *1% PVP (polyvinylpyrrolidone)*: PVP (Polysciences) is a nonionic polymer used to quench electroosmotic flow. We prepare the 1% stock solution (~ 10 mL) for O[3 month] usage. Depending on the protocol, it may be $M_w = 10^4$ or 10^6 in MQ or TBE. It is recommended to store PVP solutions overnight at 4°C to dissolve the PVP. Vortexing is not recommended because it may break the polymers.

Procedure 1: "Dye DNA (old way)"
This procedure was used for non-viscosified experiments before 9/2004.
Buffer preparation:

- Syringe ~7 mL of 5× TBE buffer through a 0.2 μm filter into a 15 mL Falcon tube.
- Seal with parafilm and bubble Ar through entire solution for 1/2 hour; use 200 μL pipette tips to extend air line to the bottom of the Falcon tube.
- Add 0.16 mL of β-mercaptoethanol, 0.16 mL 1% (ascorbic acid in MQ), and 0.4 mL 1% (PVP in MQ) to 3.28 mL degassed 5× TBE. Purge headspace with Ar for 10 s. ("Buffer")

DNA dye steps:

- Dilute 1000 μM TOTO-1 to 10 μM (0.5 μL TOTO + 49.5 μL MQ). ("a")
- Dilute TOTO further into buffer (10 μL "a" + 90 μL "Buffer") ("b")
- Dye DNA (50 μL "Buffer" + 10 μL "b" + 31 μL of 1 μg/mL DNA (cut-tip, slow)). Make sure to add the DNA last after the remaining components are mixed by gentle swirling.
- Let sit sit for several hours (3+) at room temperature wrapped in foil.
- Dilute for observation. For 2 μm-high channels a good dilution is adding 20 μL of the dyed DNA solution to 80 μL "Buffer" (gives c_{DNA}=0.07 μg/mL).

Procedure 2: "Dye DNA (new way)"
This procedure was used for non-viscosified experiments after 9/2004.
Buffer preparation:

- Syringe ~7 mL of 5× TBE buffer through a 0.2 μm filter into a 50 mL Falcon tube.
- Seal with parafilm and bubble Ar through entire solution for 1/2 hour; use 200 μL pipette tips to extend air line to the bottom of the Falcon tube.
- Add 0.16 mL of β-mercaptoethanol, and 0.4 mL 1% (PVP in 5× TBE) to 3.44 mL degassed 5× TBE. Purge headspace with Ar for 10 s. ("Buffer")

DNA dye steps:

- Dilute 1000 μM TOTO-1 to 10 μM (0.5 μL TOTO + 49.5 μL MQ). ("a")
- Dye DNA (136.3 μL 5× TBE + 3.3 μL "a" + 6 μL β-mercaptoethanol + 10.3 μL of 10 μg/mL DNA (cut-tip, slow)). Make sure to add the DNA last after the remaining components are mixed by gentle swirling.
- Wrap in foil and tape to the hotplate set at 65°C for one hour. Let sit for two hours at room temperature. We speculate the heating step accelerates dye kinetics and helps break-up possible concatemers.
- Dilute for observation. For 2 μm-high channels a good dilution is adding 10 μL of the dyed DNA solution to 90 μL "Buffer" (gives c_{DNA}=0.07 μg/mL).

Procedure 3: "Higher viscosity"

This procedure was used anytime we attempted to viscosify a DNA buffer. Some experiments also included 0.1% ascorbic acid in the final formulation but it was removed in 2004.
Buffer preparation:

- Syringe ~7 mL of 5× TBE buffer through a 0.2 μm filter into a 50 mL Falcon tube.
- Seal with parafilm and bubble Ar through entire solution for 1/2 hour; use 200 μL pipette tips to extend air line to the bottom of the Falcon tube. Repeat with a vial of 10× TBE.
- Make sucrose buffer: Add 8.16 g sucrose to 4 mL 10× TBE and 1 mL 1% PVP stock solution in 10× TBE. Vortex gently and heat at 45°C overnight to dissolve sucrose. ("sucrose buffer")

DNA dye steps:

- Dilute 1000 μM TOTO-1 to 10 μM (0.5 μL TOTO + 49.5 μL MQ). ("a")
- Dye DNA (136.3 μL 5× TBE + 3.3 μL "a" + 6 μL β-mercaptoethanol + 10.3 μL of 10 μg/mL DNA (cut-tip, slow)). Make sure to add the DNA last after the remaining components are mixed by gentle swirling.
- Wrap in foil and tape to the hotplate set at 65°C for one hour. Let sit for two hours at room temperature. We speculate the heating step accelerates dye kinetics and helps break-up possible concatemers.

- **6 cP**: Add 10 μL dyed DNA to 3.6 μL β-mercaptoethanol, 50 μL "sucrose buffer", 35 μL 5× TBE, and 5 μL 1% PVP in 5× TBE (premix components before adding DNA).
- **40 cP**: Add 10 μL dyed DNA to 3.6 μL β-mercaptoethanol and 90 μL "sucrose buffer" (premix the β-mercaptoethanol and TBE).

Be extremely careful when pipetting the DNA into the high viscosity sucrose buffer. It is advised to pipette onto the top surface of the sucrose buffer, pushing an edge of the pipette tip into the eppendorf wall for support. After pipetting, the solution must be mixed. Swirl this solution very gently by repeatedly tipping the eppendorf upside down at a rate of approximately one flip every 5 seconds. The aqueous portion will rise through the sucrose portion until mixing is complete.

3.3.2 Anti-oxidant enzymes

Though we do not use any anti-oxidant enzymes in our reported results, we did experiment with them and developed a protocol to incorporate them into the DNA formulation. The combination of glucose oxidase and catalase, in the presence of glucose, can consume 1/2 mole of O_2 per mole of glucose:

$$\begin{aligned} C_6H_{12}O_6 + O_2 &\xrightarrow{\text{glucose oxidase}} C_6H_{10}O_6 + H_2O_2 \\ H_2O_2 &\xrightarrow{\text{catalase}} H_2O + 1/2\ O_2 \end{aligned} \tag{3.2}$$

As explained above, reactive oxygen formed from molecular oxygen in solution attacks DNA and leads to bond breakage. Reactive oxygen also causes photobleaching of the dye molecules. Even though we add the anti-oxidant β-mercaptoethanol to our formulation, it is not present at high enough concentration to completely eliminate oxidative damage; typical viewing times with 4% β-mercaptoethanol as the anti-oxidant are $\sim$ 30 s before a DNA breaks. However, when glucose, glucose oxidase, and catalase are added to the formulation, oxidative damage is greatly hindered. In a glass channel, viewing times may be over 30 min for a DNA without backbone breaking. The enzyme anti-oxidants also improve resistance to photobleaching in glass channels. Figure 3-2 shows how the DNA's intensity falls with time in the presence of the anti-oxidant enzymes and 4% β-mercaptoethanol in both glass and PDMS channels.

Even though the DNA has high resistance to photobleaching and damage in glass channels with the enzymes, note that the enzymes do not work in the PDMS channels. They actually increase oxidative damage, as DNA usually stays brighter and intact for longer than 10 s in PDMS channels with only the β-mercaptoethanol anti-oxidant. It is believed that the enzymes denature on a PDMS surface (personal communication from the Barron group at Northwestern). Increasing the enzyme concentration, specifically catalase, may improve results, though this was not attempted.

Procedure: "Anti-oxidant enzymes"

Solution preparation:

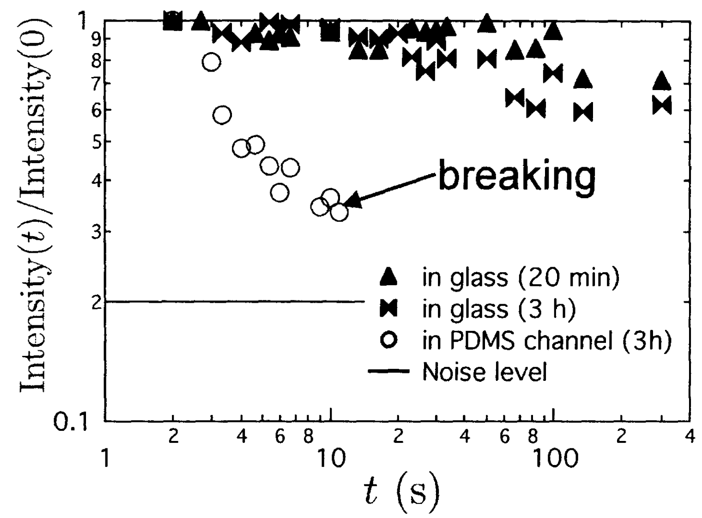

Figure 3-2: Anti-oxidant effect of enzymes. Scaled dyed DNA intensity (measured as the maximum pixel value of a bisecting line through the DNA's fluorescent cloud) for DNA 20 minutes after adding the enzymes in a thin slit of glass, 3 hours after adding the enzymes in a thin slit of glass, and 3 hours after adding the enzymes in a 2 μm-high PDMS channel (presoaked).

- Glucose oxidase: Add ~ 10 mg glucose oxidase (Sigma, G-2133; 200,000 U/g solid) to ~ 0.5 mL of MQ to make a 20 mg/mL solution. ("Glox")
- Catalase: Add ~ 3.5 mg catalase (Sigma, C-40; 13,800 U/mg solid) to ~ 1 mL of MQ to make a 3.5 mg/mL solution. ("Cat")
- Dye DNA using the same method as listed above, except include glucose in the "Buffer" so that the final concentration of the formulation is 0.45% glucose. Once the DNA is diluted to its final concentration (with 0.45% glucose), add 1 part "Cat" to 99 parts DNA solution and gently mix; then add 1 part "Glox" to the same 99 parts DNA solution and gently mix.

3.3.3 Photolithography procedure

Silicon master wafers for soft lithography were fabricated by photolithography at the MTL facilities (TRL lab) at MIT. The main goal of photolithography is to transfer a two dimensional pattern designed on AutoCAD to a thin layer of photoresist on top of a silicon wafer. This is done by creating a quartz-chrome mask from the AutoCAD file, which is simply a piece of glass that blocks light in places wherever there is chrome. Photoresists have unique dissolution chemistry when they are exposed to near-UV light versus when they are not. Therefore, after exposing a photoresist through a mask and then developing (dissolving in a solvent), one is left with a wafer with projections of photoresist in locations dictated by the mask geometry. The wavelength of exposure combined with the sophistication of exposure equipment limit the size of features that can be developed during the photolithography step. With current equipment (EV1 aligner) and using 365 nm light, the minimum size resolution is approximately 1 μm.

The wafer will eventually be used to mold PDMS, and these molding limitations must also be considered in the design of microchannels. For example, high aspect ratio (10+:1) columns of PDMS will tend to collapse under their own weight. Thus thin channels (~1-7 μm) will be needed to construct microchannels with small obstacles (~1-2 μm). One further difficulty that must be considered when working with thin PDMS channels is sagging. The channel cannot be too wide without any supporting obstacles or else it may pinch off. A rule of thumb is that a 200 μm channel is the widest channel you would want to use for a 2 μm-high PDMS channel. These factors have been considered in the design of the our photomasks.

Several resists were attempted (Positive: OCG thin resist, AZ P4620 thick resist, Negative: SU-8, and Image reversal: AZ 5214). The spun on resist thickness h becomes the height of the future microchannel molded from the wafer. Spin rates of 1000-4000 rpm are used to vary the resist thickness during the spin coating process. OCG was too thin for our purposes ($h \sim 0.8$ μm) and SU-8 was too difficult to develop for O[μm] features. We settled on image reversal resist (AZ 5214) because it could be spun on thick enough for a fillable microchannel ($h \sim 2$ μm) and it was possible to resolve our smallest features (1.6 μm-diameter obstacles). Furthermore, we developed a procedure to apply multiple layers of image reversal resist to a wafer to make thicker channels ($h \sim 4$-6 μm). We note that the positive thick resist is also a viable choice for future research in thicker channels ($h > 8$ μm).

The photolithography procedure for image reversal resists consists of 1) applying an adhesion promoter to the wafer (HMDS), 2) spin coating the photoresist onto the wafer, 3) baking the resist ($T \sim 90°$C) to remove solvent, 4) exposing the resist with near-UV light through a patterned photomask, 5) postbaking the wafer to inhibit dissolution of resist in exposed areas, 6) flood exposure of wafer with near-UV light (creates dissolution enhancers like a positive resist, but does not affect regions exposed through mask), and 7) developing the resist (*i.e.* dissolving the regions not exposed in step 4).

Procedure: "Photolithography: 1 layer"
Machine in TRL: operation

- HMDS: Apply adhesion promoter (cycle 4)
- coater: Dispense AZ 5214 at 500 rpm for 8 s, spread at 750 rpm for 6s, spin at 2000 rpm for 30 s
- prebake: Bake in convection oven for 30 min at $T = 90°$C
- EV1: Exposure (10 mW/cm^2) through a mask, hard contact, t=1.4 s
- postbake: Bake in convection oven for 30 min at $T = 95$-$102°$C
- EV1: Flood exposure (10 mW/cm^2), t=60 s
- photowet-l: Develop in AZ 422 for 3 minutes

Procedure: "Photolithography: 2 layer"
Machine in TRL: operation

- HMDS: Apply adhesion promoter (cycle 4)
- coater: Dispense AZ 5214 at 500 rpm for 8 s, spread at 750 rpm for 6s, spin at 1000 rpm for 30 s
- prebake: Bake in convection oven for 8 min at T = 90°C
- coater: Dispense AZ 5214 at 500 rpm for 8 s, spread at 750 rpm for 6s, spin at 1000 rpm for 30 s
- prebake: Bake in convection oven for 30 min at T = 90°C
- EV1: Exposure (10 mW/cm^2) through a mask, hard contact, t=2.2 s
- postbake: Bake in convection oven for 30 min at T = 95-102°C
- EV1: Flood exposure (10 mW/cm^2), t=60 s
- photowet-l: Develop in AZ 422 for 15 minutes

Height measurements were performed with the Nanospec (in MTL) on the image reversal photoresist (Film type=positive resist or thick film, index of refraction =1.69). The first procedure yields resists with $h = 2\ \mu$m and the second procedure yields h=6 μm. PDMS was then molded onto the master wafer to make the microchannels. A typical channel is shown in Fig. 3-3 (a). Cross sections of these channels were observed to double check the accuracy of the height measurement and quality of the sidewalls (Fig. 3-3 (b)).

3.3.4 PDMS molding

After the microchannel geometry is patterned into the layer of image reversal photoresist, the wafer is treated with a monolayer of a silanizing agent overnight ($Si\text{-}Cl_3\text{-}(CH_2)_2\text{-}(CF_2)_n\text{-}CF_3$, n=5, United Chemical Technologies, T2492-KG, Bristol, PA) that allows for easy peeling of PDMS later on. Next, PDMS polymer (Sylgard 184, Dow Corning) is poured onto the master wafer and cured at 65°C. Once cured, the PDMS is peeled away form the Si master and holes can be carved in it to serve as inlet and outlet reservoirs. Finally, the PDMS is bonded onto a flat surface (glass or PDMS-coated glass) to seal the microchannel.

Procedure: "PDMS molding"

- Working in the hood, place the silicon master wafer along with ~ 1 mL of silanizing agent (T2492-KG, United Chemical Technologies) contained in a *glass* cuvette in a closed contained, *i.e.* a glass dessicator. Do not use plastic pipette tips when dispensing the silanizing agent because its solvent easily dissolves plastics. In a physical vapor deposition process, the silanizing agent will deposit on the wafer to allow for easy peeling of PDMS after molding. Let sit overnight at ambient pressure, or if possible, an hour at 15" Hg. CAUTION: Hazardous solvent

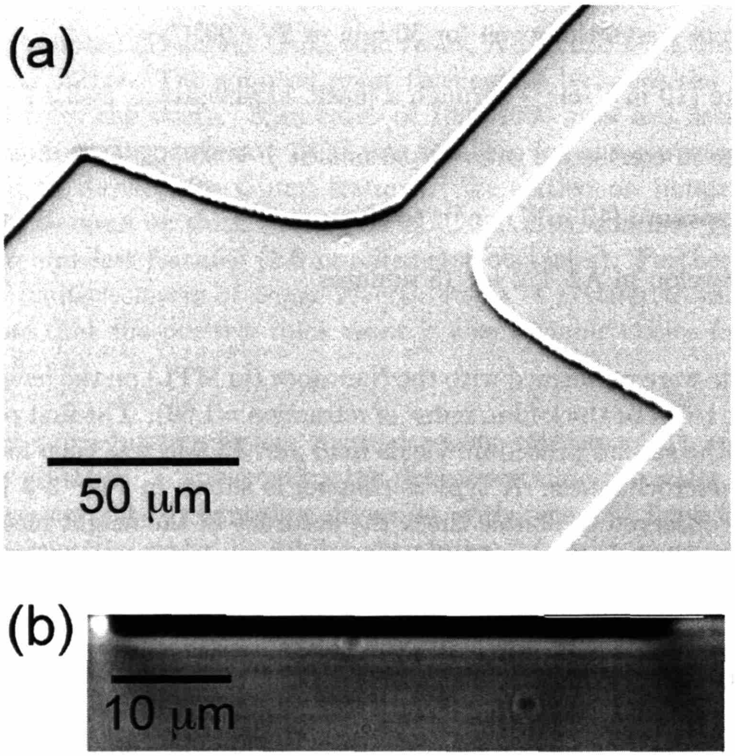

Figure 3-3: (a) SEM image of a typical PDMS microchannel molded from a single layer image reversal photoresist (h=2.0 μm). (b) Light microscopy image of a 50 μm-wide PDMS channel cross-section (h=2.0 μm).

- Pour 10 parts PDMS silicone elastomer and 1 part PDMS elastomer curing agent into a cup and mix vigorously for 2 minutes. Incomplete mixing will lead to brittle and and non-uniformly cured PDMS.
- Degas the PDMS under vacuum at room temperature for 60 min or until most of the air bubbles have left the PDMS. A recommended vacuum pressure is 15" Hg.
- Pour the degassed PDMS onto the silicon master wafer (pretreated with silane monolayer).
- Further degas the mold under vacuum for 30-60 min.
- Cure the mold at 65°C for 24 h.

3.3.5 λ DNA ligation

λ DNA has 12 complimentary nucleotides at each end of the backbone that are single-stranded overhangs. Therefore, it is possible that the ends of multiple λ DNA molecules can link together to form concatemers. The linking is a self-assembly process where first the complimentary nucleotides come into contact and hybridize (or hydrogen bond). Then a ligase enzyme and ATP act to chemically bond one piece of λ DNA to another. Based on the work of Perkins [65], we developed a protocol to ligate large λ DNA concatemers as big as $\sim 17\lambda$ DNA (O[Mbp]). However we should note that the resulting concatemers are highly polydisperse.

Procedure: "Creating λ DNA concatemers"

- Hybridize DNA by heating the following mixture (1.5 mL vial) taped to a hotplate at 65°C for 10 min: (80 μL MQ + 10 μL T4 ligase buffer (10×) + 10 μL 500 μg/mL λ DNA.
- Cool the solution slowly (ramp setting at 45°C/hr) until it reaches room temperature.
- Add 3 μL of ligase enzyme, gently mix, and then let sit at room temperature 60 min.
- Heat to 65°C for 20 min to denature the enzyme and break any non-ligated hydrogen bonds.
- Dilute the hybridized DNA to 10 μg/mL by adding 400 μL of degassed 0.5× TBE to the same vial. Gently mix. ("hDNA")
- Perform Dye Procedure 2 ("new way") using "hDNA" as the stock DNA.

3.3.6 PDMS channel soaking and glass cleaning

In most experiments, we soak our PDMS channels in 0.5× TBE to prevent permeation driven flow discussed in Chapter 4. For most of this work, we then dry the PDMS channel and place it on a clean glass slide.

Procedure: "Channel, soaking, cleaning and assembly"

- After molding and peeling the PDMS, cut ~ 4 mm ×4 mm holes at each end of a channel with a scalpel to serve as reservoirs. Cut around the borders of the channel to remove it from the mold.

- Float the PDMS block channel-side down in a small petri dish of 0.5× TBE. Place the dish in a 45°C oven for 12-36 hours. After soaking, the PDMS should be visibly less transparent.

- Rinse the PDMS channel in MQ. The rinsing is best performed by alternating between dipping the PDMS in a MQ bath and holding it under a stream of MQ.

- Gently dry the PDMS block. Drying is best performed with a wide-bore flexible tube that can be pinched down to a slit. Drying with pipette tip attachments on the hose is not recommended as it has been shown to lead to non-uniform overdrying.

- Apply the dried PDMS to a clean glass slide. We experimented with a few cleaning techniques, settling on a simple 15 min soak in 1M NaOH followed by a soak and rinse in MQ. We also tried 1) plasma cleaning for 5 min at 100 W, charge equilibration for 1 day, soaking in 1 M NaOH, and rinsing in MQ and 2) soaking in 1 M NaOH, rinsing in MQ, rinsing in 0.1 M acetic acid, rinsing in MQ, and rinsing in 0.5× TBE. Alternate method 2 generally led to significant sticking problems for the DNA (believed to be from residual acid remaining even after the two rinse steps).

Chapter 4

Background Microflows

Our experiments are designed to track single DNA molecules translating and deforming during electrophoresis. Consequently *we must eliminate or sufficiently dampen all background hydrodynamic flows in the microchannel.* Because our channels are extremely thin (height $\sim$ O[μm]), pressure-driven flows from the microchannel reservoirs are fortunately negligible (maximum v_x $\sim$O[1 μm/s]). However, other significant microflows may arise. One problematic flow, *permeation-driven flow*, arises when the buffer permeates into the polydimethylsiloxane (PDMS) microchannel walls. *Electroosmotic flow* is another background flow that arises when an electric field is applied across a microchannel with a native surface charge. Electroosmotic flow is well-known and we will briefly discuss our method to dampen it. Conversely, permeation-driven flow is a newly discovered flow that we will explore in depth, developing ways to both eliminate it and harness it for other applications.

4.1 Permeation-driven flow

Reproduced in part with permission from G. C. Randall and P. S. Doyle, "Permeation-driven flow in poly(dimethylsiloxane) microfluidic devices", *Proceedings of the National Academy of Science*, **102**, 10813-10818, (2005). Copyright 2005 by The National Academy of Sciences of the United States of America, all rights reserved.

4.1.1 Background

Over the last ten years there has been a burst of activity in the field of microfluidics and lab-on-chip devices [106]. Much of this growth can be attributed to the pioneering work of Effenhauser

[107] and Whitesides [108] who showed that inexpensive fluidic devices could be easily fabricated in poly(dimethylsiloxane) (PDMS) by replica molding from a microfabricated template. Consequently, PDMS has become the material of choice for making microfluidic devices [109–111].

While the use of PDMS in microfluidics is relatively new, this material has been used extensively in applications which require gas or vapor permeable membranes [112]. PDMS is highly permeable to organic solvents, making solvent-PDMS compatibility one of the main drawbacks of using PDMS for fluidic devices [113]. Permeation of solvent into the PDMS channel walls becomes increasingly more important as device size decreases because the surface area to volume ratio increases. Current research on cells and single molecules requires creation of devices which are only a few microns to hundreds of nanometers in height (e.g. the DNA cytometry device of Chou *et al.* [114] has height of 3 μm). The resulting microfluidic flow from the permeation flux will be important in these thin devices, but it has not been studied. Despite this, some have observed other solvent permeation effects in microchannels. In one example, protein crystallization in aqueous droplets has been observed at unexpected initial concentrations because the permeation of water through the PDMS increases the concentration in the droplets over time [115]. Until now, water permeability into the PDMS has been considered negligible for most microfluidic applications, however we will show that this small but finite permeability generates a significant flow in thin (O[μm]) channels.

For nano-scale applications that require sealed microchannel walls, a flow like this clearly must be eliminated. On the other hand, the permeation driven flow provides an alternative approach to passive flow applications. Several groups have previously demonstrated passive flow processes by filling one reservoir with liquid and leaving the other empty and open to air so that the liquid evaporates at the pinned contact line at the empty reservoir. Some examples include evaporation driven pumping [116], microsphere crystallization [117], and sample concentrating [118, 119]. A permeation driven flow can provide similar results using a driving flux at the channel walls instead of at the outlet air interface.

In this section, we model and study permeation driven flow and its applications. We model the mass transfer of water from the microchannel into the PDMS and use the lubrication approximation to solve for the gap-averaged velocity for the case of a single rectangular channel connecting two fluid reservoirs. We will then experimentally validate the flow model by tracking single beads using fluorescence microscopy. Because this flow may be undesirable for many applications, we present a simple method to eliminate it. We also discuss ways to exploit this phenomenon to passively drive pumping in a microfluidic device, to concentrate samples, and to self-assemble particles.

4.1.2 Model

Solvent permeation into the walls of a microchannel creates an incoming flow fed by the channel reservoirs. Our goal is to model this flow and the mass transfer driving it. Figure 4-1(a) shows the microchannel geometry as viewed from the side and Fig. 4-1(b) shows a three-dimensional view. The microchannel has length l, width w, and height h, and the PDMS thickness surrounding the microchannel is R. The length scales we study are $l \sim$ O[cm], $R \sim$ O[mm], $w \sim$ O[100 μm], and $h \sim$ O[μm]. We use Cartesian coordinates with origin at the floor of the channel center and with the x-axis oriented along the length of the channel, the y-axis oriented along the width of the channel, and the z-axis normal to the channel floor. Aside from the glass channel floor, all surfaces

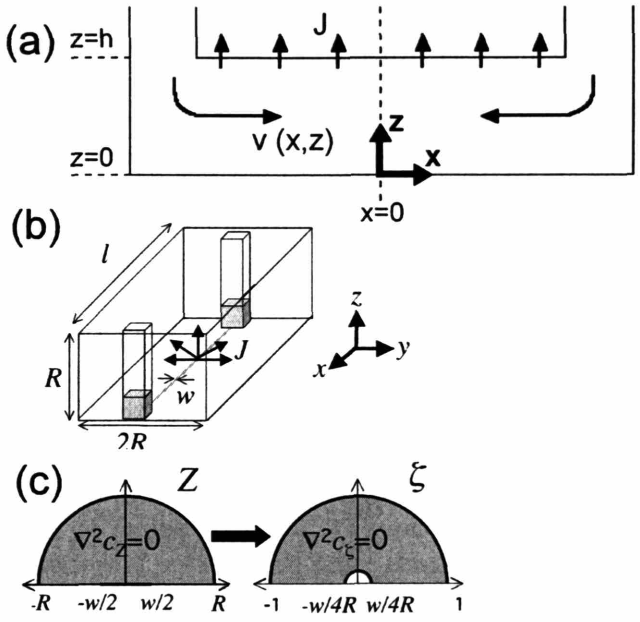

Figure 4-1: (a) Side-view of the PDMS microchannel on the microfluidic length scale h. (b) Three-dimensional view of the PDMS microchannel on the mass transfer length scale R. (c) Conformal mapping of the microchannel geometry.

are PDMS, characteristic of softlithography microfluidic devices. Because PDMS is permeable to water, there is a net flux J of water molecules out of the microchannel and into the PDMS which drives a converging microfluidic flow $\mathbf{v}(x, z)$ in this geometry[1]. We neglect y-dependence of the velocity because $h/w \ll 1$.

We use the lubrication approximation [66] to model this two-dimensional converging flow. This approximation reduces the Navier-Stokes equation to:

$$\frac{\partial^2 v_x}{\partial z^2} = \frac{1}{\eta}\frac{dP}{dx} \tag{4.1}$$

which is valid in the limits $h/l \ll 1$ and Re $h/l \ll 1$, where $\mathrm{Re} = h v_x \rho/\eta$, ρ is fluid density, and η is the fluid viscosity. For general conditions in this study (e.g. $w = 50$ μm, $h = 2$ μm, and l=2.5 cm) the lubrication approximation is valid everywhere except the O[μm] entry and side wall regions. The boundary conditions used are symmetry at $x = 0$, no slip at $z = 0$ and $z = h$, no penetration at $z = 0$, and a flux balance at $z = h$ so that $v_z(x, z = h) = \frac{J}{\rho}$.

The permeation induced velocity profile can be found by solving Eq. 4.1 and the continuity equation. Averaging v_x over the channel height gives:

---

[1] The same analysis can be applied to permeation driven flow in a channel closed at one end.

$$\langle v_x(x) \rangle = \frac{-Jx}{\rho h} \tag{4.2}$$

Thus the permeation driven microfluidic flowrate will grow linearly as the distance from the symmetry (or stagnation) plane increases and it depends inversely on the height of the microchannel. The magnitude and time dependence of this flow depend on the mass transfer rate of the solvent (water) into PDMS.

The mass transfer of water in PDMS has been previously studied [120], and results suggest near-Fickian diffusion with a diffusion coefficient $D \sim 10^{-9}$ m^2/s. On the length scale of the mass transfer (R), the channel width w appears very small, so that the mass transfer is primarily radial diffusion (Fig. 4-1 (b)). We model the mass transfer of water into the PDMS using constant-D Fickian diffusion:

$$\frac{\partial c}{\partial t} = D\nabla^2 c \tag{4.3}$$

On the mass transfer scale, $h \sim 0$ so that the diffusion problem in PDMS reduces to diffusion from a narrow strip of width w. One boundary condition is nontrivial: $c(-w/2 < y < w/2, z = 0) = c_o$, where c_o is the room temperature saturation concentration of water in PDMS. However, this geometry is similar to a classical problem of the potential flow of fluids near cracks in porous rocks [121]. We follow the same technique as Ref. [121] and construct the steady state concentration profile using a conformal map [122]. Using this result, we will then show how to compute the mean flux of water molecules leaving the channel.

Steady state permeation flow: As done in most conformal mapping problems, we translate our 2D geometry (yz-plane) to the complex plane ($Z = y + iz$) and define a complex concentration (potential) so that $c(y, z) = \Re(c_Z(Z))$. We are working under the assumptions that the channel height is negligible and the outer boundary can be approximated as a cylinder. The conformal map $\zeta = (Z + \sqrt{Z^2 - w^2/4})/(2R)$ maps the segment ($-w/2 < y < w/2,\ z = 0$) into a semi-circle of radius $w/4R$ in the ζ-plane (Fig. 1C). The exterior PDMS boundary of radius R is mapped to a semi-circle of radius 1, so we are left with a straightforward diffusion problem in the ζ-plane. Solving $\nabla^2 c_\zeta(\zeta) = 0$ with boundary conditions $c_\zeta(w/4R) = c_o$ and $c_\zeta(1) = 0$ gives:

$$c_\zeta(\zeta) = \frac{c_o \ln(\zeta)}{\ln(\frac{w}{4R})} \tag{4.4}$$

Note that the concentration profile depends only logarithmically on R, justifying our simplification of the external boundary. We can convert back to the Z-plane and take the real part of this complex concentration potential to get the steady state concentration profile $c(y, z)$. For $|Z| \gg w/2$, $c(y, z)$ is the same as that around a cylinder with radius $w/4$:

$$c(y, z) = \frac{c_o \ln(\frac{r}{R})}{\ln(\frac{w}{4R})} \tag{4.5}$$

where $r = |\sqrt{y^2 + z^2}|$. With this profile we can compute the flux of water at some position r: $J(r) = -Ddc/dr$. At steady state, there is no accumulation of water in the PDMS. Therefore we can compute the flux at some distance from the source where we know that Eq. 4.5 is valid, and use a mass balance relation to derive the mean flux at the microchannel ceiling. From this method, we find that at steady state:

$$J = \frac{-\pi D c_o}{w \, \ln\left(\frac{w}{4R}\right)} \tag{4.6}$$

Note that the steady state flux will decrease as w increases because $J \sim 1/(w \ln w)$.

Transient permeation flow: Next we examine the transient mass transfer. For the transient case, at times $t \gg w^2/4D$ (which is $t \gg 1$ s here) the concentration profile asymptotically approaches the profile around a cylinder of radius $w/4$ [121]. Therefore, we construct a similarity solution of Eq. 4.3 using the effective radius of $w/4$ for the inner channel, obtaining a transient concentration profile:

$$c(r,t) = \frac{c_o E_i\left(\frac{-r^2}{4Dt}\right)}{E_i\left(\frac{-w^2}{64Dt}\right)} \tag{4.7}$$

where E_i is the Exponential Integral Ei function. We stress that for $r > w/2$, this is asymptotically valid for our exact geometry for times $w^2/4D \ll t \ll R^2/D$. To calculate the flux at some position r, we evaluate $-D\partial c/\partial r$:

$$J(r,t) = \frac{-2Dc_o \exp\left(\frac{-r^2}{4Dt}\right)}{r \; E_i\left(\frac{-w^2}{64Dt}\right)} \tag{4.8}$$

To obtain the transient flux at the microchannel, we now consider the limits of Eq. 4.8 as r approaches $w/2$ and $t \gg w^2/4D$. For any sufficiently small r (i.e. $r < \sqrt{Dt}/2$), we have $r^2/(4Dt) \ll 1$ so that the exponential in Eq. 4.8 is approximately 1. Expanding E_i near zero to leading order gives $J(r,t) \sim 1/(r \ln t)$ near the channel during this transient period of interest. Performing a mass balance at two radii, it is easy to see that there is no local accumulation of water in this PDMS region near the channel during this transient period. Therefore, as a reasonable approximation, we can use the same mass balance technique used for the steady state analysis to determine the flux at the microchannel ceiling. The transient flux (valid for $w^2/4D \ll t \ll R^2/D$) is:

$$J(t) = \frac{-2\pi D c_o}{w \, \ln\left(\frac{w^2}{64Dt}\right)} \tag{4.9}$$

Equations 4.6 and 4.9 predict the flux at times $t \gg R^2/D$ and $w^2/4D \ll t \ll R^2/D$ respectively. With this insight into the mass transfer of water into the PDMS, we can now analyze the induced microfluidic flow. In our analysis, we experimentally determine c_o and use D as a fitting parameter whose value is bound by values reported in literature [120].

4.1.3 Experimental

The experimental observable is the gap average velocity $\langle v_x \rangle$. We extract this by using fluorescence microscopy to track the position of small 0.11 μm diameter tracer beads in the flow.

Solution: A solution of $2 \times 10^{-4}\%$ fluorescent carboxylate-modified polystyrene microspheres (diameter=0.11 μm, Molecular Probes) in ultrapure water (Milli-Q, Millipore) was prepared for observation. Before loading into the microchannels, this solution was vortexed 30 s and sonicated 30 s (Aquisonic 50HT, VWR). Bead aggregation was not observed.

Channel preparation: PDMS microchannels were fabricated by softlithography [108]. A 10:1 PDMS: crosslinking agent (Sylgard 184, Dow) was degassed for 60 minutes at 15" Hg vacuum pressure. The PDMS was then poured onto a Si master wafer with the negative of the microchannel geometry embedded in a layer of AZ 5214 image reversal photoresist (Clariant). The Si wafer was pretreated with a fluorinated silane monolayer (United Chemical Technologies) to prevent cured PDMS from sticking to the Si master. After pouring, the PDMS was allowed to degas for an additional hour at 15" Hg. The PDMS was then cured at 65°C for 24 h. Reservoirs (4 mm×4 mm) were cut at each end of the cured PDMS microchannel with a scalpel and the microchannel was placed onto a clean glass slide (soaked 15 min in 1M NaOH, rinsed with ultrapure water, and treated with 100 W RF plasma for 60 s). Unless otherwise noted, the length of each microchannel was $l = 25$ mm. 10 μL of the bead solution was added to the reservoirs and the channel filled within a minute. Larger volumes can cause diffusion of water from the reservoir sidewalls to perturb flow rates at long times ($O[(l/2)^2/D] \sim O[\text{day}]$). The reservoirs were replenished with 5 μL approximately every 2 hours. Significant sagging of the PDMS ceiling was not observed as 1.6 μm beads uniformly passed through a 2.0 μm-high channel and bead diffusion experiments showed no correlation with y-position away from the walls. We gravimetrically measured the solubility of water in PDMS to be $c_o = 40$ mol/m^3 at 21°C in agreement with Ref. [120].

Observation: The device was placed on an inverted microscope (Axiovert 200, Zeiss) and the tracer beads were observed through a 100×, 1.4 NA oil-immersion objective. Images were captured with an EB-CCD camera (C7190-20, Hamamatsu) and NIH Image software. Room conditions were steady at 21 ± 0.5°C and $33 \pm 3\%$ relative humidity. We determined the gap average velocity for each presented data point by computing the velocity of 15 tracer beads in the x-direction. To do this, we determined the center of mass position of a bead at two different times, requiring that $\Delta x \sim 35 - 70$ μm depending on the velocity. The gap average velocity for a bead was then $\Delta x / \Delta t$. Note that a typical value of Δt was 1 s in the 2 μm-high channels. In this time a bead can diffuse ~ 4 μm in the z-direction, which assures us that we are measuring the gap average velocity. These measurements were made at y positions at least 5 μm from the side walls, where we confirmed that the $\langle v_x \rangle$ profile was independent of y.

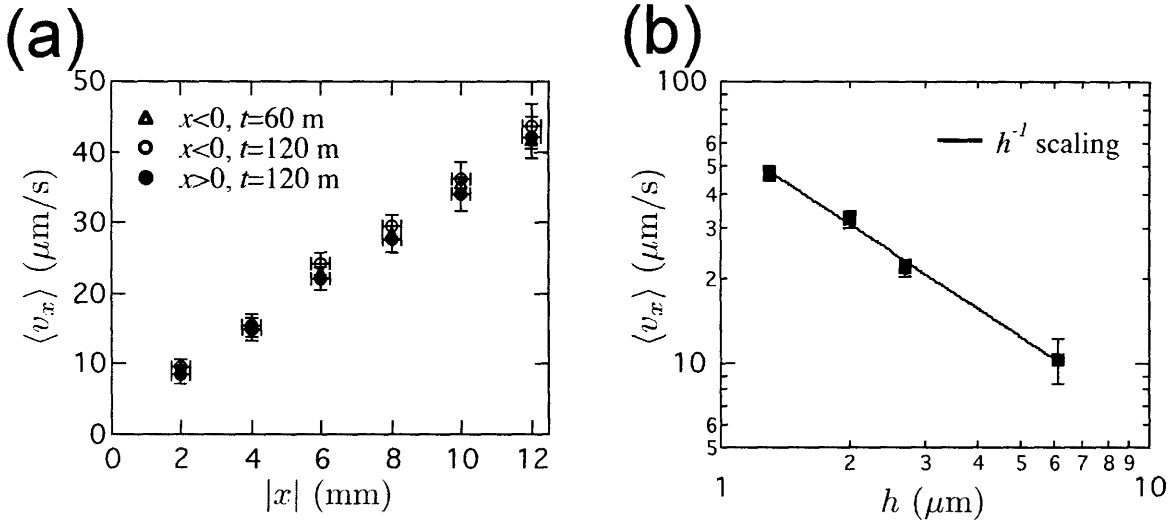

Figure 4-2: (a) Steady permeation velocity as a function of distance from the center ($|x| = 0$) in a microchannel with $w = 50$ μm, $h = 2$ μm, and $R = 1.5$ mm. (b) Steady permeation velocity (evaluated at $t = 150$ min, $x = 9.5$ mm) as a function of height in microchannels with $w = 50$ μm and $R = 5$ mm.

4.1.4 Results

We investigated the dependence of $\langle v_x \rangle$ on x and h in order to validate the lubrication approximation analysis by tracking the velocity of 0.11 μm beads in the PDMS microchannels. Figure 4-2(a) shows the steady state permeation velocity as a function of the distance $|x|$ from the microchannel center. The dimensions of this microchannel were $w = 50$ μm, $h = 2$ μm, and $R = 1.5$ mm. The velocity clearly increases linearly with $|x|$ and, noting that both $x < 0$ and $x > 0$ data is present, it is symmetric about $x = 0$. From the slope we calculate the flux to be $J = 7 \times 10^{-6}$ kg/(m^{2}s), which is interestingly $\sim$ 20% of the evaporation rate of water at these conditions. Figure 4-2(b) shows the steady state permeation velocity at $x = 9.5$ mm. The velocity scales as h^{-1} as predicted and is much more pronounced in thin channels. Together, these experiments confirm that the steady state microfluidic velocity can be modeled by the lubrication approximation. Next we examine how this flow depends on the mass transfer.

Using Eq. 4.2 and the expressions for $J(t)$ and J from our model, we can predict the transient and steady state permeation velocities respectively. Figure 4-3(a) shows the time-dependent permeation velocity at $x = 9.5$ mm as a function of PDMS thickness. Lines are included at long times showing the expected steady state velocities for each R using the measured value of $c_o = 40$ mol/m^3 and a fitting parameter $D = 8.5 \times 10^{-10}$ m^2/s. This best fit D for transient and steady data is in the range observed in recent diffusion experiments in PDMS [120]. Importantly, note that the steady state velocities are weakly dependent on R, as predicted by Eq. 4.6, which is a consequence of radial diffusion from a thin line. Also, note that permeation can deliver steady velocities for several hours. In Fig. 4-3(b), we focus on the short-time transient velocity and include channels of various widths. The line accompanying each constant-width data set is Eq. 4.9, again using $c_o = 40$

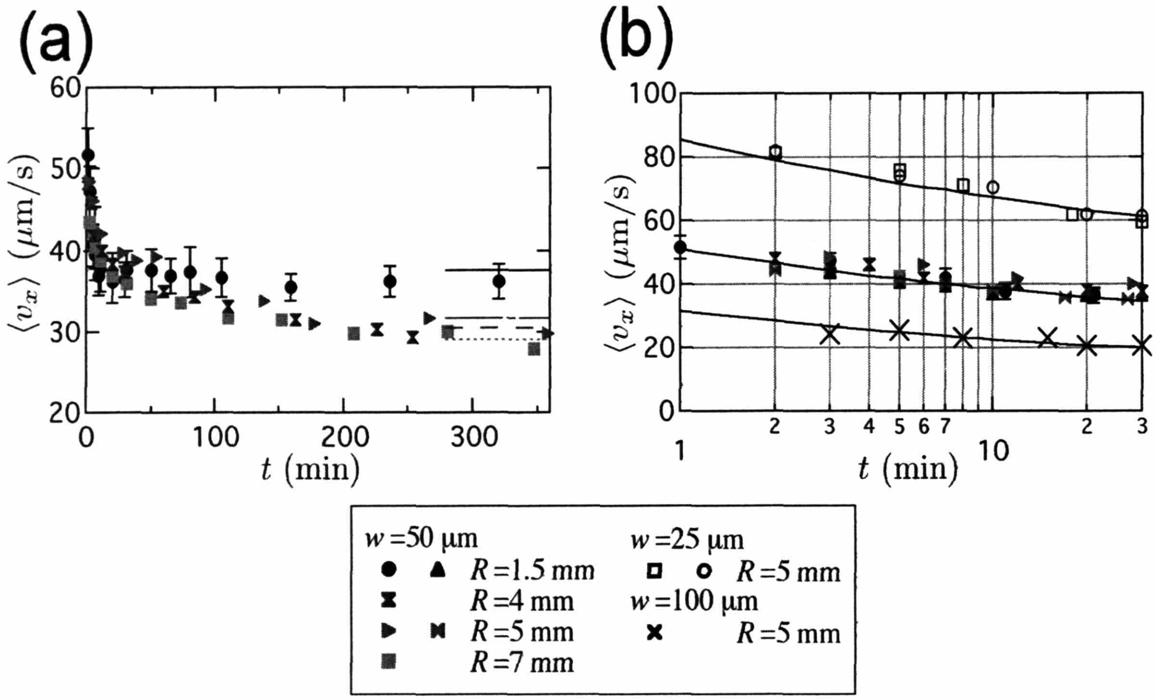

Figure 4-3: (a) Permeation velocity (x = 9.5 mm) as a function of time and PDMS thickness (see Legend) in microchannels with w = 50 μm and h = 2 μm. Lines are the calculated steady state velocities for each R (moving down, R=1.5, 4, 5, and 7 mm) using $D = 8.5 \times 10^{-10}$ m^2/s. Only one set of the self-similar error bars is shown for clarity. (b) Transient permeation velocity for different channel widths with h = 2 μm. Lines are the calculated transient velocities using $D = 8.5 \times 10^{-10}$ m^2/s.

mol/m^3 and $D = 8.5 \times 10^{-10}$ m^2/s. Note that the wider channels do have lower induced velocities as expected. Additionally, the transient scaling has a much flatter fall-off with time than the $t^{-1/2}$ scaling predicted for planar diffusion, a consequence of the logarithmic time scaling (Eq. 4.9) of radial diffusion. Finally, note that the w = 50 μm data for various R show uniform behavior during the transient penetration into the PDMS, which is expected since the outer boundary condition has no effect at times $t \ll R^2/D$.

4.1.5 Discussion and applications

Comparison to Poiseuille flow: Figures 4-2 and 4-3 show strong experimental support that the models presented can reliably predict the permeation induced microflow. We can compare the gap average velocity to that of a mean Poiseuille velocity $U_{\text{Poiseuille}}$ to get a better feel for when this flow is important:

$$\frac{\langle v_x \rangle}{U_{\text{Poiseuille}}} \sim \frac{J\eta l^2}{\rho h^3\,\Delta P} \tag{4.10}$$

where ΔP is an externally applied pressure drop. At large values of this parameter, *e.g.* for very thin channels, the permeation induced velocity will dominate the applied pressure driven flow. More specifically, for $h < 10$ μm, $\langle v_x \rangle / U_{\text{Poiseuille}} \gg 1$ for the flow induced by a 1 mm hydrostatic head. Therefore, it is impossible to create a stagnant fluid environment in thin, untreated PDMS channels. Consequently, knowledge of permeation induced flow is extremely important for designing the next generation of O[μm] microdevices in PDMS.

Eliminating the flow: For many applications in O[μm] sized PDMS channels, permeation induced flow is undesirable. Therefore it would be useful to try to eliminate it by inhibiting the mass transfer of water into the PDMS. The simplest way to do this is to supersaturate the PDMS with water by soaking it in a bath of heated water. We soak a PDMS microchannel in 50°C water for 24 h, rinse it, gently dry it, and then use it as in the above experiments. We observe that after a short equilibration time of 10-20 minutes (presumably to re-soak a thin layer of PDMS that has dried during handling), the permeation driven flow subsides. We show this by tracking the mean square displacements ($\langle \Delta x^2 \rangle$ and $\langle \Delta y^2 \rangle$) of the tracer beads vs. lag time τ (Fig. 4-4) using 120 s of total trajectory time for each time series at a position x=9.5 mm in the microchannel. For reference, we include the $\langle \Delta x^2 \rangle$ expected at $x = 9.5$ mm if the permeation driven flow persisted (dashed line). Without flow, we expect that both $\langle \Delta x^2 \rangle$ and $\langle \Delta y^2 \rangle$ equal $2D_{\text{bead}}\tau$ expected from the Stokes-Einstein relation. For times up to 2 h, both $\langle \Delta x^2 \rangle$ and $\langle \Delta y^2 \rangle$ equal $2D_{\text{bead}}\tau$ and the flow is not detectable. This 2 h passivation time is approximately the time it takes for this piece of supersaturated PDMS to dry at room conditions. More robust passivation methods such as using a coating of parylene [123] or teflon [124] would be desirable as research in PDMS devices moves to the micro- and nano-scales.

Applications: We have already mentioned the potential to use this flow for passive pumping, as it can deliver a steady flow for several hours. In fact it is possible to passively generate a converging flow in a single channel, a difficult feat by conventional techniques. A steady converging flow could prove to be a powerful way to quantify chemical interactions at the channel center where two different streams would meet. For example, it may prove useful to monitor chemical reactions or gel-formation phenomenon at the channel center.

Other possible applications that we are able to demonstrate are passively stacking colloids and passively concentrating chemicals. Figure 4-5 shows light microscopy images of passively fabricated crystalline microstructures. To form these arrays, we applied 2% solutions of various bead sizes to the reservoirs of a thin PDMS microchannel ($w = 50$ μm, $h = 2$ μm, $R = 5$ mm, and $l = 1$ cm). The permeation-driven flow carried the beads toward the center of the channel where they assembled into the displayed structures. With this assembly technique we have created a microstructure with controllable pore size. The ability to create regions with controlled porosity inside a microchannel is a potentially useful tool for biomolecule separations (e.g. DNA). This bead stacking method will also be useful for micro-bead catalyst processes [125] because beads can be stacked at the center of a channel without the need for any supporting weirs. Consequently, beads much smaller than typical microfabrication limits could be used for these catalytic/enzymatic processes. In comparison to other bead stacking techniques, permeation driven stacking is limited to thin channels but has the

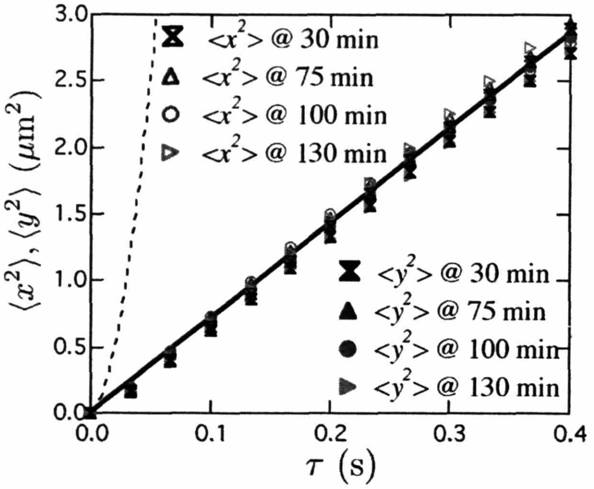

Figure 4-4: Mean square displacement (MSD) vs. time of the tracer beads in a pre-soaked PDMS microchannel with $w = 50$ μm, $h = 2$ μm, and $R = 5$ mm. Open symbols are for the x-direction and filled symbols are for the y-direction. Data is taken at several times after filling the microchannel at the position $x = 9.5$ mm. The dashed line is the expected MSD if the permeation driven flow persisted and the solid line is the Stokes-Einstein MSD.

advantage of forming layered microstructures in the center of a channel without supporting weirs.

In addition to forming stacked microstructures, we can concentrate chemical species with this flow. Concentrating chemicals is particularly important in micro-detection devices because the small sample volume combined with potentially low species concentrations leaves very few species for detection [118]. Concentration is also important at the beginning of many separation processes (e.g. DNA) which require an initial highly concentrated plug of material. Permeation driven flow offers a way to concentrate chemicals at specific regions in a channel. For example, a symmetric "T" design could concentrate species at the channel intersection where they can be driven by a field for a separation application. The characteristic concentrating length scale is $\sqrt{\frac{D_{\text{mol}}\rho h}{J}}$, where D_{mol} is the diffusivity of the desired concentrated molecule in water. At this length scale diffusive fluxes and convective fluxes balance near the stagnation plane. Because D_{mol} grows as molecular size decreases, this length scale may be much larger than molecular dimensions. The typical channels in this study would be able to concentrate molecules in regions with lengths on the order of 0.5 mm for a small molecule like fluorescein to 50 μm for a macromolecule like λ-DNA. To show chemical concentration, we load the left reservoir of a 2 μm-high channel with water and the other with $2 \times 10^{-2}\%$ fluorescein. Assuming that the fluorescein concentration is proportional its fluorescence light intensity, we can quantify the degree of concentration of the fluorescein at the center of the microchannel. Figure 4-6 shows the centerline ($y = 0$) pixel intensity as a function of distance from the channel center ($x = 0$) 60 minutes after loading the dilute fluorescein solution. The image is a magnification of the center of the actual channel where darkness corresponds to high intensity. Care was taken not to saturate our 8-bit intensity resolution and to capture short (< 2 s) images so that photobleaching was not a factor. After the pixel intensity was noise filtered, the inlet fluorescein had a baseline intensity of 10. At the channel center, the intensity averages to a value near 150,

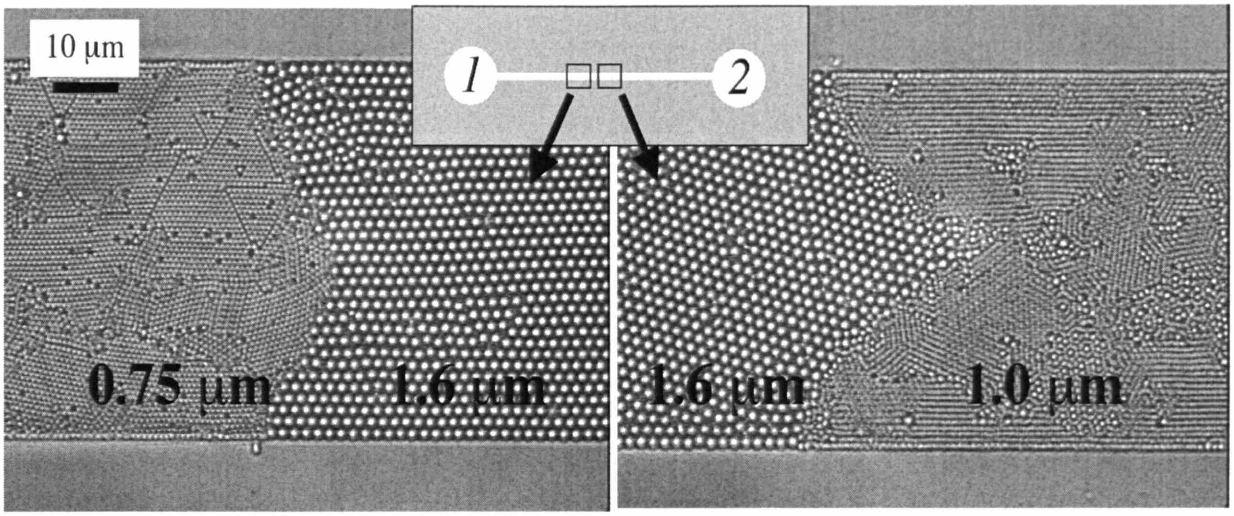

Figure 4-5: Observation of permeation driven bead packing (bead diameters of 0.75, 1.0, and 1.6 μm) in a channel with $h = 2$ μm. Both images are taken on the left side of the symmetry plane and the crystal interface propagates from right to left.

corresponding to $\sim 15\times$ concentration of the fluorescein. This agrees with a back-of-the-envelope calculation using Eq. 4.2 for the degree of concentration for a 0.5 mm-long sample volume at the center of this channel.

4.2 Electroosmotic flow

4.2.1 Background

Electroosmotic flow is the hydrodynamic flow generated when an electric field is applied across a channel with charged walls. The surfaces used in the microfluidic devices in this work, *i.e.* glass and PDMS, carry a negative charge in TBE buffers (pH$\sim$8) from dissociation of -Si(OH)$_3$. The negative surface charge causes the positive ions in the buffer to accumulate at the surface (in the O[nm] double layer) so that there is a local imbalance of charge in the fluid near the wall. The excess charge in the double layer will be positive for PDMS or glass, so fluid will move towards the negative electrode when an electric field is applied. Because the fluid is contained by charged walls on all sides, the fluid moving at the walls will also drag the remaining fluid in the bulk of the channel. The velocity of the electroosmotic flow [66, 69] is given by the Smoluchowski equation in the small-Debye layer thickness limit:

$$\mathbf{v} \approx \frac{\phi_\zeta \epsilon_{de} \mathbf{E}}{\eta} = \mu_{EOF} \mathbf{E} \tag{4.11}$$

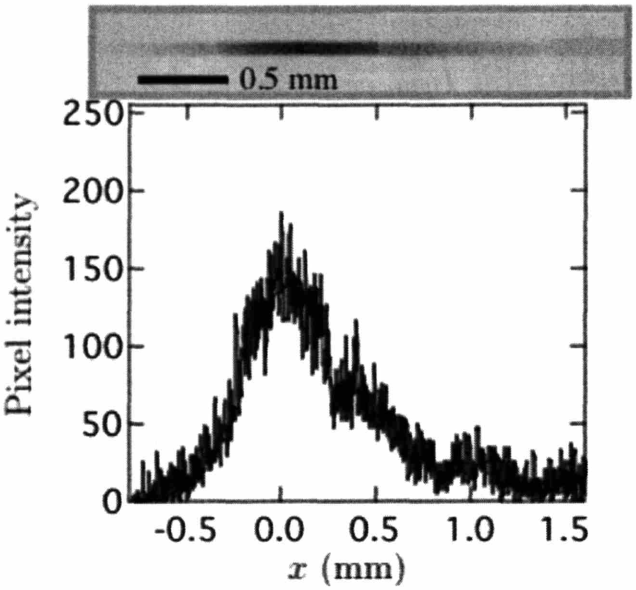

Figure 4-6: Centerline (y=0) fluorescence intensity of fluorescein concentrating near the center of a microchannel (w = 50 μm, h = 2 μm, R = 5 mm, and l = 2.5 cm) after 60 minutes of flow. The composite image is the series of four snapshots about x = 0 used to obtain this data, with high intensity corresponding to dark areas.

where ϕ_ζ is the zeta potential of the surface, ϵ_{de} is the fluid permittivity, η is the fluid viscosity, and $\mathbf{E}$ is the electric field. In a straightwalled channel outside of the O[nm] Debye layer, the induced electroosmotic flow has a plug profile. The zeta potential depends on the surface charge density, bulk ion concentrations in the fluid, and temperature. Typical room temperature zeta potentials are $\phi_\zeta \sim$ 35 mV for PDMS, $\phi_\zeta \sim$ 15 mV for PMMA, and $\phi_\zeta \sim$ 65 mV for glass at pH=8 with a high ionic strength buffer (O[0.1 M]) [126, 127]. Often we will combine some of these variables into one parameter μ_{EOF} which we will call the electroosmotic mobility. Hence, typical electroosmotic mobilities for 1 cP fluids are μ_{EOF} ~2.5 (μm/s)/(V/cm) for PDMS, μ_{EOF} ~1.2 (μm/s)/(V/cm) for PMMA, and μ_{EOF} ~5 (μm/s)/(V/cm) for glass. We exclusively use PDMS channels. PDMS can be irreversibly sealed to glass by plasma treatment (though we often do not perform this step) which may increase μ_{EOF} further. At lower ionic strength (O[0.01 M]), μ_{EOF} may increase by a factor of 2-4 after plasma treatment, however at high ionic strength (O[0.1 M]) the increase may only be $\sim$ 33% [128]. Nevertheless, note that these high ionic strength electroosmotic mobilities are greater in magnitude than DNA's electrophoretic mobility (μ_{EL} ~-1.3 (μm/s)/(V/cm) at 0.17 M TBE) so that if electroosmotic flow is not eliminated, DNA will move in the *wrong direction* toward the negative electrode.

4.2.2 Quenching electroosmotic flow

To be able to conduct proper electrophoresis experiments, electroosmotic flow much be sufficiently quenched so that the DNA's motion is governed by electrophoretic forces. Unlike pressure-driven or permeation-driven flows however, electroosmotic flow is plug-like. Hence, its presence will only

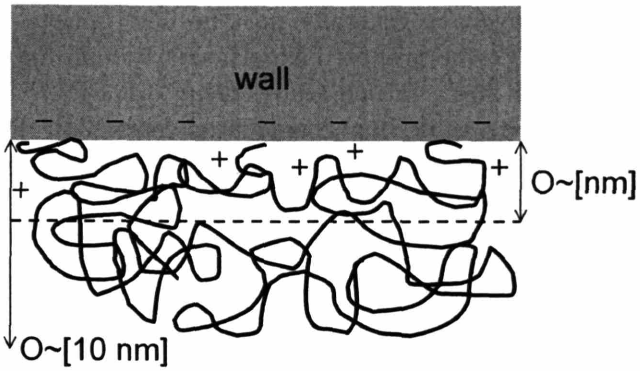

Figure 4-7: Close-up of a microchannel wall with electroosmotic quenching additives. These polymer additives physically or chemically attach to the wall with film thicknesses greater than the O[nm] double layer thickness.

change the magnitude of the electrokinetic motion. Nevertheless, we have just shown that uncontrolled electroosmotic flow will cause DNA to move the wrong direction. Several methods exist to sufficiently quench electroosmotic flow so that $\mu_{EOF}/\mu_{EL} \sim 0.1$, where μ_{EL} is the electrophoretic mobility. All of these quenching methods rely on using polymer additives to adhere (chemically or physically) to the channel walls to increase the local viscosity in and near the electric double layer (Fig. 4-7).

Before we address electroosmotic flow quenching, we first recall that the microchannels we use are PDMS/glass hybrid channels, meaning that the bottom surface is glass and all other surfaces are PDMS. Studies to determine μ_{EOF} in these hybrid channels show that the electroosmotic flow can be slightly higher than in entirely PDMS channels [127] and that electroosmotic flow gradients may exist [129]. However these nonidealities are most important at low ionic strength and with plasma sealing; our experiments generally employ high ionic strength and no plasma sealing. At 0.1 M ionic strength ($\sim 2.2\times$ TBE), μ_{EOF} is nearly constant (~ 2.5 (μm/s)/(V/cm)) for PDMS/PDMS and PDMS/glass channels [127].

Several groups have investigated chemically grafting or depositing polymers to the surface of glass and PDMS. Harden, Long and Ajdari [130] developed a theoretical treatment of the resulting electroosmotic flow from grafting both sparse and dense polymers to surfaces and Tessier and Slater performed similar Monte Carlo simulations [131]. This method has been implemented by several groups working in glass channels, *e.g.* Ferree and Blanche [46], by first applying a self-assembled monolayer to the glass surface and then growing a polyacrylamide brush from the monolayer. Modification of PDMS is less documented, however it has been shown to be done by radiation-induced graft polymerization, silanization, or chemical vapor deposition [132]. These chemical modification techniques are both complex to implement (especially in PDMS/glass devices) and still under development.

In practice, electroosmotic quenching in PDMS channels has generally been implemented by physically adsorbing polymers to the channel walls. The two primary methods are growing *polymer multilayers* [133] and adding a dilute polymer to the experimental buffer to provide a *dynamic coating* [134, 135]. Electrophoresis experiments generally require neutral polymers to coat the channel walls, so growing multilayers is generally not the best option. As long as the polymer additive does not significantly affect the proposed experiment, dynamic coating is by far the easiest method to quench electroosmotic flow. In one study, using 0.1% PVP ($M_w = 10^6$, $c^* \sim 1\%$) in 1×TBE reduced μ_{EOF} to 6% of its value in the untreated case [134]. PVP is nonionic and does not react with any of our buffer components, so we choose this dynamic coating method to quench electroosmotic flow in our experiments.

4.2.3 Experimental

We performed control experiments to gauge how effective the dynamic coating is in quenching electroosmotic flow. These experiments were performed with 2 μm-high PDMS/glass channels with buffers of two ionic strengths (I): 1) 5×TBE, 4% β-mercaptoethanol, 1% tergitol (NP-10), and 0.1% polyvinylpyrrolidone (PVP, Polysciences, $M_w = 10,000$) (η=1 cP, pH=8.3, I ~0.17 M) and 2) 0.5×TBE, 4% β-mercaptoethanol, 1% tergitol (NP-10), and 0.1% PVP (Polysciences, $M_w = 10,000$) (η=1 cP, pH=8.3, I ~0.02 M).

We measured and observed electroosmotic mobility μ_{EOF} by tracking the position of uncharged surfactant-stabilized kerosene microemulsion droplets (Ademtech, 500 nm-diameter) in each of these buffers using the PVP polymer additive to dynamically coat the walls. We determine μ_{EOF} for each bead by first simply taking the distance moved downstream and dividing by the time it took to move that distance to obtain a velocity, and then using the Smoluchowski relation (Eq. 4.11) to extract the electroosmostic mobility. Furthermore, we dyed T4 DNA with TOTO-1 (4.7 bp:dye) and added it to the solution at a very dilute concentration of 0.06 μg/mL so that we could simultaneously measure the bead velocity and the DNA velocity for a given electric field. The beads do not fluoresce, so we track them using visible light and a Hitachi (KP-M1AN) camera. We track DNA using our standard fluorescence microscopy techniques and a Hamamatsu EBCCD camera (C7190-20) as explained in Chapter 3.

The reported DNA mobility is actually the electrokinetic mobility ($\mu_{DNA} = \mu_{EOF} + \mu_{EL}$) where μ_{EL} is the electrophoretic mobility. For simplicity, because of the low value of μ_{EOF} in quenching buffers, we will often discuss DNA mobility in this thesis as if $\mu_{EOF} = 0$ and always report the observed electrokinetic mobility μ_{DNA} as the "electrophoretic" mobility. It is only in this section where we distinguish μ_{DNA} and μ_{EL}.

4.2.4 Results

The mobility measurements are summarized in Table 4.2.4. We find that at high ionic strength (5×TBE) the electroosmotic mobility has been quenched to an order of magnitude smaller than the resulting DNA mobility, however at low ionic strength (0.5× TBE), it is on the same order as the resulting DNA mobility.

The ability to dynamically quench electroosmotic flow is primarily determined by the size of the polymer additives relative to the double layer thickness. However, using polymers that are too large may cause significant conformation entanglements with the DNA under analysis. PVP with

Table 4.1: Summary of measured mobilities ([μm/s]/[V/cm]) in a 2 μm-high PDMS microchannel (glass bottom) at 1 cP in high and low ionic strength (I) dynamic coating buffers.

	5X TBE(I=0.17 M)	0.5X TBE (I=0.02 M)
μ_{EOF}	0.15	1.2
μ_{DNA}	-1.3	-1.8

a 10^4 molecular weight is ideal for these experiments because it is small enough that it will not significantly alter a sample DNA's conformation during electrophoresis and it is large enough to sufficiently quench electroosmotic flow. However, we are forced to operate at high ionic strength ($I > 0.1$ M) in our DNA electrophoresis experiments to maintain the electroosmotic quenching.

4.3 Conclusions and outlook

In this chapter we have reviewed potential background flows that may arise in our PDMS microfluidic channels which may influence our DNA electrophoresis tracking results and modeling. We first noted that pressure-driven flows from reservoirs are generally negligible because the channels we use are extremely thin (h=2 μm). However, because the channels are so thin, a significant *permeation-driven* flow may result where the buffer permeates into the PDMS walls. This novel flow was not previously discovered in PDMS channels. We presented a model and experimental validation of the flow driven by permeation of a solvent into a PDMS wall. Results showed that the process can be described by the lubrication approximation and radial diffusion, which explains the increase in flow with decreasing channel height and the weak dependence of the flow on the PDMS thickness. In our DNA electrophoresis experiments this flow is undesirable, but we have shown that it can be eliminated by inhibiting the mass transfer of the solvent into the PDMS. On the other hand, we demonstrate that this flow can be harnessed for several passive flow applications like pumping, stacking microspheres, and concentrating chemicals. Permeation driven flow clearly offers a new technology to manipulate fluids and colloids on the micro- and nano-scale. But equally as important, as PDMS devices move from micro- to nano-scale, this flow will dominate externally driven flows. Therefore, knowledge of what drives it and what stops it is invaluable to the success of these future devices.

Finally, we addressed the well-known problem of electroosmotic flow that arises in a channel with charged walls in an electric field. We showed that we were able to adopt a procedure to dynamically quench electroosmotic flow by adding PVP molecules to our buffer. The resulting electroomostic flow is an order of magnitude smaller than the DNA electrophoretic velocity, however we are restricted to high ionic strength experiments.

Chapter 5

DNA Dynamics in Confinement

Quite often electrophoresis microchannels are thin (O[μm]) in order to minimize effects that can cause separation dispersion such as Joule heating and residual pressure-driven flows [136]. Additionally, many of the new DNA mapping devices require extension of DNA in narrow slits and channels. In order to model DNA deformation in these devices, we must first be able to measure and predict how a DNA molecule's transport coefficients and conformation change when it is *confined to a slit with a height of O[R_g].* The goal of this chapter is not to attempt an exhaustive study of the entire parametric space of polymer confinement. On the contrary, the goal is to examine only the DNA molecules we are considering in electrophoresis experiments (λ, 2λ, and T4 DNA), and measure how their diffusivity and relaxation time change with O[μm] confinement. The results will provide general insight into how polymers behave in thin slits with confinement of O[R_g].

First we will review theories for polymer conformations and dynamics in confinement. Then we present single molecule experimental results showing how DNA diffusivity and relaxation time change when confined in thin slits with heights comparable to the radius of gyration. Using some previously proposed and some new scaling arguments, we will show that although excluded volume effects are not easily observable in O[R_g] confinement, altered hydrodynamic interactions can significantly change the polymer dynamics.

5.1 Polymers in confinement

Reprinted (some excerpts) with permission from Y.-L. Chen, M. D. Graham, J. J. dePablo, G. C. Randall, M. Gupta, and P. S. Doyle, "Conformation and dynamics of single DNA molecules in parallel-plate slit microchannels", *Physical Review E*, **70**, 060901, (2004) [137]. Copyright (2004) by the American Physical Society.

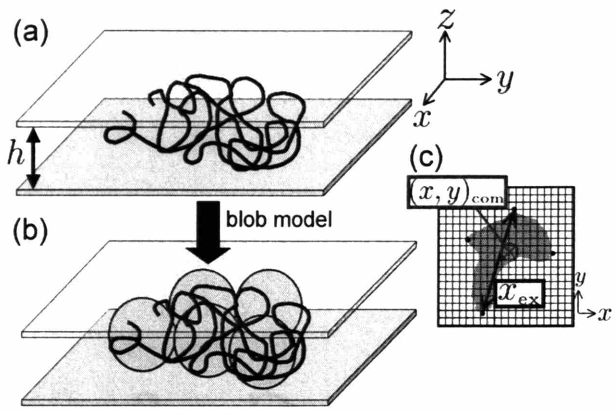

Figure 5-1: (a) Schematic of a DNA molecule confined in a slit. (b) Schematic of a blob model. (c) Experimental observables: $(x, y)_{\rm com}$ and $x_{\rm ex}$.

When a single polymer is placed in a confined geometry, both its static and dynamic configurational properties change. The statics and dynamics of confined polymers have been addressed by blob scaling models [138, 139], simulations [137, 140–143], and analytical theories [144].

We will conisder a polymer confined in an infinite slit with height h (Fig. 5-1 (a)). Both *excluded volume* and *hydrodynamic interactions* become important to consider for a polymer in confinement. Excluded volume will increasingly shift the configuration distribution to larger in-plane extension as confinement increases. Consequently the radius of gyration of the polymer R_g will expand in the plane parallel to the slit. Furthermore, hydrodynamic interactions with the walls will arise and intrachain hydrodynamic interactions will become screened as confinement increases, both acting to increase the drag on the polymer and decrease its diffusivity D. *Both* the excluded volume and hydrodynamic interactions will cause the polymer's relaxation time τ ($\sim R_g/D$) to increase with confinement.

Blob model scaling arguments [138, 145] provide valuable insight into how a polymer's static and dynamic configurational properties change with confinement. A blob model attempts to obtain general scaling relationships for configurational properties, without solving detailed statistical mechanics, by modeling the confined polymer as a series of connected blobs of size h (Fig. 5-1 (b)). Recall that a chain consisting of N monomers of size l_k in the bulk has a radius of gyration $R_{g,\rm bulk} \sim l_k N^\nu$ where $\nu \approx 3/5$ (the Flory-Edwards scaling exponent) for a good solvent. In a thin slit the polymer can be thought of as a chain of blobs (N_{blob}) which span the slit dimension h, each blob containing g monomers, giving $g \sim (h/l_k)^{1/\nu}$. The number of blobs can then be expressed as $N_{blob} = N/g \sim (R_{g,\rm bulk}/h)^{1/\nu}$. The entire blob polymer behaves as a Rouse chain since hydrodynamic interactions are screened at distances larger than h.

Static properties: In a slit, the extension x_{ex} (or characteristic size) of the chain is equivalent to that of a self-avoiding walk of blobs in two dimensions yielding:

$$\frac{x_{ex}}{R_{g,\rm bulk}} \sim \frac{h N_{blob}^{\nu_{2D}}}{R_{g,\rm bulk}} \sim \left(\frac{R_{g,\rm bulk}}{h}\right)^{\nu_{2D}/\nu-1} \sim \left(\frac{R_{g,\rm bulk}}{h}\right)^{1/4} \tag{5.1}$$

where we have set ν_{2D}, the Flory-Edwards scaling exponent for a chain in two dimensions, equal to 3/4 for a good solvent [36, page 1006]. According to Eq. 5.1, the molecule will extend with a fairly weak power law scaling, so that a DNA molecule confined to a slit 10 times thinner than its radius of gyration will only expand on average to ~ 1.7 times its bulk radius of gyration. We will only be concerned with confinement on the order of R_g at most, therefore perturbations to the component of the radius of gyration parallel to the walls will be small [137]. In other words, the excluded volume effect from confinement of $O[R_g]$ will not be important. Instead, our work will concentrate on how the hydrodynamic interactions from the confining walls affect the dynamic parameters (D and τ).

Diffusivity: Before addressing a confined polymer's diffusivity, it is first instructive to study how a spherical bead's diffusivity changes in confinement. The diffusion dynamics of a spherical colloid moving in an unbounded fluid was first addressed by Einstein in 1905. The diffusion coefficient of the colloid is given by the well-known Stokes-Einstein relation [146]:

$$D_{\text{bulk}} = \frac{kT}{\zeta} = \frac{kT}{6\pi\eta R} \tag{5.2}$$

where kT is the Boltzmann temperature, ζ is the drag coefficient, η is the viscosity of the fluid, and R is the radius of the sphere. In this chapter we will use the subscript "bulk" to indicate an unbounded fluid. In other chapters it should be obvious if the parameter is for a confined channel or in an unbounded fluid. Placing a wall near the colloid modifies the flow field around it because the fluid must satisfy the no-slip boundary condition at the wall. Qualitatively, the result is that the sphere's drag (ζ) increases and consequently, its diffusivity decreases. The presence of the wall breaks the translation symmetry so components of the drag force parallel to the wall will differ from those perpendicular to the wall. Our work will solely consider diffusivity components in the plane parallel to the walls ("inplane") since this is the parameter most valuable for modeling DNA in planar microfluidic electrophoresis devices.

Faxen was able to solve the single wall problem for the inplane diffusivity of a spherical colloid a distance z from a planar wall:

$$D = D_{\text{bulk}}\Big(1 - \frac{9R}{16z} + \dots\Big) \tag{5.3}$$

More generally, this problem can be treated with the method of images [146] which states that the flow field induced by any colloid near a wall is the same as a superposition of the unbounded flow fields generated by the colloid and its mirror image on the other side of the wall. Our work is concerned with dynamics in slits and hence confinement by *two walls*. This two-wall problem becomes analytically intractable (except for special situations) for a spherical colloid without further approximations. One special situation is when the sphere is at the center of a slit of height h. Faxen showed that the diffusivity varied as:

$$D = D_\infty\left[1 - 1.004\left(\frac{2R}{h}\right) + 0.418\left(\frac{2R}{h}\right)^3 + 0.21\left(\frac{2R}{h}\right)^4 - 0.169\left(\frac{2R}{h}\right)^5 + \dots\right] \tag{5.4}$$

Other more general approximations exist that have shown good agreement with experiments, such as the Oseen linear superposition approximation, which approximates the drag coefficient due to two walls as the sum of two single wall drag coefficients [147, 148].

The translation dynamics for a polymer are more complicated than for a sphere because of intra-chain hydrodynamic interactions and the polymer's ability to deform. A standard model for a polymer is a series of beads connected by springs or rods. As mentioned in Chapter 2, it is analytically intractable to solve for the hydrodynamic interaction flow field generated by all portions (or beads) of the polymer chain. However, the Zimm model employs a preaveraging approximation for simplification. Using the Zimm model and renormalization group theory, the polymer's diffusion coefficient in an unbounded fluid (good solvent) is [34, page 103]:

$$D_{\text{bulk}} = 0.203\frac{kT}{\sqrt{6}\eta R_g} \tag{5.5}$$

Note that the diffusion coefficient scales inversely with the coil size (R_g) and not the total polymer contour length (L), a characteristic effect of collective hydrodynamic interactions in the polymer. When a polymer is placed in a slit, just as in the case for a sphere, its diffusivity decreases due to the increase in drag. But unlike the single sphere problem, drag is further increased because hydrodynamic interactions *between different pieces of the polymer* become screened on the length scale of confinement. Again we resort to blob model scaling arguments to gain insight into how D changes for a polymer confined in a slit of height h.

In a slit (or capillary) hydrodynamic interactions are assumed to be strongly screened over length scales larger than h so the net drag on the chain scales as $\zeta \sim N_{blob}\zeta_{blob} \sim N_{blob}h \sim (R_{g,\text{bulk}}/h)^{1/\nu}h$. Using then the fact that $D \sim 1/\zeta$ and $D_{\text{bulk}} \sim R_{g,\text{bulk}}^{-1}$ gives

$$\frac{D}{D_{\text{bulk}}} \sim \left(\frac{R_{g,\text{bulk}}}{h}\right)^{1-1/\nu} \sim \left(\frac{R_{g,\text{bulk}}}{h}\right)^{-2/3} \tag{5.6}$$

A polymer confined in a slit 10 times thinner than its radius of gyration will have a resulting diffusivity of $\sim 0.2D_{\text{bulk}}$. This scaling for D is expected to hold for both a thin slit and a square capillary.

Relaxation time: In addition to translational motion, polymers also can stretch and then relax back to equilibrium configurations. As explained in Chapter 2, these dynamics are approximately described by a series of stress relaxation modes, of which the longest relaxation time τ dominates at long time. The Zimm model relaxation time in a good solvent scales as [34]:

$$\tau_{\text{bulk}} \sim \frac{\eta (N^{\nu} l_k)^3}{kT} \tag{5.7}$$

where N is the number of Kuhn steps and l_k is the Kuhn length. When a polymer is placed between confining walls, τ_{bulk} is altered because of increased drag and excluded volume effects that change the equilibrium conformation distribution. Although we noted above that we are not considering high confinement ($R_g/h > 1$) in this work, it is useful to determine the expected blob scaling for relaxation time. A blob model of the chain in a slit yields a two-dimensional (2D) self-avoiding polymer of N_{blob} subunits. The simplest way to show how the relaxation time scales is to determine the characteristic time to move on the coil length scale x_{ex}^2/D [149]. Using Eqs. 5.1 and 5.6, we can show that:

$$\frac{\tau}{\tau_{\text{bulk}}} \sim \left(\frac{R_{g,\text{bulk}}}{h}\right)^{\frac{2\nu_{2D}+1}{\nu}-3} \sim \left(\frac{R_{g,\text{bulk}}}{h}\right)^{7/6} \tag{5.8}$$

It is important to remember that for O[R_g] confinement, the polymer will not be compressed enough to form many blobs so that we may not necessarily observe the blob model scaling. If we simply assume the polymer's drag coefficient will increase due to hydrodynamic screening with the walls, one may expect a relation like Eq. 5.4 to hold for the diffusivity. Furthermore, since $\tau \sim x_{\text{ex}}^2/D \sim R_{g,\text{bulk}}^2/D$ in this regime where excluded volume effects do not expand the chain, we would expect τ to follow the inverse of Eq. 5.4 at weak confinement (substituting R_g for R)[1]:

$$\tau = \tau_{\text{bulk}} \frac{1}{\left[1 - 1.004\left(\frac{2R_g}{h}\right) + 0.418\left(\frac{2R_g}{h}\right)^3 + 0.21\left(\frac{2R_g}{h}\right)^4 - 0.169\left(\frac{2R_g}{h}\right)^5 + \ldots\right]} \tag{5.9}$$

In reality, DNA dynamics in an O[R_g] slit will lie in the crossover region between simple long-range hydrodynamic screening ($R_g/h \sim 0.1$) and blob scaling models ($R_g/h > 1$).

5.2 Results

Experimental: The experimental procedure requires standard techniques described more generally in Chapter 3. DNA molecules were stained with a fluorescent dye (TOTO-1, 4.7:1 bp:dye molecule) and diluted in one of two buffers: 1) 2.2×TBE, 3% β-mercaptoethanol, 0.07 % PVP (M_w=10^6, $c^\star \sim$ 1%), and 0.07% ascorbic acid (viscosity η=1.3 cP, pH=8.4) or 2) 5×TBE, 4% β-mercaptoethanol, 0.1 % PVP (M_w=10^4, $\ll c^\star$, viscosity η=1.0 cP, pH=8.4). The DNA sizes used were: λ DNA (48.5 kbp), 2λ DNA (97 kbp), and T4 DNA (169 kbp). Buffer 1 was used for the λ and 2λ experiments while buffer 2 was used for the T4 experiments. Standard values of $D_{\text{bulk}} = 0.45$ μm^2/s and $\tau_{\text{bulk}} = 0.1$ s were used for λ DNA diffusivity and relaxation time [60, 61]

---

[1] Substituting $R = R_h$, the hydrodynamic radius of the polymer, may be more rigorous here, however the values will be close.

in unbounded fluid at 1 cP. Standard Zimm model scalings were used to extrapolate values for 2λ and T4 DNA and to account for any viscosity differences.

We observed single DNA in 2 μm-high microchannels with a width of 50 μm. The primary experimental observables were the DNA's center of mass in the xy-plane $(x_{\text{com}}, y_{\text{com}})$ and the DNA's extension x_{ex} (Fig. 5-1 (c), for further details, see Sec. 6.2.2). The choice of DNA molecules to study was made based on manual recognition of coil size and brightness. Furthermore, no molecule was chosen within 10 μm of a sidewall. From the observable data, we extract D by fitting a line to the mean square displacement of the center of mass y-coordinate $\langle (y_{\text{com}}(t) - y_{\text{com}}(0))^2 \rangle$ versus t. The fit is taken between 0.2-2 s and since $\langle (y_{\text{com}}(t) - y_{\text{com}}(0))^2 \rangle \sim 2Dt$, D is determined as half the slope of this line. Only y-coordinates are used since they are much less sensitive to possible background flows in the microchannel. By matching our x-coordinate data, we confirmed that background flows were generally on the order of 0.1 μm/s under good conditions. The ensemble sizes are approximately 8-15 and each trajectory was 20-30 s (total tracking time of 200-350 s). We confirmed with random walk simulations (not shown) that this was enough data to use a 2 s lag time for line-fitting. Furthermore, we confirmed that the y_{com}-displacement ensembles were predictably normally distributed and fit well by the extracted value of D from the linear fit (not shown).

We extract τ by fitting an exponential to the extension autocorrelation function data for stretched DNA [98] because $\langle x_{\text{ex}}(t) x_{\text{ex}}(t) \rangle = \left(x_i^2 - \langle x_{\text{ex}}^2 \rangle_0 \right) \exp(-t/\tau) + \langle x_{\text{ex}}^2 \rangle_0$ where x_i is the initial stretch and $\langle x_{\text{ex}}^2 \rangle_0$ is the mean square extension of an equilibrium coil in the slit. These DNA were strongly stretched by being electrophoretically driven into on a 0.8 μm-radius obstacle. They were then tracked in an open region of a microchannel as they relax with the field off. An ensemble size of 20 molecules was used for each DNA size. We begin the exponential fit when $x_i/L \sim 0.30$ and end it when $x_{\text{ex}}/L \sim 0.15$ with τ as the only free parameter.

Diffusion results: Fig. 5-2 (a)-(c) shows all tracking data (split into 3-s trajectories) used to obtain diffusivity data for each DNA size. These distributions are closely symmetric indicating the lack of a major background flow. Fig. 5-2 (d) shows the mean square displacement data for the three DNA sizes up to a 3-s lagtime. The resulting diffusivity values are listed in Table 5.1.

Relaxation results: Fig. 5-3 shows the relaxation data for each DNA size, along with the ensemble average fractional extension autocorrelation function $(\langle x_{\text{ex}}(t) x_{\text{ex}}(t) \rangle - \langle x_{\text{ex}}^2 \rangle_0)/L^2$. The resulting relaxation times from the exponential fits are listed in Table 5.1.

Discussion: Fig. 5-4 shows the diffusivity and relaxation time data (scaled by the unbounded solution values) as a function of confinement $R_{g,\text{bulk}}/h$. We also include the blob scalings (Eqs. 5.6 and 5.8, dark lines) and Faxen's centered, two-wall power series (Eqs. 5.4 and 5.9, dotted lines). Though we only probe confinement from $0.1 < R_g/h < 1$, we are able to capture the blob model scaling for D. On the other hand, the relaxation scaling relies on both deformation and hydrodynamic screening, and since these conditions are not in the deformation regime, the relaxation data falls in the crossover region between far-field hydrodynamic screening and blob model scaling.

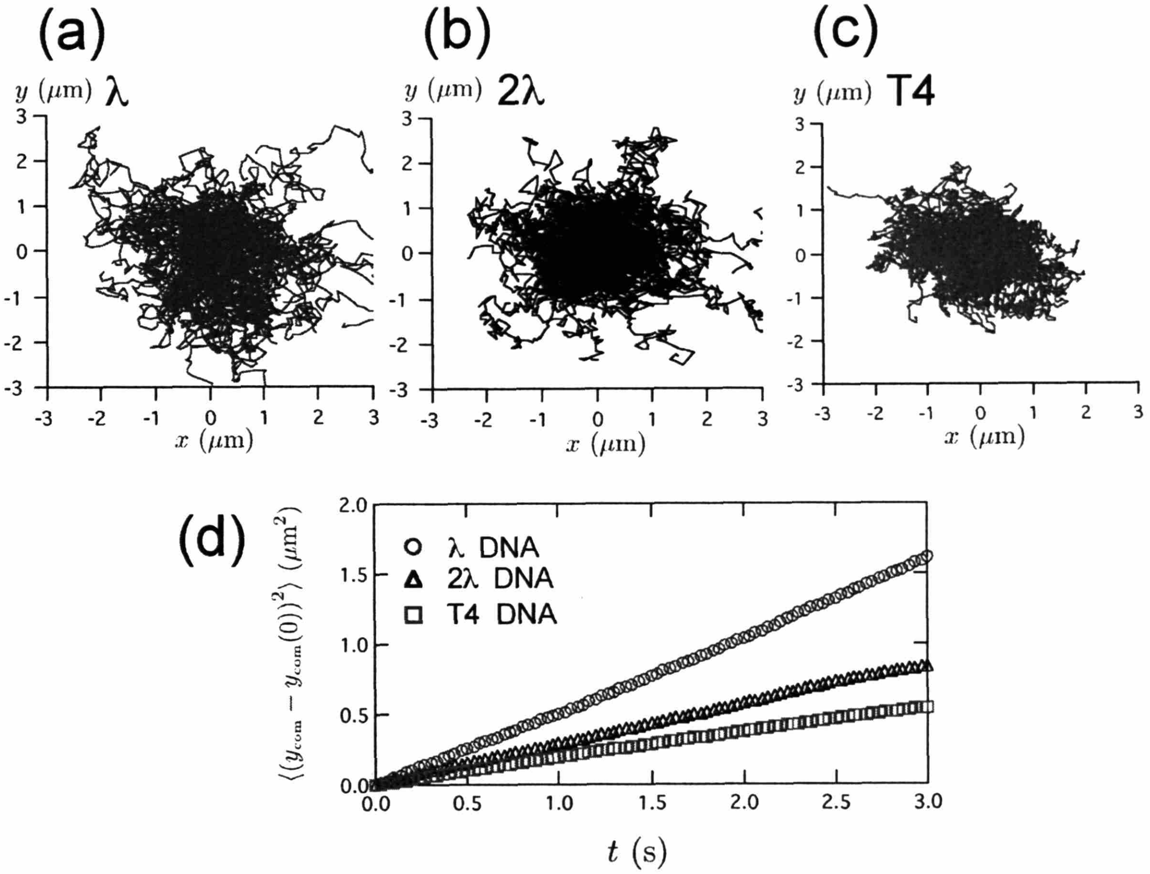

Figure 5-2: DNA diffusion study results. (a)-(c) 3-s long xy center of mass trajectories of DNA molecules in a 2 μm-high microchannel, all normalized to begin at (0,0). (a) λ DNA (1.3 cP), (b) 2λ DNA (1.3 cP), and (c) T4 DNA (1 cP). (d) Mean square displacements of y_{com} for λ, 2λ, and T4 DNA.

Table 5.1: Summary of dynamic parameters D and τ measured in a h=2 μm thin channel.

DNA, size	solvent η	$\langle x_{\text{ex}}^2 \rangle_o$ (μm^2)	D (μm^2/s)	τ (s)
λ, 48.5 kbp	1.3 cP	4.1	0.26	0.19
2λ, 97 kbp	1.3 cP	9.0	0.14	0.7
T4, 169 kbp	1 cP	22.0	0.092	1.7

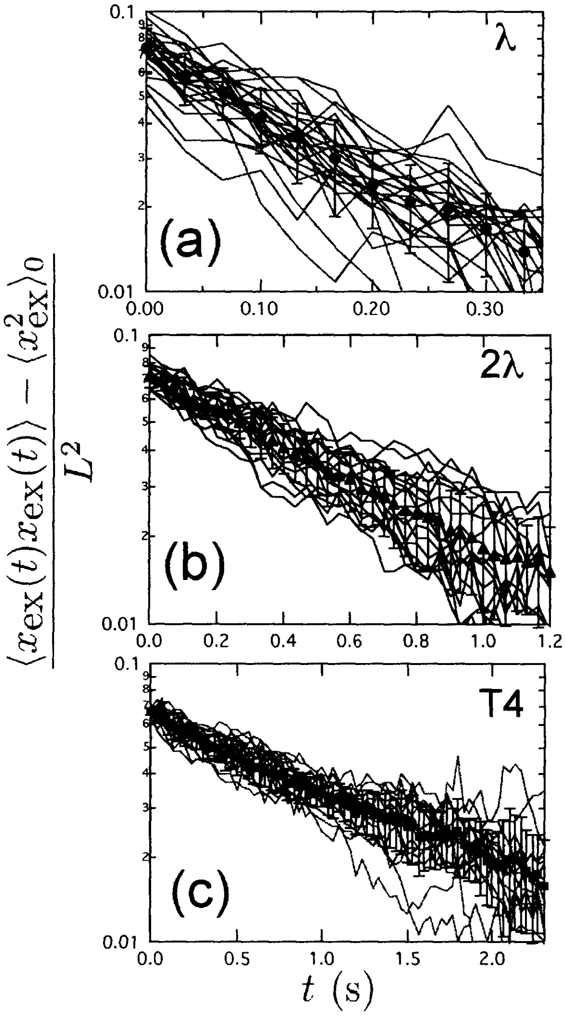

Figure 5-3: DNA relaxation results. Mean square fractional extension for (a) λ DNA (1.3 cP) (b) 2λ DNA (1.3 cP) and (c) T4 DNA (1 cP) relaxing in a 2 μm-high microchannel. The lines are single molecule traces and the symbols are the ensemble average.

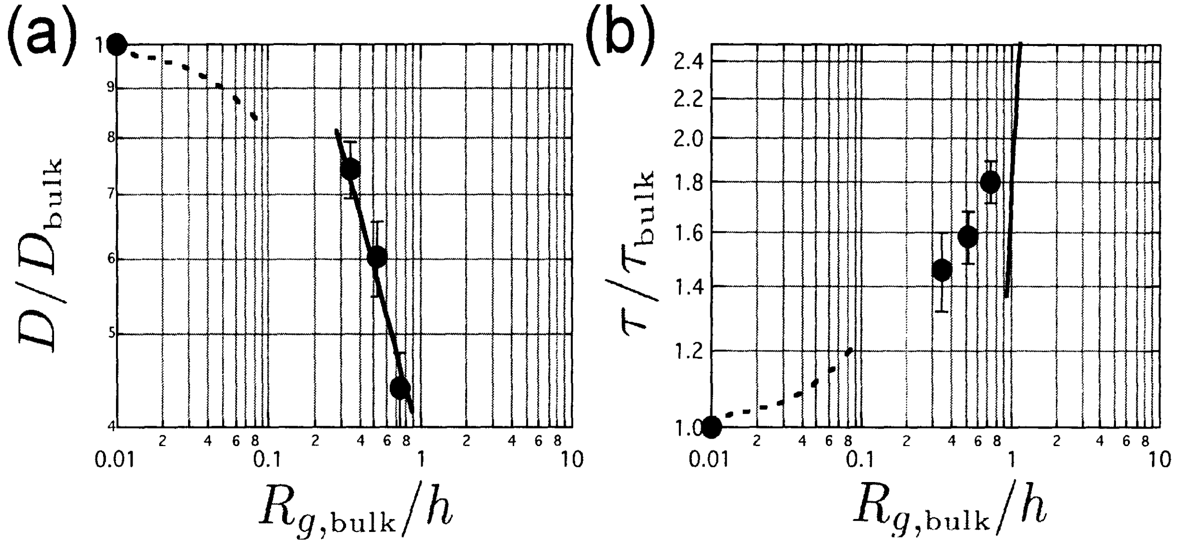

Figure 5-4: Transport coefficients in confinement. (a) Diffusivity and (b) relaxation time, both scaled by bulk values. The solid black lines are the blob scalings (Eqs. 5.6 and 5.8) and the dashed lines are Faxen's centered, two-wall power series (Eqs. 5.4 and 5.9).

5.3 Conclusions and outlook

In conclusion, we have experimentally measured D and τ for λ, 2λ, and T4 DNA in 2 μm high microchannels. The results confirm general observations about polymers confined in slits of O$[R_g]$ thickness: 1) hydrodynamic interactions become screened and $D/D_{\text{bulk}} \sim (R_{g,\text{bulk}}/h)^{-2/3}$ and 2) excluded volume deformation is negligible so that τ/τ_{bulk} does not follow the blob scaling of $(R_{g,\text{bulk}}/h)^{7/6}$, though $\tau/\tau_{\text{bulk}} > 1$ due to hydrodynamic screening.

Should this study continue in an attempt to more fully probe the confinement parameter space, the two primary limitations would be 1) access to only three easily identifiable DNA sizes and 2) access to microchannels only as thin as 1.3 μm. However, it is possible to make channels as thin as 0.8 μm with a positive photoresist mask and even 0.2 μm by etching silicon. Also, we hope in the near future that DNA larger than T4 will be commercially available. A promising study would probe higher confinement, *e.g.* $R_g/h \sim 1 - 10$, to fully address blob scalings and beyond ($h \sim l_p$).

Chapter 6

DNA Deformation in Electric Field Gradients

Reproduced in part with permission from G. C. Randall and P. S. Doyle, "DNA Deformation in Electric Fields: DNA Driven Past a Cylindrical Obstruction", *Macromolecules*, **38**, 2410-2418, (2005). Copyright 2005 American Chemical Society.

There is a large incentive to both fundamentally understand methods of DNA deformation and to devise ways to stretch and compress DNA in microdevices at will. For example, studying DNA deformation is crucial to understand biomolecular processes that require conformation flexibility, such as the transport of viral DNA into cells [150]. Furthermore, stretching and compression of DNA can be useful unit operations for lab-on-chip devices, *e.g.* researchers are currently trying to scan and sequence a single fully stretched DNA strand basepair-by-basepair [26].

Flexible polymers like DNA deform from their native coil configurations in a solvent by applying forces either mechanically, with a hydrodynamic flow, or because DNA is negatively charged, with an electric field. For example, researchers have stretched tethered DNA with optical tweezers [54], uniform flows [45], and uniform electric fields [46]. From the perspective of engineering continuous processes, it can be more interesting to study how free DNA deforms in a *force field gradient.* For example, in a hydrodynamic flow, any obstacle or channel contraction/expansion induces velocity gradients that deform a flexible polymer. Single polymer deformation in hydrodynamic flows (like uniform extensional flow [86, 89], shear [92], or mixed flow [93, 94]) has previously been observed and characterized. Similarly, *electric field gradients* created by obstacles or by a channel contraction/expansion presumably will deform DNA. There have been many studies of DNA electrophoresis through barriers and obstacles in microchannels [14, 19–21, 23, 151–153] where electrophoretic DNA stretching and compression may play an important but generally overlooked role. For example, our group has shown that the performance of a hooking hairpin DNA separation mechanism is highly dependent on electrophoretic stretching from obstacle induced gradients [152, 153]. In addition, simulation work has shown that DNA can deform electrophoretically in entropic traps, *i.e.* nano-sized channel contractions, if the realistic curved electric field lines are incorporated [154].

This recent work suggests that DNA deform from electric field gradients created in microfluidic devices, however no studies have addressed the details of how these charged polymers electrophoretically deform. In this chapter we focus on the dynamics of DNA deformation in electric field gradients, developing a kinematic model with experimental verification. We consider two case studies: electrophoretic deformation induced by 1) a large non-conducting, cylindrical obstacle and 2) a hyperbolic contraction.

6.1 Electrophoretic deformation

We consider large double-stranded DNA fragments, typically of size 50-1000 kbp (~0.01-1% of a typical human chromosome), and free of all *in vivo* proteins. The DNA molecule is primarily characterized by its persistence length l_p, contour length L, diffusivity D, and longest relaxation time τ. The large DNA considered here have $L \gg l_p$ so that they adopt coiled configurations (with radius of gyration R_g) at equilibrium in aqueous solvents. Backbone phosphate groups render DNA a uniformly negatively charged polymer at moderate pH. In the presence of a uniform electric field $\mathbf{E}$, DNA coils move through solution at a size-independent velocity $\mu\mathbf{E}$ where μ is the electrophoretic mobility [155]. Just as velocity gradients deform polymers in hydrodynamic flows, electric field gradients can deform polyelectrolytes during electrophoresis. Refer to Chapter 2 for a review of polymer deformation in a flow field.

In order to examine how a charged polymer like DNA deforms in *electric field gradients* we must determine the dominant electric and hydrodynamic forces during electrophoretic stretching. Long *et al.* [156] have previously addressed the simultaneous action of electric and hydrodynamic forces on polyelectrolytes. In their model, they discretize the polyelectrolyte as a bead-spring chain and linearly superimpose electric, hydrodynamic, and Brownian forces so that the velocity of one bead of the bead-spring model is:

$$\frac{d\mathbf{x}_n}{dt} = \frac{1}{\zeta_n}[\mathbf{T}(\mathbf{x}_n) + \mathbf{g}(\mathbf{x}_n)] + \mathbf{u}^{\infty}(\mathbf{x}_n) + \mu\mathbf{E}(\mathbf{x}_n) + \mathbf{u}_{\text{HI}}(\mathbf{x}_n) \tag{6.1}$$

where ζ_n is the bead drag coefficient, and for the n^{th} bead, $\mathbf{x}_n$ is the position vector, $\mathbf{T}(\mathbf{x}_n)$ is the force due to gradients in tension along the polymer, $\mathbf{g}(\mathbf{x}_n)$ is the Brownian force, $\mathbf{u}^{\infty}(\mathbf{x}_n)$ is the imposed flow field, $\mathbf{E}(\mathbf{x}_n)$ is the imposed electric field, and $\mathbf{u}_{\text{HI}}(\mathbf{x}_n)$ is the induced velocity from hydrodynamic interactions from all other beads of the polyelectrolyte. Figure 6-1 shows a schematic of this problem. Note that the pure hydrodynamic deformation discussed in Chapter 2 occurs when $\mathbf{E} = \mathbf{0}$ and both $\mathbf{u}^{\infty}$ and $\nabla\mathbf{u}^{\infty}$ are nonzero. In our study we will address electrophoretic deformation with $\mathbf{u}^{\infty} = \mathbf{0}$ and both $\mathbf{E}$ and $\nabla\mathbf{E}$ nonzero. A general form for $\mathbf{u}_{\text{HI}}(\mathbf{x}_n)$ is [156]:

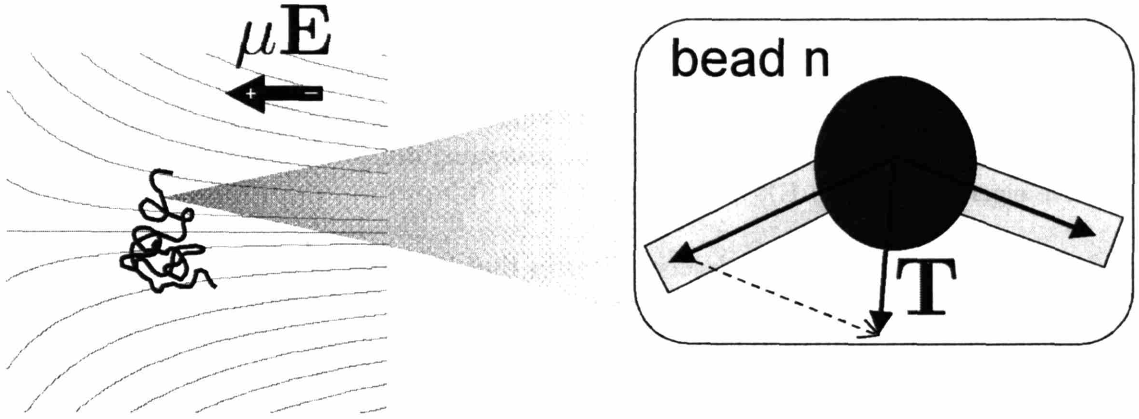

Figure 6-1: Schematic of a DNA molecule in an electric field gradient and a close-up of bead n of a bead spring model. The tension force at bead n ($\mathbf{T}$) is the sum of the adjacent spring forces.

$$\mathbf{u}_{\mathrm{HI}}(\mathbf{x}_n) = \sum_m \mathbf{H}_{nm}[\mathbf{T}(\mathbf{x}_m) + \mathbf{g}(\mathbf{x}_m)] + \sum_m \mathbf{H}^{\mathrm{EL}}_{nm}[q_m \mathbf{E}(\mathbf{x}_m)] \tag{6.2}$$

where q_m is the charge of the m^{th} bead, $\mathbf{H}_{nm}$ mediates flow disturbances due to non-electric forces from bead m on bead n (which is the Oseen tensor in the far-field limit), and $\mathbf{H}^{\mathrm{EL}}_{nm}$ mediates similar flow disturbances due to electrophoresis of a charged bead. The flow disturbance for the electrophoresis of a point charge is [62]:

$$\mathbf{H}^{\mathrm{EL}}_{nm} = (\boldsymbol{\delta}_{nm} + \frac{\mathbf{x}_n \mathbf{x}_m}{r^2_{nm}}) \frac{e^{-\kappa r_{nm}}}{8\pi\eta r_{nm}} \tag{6.3}$$

where $\boldsymbol{\delta}_{nm}$ is the identity tensor, r_{nm} is the distance between beads n and m, η is the solvent viscosity, and κ^{-1} is the solvent Debye length. Note the exponential decays on the length scale of the Debye length. Therefore, for very thin Debye layers ($\kappa^{-1} \ll l_p$, generally the case for DNA electrophoresis buffers), $\mathbf{H}^{\mathrm{EL}}_{nm} \sim \mathbf{0}$. Physically, the hydrodynamic interactions are screened by the mobile counterions in the Debye layer moving in the opposite direction to the polyelectrolyte. Consequently, we see what Long *et al.* term "electrohydrodynamic equivalence", *i.e.* the hydrodynamic interactions are mediated by the Oseen tensor if the tension is generated by *either* electric or hydrodynamic deformation. With $\mathbf{H}^{\mathrm{EL}}_{nm} \sim \mathbf{0}$, Eq. 6.1 is like the Langevin equation for the Zimm model [34], so the governing polyelectrolyte dynamic parameters (D and τ) are also independent of whether tensions are generated by electric or hydrodynamic forces. Therefore, a chain relaxing in a uniform $\mathbf{E}$ is equivalent to that in a uniform $\mathbf{u}^{\infty}$. Recall that this model is based on a bead-spring discretization of the polyelectrolyte. A different approach has been pursued numerically to account for the anisotropy of the electrophoretic mobility of a slender body by discretizing the polyelectrolyte as freely rotating ellipsoids [76]. This alternative detailed model treats ζ_n and μ as tensors which have slightly different forms for slender bodies. Such a discretization implies hydrodynamic stretch is slightly longer than an equivalent electrophoretic stretch near full extension. However experimental results [46] for tethered λ- to 3λ-DNA suggest that "electrohydrodynamic equivalence" persists even near 75% extension. In summary, no matter how tensions are created in the chain, either due to $\nabla \mathbf{u}^{\infty}$ or $\nabla \mathbf{E}$, they generate long-range hydrodynamic interactions. To analyze deformation of the chain in an electric field gradient, we invoke electrohydrodynamic equivalence to interrogate $\mu \mathbf{E}$ in the same fashion as the velocity field in hydrodynamic flows. Hence we define the electrophoretic Deborah number De=$\dot{\epsilon}^{\mathrm{EL}} \tau$ as the governing dimensionless parameter, where $\dot{\epsilon}^{\mathrm{EL}}$ is the positive eigenvalue of $\nabla(\mu \mathbf{E})$.

Although electrohydrodynamic equivalence dictates that local deformation of DNA is nearly identical from both $\nabla \mathbf{u}^{\infty}$ or $\nabla \mathbf{E}$ effects, the fields $\mathbf{u}^{\infty}$ and $\mathbf{E}$ are quite different in identical geometries. Recall that the primary sources of both flow and field gradients in microchannels are obstacles and channel contractions. The main difference between hydrodynamic and electric fields generated in these devices is the no-slip boundary condition required at all surfaces in hydrodynamic flows. Consequently, near a wall or obstacle surface, a flow field is locally "shear-like" with both extensional and rotational components. On the other hand, in the absence of time dependent magnetic fields, electrophoretic deformation is always *locally pure elongation* because the electrophoretic velocity gradient is symmetric (without a local rotational component) for a potential field ($\nabla \times \mu \mathbf{E} = 0$). Of secondary importance, an electric field is a harmonic field in which field disturbances from obstacles with radius R_{obs} decay as R_{obs}^2/r^2, whereas a low-Reynolds number hydrodynamic flow induces a creeping (biharmonic) flow in which disturbances to the flow from obstacles decay more slowly as R_{obs}/r.

The above analysis applies nicely at low external fields, however because electric and hydrodynamic forces and flows are intimately coupled, complex nonlinear electrophoretic effects may arise at high field strengths (O[kV/cm]). These nonlinear electrophoretic effects arise when the double layer of the moving object becomes polarized. Polarization induces secondary fields and flows that affect the mobility [72, 79–81] and also imposes a dielectrophoretic body force. Previous dielectrophoresis research has shown that DNA molecules do indeed polarize positively in AC fields [157–159], and can even exhibit polarization-induced aggregation both in high AC or DC fields [83–85]. In our experiments, we use field strengths and molecule sizes where the dielectrophoretic force and other induced nonlinear effects are negligible. However, in the Chapter 8 we speculate on how these nonlinearities affect DNA deformation at high field strength.

6.2 Gradients induced by a large cylinder

6.2.1 Field characterization

Analytical solution: In our first case study, we investigate DNA deformation in the electric field near a large ($R_{\mathrm{obs}} \gg R_g$) insulating cylinder. This problem serves as a prime example for many lab-on-chip applications which often contain obstacles, and the same analysis can be used for other more complex geometries. By solving $\nabla^2 \phi = 0$ around an insulating cylinder, we can obtain an analytical solution for the electric field ($\mathbf{E} = -\nabla \phi$). Therefore the electrophoretic velocity ($\mu \mathbf{E}$) of a charged object with mobility μ around an insulating cylinder in an obstacle-centered coordinate system is:

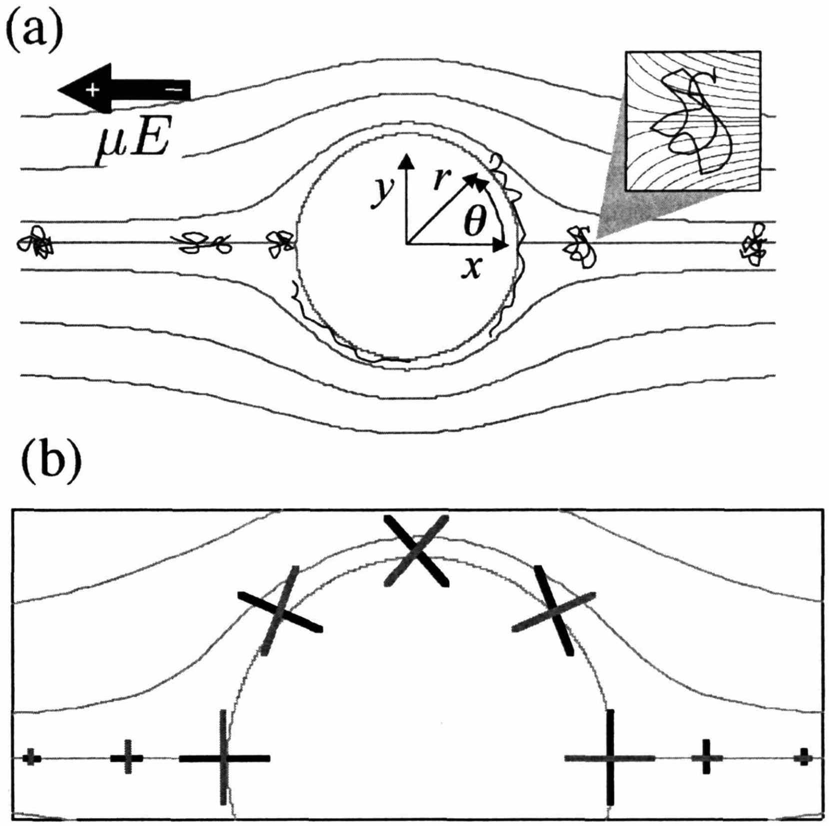

Figure 6-2: (a) Schematic of a DNA molecule electrically driven into an insulating obstacle (moving right to left). (b) Axes of extension (black) and compression (gray) along the centerline trajectory with magnitude scaled by the local electrophoretic strain rate $\dot{\epsilon}^{\mathrm{EL}}(r)$.

$$\mu \mathbf{E}(r,\theta) = \mu E\cos\theta\Big(\frac{R_{\mathrm{obs}}^2}{r^2}-1\Big)\mathbf{e_r} + \mu E\sin\theta\Big(\frac{R_{\mathrm{obs}}^2}{r^2}+1\Big)\mathbf{e}_\theta. \tag{6.4}$$

In all cases, we consider molecules *impacting the cylinder from the right* along the centerline (θ=0, See Fig. 6-2 (a)) .

We seek to study the deformation of DNA in this field in the limit $R_{\mathrm{obs}} \gg R_g$. The electrophoretic velocity field gradient of Eq. 6.4 (in polar coordinates) is:

$$\mu\nabla\mathbf{E}(r,\theta) = \begin{bmatrix} \frac{-2\ \mu E\cos\theta\ R_{\mathrm{obs}}^2}{r^3} & \frac{-2\ \mu E\sin\theta\ R_{\mathrm{obs}}^2}{r^3} \\ \frac{-2\ \mu E\sin\theta\ R_{\mathrm{obs}}^2}{r^3} & \frac{2\ \mu E\cos\theta\ R_{\mathrm{obs}}^2}{r^3} \end{bmatrix}. \tag{6.5}$$

We can extract the electrophoretic strain rate $\dot{\epsilon}^{\mathrm{EL}}(r)$ by determining the eigenvalues:

$$\pm\dot{\epsilon}^{\mathrm{EL}}(r) = \pm\frac{2\mu E R_{\mathrm{obs}}^2}{r^3} \tag{6.6}$$

and the axes of extension and compression by determining the eigenvectors:

$$\mathbf{p}_{\pm}(\theta) = \frac{1}{\sqrt{2 \mp 2\cos\theta}}\Big((\cos\theta \mp 1)\ \mathbf{e}_r + \sin\theta\ \mathbf{e}_\theta\Big). \tag{6.7}$$

Figure 6-2 (b) shows the axes of extension and compression (with magnitudes scaled by $\dot{\epsilon}^{\mathrm{EL}}(r)$) for a centerline impact from the right. Note that both the strain rate and axes of extension and compression induced by an insulating cylinder are *spatially inhomogeneous*. The maximum value of the radial-dependent strain rate is $2\mu E/R_{\mathrm{obs}}$ at the obstacle surface and it falls off steeply away from the obstacle ($\sim R_{\mathrm{obs}}^3/r^3$). Thus the strongest DNA deformation will occur near the obstacle surface. The axis of extension begins in the y-direction for an approaching molecule, however it rotates around the obstacle, finally ending in the x-direction at the backside. Thus we may imagine that a flexible polyelectrolyte will extend perpendicular to the field on the front side of the obstacle, compress on the backside, and then extend in the field direction as it leaves the obstacle. Recall that the Deborah number $\mathrm{De} = \dot{\epsilon}\tau$ governs polymer deformation in flow gradients. Since $\dot{\epsilon}^{\mathrm{EL}}(r)$ is inhomogeneous, we define De based on the maximum strain rate so that $\mathrm{De} = 2\mu E\tau/R_{\mathrm{obs}}$, which makes intuitive sense since $\dot{\epsilon}^{\mathrm{EL}}(r)$ falls off rapidly away from the obstacle. However, it is important to remember that deformation can occur away from the obstacle, either before or after impact. Thus we also define the local r-dependent Deborah number $\mathrm{De}_{\mathrm{local}}(r) = \dot{\epsilon}^{\mathrm{EL}}(r)\tau$.

Inhomogeneous field deformation: The inhomogeneous nature of the field requires special attention. Other groups have studied polymers deforming in inhomogeneous flows (for example [160–164]). In particular, Panwar and Kumar [164] observed that deformation is lower than in homogeneous flows and it is highly sensitive to the polymer's Brownian trajectory. Szeri, Wiggins, and Leal [161] have theoretically addressed deformation kinematics in 2D inhomogeneous fluid flows. They represent a deformable object's orientation and length by a state vector, and show that the deformation of the state vector depends on the object's history because its equations of motion are non-autonomous. Consequently the strong stretching condition is not necessarily (using our variables) $\mathrm{De}_{\mathrm{local}}(r) > 1/2$. More generally, in an inhomogeneous field this strong stretching condition depends on the history of deformation, *i.e.* the object's initial orientation and path interval. Our case study of deformation near an insulating cylinder is an "open" problem as opposed to a time periodic problem, which means that it is not obvious what time to choose to evaluate the strong stretching condition [161]. However, the problem simplifies along the obstacle centerline. On the centerline, the equilibrium orientation $\mathbf{p}_+$ is constant which means that $\mathrm{De}_{\mathrm{local}}(r) > 1/2$ again satisfies the strong stretching condition. Our analysis only pertains to these centerline collisions. However, we do remark that off-center collisions can stretch, but these DNA will experience lower strain and the adverse effects of an inhomogeneous field. To summarize, a DNA molecule approaching the cylinder along the centerline experiences a pseudo-homogeneous extensional field, which we can envision as an extensional field quickly ramping to its maximal value at the obstacle surface with the local strain rate governing the strong stretching criterion.

We adopt a local analysis to address deformation away from the obstacle in the inhomogeneous field gradient. For this inhomogeneous field $\epsilon^{\mathrm{EL}} = \int_0^{t_{\mathrm{res}}} \dot{\epsilon}^{\mathrm{EL}}[\mathbf{x}(t)]dt$. We will present two options to compute electrophoretic strain for our study of centerline collisions: 1) assume $r = \infty$ at $t = 0$ or 2) assume $r = r_0$ at $t = 0$, where r_0 is the location where $\mathrm{De}_{\mathrm{local}}(r) > 1/2$. The first choice amounts to accumulating strain throughout the molecule's entire history whereas the second choice applies a De-dependent cut-off that initiates strain accumulation as soon as the electrophoretic strain rate is strong enough to induce a coil-stretch transition. We will term the accumulated strain as ϵ^{EL} for the first option and $\epsilon^{\mathrm{EL}}_{\mathrm{eff}}$ for the second. Using both definitions, we can quantify the pre-impact deformation on the front of the obstacle by computing the accumulated strain felt by a molecule before impact (neglecting diffusion). The accumulated molecular strain ϵ^{EL} for centerline impacts ($\theta = 0$) approaching the front stagnation point is:

$$\begin{aligned} \epsilon^{\mathrm{EL}}(r) &= \int_{\infty}^{r} \frac{\dot{\epsilon}^{\mathrm{EL}}(r)dr}{\mu E(r)} \\ &= \ln\left[\frac{(r/R_{\mathrm{obs}})^2}{(r/R_{\mathrm{obs}})^2 - 1}\right]. \end{aligned} \tag{6.8}$$

The same calculation can be performed by assuming that a molecule will not appreciably deform until $\mathrm{De}_{\mathrm{local}}(r_o) > 1/2$:

$$\epsilon^{\mathrm{EL}}_{\mathrm{eff}}(r) = \ln\left[\frac{(r/R_{\mathrm{obs}})^2}{(r/R_{\mathrm{obs}})^2 - 1}\frac{(r_o/R_{\mathrm{obs}})^2 - 1}{(r_o/R_{\mathrm{obs}})^2}\right]. \tag{6.9}$$

Note that $\epsilon^{\mathrm{EL}} = \epsilon^{\mathrm{EL}}_{\mathrm{eff}}$ in the limit $\mathrm{De} \to \infty$ so that these two measures of strain only differ at low De. This is evident in Fig. 6-3 which shows the expected accumulated strain $\epsilon^{\mathrm{EL}}_{\mathrm{eff}}$ as a function of De and distance from the obstacle. Note that molecules impacting the obstacle experience the same ϵ^{EL} independent of De. However, Fig. 6-3 shows that the amount of effective strain experienced in the strong part of the extensional field varies with De. As De decreases the effective strain before impact becomes more and more like a step function. For small De, an impacting molecule experiences a rapid transition from a negligible to a strong extensional field, whereas at higher De, pre-straining deforms the molecule as it approaches the obstacle. This is the important distinction between ϵ^{EL} and $\epsilon^{\mathrm{EL}}_{\mathrm{eff}}$ and the primary reason we have defined $\epsilon^{\mathrm{EL}}_{\mathrm{eff}}$. DNA deformation in the inhomogeneous field can be stronger at larger De due to both the larger electrophoretic strain rate *and* a larger $\epsilon^{\mathrm{EL}}_{\mathrm{eff}}$. Note that because of the R^3_{obs}/r^3 dependence of $\dot{\epsilon}^{\mathrm{EL}}$, the effective pre-impact strain is not large ($\epsilon^{\mathrm{EL}} \sim 1 - 1.5$). However, the stretching of polymers in extensional flows is very sensitive to the initial configuration of the chain [86], so this pre-straining should not be dismissed.

Bead tracking: To validate that Eq. 6.4 is the real experimental electrophoretic velocity field and that the obstacle is insulating, we track electrophoretic motion of fluorescent beads (Fig.6-7 (a)). We find that the obstacle is insulating and sufficiently isolated from wall effects since the field lines of our confined system match the solution for an isolated insulating cylinder (confirmed by finite element calculations).

With the above formalism, we seek to experimentally study DNA deformation in the electric field gradients induced by an insulating cylinder. Specifically, we will investigate single molecule extension-strain dynamics, the stretch-compress-stretch dynamics that arise from rotation of the axis of extension and compression, and the pre-strain effect.

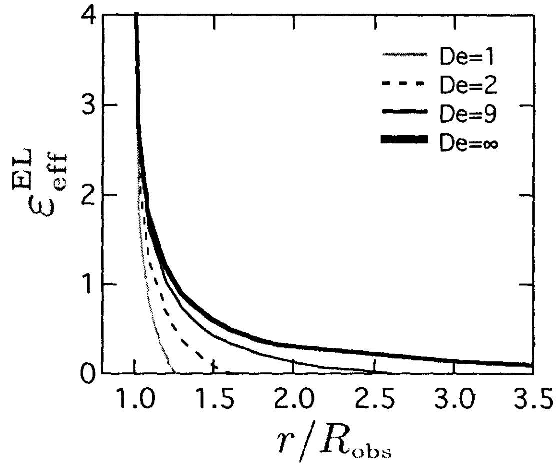

Figure 6-3: Effective integrated strain for a point-like molecule approaching the obstacle stagnation point along the centerline (θ=0). This assumes no stretching occurs unless $\text{De}_{\text{local}}(r) > 1/2$. Note that $\epsilon^{\text{EL}} = \lim_{\text{De}\to\infty} \epsilon^{\text{EL}}_{\text{eff}}$.

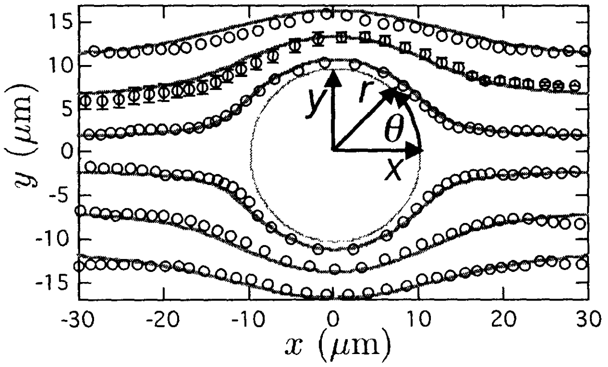

Figure 6-4: Electrophoretic traces of 0.5 μm diameter carboxylated beads at E=29 V/cm around a PDMS obstacle (R_{obs}=10 μm). Solid lines indicate expected 2D trajectories around an insulating cylinder in an unbounded conductor.

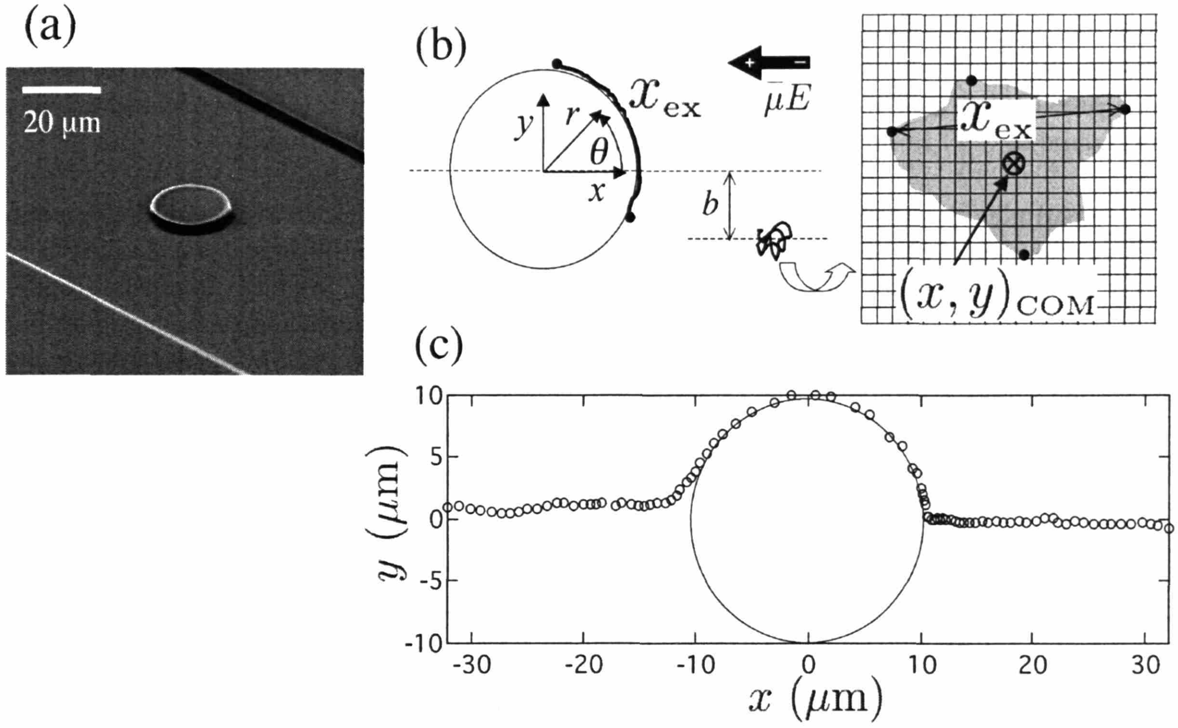

Figure 6-5: (a) SEM image of a 2 μm high cylindrical PDMS post ($R_{\mathrm{obs}} = 10$ μm). (b) Experimentally observable variables for an impact. (c) An example of a λ-DNA center of mass trajectory at De=2 in the 1.3 cP buffer. The time between each symbol is 1/30 s.

6.2.2 Experimental

We used our standard soft lithography [108] procedure (Chapter 3) to construct 5-10 mm-long, 100 μm-wide, and 2 μm-high PDMS (polydimethylsiloxane) microchannels with an isolated 10 μm-radius obstacle. Reservoirs (4 mm×4 mm) were cut at each end of the cured PDMS microchannel with a scalpel and the channels were soaked for 12 hours at 50°C in 0.5×TBE to eliminate permeation driven flow [165]. Figure 6-5 (a) shows a SEM image of an isolated obstacle.

Monodisperse λ-DNA were stained with a fluorescent dye (TOTO-1, 4.7:1 bp:dye molecule) and diluted in one of two buffers: 1) 2.2×TBE, 3% β-mercaptoethanol, 0.07 % PVP (M_w=10^6, $c^\star$=1.5%), and 0.07% ascorbic acid (viscosity η=1.3 cP, pH=8.4) or 2) 2.2×TBE, 3% β-mercaptoethanol, 0.07 % PVP, 0.07% ascorbic acid, and 31% sucrose (η=6 cP, pH=7.9). The viscosities were measured by bead tracking [166]. We chose the high viscosity buffer to slow down the dynamics to experimentally observable speeds. The additives were chosen to dynamically eliminate electroosmotic flow and scavenge oxygen. The measured electrophoretic mobility was $\mu = -1.7 \pm 0.2$ $\frac{\mu\mathrm{m}}{\mathrm{s}}/\frac{\mathrm{V}}{\mathrm{cm}}$ in the 1.3 cP buffer and $\mu = -0.25 \pm 0.03$ $\frac{\mu\mathrm{m}}{\mathrm{s}}/\frac{\mathrm{V}}{\mathrm{cm}}$ in the 6 cP buffer. With the Debye approximation of the zeta potential, $\mu = \kappa^{-1}\sigma_{\mathrm{DNA}}/(4\pi\eta)$ where σ_{DNA} is the DNA surface charge density [3]. Thus the observed decrease in mobility for the 6 cP solvent is in the expected range given its higher viscosity ($\eta_2/\eta_1 \sim 4.6$), lower dielectric constant [167] (so that $\kappa_1^{-1}/\kappa_2^{-1} \sim 1.1$), and lower pH (we calculate $\sigma_{\text{DNA},1}/\sigma_{\text{DNA},2} \sim 1.2$ using pKa values for H_3PO_4 along the DNA backbone). We acknowledge that this is a simplified check of how the mobility changes in different solvents and that other complex effects, specifically those from the dye interactions, may also be important to consider. As explained previously, this dyed λ DNA has a contour length of L=21 μm (Chapter 3) and a longest relaxation time of τ=0.19 for the 1.3 cP buffer and τ=0.9 s for the 6 cP buffer.

A typical experiment consisted of first gently rinsing and drying the microchannel and then applying it to a clean glass slide (plasma cleaned at 100 W for 5 min, charge equilibrated 1 day, soaked in 1M NaOH for 15 min and rinsed in ultrapure water (MilliQ, Millipore)). We then immediately filled the channel with DNA solution and applied an electric field across the reservoirs through platinum electrodes. We observed single DNA molecule dynamics using an inverted fluorescence microscope (Axiovert 200, Zeiss) with a 63× 1.4 NA objective. Images were captured at 30 frames per second with an EB-CCD camera (C7190-20, Hamamatsu) and NIH Image software. Digitized images had 8-bit pixel intensity values which ranged from 0-255.

Figure 6-5 (b) shows a cartoon of a typical digitized λ-DNA image from the 63× lens. At this magnification, the digitized image has a pixel size of 0.21 μm square. For analysis, we filter the background by subtracting the maximum pixel value of the perimeter of the first frame of a movie from all the pixels in that movie. We extracted two observables from the captured images of a DNA molecule: the center of mass coordinate of the DNA $(x, y)_{\text{com}}$ and the DNA's longest extension x_{ex}. The center of mass of a molecule was computed by finding the first moment of the post-filtered image intensity distribution [168]. This process was automated for multiple frames of data and it yielded the center-of-mass trajectory $\mathbf{x}(t)$ of the DNA (*cf.* Fig 6-5 (c)). To determine the extension, we first located the coordinates of the left-most, right-most, top, and bottom pixels of the DNA image with an intensity value of at least 8 (after background filtering). The extension x_{ex} is then defined as the length of the longest line connecting any two of these points (Fig. 6-5 (b)). For extreme extensions on the obstacle (*i.e.* if $x_{\text{ex}} > 7$ μm), we manually locate the two endpoints of the chain and x_{ex} is the end-to-end arc length (Fig. 6-5 (b)). We define the impact parameter b as the y-offset between the impacting DNA's center of mass and the obstacle center, taken at a distance $2R_{\text{obs}} + R_g$ from the obstacle center (Fig. 6-5 (b)). This position was chosen to evaluate b because the DNA is far enough away from the obstacle to not experience high electric field gradients, yet close enough so that Brownian drift does not significantly coarsen our analysis. For this study, we only analyze centerline collisions with $|b| < 1$ μm. We can compute ϵ^{EL} for a single DNA impact using its center-of-mass trajectory and the relation $\epsilon^{\text{EL}}[\mathbf{x}(t)] = \sum_{\text{frames}} \dot{\epsilon}^{\text{EL}}(\mathbf{x}_{\text{frame}})\Delta t_{\text{frame}}$ where the sum is over all frames in a movie, $\mathbf{x}_{\text{frame}} = (x, y)_{\text{com}}$ is the center of mass in a given frame, and the frame rate $\Delta t_{\text{frame}} = 1/30$ s. When the center of mass is located inside the obstacle, we use $\dot{\epsilon}^{\text{EL}}(R_{\text{obs}})$ for the strain rate. For different De, we begin data accumulation at a slightly different initial position $\mathbf{x}(0)$ based on limitations on our field of view and need for post-impact data. Therefore we renormalize our ϵ^{EL} data by adding in a small deterministic correction that is the molecular strain experienced before observation $\epsilon^{\text{EL}}[\mathbf{x}(0)]$. Note that this correction is small ($\epsilon^{\text{EL}}[\mathbf{x}(0)] < 1/2$). Therefore, our presented strain values are $\epsilon^{\text{EL}} = \epsilon^{\text{EL}}[\mathbf{x}(t)] + \epsilon^{\text{EL}}[\mathbf{x}(0)]$.

6.2.3 Results

For DNA electrophoretically driven into a large insulating obstacle ($R_{\text{obs}} = 10$ μm) along its centerline ($|b| < 1$ μm), we investigate the coil-stretch transition, pre-impact deformation, single molecule

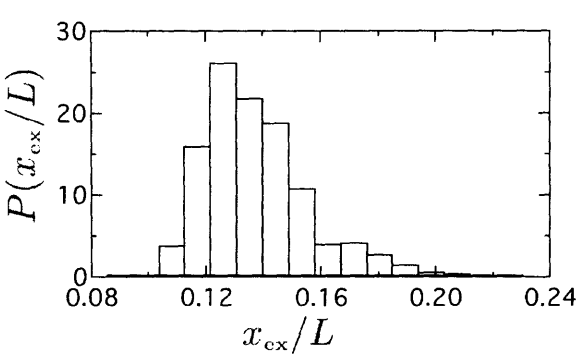

Figure 6-6: Equilibrium probability distribution of the λ DNA fractional extension.

extension-strain dynamics, and the stretch-compress-stretch dynamics that arise from rotation of the axis of extension and compression. This kinematic analysis is based on deformable objects much smaller than the obstacle size.

In order to quantify deformation it is first helpful to know how extended a DNA coil is in the absence of any electric field gradients. Diffraction of light will tend to smear and slightly enlarge our images of DNA coils. Figure 6-6 shows the experimentally measured probability distribution $P(x_{\mathrm{ex}}/L)$ of the equilibrium coil fractional extension for 1000 frames of images of λ-DNA using the 63× lens. The mean of the distribution, denoted $\langle x_{\mathrm{ex}}\rangle_0/L$ is 0.13. Due to blooming [100], this distribution is dependent on the camera, light source, lens, and dye ratio. Although we do not expect much more than a 10% departure from our measured $\langle x_{\mathrm{ex}}\rangle_0/L$ with large adjustments of the image capture settings, care was taken to keep all of these settings constant in all experiments.

Coil-Stretch transition: We first validated that De correctly describes the action of the obstacle-induced electric field gradients on a DNA molecule by investigating the predicted critical coil-stretch transition at De=1/2. Figure 6-7 (a)-(d) shows the longest extension x_{ex} of a λ-DNA molecule as a function of time during centerline ($b = 0$) collisions with large obstacles. Comparing Fig. 6-7 (a) with 6-7 (b), we see that at subcritical De (De=0.25) no molecules stretch beyond typical equilibrium values, whereas at supercritical De (De=1) some do stretch. Keeping the two electric field strengths constant, thereby fixing Pe, we increase De by reducing the obstacle size from R_{obs} =10 μm to 3 μm. By comparing Fig. 6-7 (a) with 6-7 (c), *i.e.*, passing from subcritical to supercritical De, we again observe the critical stretching transition. Similarly, Fig. 6-7 (d) shows stronger stretching than the collisions of Fig. 6-7 (b). Note that the only difference between these sets of experiments is the obstacle size. Our results indicate that electric field gradients, characterized by De, govern the stretching of DNA molecules around large obstacles.

Pre-impact deformation: In our examination of electrophoretic deformation, we first address the effect of the inhomogeneous electric field deforming the DNA molecules *before impacting* the large obstacle. The definition of "impact" is subtle since, in the absence of large normal forces, no DNA molecule is ever completely in direct contact with the obstacle because of a lubricating layer of solvent molecules. We empirically define "impact" with the obstacle when the leading edge of a DNA's fluorescent cloud has stopped moving toward the obstacle center. For λ-DNA in this study, impact typically occurs when the center of mass is at about r/R_{obs} ~1.1, although it can

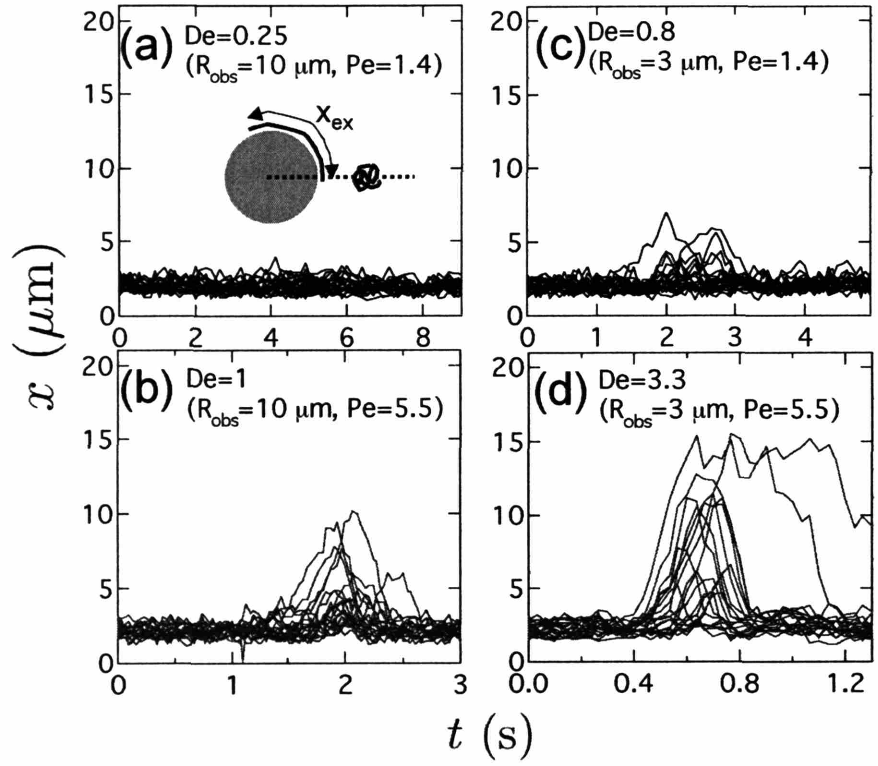

Figure 6-7: Dynamic extension of centerline (b=0) collisions with a large obstacle. R_{obs}=10 μm [(a) and (b)], and 3 μm [(c) and (d)]. The contour length of the stained λ-DNA is 21 μm..

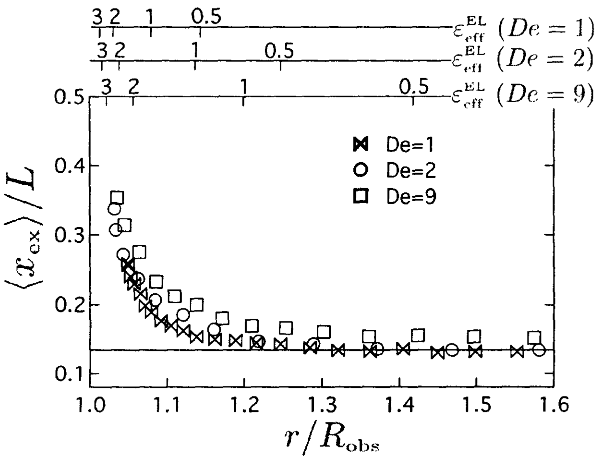

Figure 6-8: Average fractional extension of λ-DNA molecules approaching a large insulating cylinder (ensemble size=30). The upper axes give the effective accumulated strain and the horizontal baseline is the equilibrium average extension ($\langle x_{ex} \rangle_0 / L = 0.13$). The De=9 data is slowly approaching this baseline but our field of view did not allow observation beyond $r/R_{obs} \sim 1.6$.

occur near r/R_{obs} ~1 for molecules with a high degree of pre-impact deformation. Figure 6-8 shows the average fractional extension of DNA molecules approaching the obstacle along its centerline at De=1, 2, and 9. As De increases, the degree of pre-impact deformation increases because of the combined effects of larger De and larger ϵ^{EL}_{eff}. However, as we presumed, this effect is small because these molecules only experience $\epsilon^{EL} \sim 1$ before they impact the obstacle.

Extension-strain dynamics: We now turn to single molecule extension-strain dynamics. Figure 6-9 (a)-(c) shows the fractional extension x_{ex}/L of single λ-DNA molecules colliding into the obstacle as a function of accumulated strain over each molecule's center of mass trajectory at De=1, 2, and 9. Due to the small numerical difference between ϵ^{EL}_{eff} and ϵ^{EL} after impacting the obstacle, we chose to plot the data in terms of ϵ^{EL}. The transition from solid lines to dashed lines indicates that some portion of the molecule has crossed the bisecting plane x=0. By comparing the trajectories to the affine scaling ($\sim e^{\epsilon^{EL}}$), we see an approach to affine deformation as De increases. We also note that the ensemble average fractional extension as a function of strain at De = 2 is in close agreement with the results from uniform extensional flow [89], a result not completely evident beforehand due to the inhomogeneity of this field and the electrophoretic deformation. This close similarity stems from electrohydrodynamic equivalence and the extremely fast decay of $\dot{\epsilon}^{EL}(r)$ which gives a pseudo-homogeneous extensional field. The diversity in extension-strain dynamics is reminiscent of hydrodynamic extensional flow studies [86, 89], which show that the unraveling of an individual polymer is highly sensitive to its initial configuration. Perkins *et al.* [86, 89] have previously observed that some polymer configurations (like a tight coil or a "folded" molecule) are more resistant to extensional deformation. Figure 6-10 (a), which shows an impact at De=2, provides a visual example of a molecule that experiences significant strain ($\epsilon^{EL} > 3$) near the front stagnation point, yet never appreciably stretches. For comparison, Fig. 6-10 (b) shows a different molecule at the same De and comparable accumulated strain that significantly stretches. The phenomenon called "molecular individualism" [86, 87] will be an important and recurring theme in our DNA stretching studies.

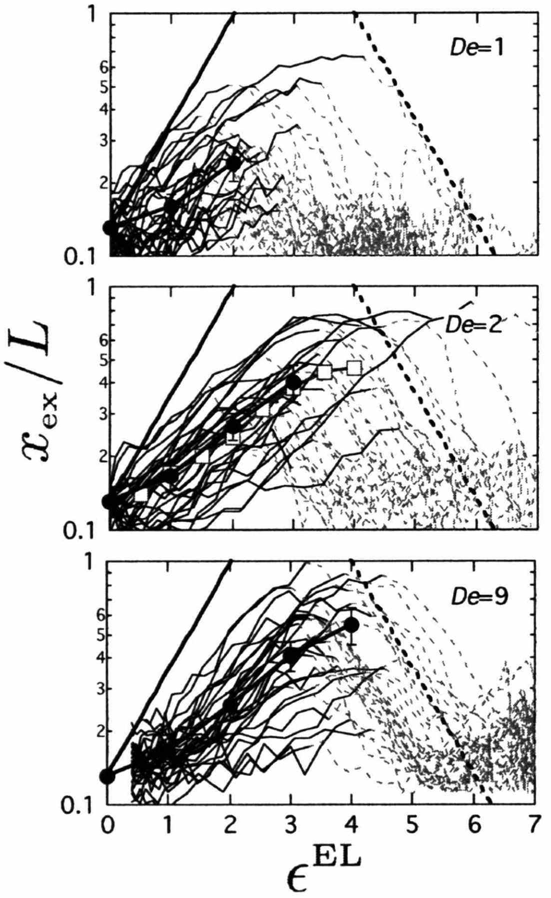

Figure 6-9: Extension-strain curves for 30 λ-DNA molecules colliding into a large ($R_{obs} = 10$ μm) insulating cylinder at (a) De=1, (b) De= 2, and (c) De=9 along the centerline. Each curve represents the trajectory of a single molecule. Curves switch from solid black to dashed gray when a piece of the DNA crosses the plane x=0. Ensemble average and standard error are shown by filled circles and for (b), the results of Smith and Chu [89] are shown by red squares. Affine extension ($\sim e^{\epsilon^{EL}}$, solid line) and compression ($\sim e^{-\epsilon^{EL}}$, dashed line) scalings are shown for reference.

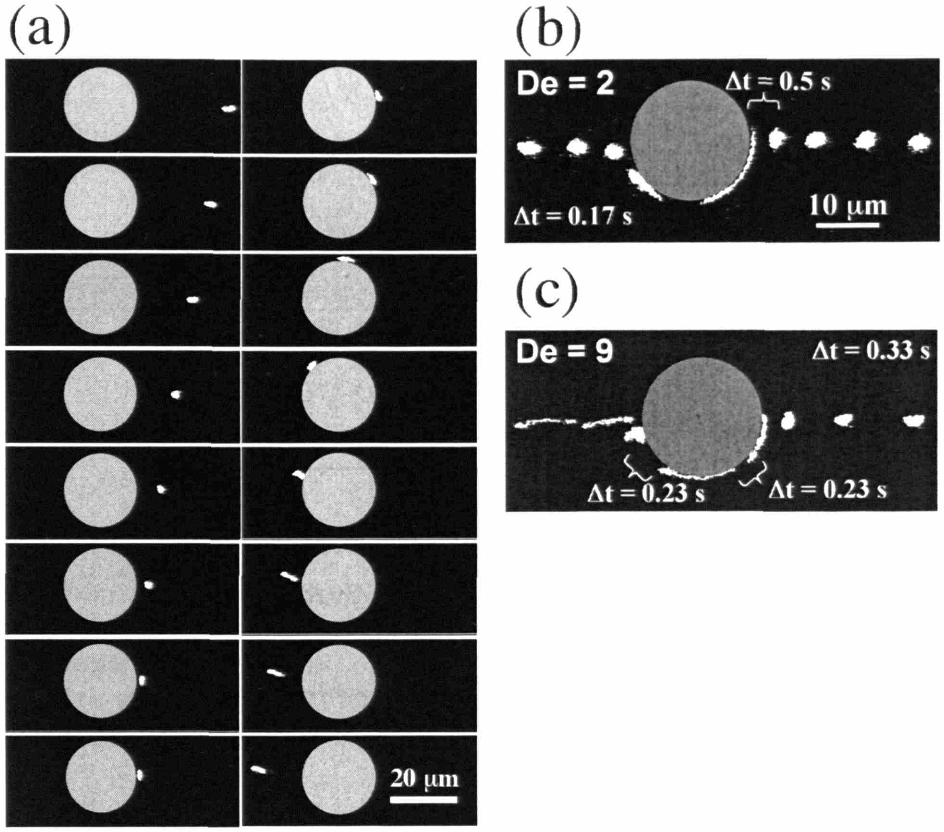

Figure 6-10: (a) Sample images of a λ-DNA collision at De=2 (in 1.3 cP buffer) without significant deformation. The time steps between frames are 0.1 s. (b) A sample impact (right-to-left) at De=2 in 1.3 cP buffer with timesteps of 0.17 s unless otherwise noted. (c) An impact at De=9 in the 6 cP buffer with 0.33 s timesteps unless otherwise noted.

Returning to Fig. 6-9 (a)-(c), note that the DNA begins to compress as it passes the x=0 plane. This was predicted by our previous kinematic arguments because the axes of extension and compression rotate along a given field line, and as a DNA molecule passes x=0, it becomes more closely aligned with the axis of compression. It is very interesting that almost every molecule compresses at the affine limit ($\sim \mathrm{e}^{-\epsilon^{\mathrm{EL}}}$). Furthermore, note that some molecules stretch again after this compression. This trend grows stronger as De increases from 2 to 9 and can be easily visualized in Fig. 6-10 (b) and 6-10 (c).

Backside compression: We now look more closely at the compression and post-impact stretch of DNA on the backside of the obstacle. Figure 6-11 (a) and (b) show x_{ex} versus t/τ of λ-DNA molecules deforming on the backside of the large obstacle at De=2 and 9. The time has been renormalized so that $t = 0$ is when a stretched molecule has compressed to $x_{\mathrm{ex}}/L = 0.3$, and we have removed the small number of molecules that do not stretch this much on the front of the obstacle. We provide the equilibrium fractional extension as a baseline and scalings for affine compression ($\langle x_{\mathrm{ex}}\rangle/L \sim \mathrm{e}^{-\dot{\epsilon}^{\mathrm{EL}}t}$) and thermal relaxation ($\langle x_{\mathrm{ex}}\rangle/L \sim \mathrm{e}^{-t/(2\tau)}$). Figure 6-11 (a) and (b) verify that the DNA molecules compressing at the obstacle backside re-coil at the affine limit,

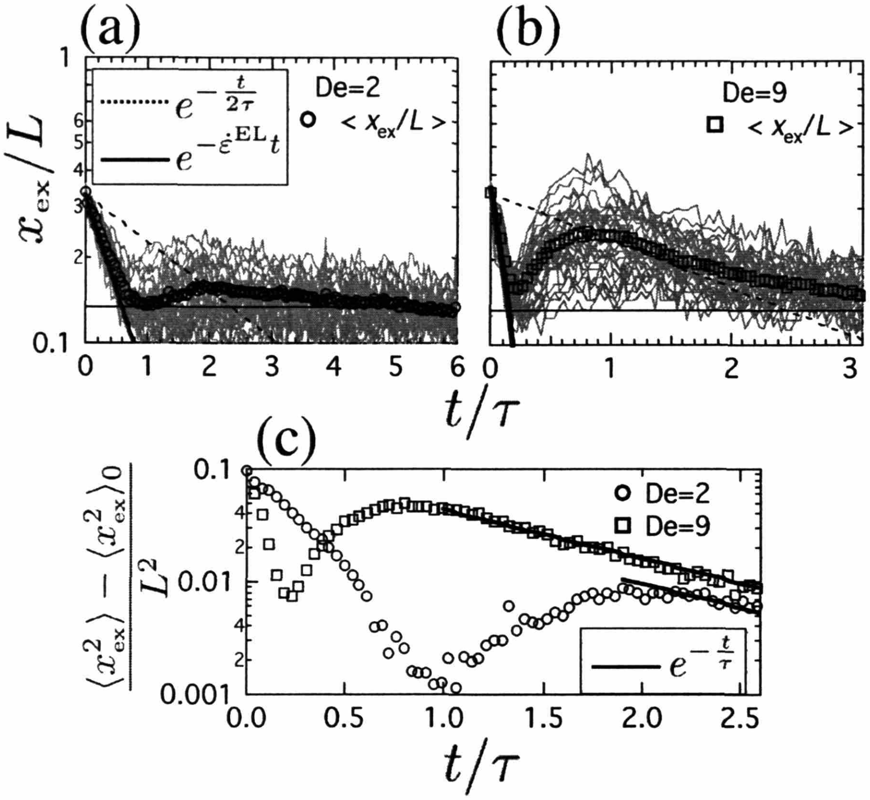

Figure 6-11: Dynamic extension during compression on the backside of a large obstacle at (a) De=2 and (b) De=9. Time was reset to zero when a compressing DNA had $x_{\mathrm{ex}}/L = 0.3$. The thin horizontal line is $\langle x_{\mathrm{ex}}\rangle_0/L$. The gray lines are data for individual molecules (30 total) and the symbols are the ensemble average. The solid line scaling is the affine scaling and the dashed line scaling is the thermal relaxation scaling. (c) Mean square fractional extension with thermal relaxation scaling (solid lines) after the molecules leave the obstacle for the same data.

faster than thermal relaxation. For example, at De=9, the DNA returns from stretched to coil configurations in $\sim 0.2\tau$. Affine compression is expected because a stretched DNA on the backside is more closely aligned with the primary axis of compression, and when stretched out, there is little resistance to the compressive forces for such a flexible polymer – the DNA easily buckles and crumples into a compact configuration. Notice in Fig. 6-11 (a) and (b) that after ample compression on the obstacle backside, some molecules then extend along the axis of extension oriented in the x-direction (*cf.* Fig. 6-10 (c)). This effect is more prominent at high De, which we explain below by considering the details of the DNA configuration and the inhomogeneous strain rate.

Post-impact stretching: To explain the stretching on the backside of the obstacle, or "post-impact stretching", it is helpful to highlight the differences between DNA molecules stretching at the front and at the back of the obstacle. We have already noted that the primary direction of post-impact stretch is in the x-direction whereas it is in the y-direction in the front. Deformation at the backside further differs from that at the front because the starting DNA conformation is not an equilibrium coil. For example, molecules which significantly stretch on the front of the

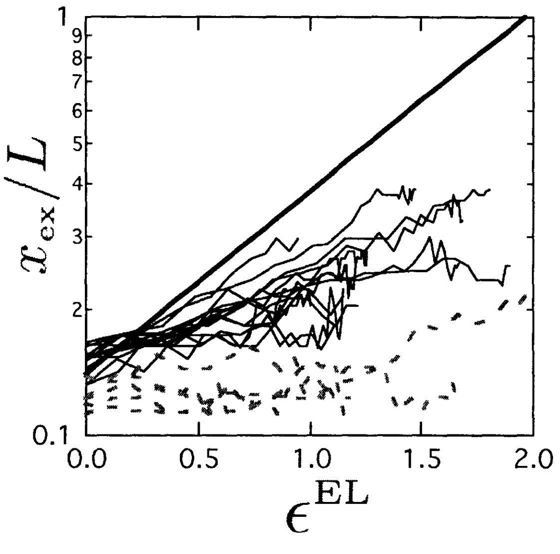

Figure 6-12: Dynamic post-impact extension at De=9. The strain was reset to zero when the compressing DNA achieved a minimum x_{ex}/L near the back stagnation point. Black trajectories correspond to molecules $\geq$ 50% extended on the front of the obstacle, while dashed green trajectories are molecules which stretch <30%. Plotted trajectories terminate when the extension begins to drop due to relaxation. The solid line is the affine scaling.

obstacle are then compressed into "crumpled" configurations as they round the obstacle and do not have time return to an equilibrium configuration. Figure 6-12 shows the post-impact stretch data renormalized so that $\epsilon^{EL}=0$ when the chain stretch x_{ex} takes its minimum value near the rear stagnation point. The population is divided into "crumpled" molecules that have strongly stretched on the front side ($x_{ex}/L \geq 0.5$) and those that only weakly stretched ($x_{ex}/L < 0.3$). There is a strong correlation between molecules that were strongly stretched on the front and those molecules that extend faster at the backside. In general, we find that crumpled DNA configurations tend to stretch faster than equilibrium coils and speculate that this may be because they lack significant configuration complexities.

Continuing our comparison of stretching at the front and back of the obstacle, the local strain rate during backside stretching will also be weaker than at the front. This is because of the DNA's finite size (λ-DNA has $\langle x_{ex}\rangle_0$=2.8 μm) and because the DNA is moving away from the obstacle as it stretches. For example, at a distance of $\langle x_{ex}\rangle_0$ from the obstacle surface, $\mathrm{De}_{\mathrm{local}}$ is reduced to 1/2 De. Consequently, a crumpled molecule leaving the back of an obstacle at De=1 or 2 would have a low $\epsilon^{EL}_{\mathrm{eff}}$, *i.e.* it does not experience significant time in the strong region ($\mathrm{De}_{\mathrm{local}} > 1/2$) of the extensional field. In contrast, a stretching DNA at the front of the obstacle can move very close to the obstacle surface (where the strain rate is maximum) and it can adopt long-lived (high strain) metastable configurations. The combined effects of the DNA configuration, DNA finite size, and the inhomogeneous strain rate explain the large difference we see in the extension of DNA leaving the obstacle at De=2 and 9. Importantly, this post-impact stretch is still limited by the post-impact strain, which is only in the range of $\epsilon^{EL} \sim 1 - 1.5$. So, for larger De we postulate that extensions occurring at the rear of the obstacle will not greatly exceed 40% (affine limit).

Finally, note that after the post-impact stretch, the molecules thermally relax back to an equilibrium coil as they move away from the obstacle. We show this explicitly in Fig. 6-11 (c). Here we subtract the mean square equilibrium stretch ($\langle x_{\mathrm{ex}}^2\rangle_0/L^2 = 0.018$) in order to see the exponential relaxation scaling for such small perturbations from equilibrium. The ensemble average longest relaxation time is equivalent to τ, so that the average time it takes these molecules return to coil configurations is independent of $\mu\mathbf{E}$, as predicted.

6.3 Gradients induced by a hyperbolic contraction

6.3.1 Field characterization

Analytical solution: The homogeneous electric field between two insulating hyperbolic walls is $\mathbf{E} = -\dot{\epsilon}^{\mathrm{EL}}\mathbf{e}_x + \dot{\epsilon}^{\mathrm{EL}}\mathbf{e}_y$. This can be obtained by inspection, since the field lines are hyperbolic curves (*i.e.* "potential stream function" $\Psi = \dot{\epsilon}^{\mathrm{EL}}xy$). Since no current can pass through a potential stream line ($\mathbf{n}\cdot\nabla\phi = 0$ where $\mathbf{n}$ is normal to the potential stream line), placing an insulating boundary on any potential stream line will not change the field. This field is strictly valid in the ideal case of no entrance and exit regions in the hyperbolic contraction. A finite element analysis of the real channel geometry will be discussed below.

Hyperbolic geometry: We investigate the stretching of DNA molecules in a hyperbolic contraction microchannel as shown in Fig. 6-13. In this channel (Fig. 6-13 (a)), DNA are driven by an electric field to the hyperbolic contraction from the right down a wide inlet channel of width w_1 and length l_1. The sidewalls then contract according to a hyperbolic equation of the form: $y = C/(x + 2C/w_1)$ where x and y are a set of coordinates with origin along the symmetry line of the channel at the point where the hyperbolic begins (Fig. 6-13 (b)). The length of the contraction is l_c. After moving through the contraction, the DNA then migrate down a narrow channel of width w_2 and length l_2, and afterwards move though an abrupt expansion and travel to a waste reservoir down a channel of length w_3 and length l_3. The dimensions used in this study were: w_1 = 200 μm, w_2 = 3.8 μm, w_3 = 200 μm, l_1 ~1.5 mm, l_2 =1.52 mm, l_3 ~1.5 mm, and l_c = 80 μm. The hyperbolic constant C ($= w_2 l_c/(2 - 2w_2/w_1)$ was 155 μm^2.

For the remaining analysis, we will non-dimensionalize the downstream position, electrophoretic velocity, and electrophoretic strain rate as:

$$\begin{aligned}\hat{x} &= \frac{x}{l_c}\\ \hat{\mathbf{E}} &= \frac{\mathbf{E}}{E_1}\\ \hat{\dot{\epsilon}} &= \dot{\epsilon}^{\mathrm{EL}}\frac{l_c}{\mu E_1}\end{aligned} \tag{6.10}$$

where E_1 is the uniform electric field in the inlet region of length l_1 and we have dropped the EL superscript for non-dimensional electrophoretic strain rate. We will similarly drop the EL superscript to report electrophoretic strain.

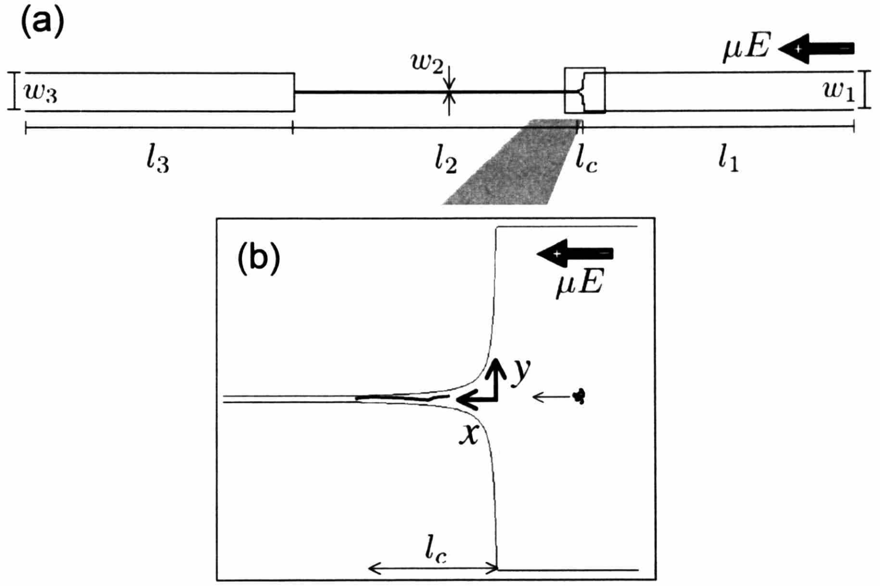

Figure 6-13: (a) Diagram of the hyperbolic contraction geometry. (b) Close-up of the hyperbolic contraction (length l_c) and xy-coordinate system. The vector $\mu\mathbf{E}$ points in the direction of DNA motion (right to left).

In Fig. 6-14 (a) we show a finite element calculation of the 2-dimensional (2D) electric field strength $|\hat{\mathbf{E}}|$ along with expected trajectories in the hyperbolic section of the channel. The molecules move right to left and accelerate through the hyperbolic to a maximum electrophoretic velocity in the narrow section of the channel. Fig. 6-14 (b) shows the scaled electrophoretic velocity in the hyperbolic region of the channel from the finite element computation. This data is for the $y = 0$ trajectory, however we confirmed that other trajectories exhibit a similar velocity trend. The electrophoretic velocity for an idealized hyperbolic channel without any end effects is indicated by the thin line. Note that for this device the velocity is ~ 53 times greater in the narrow section than at the inlet and there is an approximately constant velocity gradient in the hyperbolic region. There are however entrance and end effects that are more evident in Fig. 6-14 (c), which shows $\partial|\hat{\mathbf{E}}|/\partial\hat{x}$ ($= \hat{\dot{\epsilon}}$). Again, the strain rate for an ideal channel without entrance or exit effects is indicated by a thin line. Because of the large change in channel dimensions, the entrance region extends a full contraction length before the contraction begins and persists into about 25% of the contraction length. At this point the strain rate is constant until about the last 5% of the contraction, at which point it abruptly falls to zero. Fig. 6-14 (d) shows the electrophoretic strain integrated along the $y = 0$ trajectory (s is the distance along the trajectory path):

$$\begin{aligned}\epsilon &= \int_{\text{path}} \frac{\dot{\epsilon}(s)ds}{|\mu\mathbf{E}|(s)} \\ &= \int_{(-\infty,0)}^{(\hat{x},0)} \frac{\hat{\dot{\epsilon}}(\hat{x})d\hat{x}}{|\mu\hat{E}|}\end{aligned} \tag{6.11}$$

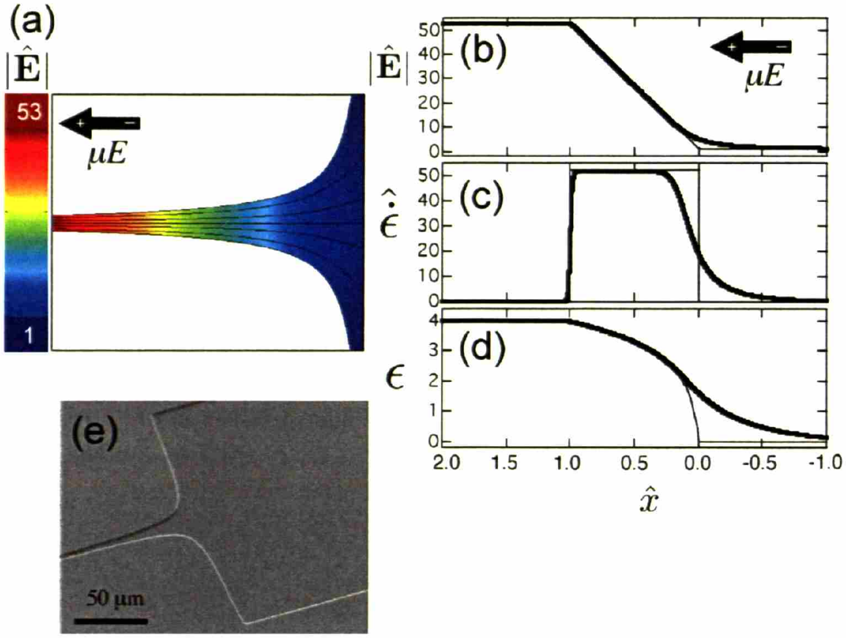

Figure 6-14: (a) Dimensionless electric field strength in the hyperbolic region from finite element calculation. (b) Dimensionless electric field strength along the $y = 0$ trajectory. (c) Dimensionless strain rate along the $y = 0$ trajectory. (d) Strain accumulated along the $y = 0$ trajectory. The thin lines in (b)-(d) are for an ideal hyperbolic contraction without entrance or exit effects. (e) SEM image of a PDMS hyperbolic contraction.

along with the strain of the ideal hyperbolic channel ($\ln[(\hat{x} + C/(l_c w_1))/(C/(l_c w_1))]$). Note that this geometry allows for a total strain of 4, however a significant strain ($\epsilon \sim 2$) is achieved in the nonhomogeneous entrance region. A similar nonhomogeneous field was treated in the case of a cylindrical obstacle and a general treatment of deformation in non-homogeneous fields can be found in Ref. [161]. The primary effect of the nonhomogeneous entrance region will be to reduce the effective strain experienced in the strong extensional region (De> 1/2) when De is low. Additionally, it will also slightly shift the DNA's configuration distribution at the hyperbolic inlet to slightly more extended states [169]. However, we stress that this shift is far less than the shift required to sufficiently avoid molecular individualistic effects.

Bead tracking: We performed bead electrophoresis experiments to characterize the electric field in the hyperbolic contraction. A 0.01% solution of carboxylated polystyrene fluorescent beads (negatively charged, $R_{\text{bead}} = 0.16$ μm, Polysciences) was prepared in the 1 cP buffer along with an additional 0.5% tergitol (NP-10, J.T. Baker) to prevent beads from sticking to the channel walls. The bead solution was loaded into a hyperbolic channel and an electric field was applied to drive the beads into the contraction. The maximum field strength at the contraction exit was E_2 =425 V/cm, which is the near the highest field strength achieved in the DNA deformation study. Nonlinear electrophoretic effects discussed in Refs. [72, 79–81] are negligible at these conditions. We tracked the center of mass position of 25 beads. Their trajectories, which are predictably hyperbolic in shape, are shown in Fig. 6-15 (a). Figure 6-15 (b) shows a semi-log plot of the x-position of each bead versus time. The thick line is the affine scaling $x \sim \exp(\dot{\epsilon}^{EL} t)$ in the uniform part of the extensional field. For each bead trace we fit for an experimentally observable strain rate $\dot{\epsilon}^{EL}_{\text{obs}}$ with $\hat{x} = \hat{x}(0)\exp(\dot{\epsilon}^{EL}_{\text{obs}} t)$ from $\hat{x}(0) = 0.2$ up until $\hat{x}(t) = 0.9$. The ensemble average strain rate was determined to be $\langle \dot{\epsilon}^{EL}_{\text{obs}} \rangle = 4.4 \pm 0.3$ s^{-1}. We also independently measured the velocity of beads in the narrow section (l_2) of the hyperbolic and then divided by the contraction length l_c to obtain $\langle \dot{\epsilon}^{EL}_{\text{obs}} \rangle = 4.4 \pm 0.3$ s^{-1}. Hence each bead accelerates affinely, as expected for this well-behaved field. In DNA experiments, we determine the strain rate using the latter method, *i.e.* by measuring the velocity of DNA molecules in the narrow section (l_2) of the device and computing $\dot{\epsilon}^{EL} \approx \mu E_2 / l_c$. Now that we have characterized the channel, we study how DNA coils deform in it.

6.3.2 Experimental

We used standard soft lithography [108] procedures (Chapter 3) to construct 2 μm-high PDMS (polydimethylsiloxane) microchannels with geometry as described above. Figure 6-14 (e) shows an SEM image of a typical hyperbolic channel.

T4 DNA (169 kbp, L = 70 μm stained, $R_g \sim$ 1.5 μm) were stained with a fluorescent dye (TOTO-1, 4.7:1 bp:dye molecule) and diluted in one of the following buffers: 5×TBE, 4% β-mercaptoethanol, and 0.1% polyvinylpyrrolidone (PVP, Polysciences, $M.W. = 10,000$) (η=1 cP, pH=8.3) or 5×TBE, 4% β-mercaptoethanol, 0.1% PVP (Polysciences, $M.W. = 10,000$), and 31% sucrose (η=6 cP, pH=7.9). The 6 cP buffer was only used for our De=23 study to slow down dynamics to experimentally observable speeds. The PVP is added to the formulation to dynamically coat the microchannel walls to minimize electroosmotic flow. The measured electrophoretic mobility of the DNA was $\mu = -1.3 \pm 0.2$ $\frac{\mu\text{m}}{\text{s}} / \frac{\text{V}}{\text{cm}}$ in the 1 cP buffer and $\mu = -0.17 \pm 0.02$ $\frac{\mu\text{m}}{\text{s}} / \frac{\text{V}}{\text{cm}}$ in the 6 cP buffer. The DNA were fairly monodisperse, though some break during storage and handling. Approximately 2/3 of the DNA coils are intact T4 molecules in these experiments. Broken molecules

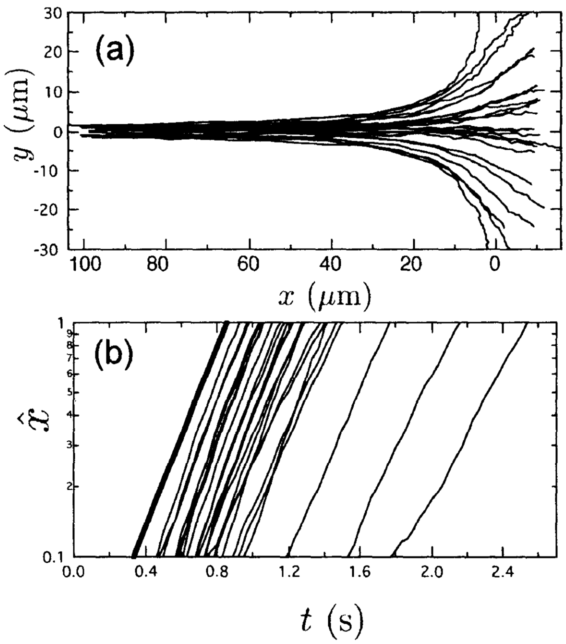

Figure 6-15: (a) Trajectories of carboxylated bead electrophoresis for field characterization (field strength in $l_2 \equiv E_2 = 425$ V/cm, $R_{\text{bead}} = 0.16$ μm, 1 cP). (b) Semilog $\hat{x}(t)$ traces for the above bead electrophoresis data. The thick line is the affine scaling using $\dot{\epsilon}^{EL} = 4.4$ s^{-1}.

are generally easy to spot as they tend to be approximately half the size of an intact T4 molecule. Nevertheless, a possible source for error in these studies is the quality of the DNA ensemble.

A typical experiment consisted of first soaking the PDMS channel for 12 hours at 45°C in 0.5×TBE to eliminate permeation driven flow [165]. Next, we gently rinsed and dried the microchannel and applied it to a clean glass slide (soaked in 1M NaOH for 15 min and rinsed in ultrapure water (MilliQ, Millipore)). We then immediately filled the channel with DNA solution and applied an electric field across the reservoirs through platinum electrodes. After 15 minutes of equilibration, we observed single DNA molecule dynamics using an inverted fluorescence microscope (Axiovert 200, Zeiss) with a 63× 1.4 NA objective and 100 W mercury lamp light source operating at 50% intensity (HBO 103, Zeiss). Images were captured at 30 frames per second with an EB-CCD camera (C7190-20, Hamamatsu) and NIH Image software. Digitized images had 8-bit pixel intensity values which ranged from 0-255. The primary experimental observable is the extension of the DNA x_{ex} (Fig. 6-5). For a stretched molecule, x_{ex} is simply the distance between the front (x_f, y_f) and back coordinates (x_b, y_b). We manually adjust for the effect of a curved contour length in the hyperbolic for any molecules that stretch over 40 μm long with a back coordinate $|y_b| > 20$ μm. An equilibrium T4 coil in the inlet section (l_1) of a 2 μm-high channel had a mean maximum linear dimension $\langle x_{\text{ex}} \rangle = 4.6 \pm 0.8$ μm ($\langle x_{\text{ex}}/L \rangle = 0.07$).

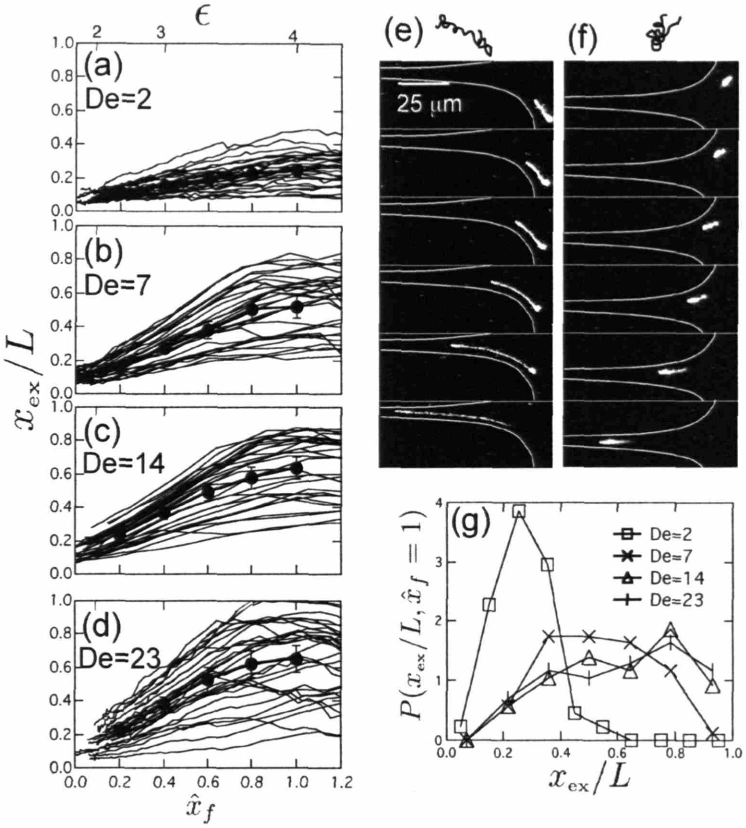

Figure 6-16: Fractional extension of T4 DNA in the hyperbolic contraction (no gel) at (a) De=2 (b) De=7 (c) De=14 and (d) De=23 (ensemble sizes of n=30 shown). Ensemble averages and standard errors are shown by the filled circles. (e)-(f) Sample images (0.17 s timesteps between frames) of T4 DNA stretching in the hyperbolic contraction at De=7. The hyperbolic sidewalls are drawn in for reference. (e) A "dumbbell" molecule in an initially open configuration. (f) A "folded" molecule in an initially closed configuration. (g) Probability distribution (n=60) of T4 DNA fractional extension as its front leaves the hyperbolic contraction at each De studied.

6.3.3 Results

Extension-strain dynamics: Figure 6-16 (a)-(d) shows the fractional extension x_{ex}/L of T4 DNA driven through the contraction by electric fields at De=2, 7, 14, and 23. The fractional extension data is plotted against both the x-coordinate of the front of the DNA molecule $\hat{x}_f = x_f/l_c$ (lower axis) and the electrophoretic strain (top axis) calculated from Fig. 6-14 (d). The strain experienced by a DNA molecule is difficult to rigorously define since a stretched T4 molecule can span a large fraction of the contraction and even sample different strain rates in the entrance region. Recall that electrophoretic strain is a measure of how ideal charged objects move exponentially apart in a field gradient. Because we are studying how the front of the DNA moves away from its back, we have chosen to plot the strain at the front coordinate of the molecule.

Just like in Fig. 6-7, we determined that the coil stretch transition in the hyperbolic contraction

Table 6.1: Summary of ensemble average fractional extension and standard deviation at the contraction exit.

De	$\langle x_{\mathrm{ex}}/L \rangle$ at $\hat{x}_f = 1$
2	0.26 ± 0.10
7	0.54 ± 0.17
14	0.61 ± 0.21
23	0.60 ± 0.24

occurs as expected at De$\sim$1/2. Given electrohydrodynamic equivalence [156], one might first expect the stretching data at De> 1/2 to closely match results of Refs. [86, 89, 169]. However the field is not strictly homogeneous. Recall that $\hat{\dot{\epsilon}}$ ramps to its maximum value from $-1 < \hat{x} < 0.25$ and also note that the extended lengths of these T4 molecules are on the order of the length of the contraction. We find that the De=2 fractional extension is noticeably lower than expected, as previous experiments [86, 89, 169] and simulations [170] show $\langle x_{\mathrm{ex}}/L \rangle \sim 0.5$ and some steady-state configurations with $x_{\mathrm{ex}}/L \sim 0.75$ after a strain of 4. We attribute this difference primarily to the inhomogeneous entrance region where $\hat{\dot{\epsilon}}$ slowly ramps from 1 to 53. At De=2, the strong stretching criterion (De> 1/2) is not achieved until $\hat{x} \sim 0$. Thus, the accumulated 1.5 units of strain occurring before $\hat{x} \sim 0$ cannot induce strong deformation, which decreases the strain experienced in the strong stretching regime to 2.5. Our ensemble average ($\langle x_{\mathrm{ex}}/L \rangle = 0.26$) corresponds closely to homogeneous flow studies [89] after $\epsilon = 2.5$. We conclude that these molecules do not experience enough strain in the strong stretching regime for any to achieve steady-state extensions.

Conversely, at higher De, the strong stretching condition is met well before the contraction and the molecules experience $\epsilon \sim 4$. This is ample strain for *some* molecules in the ensemble to reach steady state extension at the outlet and the extension data more closely follows previously published results in flows [89] (*i.e.* $\langle x_{\mathrm{ex}}/L \rangle = 0.6$ at De=14 after $\epsilon = 4$). This close agreement implies that the entrance region and DNA finite size effects are not significantly altering the ensemble stretching dynamics. Consequently we see a variety of extension behavior, with some molecules extending much faster than others. This is characteristic of molecular individualism [86, 87], *i.e.* the extension dynamics are highly sensitive the polymer's initial configuration. This conformation effect is well-documented both experimentally [86, 89] and by simulation [91] and we demonstrate it qualitatively by examining two particular configurations in Fig. 6-14 (e) and (f), which show individual DNA molecules stretching at De=7. Fig. 6-14 (e) shows a T4 DNA molecule that enters the contraction in an open dumbbell-like configuration [86, 89] and then significantly stretches. However Fig. 6-14 (f) shows a T4 DNA molecule that enters in a compact coiled configuration [86, 89] and does not stretch much in the contraction. This sensitive dependence of stretching on the initial configuration makes stretching DNA *uniformly* at a moderate strain impossible.

Figure 6-14 (g) shows the fractional extension probability distributions for T4 when the front of its fluorescence cloud exits the hyperbolic ($\hat{x}_f = 1$) at various De. Table 6.1 reports each ensemble's mean and standard deviation. It is clear that as De increases, the distributions shift to higher extensions. However, using kink dynamics arguments [171], one might expect this shift to saturate around De=40. Judging by the similarity in the De=14 and De=23 data, it is clear that our study comes close to this saturation point. Hence, in a finite-strain hyperbolic contraction, though some DNA may stretch near full contour length, other DNA will only weakly stretch. This leads to a broad extension probability distribution even at high De.

6.4 Conclusions and outlook

These studies show how one can harness electric field gradients to manipulate flexible charged macromolecules. Specifically, we examined the deformation history of single DNA molecules in the electric field gradients near a large insulating cylinder and a hyperbolic contraction.

For the cylinder, the molecules slightly stretch along the axis of extension before impact, but still showed characteristic configuration-sensitive extension-strain trajectories of an elongational field. Moreover, these stretched DNA affinely compress at the backside of the obstacle, and can re-stretch in the field direction as they leave the obstacle. This post-impact stretch was much more pronounced at De=9 than De=2, which we argued was due to the DNA's crumpled configuration, its finite size, and the steeply decaying inhomogeneous strain rate. Finally, the molecules thermally relax in low field gradient regions away from the obstacle. The terminal relaxation time is identically τ. The results were highly comparable in the hyperbolic contraction, however at De=2, no molecules were able to experience enough strain in the strong field gradient region to reach steady state extension.

More generally, we presented situations where the electrohydrodynamic equivalence is valid in free solution, as both electric field gradients and elongational flows create strong extensional fields. A more dramatic example of this equivalence would be to demonstrate coil-stretch hysteresis [90] with electric field gradients. This study is also a unique analysis of deformation dynamics in an *inhomogeneous* (though pseudo-homogeneous) extensional field. We stress that electric field gradients provide a convenient way to induce purely extensional fields without shear components near surfaces.

The two case studies chosen can be considered archetypal examples of two possible types of field gradients: stagnation and accelerating fields. As in the case of hydrodynamic stretching, the most prominent feature of these stretching experiments is molecular individualism. However, knowing how DNA molecules will extend and compress in field gradients offers a powerful new tool for microfluidic process design. One may consider these case studies as first order examples; more complex obstacle geometries or channel contractions/expansions can be envisioned for custom DNA manipulations. Potential applications include pre-straining configurations, compression, or stretching of DNA. For example, we have observed history-dependent DNA deformation dynamics from "pre-crumpled" molecules. Additionally, we are able to quickly compress a stretched DNA molecule by introducing it to a stagnation point near a large obstacle. This may be a valuable tool for collision-based DNA mapping applications that rely on frequent transitions from stretched to compact configurations. But we also foresee creation of custom geometries to fully stretch DNA with electric fields so that nano-analytical methods may be incorporated to decode or map gene locations [26].

Chapter 7

Collision of a DNA Molecule with a Post

Polymer collisions occur in many settings, ranging from biological macromolecule interactions [172], to the rheology of polymer melts [173], to DNA electrophoresis [3]. The collision of a polymer molecule with a stationary obstacle is a simply posed but non-trivial problem. For sufficiently strong impacts, a coiled polymer hooks around the obstacle to form a hairpin configuration. A hooked molecule then unhooks from the obstacle and recoils (Fig. 7-1 (a)). Although analogous to a classical rope-and-pulley problem, this microscale problem is complicated by the polymer's elasticity and fluctuating configuration. As discussed in Chapter 1, the most relevant application of the polymer-obstacle collision problem is the separation of large DNA fragments, for which these collisions are the length-dependent separation mechanism. In order to apply the microscale single collision problem to this macroscale application, one would need to address questions like: How often does a DNA polymer form a hook? How long does a hooked DNA remain on the obstacle? What is the separation performance of this mechanism? As we will review, these questions have been partially addressed in some recent papers, mostly from a macroscale approach. However, no one has performed controlled microscopic experiments to extract the hooking probability and the probability distribution of the unhooking time. Furthermore, no one has constructed a comprehensive model that can reproduce the multitude of hooking dynamics observed experimentally.

In this Chapter, we study the electrophoretic collision of a DNA molecule with a *small obstacle*. We decompose the single collision problem into two probabilistic events: 1) the probability of forming a hooked configuration P_{hook} and 2) the probability distribution of unhooking times $P(t_H)$. Using microscopy and automated tracking and collision time algorithms, we are able to directly determine both P_{hook} and $P(t_H)$ of DNA on microfabricated obstacles. Furthermore we expand on previously proposed models and develop new models that reproduce observed collision time results.

7.1 Previous single obstacle collision studies

7.2 Experimental and analytical procedures

7.3 Results

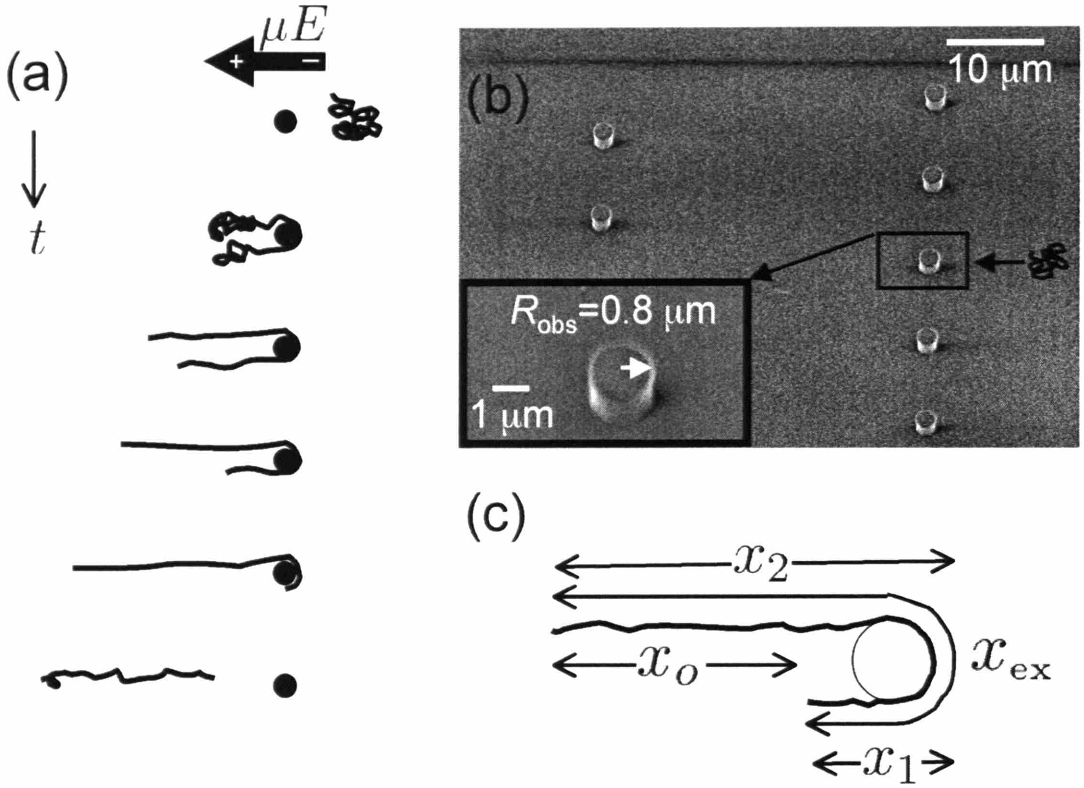

Figure 7-1: Single obstacle hooking of DNA. (a) Schematic of a typical hooking event. (b) SEM image of our PDMS obstacle array and an expanded view of a single post. (c) Length definitions of an unhooking DNA.

7.4 Collision time models

7.5 Conclusions and outlook

7.1 Previous single obstacle collision studies

As mentioned in Chapter 1, Austin and Volkmuth [6, 7, 174] observed DNA hooking collisions in an intended microfabricated pore separation device. Though these collisions were not ideal for a pore separation, they noted that the unhooking mechanism is itself strongly length dependent and thus could lead to size-separation in a less dense obstacle course. This hypothesis was tested with simulations [1, 10–13, 15] and later proved with experiments [14, 16].

Before any of this work, Song and Maestre [96] observed similar hairpin hooks during T4 gel electrophoresis experiments. They selected a few collisions with nearly symmetric arms and found that that total extension of the molecules remained constant until the last 15% of the total unhooking time. They also showed that often, the long arms and short arms respectively grow and decay exponentially in time. These are the types of results one would expect for a classical rope releasing from a frictionless pulley. However, the time constants for each arm's motion were usually different and, in some cases, the long arms grew linearly with time. For comparison they performed a macroscopic experiment by tracking a Slinky unhooking off a post and obtained similar trajectories for the long and short arms, *i.e.* different time constants. Having different time constants is not expected for a rope-on-pulley, so they qualitatively concluded that elasticity and tension fluctuations must be important in the DNA unhooking event. Nevertheless, the rope-on-pulley model adequately models *some* collisions and it was used in subsequent experimental investigations of DNA releasing from an obstacle [7, 175]. The goal of these works was to measure how the obstacles slow down a large ensemble of DNA molecules *on average* and hence evaluate their effectiveness as a separation mechanism. Neither study concentrated on the quantitative *ensemble dynamics* of the single collision event and essentially focussed on special cases that mimicked the rope-on-pulley problem. We do note however, that Volkmuth *et al.* [7] cite a first passage time approximation to the rope-on-pulley problem in which they include diffusive noise in the model. We will return to this notion later.

Using simulations, other groups continued along these lines to determine length-dependent behavior of DNA mobility through a group of point-like obstacles [1, 10–12]. These studies began by looking at the *single collision* event of a Rouse-like bead-spring chain at high fields, and results showed that the average single obstacle unhooking time $\langle t_H \rangle$ scaled as $\langle t_H \rangle \sim L/(\mu E)$, where L $(= Nl_k)$ is the DNA's contour length. Geometric arguments were used to scale these single collision results to an obstacle course separation device [12], yielding an average mobility of $\langle \mu \rangle \sim 1 - N^{3/2}$. Other innovations in single obstacle simulation work include: study of the hooking probability on a point obstacle as a function of impact offset [12], inclusion of approximate hydrodynamic interactions [1], and introduction of the notion of "roll-off" collisions on finite size obstacles [13]. Additionally Patel and Shaqfeh [15] simulated chains moving through arrays of multiple obstacles and investigated the effect of obstacle ordering and density.

These initial experimental observations and simulations held that a DNA size separation was possible and the first experimental work to show this was by Doyle *et al.* [176]. For obstacles, they used 1 μm magnetic beads that self assembled into columns in an applied magnetic field (6 μm spacing). They were able to separate 3 sizes of DNA (48.5, 97, 145.5 kbp; 15, 33.5, and 48.5 kbp) with resolutions between 1-3. Follow-up work was performed in slightly more dense obstacle courses at higher fields [16] and in extremely dense courses [177], though as the obstacle density increases, the separation mode switches from collision unhooking time to pore sieving.

Following these experiments, macroscale separation models were proposed to explain the dependence of the average mobility $\langle \mu \rangle$ and dispersivity $D^\star$ on the DNA length in an obstacle array with the hooking separation mechanism. Dorfman and Viovy [178] first presented a Markovian model that required parameters P_{hook} for the hooking probability and $\langle t_H \rangle$ for the average retention time on the obstacle. Using scalings of $\langle t_H \rangle \sim E^{-1}$ and P_{hook} independent of E, their model predicts that separation resolution is independent of E and that that band broadening scales like E^{-1}. In order to make quantitative predictions, they obtained data from a single obstacle in an array, which showed that the unhooking time probability distribution $P(t_H)$ could be modeled as a Poisson distribution [179]. However, these results confirmed that their Markovian model is invalid for these dense arrays because a collision at a given post is not independent of the DNA's collision history (the previous collision to be exact). Minc, Viovy, and Dorfman then adjusted the model to include non-Markovian transport through the post array [180]. Using non-separable continuous time random walk calculations [181], their resulting predictions are able to capture some observed results in dense obstacle arrays, *e.g.* the number of rows between collisions and the average mobility in the obstacle course, though it over-predicts the dispersivity. The argue that a better trapping model may improve agreement.

After reviewing past work on single obstacle-single DNA hooking collisions and obstacle array studies, it is clear that a systematic analysis of the microscale collision dynamics is lacking. A systematic analysis could extract the hooking probability and collision time distribution by tracking a uniform ensemble of DNA molecules distributed perpendicular to the field impacting a finite size obstacle. Simple rope-on-pulley models have been able to predict high field scalings for the unhooking time of ideal collisions. However when considering this entire impacting ensemble, there are many experimentally observed collisions, especially at low and moderate fields, that do not behave like the rope-on-pulley model. This has been known since Song and Maestre's work [96] but never explored. Furthermore, other than the first passage time model presented by Volkmuth *et al.* [7], no other work has investigated the role of arm fluctuations on unhooking time, and no work has considered how these fluctuations affect the collision time distribution.

In this Chapter we will experimentally investigate single DNA molecules forming hairpin hooks on single obstacles. Unlike previous experimental citations, we will systematically decompose the ensemble of impacting DNA into "hooked" and "roll-off" sub-populations, thereby determining the probability of hooking. We will investigate the effects of finite size obstacle-induced electric field gradients on the hooking probability and also compare results to the point obstacle limit. Furthermore we will compute unhooking time distributions for different size hooked molecules at different dimensionless fields. We will decompose the conformations of hooked collisions into idealized rope-like collisions and non-ideal variable extension collisions and investigate their effect on unhooking time distributions. Finally we present both a "unifying" deterministic model and a first passage time unhooking model that includes effects of length fluctuations on unhooking collisions. Improved knowledge of the microscale single collision hooking probability and unhooking time distribution will benefit design and modeling of these obstacle arrays for DNA separations.

7.2 Experimental and analytical procedures

Dimensionless field strength: The Peclet number Pe is a measure of how the persistence length of DNA orients in an electric field. It can also be interpreted as: a measure of molecular diffusion (diffusivity D) to advection in a field on the persistence length (l_p) scale or a measure of persistence length diffusion to advection on the molecular scale. Pe serves as the nondimensional group used to generalize the process of polymer unhooking from an obstacle; it addresses when a hooking collision can occur and to what extent the hairpin arms stretch. Alternate versions of this dimensionless field strength have been used in the past DNA-obstacle work reviewed above. However, since polymer unhooking involves a competition between stretched polymer arms, it is most natural to think of Pe as the proper way to nondimensionalize the extension of a tethered polymer in a uniform flow U or field E.

In flow, the drag force on the chain is ζU and in the low-force limit ($f \sim kTx_{\text{ex}}/(Ll_p)$), the fractional extension x_{ex}/L scales as:

$$\begin{aligned}\frac{x_{\text{ex}}}{L} &\sim \frac{l_p}{kT}U\zeta \\ &= \frac{Ul_p}{D}\end{aligned} \tag{7.1}$$

Using electrohydrodynamic equivalence [182], we define Pe as Pe= $\mu El_p/D$ in electrophoretic fields. To keep the fractional extension constant, Pe must be kept constant. Note that Pe scales as N^{ν}, which is approximately the scaling Perkins *et al.* [45] empirically determined to achieve a family of universal extension curves of tethered DNA. Additionally, the free draining version of Pe was employed by Patel *et al.* [15] to collapse a family of Rouse bead-spring chain unhooking simulations onto one master collision time curve.

Experimental procedure: We used our standard soft lithography [108] procedure (Chapter 3) to construct 25 mm-long, 50 μm-wide, and 2 μm-high PDMS (polydimethylsiloxane) microchannels with a sparse array of 0.8 μm-radius obstacles. The obstacles were spaced 70 μm center-to-center in the field direction and were staggered transverse to the field with a 10 μm center-to-center spacing. Reservoirs (4 mm×4 mm) were cut at each end of the cured PDMS microchannel with a scalpel and the channels were soaked for 12 hours at 50°C in 0.5×TBE to eliminate permeation driven flow [165]. Figure 7-1 (b) shows a SEM image of the obstacle array and an isolated obstacle.

We used λ-DNA and T4 DNA in this study. The DNA were stained with a fluorescent dye (TOTO-1, 4.7:1 bp:dye molecule) and diluted in the following buffers: 1) 2.2×TBE, 3% β-mercaptoethanol, 0.07 % PVP (M_w=10^6, $c^\star \sim 1\%$), and 0.07% ascorbic acid (used for λ DNA, pH=8.4) and 2) 2.2×TBE, 3% β-mercaptoethanol, and 0.07 % PVP, (used for T4 DNA, η=1 cP, pH=8.4). The viscosities were measured by bead tracking [166]. The additives were chosen to dynamically eliminate electroosmotic flow and scavenge oxygen. The measured electrophoretic mobility was $\mu = -1.7\pm0.2\ \frac{\mu\text{m}}{\text{s}}/\frac{\text{V}}{\text{cm}}$. As explained previously, this dyed λ DNA has a contour length of L=21 μm (Chapter 3) and a longest relaxation time (Chapter 5) of τ=0.19 s. The T4 has a stained contour length of 70 μm and τ=1.7 s.

A typical experiment consisted of first gently rinsing and drying the microchannel and then applying it to a clean glass slide (plasma cleaned at 100 W for 5 min, charge equilibrated 1 day, soaked in 1M NaOH for 15 min and rinsed in ultrapure water (MilliQ, Millipore)). We then immediately filled the channel with DNA solution and applied an electric field of 5.2 to 23.4 V/cm across the reservoirs through platinum electrodes. We observed single DNA molecule dynamics using an inverted fluorescence microscope (Axiovert 200, Zeiss) with a 100× 1.4 NA objective for λ DNA and a 63× 1.4 NA objective for T4 DNA. Images were captured at 30 frames per second (Δt_{frame} = 0.0333 s) with an EB-CCD camera (C7190-20, Hamamatsu) and NIH Image software. Digitized images had 8-bit pixel intensity values which ranged from 0-255.

Analysis: To extract data, we first filtered the background noise by subtracting the maximum pixel value of the perimeter of the first frame of a movie from all the pixels in that movie. The primary observable from the captured images of a DNA collision was the center of mass coordinate of the DNA $(x, y)_{\text{com}}$. We adopted an obstacle-centered coordinate system for each collision, with the x-coordinate in the field direction and the y-coordinate transverse to the field (Fig. 7-2 (a)).

The center of mass of a molecule was computed by finding the first moment of the post-filtered image intensity distribution [168]. This process was automated for multiple frames of data and it yielded the center-of-mass trajectory $\mathbf{x}_{\text{com}}(t)$ of the DNA (*cf.* Fig 6-5 (c)). We determine the extension of the short (x_1) and long (x_2) arms of an unhooking DNA by the distance between the end of each arm and the front of the obstacle. Calculations account for the curvature of the contour around the obstacle. The total extension x_{ex} of the DNA is then $x_{\text{ex}} = x_1 + x_2$. Furthermore, we define the difference in arm lengths x_o as $x_o = x_2 - x_1$. Refer to Figure 7-1 (c) for a diagram of these observable lengths.

We obtain obstacle positions for each 2000 frame movie of data by averaging the pixel values of all frames. Obstacles are easily observed as vacancies in the smeared DNA traces of the pixel average. We then define the impact parameter for a collision b as the y-offset between the impacting DNA's center of mass and the obstacle center, taken at a distance $R_{\text{obs}} + 2R_g$ from the obstacle center (Fig. 7-2 (a)). This position was chosen to evaluate b because the DNA is far enough away from the obstacle to not experience high obstacle-induced electric field gradients, yet close enough so that Brownian drift does not significantly coarsen our analysis. For this study, we only analyze collisions with $|b| < R_{\text{obs}} + R_g$. No hooking collisions were observed for DNA with $|b| > R_{\text{obs}} + R_g$.

Using the center of mass trajectories of the colliding DNA, we can compute the collision hold-up time t_H. For all collisions we consider, the coiled DNA is moving from right to left, *i.e.* from positive x to negative x. A typical $x_{\text{com}}(t)$ trajectory (T4 DNA, Pe=8) is shown in Fig. 7-2 (b). A collision trajectory $x_{\text{com}}(t)$ shows a decrease x_{com} until the DNA impacts the obstacle. Impact is then followed by a plateau in $x_{\text{com}}(t)$ when the molecule is hooked on the obstacle. At this point the DNA configuration resembles a hairpin. Finally, when the molecule unhooks, $x_{\text{com}}(t)$ decreases again. The pre- and post- impact slope of $x_{\text{com}}(t)$ should be equal to μE. We note that in some cases, particularly for long collision times (or highly extended DNA), the slope of $x_{\text{com}}(t)$ is briefly slightly steeper than μE as the molecule is leaving the obstacle. This can be seen in Fig. 7-2 (b) at around $t = 12$ s. A more persistent steep slope was observed previously by others in a moderately dense magnetic bead obstacle field [179]. We speculate that their unexplainable persistent increase in slope was due to the peculiarities of that particular device, perhaps from acceleration of a stretched configuration in the field gradients near the surfaces of the many surrounding obstacles. We attribute our transient increase in slope to stress relaxation of a non-uniform tension profile, which causes the molecule to recoil toward the high-intensity front as it moves. The images of Fig. 7-2 (b) show that the region of steeper slopes for $x_{\text{com}}(t)$ corresponds precisely to when the short arm is releasing from the obstacle. From these images, it is clear that the back of the DNA accelerates toward the front during unhooking, leading to the transient increase in slope of $x_{\text{com}}(t)$. Often the $x_{\text{com}}(t)$ trace abruptly jumps back up (near the large circle marker) when the rear of the DNA relaxes into a ball. This rare, short-lived slope increase is of secondary importance to determination of the overall collision time.

We extract t_H for each collision as the difference in time intercepts for lines fit to the approach and release trajectories (Fig. 7-2 (b)). The line fit for the approach data uses two fit parameters (slope and intercept) whereas the line fit for the release data uses just an intercept because the slope is constrained to match the approach slope. The approach data is fit from the first data point until $x_{\text{com}} < R_{\text{obs}} + 2R_g$ (shown by the square in Fig. 7-2 (b)). The release data is fit from when $x_{\text{com}} < -x_{\text{ex}}/2$ (shown by the circle in Fig. 7-2 (b)).

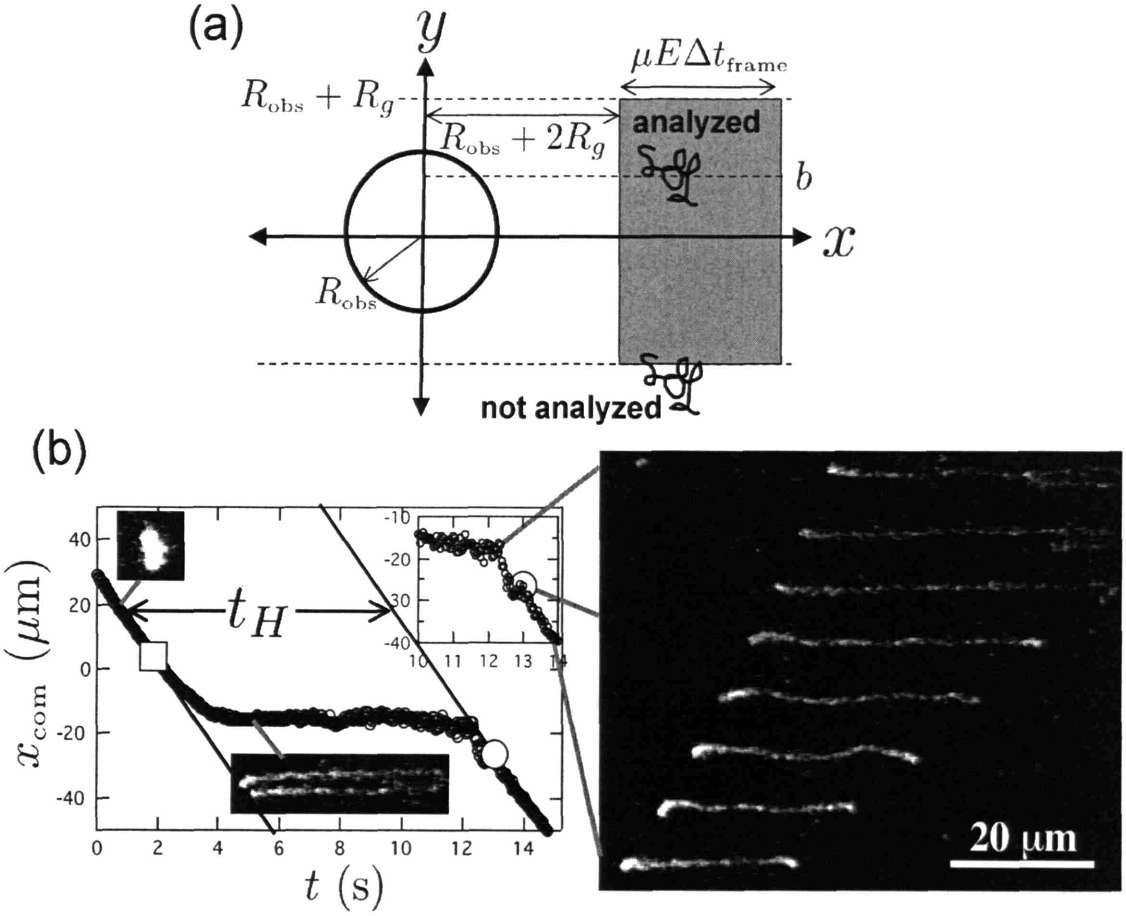

Figure 7-2: Experimental analysis. (a) Region where DNA molecules are chosen for the impact ensemble. (b) A sample unhooking trajectory (T4 at Pe=8) along with characteristic DNA configurations. The images of DNA releasing from the obstacle are 0.33 s apart.

7.3 Results

By observing many single obstacle collisions in the impacting ensemble with $|b| < R_{\text{obs}} + R_g$, we compiled collision time distributions. Figure 7-3 (a) shows a collision time histogram at Pe=8 of 542 λ DNA molecules evenly distributed in $|b| < R_{\text{obs}} + R_g$. We note immediately that the histogram is characterized by a large peak at short times followed by a more slowly decaying peak at long times. The large short time peak corresponds to those DNA that bypass or "roll-off" the obstacle. The notion of a roll-off event was introduced by Saville and Sevick's simulations [13]. In a roll-off, the DNA's configuration is not able to deform around the obstacle so that competing hairpin arms never form. Figure 7-3 (b) and (c) shows experimental images of a roll-off and a hook. Collision times for roll-offs are very short, usually an order of magnitude smaller than unhooking collision times. We can decompose the ensemble into roll-offs and hooking events using the definition that a hooking collision has a piece of its configuration, at some instant, in all four quadrants of the obstacle-centered coordinate system. Using this classification, we decompose the collision time data into two separate histograms, one for roll-offs (412 molecules) and one for hooks (132 molecules). This decomposition is shown in the λ DNA Pe=8 example in Fig. 7-3 (d) and (e). Indeed, the roll-offs compromise the large peak at $t < 0.05$ s, whereas hooking collisions are characterized by a distribution skewed with a slowly decaying tail.

7.3.1 P_{hook}: Hooking probability

Reprinted (some excerpts and figures) with permission from G. C. Randall and P. S. Doyle, "Electrophoretic Collision of a DNA Molecule with an Insulating Post", *Physical Review Letters*, **98**, 058102, (2004) [152]. Copyright (2004) by the American Physical Society.

In the above example of λ DNA at Pe=8, 24% of the molecules of the impact ensemble form hooks. The geometric parameters R_{obs}/R_g (ratio of the obstacle radius to the DNA equilibrium radius of gyration) and b/R_g (ratio of the offset between an impacting molecule's center of mass and the obstacle center to R_g), are naturally important for determination of the hooking probability. As both R_{obs}/R_g and b/R_g increase, it becomes less likely for an impacting DNA configuration to span the obstacle, so more and more collisions are roll-offs [13]. The hooking probability for a point obstacle can be computed using the DNA's equilibrium configurational distribution function, or as shown in Ref. [12], by a computer simulation. At the point limit $R_{\text{obs}}/R_g \ll 1$, the hooking probability is purely geometric. However, we propose that for a small but finite size obstable, induced electric field gradients can greatly affect the hooking probability. In this section we look more closely at the transition between roll-offs and hooking collisions. Applying results from Chapter 6, in addition to b/R_g and R_{obs}/R_g, this roll-off to hook transition is governed by a dynamic parameter De= $\dot{\epsilon}^{\text{EL}}\tau$, the ratio of the rate of maximum DNA deformation to DNA relaxation in an obstacle-induced field gradient.

Most materials used for obstacles in lab-on-chip processes, *e.g.*, glass, plastics, colloids, or emulsion drops, are insulating. In Chapter 6, we showed that a PDMS post obstacle induces electric field gradients like an ideal isolated, insulating cylinder and therefore deforms nearby DNA during electrophoresis. There we noted that we can examine deformation kinematics by extracting the velocity field gradient eigenvalues ($\pm 2\mu E R_{\text{obs}}^2/r^3$ for an insulating cylinder) and eigenvectors. The

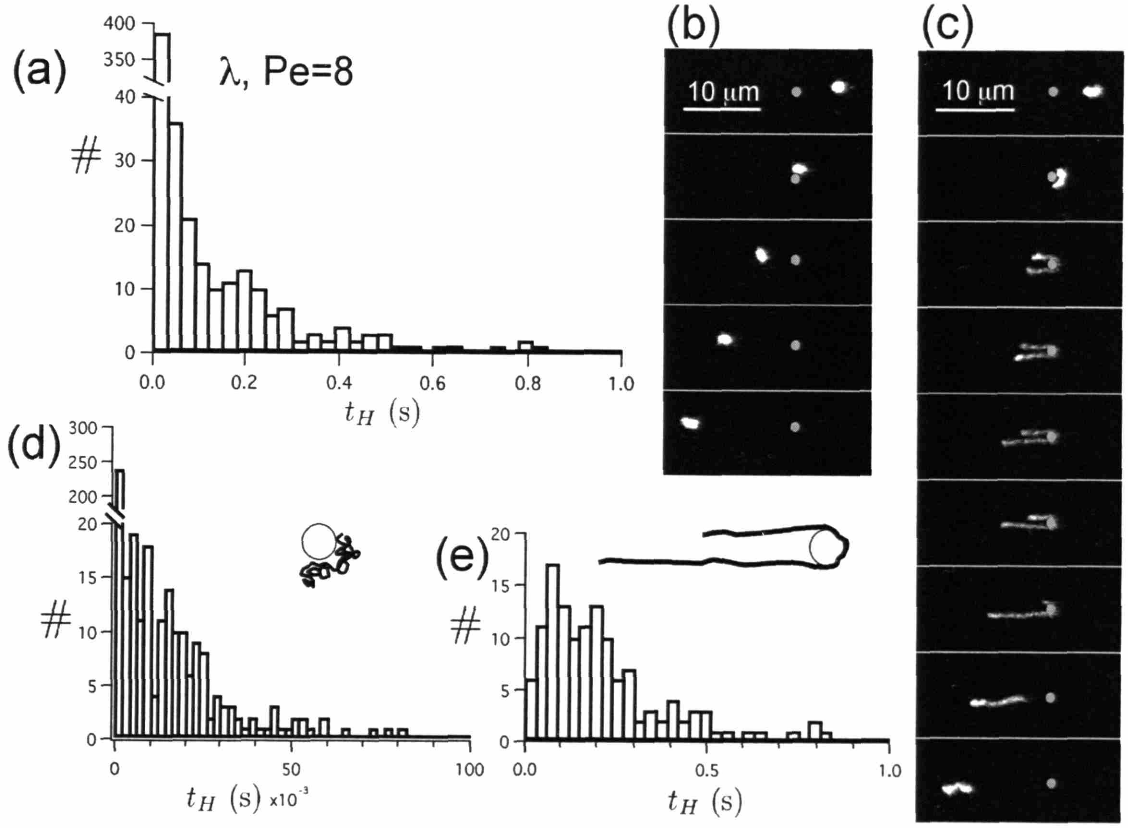

Figure 7-3: Roll-off and hook decomposition. (a) Collision time histogram for 542 λ DNA molecules at Pe=8. (b) and (c) Time-lapse images (0.17 s intervals) of (b) a roll-off collision and (c) a hooking collision of λ-DNA with an obstacle (R_{obs}=0.8 μm) at E= 15 V/cm (Pe=5.5, De=13). Obstacles are artificially added for clarity. (d) Roll-off histogram and (e) hooking collision histogram extracted from (a).

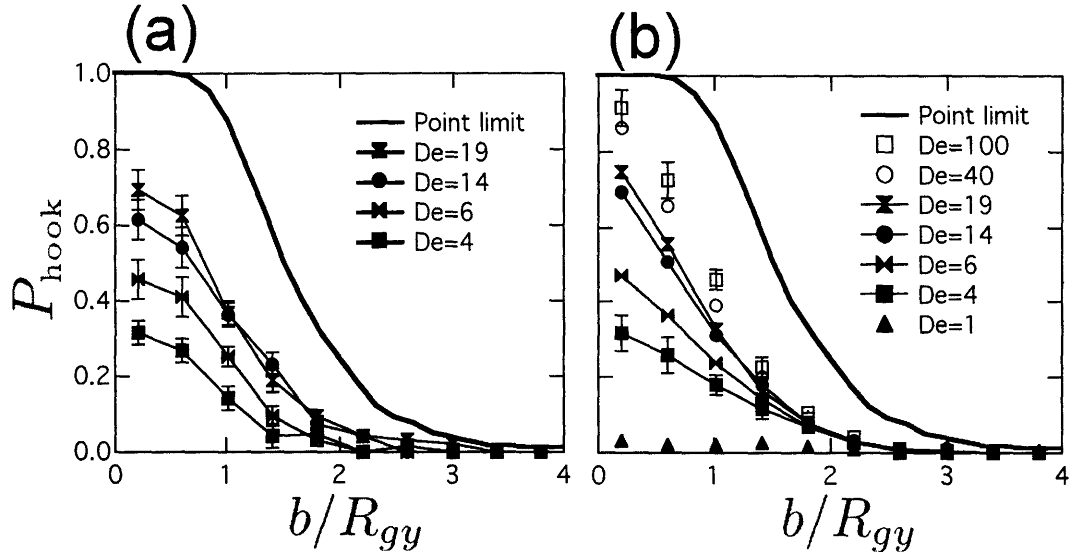

Figure 7-4: Hooking probability. (a) Experimental results for hooking probability of impacting DNA on the 0.8 μm-radius PDMS obstacle as a function of De and impact parameter. (b) Simulation results for similar conditions. The black line included in both plots is the point obstacle limit for hooking probability.

positive eigenvalue is the strain rate $\dot{\epsilon}^{\text{EL}}$, and its corresponding eigenvector is the primary axis of extension, which are both spatially inhomogeneous. We defined De using the largest strain rate $\dot{\epsilon}^{\text{EL}}(R_{\text{obs}}) = 2\mu E/R_{\text{obs}}$, so that De$= 2\mu E\tau/R_{\text{obs}}$. Recall that for De$< 0.5$ the molecule's internal relaxation modes dominate the effect of the field gradient and minimal stretching occurs, whereas for De> 0.5 the field dominates and the molecule will strongly stretch [88]. Furthermore, we saw that the stretching behavior of DNA in an extensional electric field varied greatly from molecule to molecule. The impact of a DNA molecule with these small but finite obstacles is a scaled down version of the cylinder study in Chapter 6. Deformation of DNA molecules from the obstacle-induced field gradients is intimately linked to hook formation. This is a strong indication that the fate of an *individual* colliding DNA on a finite size obstacle depends on its deformation in an extensional field.

To test this hypothesis we directly measure P_{hook} experimentally using the impact ensemble $|b| < R_{\text{obs}} + R_g$ and various electric fields, defining a hooking collision as any collision in which the DNA molecule is simultaneously present in all four quadrants of our obstacle-centered coordinate system. Figure 7-4 (a) shows the results of P_{hook} as a function of the impact parameter and De for collisions of λ DNA into obstacles with R_{obs}=0.8 μm. The impact parameter results are scaled by the y-component of the radius of gyration R_{gy}. For limiting behavior, we include simulation results of a point obstacle collision ($R_{\text{obs}}/R_g \ll 1$)[1]. Note that the hooking probability is significantly lower than in the point obstacle limit and increases as De increases. In the point obstacle limit, P_{hook} is *purely geometric*, dependent only on the DNA coil size. However, because P_{hook} increases with

---

[1] We create ensembles of 500 bead-spring chains (30 beads connected by worm-like springs [176]) to model λ DNA, and displace each chain's center-of-mass y-coordinate to $+b$ (recall y_{obs}=0). If any bead in a chain has a y-coordinate ≤ 0, then this configuration is considered a hook. Results agree with dynamic simulations of [12].

De, a dynamic effect underlies hook formation for finite-sized obstacles ($R_{\rm obs}/R_g > 1$), a result not predicted by any previous models.

To probe the impact dynamics at large De, we employ a Brownian dynamics simulation technique [33, 176]. Figure 7-4 (b) shows $P_{\rm hook}$ as a function of b/R_g using a bead-spring chain (30 beads connected by worm-like springs [176]) and an insulating obstacle. As De increases above De$\sim$ 40, we observe saturation of $P_{\rm hook}$ below the point obstacle limit. At such strong strain rates, a coil affinely deforms into folded or kinked configurations whose average extension as a function of accumulated strain saturates and becomes independent of De for De$>$ 40 [170, 171]. Therefore, because elongation and hooking are intimately linked, we conclude that in the regime where $R_{\rm obs}/R_g > 1$ and $0.5 <$ De < 40 we expect a *field-dependent* and *length-enhanced* hooking probability. By *length-enhanced* we mean that, for a given E and $R_{\rm obs}$, larger molecules are more likely to form hooks not only due to their larger cross-section, but also due to field-gradient stretching effects (larger De). A field-dependent hooking probability is not completely evident at first glance given that these obstacles are much smaller than the DNA's contour length. However if $R_{\rm obs}/R_g \sim 1$ and De > 0.5, the obstacle will induce extensional deformation.

Though we have clearly shown that field gradients can enhance the hooking probability, we have not been able to show how to predict $P_{\rm hook}$ on finite size obstacles *a priori*. To do so requires a non-equilibrium statistical mechanics treatment of a polymer in an extensional field, *e.g.* [183], a problem that has not been solved far from equilibrium. Nevertheless, this analysis obtains the two governing dimensionless groups as well as the limiting behavior, so that empirical or approximate methods may be used to predict $P_{\rm hook}$ in the future.

7.3.2 $P(t_H)$: Unhooking time distribution

Hooking events result in order of magnitude longer hold-up times than roll-offs, and as we have just seen, have a length dependent probability of formation. Furthermore, the hold-up time for hooking events is length dependent. Here we put roll-offs aside and study hooking collisions in more detail.

Unhooking time distributions: Figure 7-5 shows the unhooking time probability distributions $P(t_H/\langle t_H\rangle)$ for λ DNA at Pe=2 and 8 and T4 at Pe=8. We overlay the unhooking time distribution obtained by the simulations of André *et al.* [1] of fully extended rope-like DNA unhooking from a point-like obstacle with an initial Gaussian distribution of the difference in arm lengths x_o. This overlay was initially attempted for comparison, not because we expected agreement. Real collisions include effects from the finite obstacle size, impact parameter offset, and complex unraveling dynamics that all are not included in the simulation. However, despite the many real complexities, we see that all three $P(t_H/\langle t_H\rangle)$ distributions are close to the simplified simulation model result. We do note that the experimental results are skewed toward shorter collision times, likely due to off-center impacts present in the experiments. Furthermore, these experimental distributions have longer tails at high collision time, an effect that is magnified at high Pe. These long-time events correspond to collisions that form symmetric arms so that fluctuations in the arm length are important to the DNA's release. At high Pe, fluctuations of tethered chains significantly decrease in magnitude [45] so that metastable U-shaped configurations can have a "long" lifetime. Despite the similarities of these scaled collision time distributions with the simulation results, we do not anticipate that the simulation and experimental values and scalings for $\langle t_H\rangle$ to agree. However

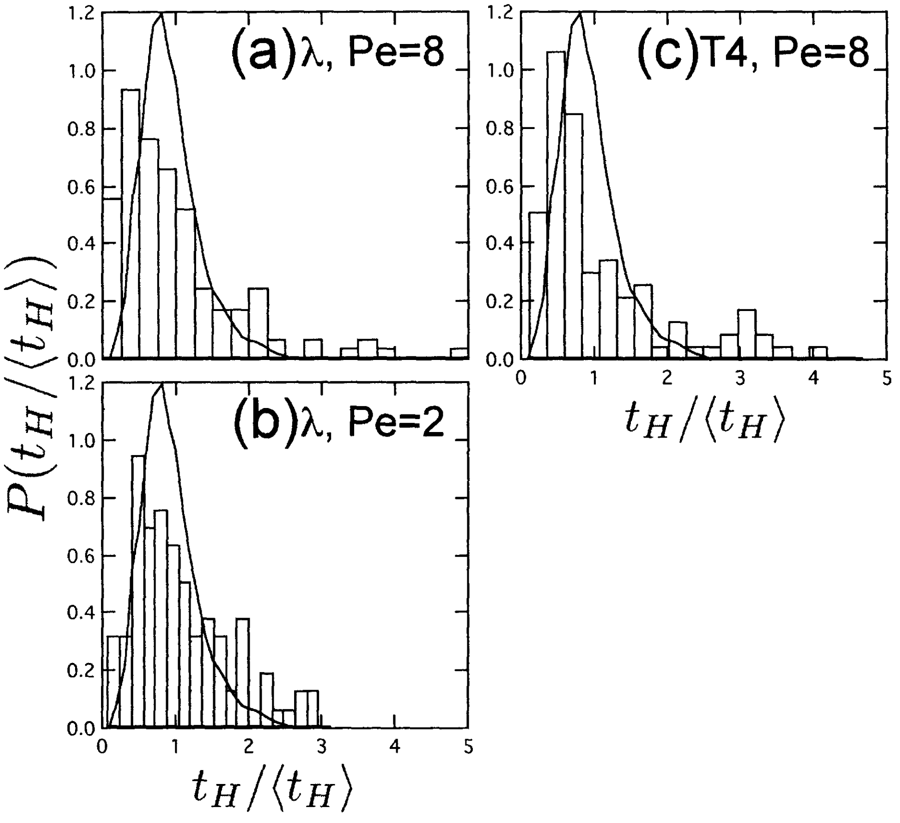

Figure 7-5: Hooking probability distributions. (a) λ DNA at Pe=8, (b) λ DNA at Pe=2, and (c) T4 DNA at Pe=8. The line is the result from André *et al.*'s [1] simplified simulations.

the unexpected similarities in the distribution functions do raise an important question. Is there a unique way to model the complex unhooking behavior observed experimentally that agrees with idealized models presented previously? To answer this, we must probe deeper into study of a single collision and examine *individual* DNA configurations during unhooking.

Hooking collision classes: Figure 7-6 shows experimental images of different T4 molecules hooking on a single obstacle at Pe=8. Hooking collisions can be classified into four general categories named for their shape: U, J, W, and X (for "extending") collisions. U and J collisions have a relatively constant extension ($x_{\text{ex}} = x_1 + x_2 \sim$ constant) during the unhooking process and behave like a rope on a frictionless pulley. This constant extension, which we term $\mathcal{L}$, depends on Pe. These are the types of ideal collisions observed in previous studies. The main distinction is that U collisions (Fig. 7-6 (a)) have nearly symmetric arms so that arm length fluctuations are important to consider when modeling the unhooking time. W collisions (Fig. 7-6 (c)) are collisions that result in entangled configurations upon impact with the obstacle (see Fig. 7-6 (c) inset). Quite often they result from the two ends of the DNA ending up on the same side of the obstacle after impact. X collisions (Fig. 7-6 (d)) are those with a long arm that is still extending while the short arm begins to retract.

For now we do not distinguish between U and J collisions, leaving this for the modeling section.

Table 7.1: Summary of hooking collision classification results.

(DNA, Pe)	U/J	X	W
(λ, Pe=2)	83%	17%	0%
(λ, Pe=8)	43%	57%	0%
(T4, Pe=8)	29%	60%	11% (5% metastable)

We distinguish the U/J collisions from the X collisions simply based on their total extension when the short arm begins to retract; U/ J collisions have $x_{\text{ex}} = \mathcal{L}$ whereas X collisions have $x_{\text{ex}} < \mathcal{L}$. We determine $\mathcal{L}$ at a given Pe by taking the average of x_{ex} for only hooking events that result in symmetric arms ($\mathcal{L} = \langle x_{\text{ex}} \rangle_{\text{symmetric}}$). Obviously there will generally be some spread in the extension data, so we empirically classify molecules with x_{ex} within 10% of $\mathcal{L}$ to be a U/J collision. $\mathcal{L}$ is approximately equal to the extension derived from empirical master curves for equilibrium tethered DNA in uniform flows and fields in Refs. [45] and [46].

Figure 7-7 shows an example comparison of (a) a U/J collision (data from the molecule shown in Fig. 7-6 (a)) with (b) an X collision (data from the molecule shown in Fig. 7-6 (d)). Both plots show the lengths of the short arm, long arm, and total extension (nondimensionalized by $\mathcal{L}$) during the unhooking process; similar plots to Fig. 7-7 (a) were presented in Refs. [96] and [11]. Although we present only one example of each collision type's arm length trajectory, we note that universally: 1) U/J collisions have a relatively constant total extension ($(x_1(t)+x_2(t))/\mathcal{L} \sim 1$) with exponential growth/decay of the two arms and 2) X collisions have $(x_1(t)+x_2(t))/\mathcal{L} < 1$, and that $(x_1(t) + x_2(t))/\mathcal{L}$ grows for the duration of the unhooking process. Furthermore, the long arm of X collisions tends to grow linearly, leading to the conclusion that the long arm of an X hook is *still extending* in the uniform field even while the short arm retracts. We will return to Fig. 7-7 to discuss model predictions of the arm length dynamics.

For the T4 DNA at Pe=8 (Fig. 7-6), 60% of the hooking collisions were X collisions, 29% were U/J collisions, and 11% were W collisions. About half of the W collisions are *metastable*, meaning that they eventually unravel into one of the other collision classes before the molecule unhooks. The other half quickly disengage from the obstacle. Table 7.1 summarizes our classification results for the three main studies of Fig. 7-5. We see that the number of X collisions grows with Pe, which makes sense since they result from incomplete extension of the long arm. At high Pe, tensions grow nonlinearly in the short arm that can lead to quick retraction, whereas at low Pe, thermal energy has a greater effect on stabilizing asymmetric configurations. This result suggests that infinite-Pe rope-on-pulley models may not be as applicable to experiments since most collisions will be X collisions. The number of W collisions grows with size and is presumably a function of R_{obs}/R_g. This makes sense since at small R_{obs}/R_g configuration folds are more likely to wrap around both sides of the obstacle. We note however, that in the point obstacle limit, the simulations of Ref. [12] appear to show only a small percentage ($< 5\%$) of W collisions.

We can draw an analogy between the formation the these characteristic unhooking configurations with the extension of a polymer in an extensional field: both processes require dynamic restructuring of a complex and kinked Gaussian thread during a strong deformation process. Much like the effect of molecular individualism on the stretching results in an extensional field (Chapter 2), we

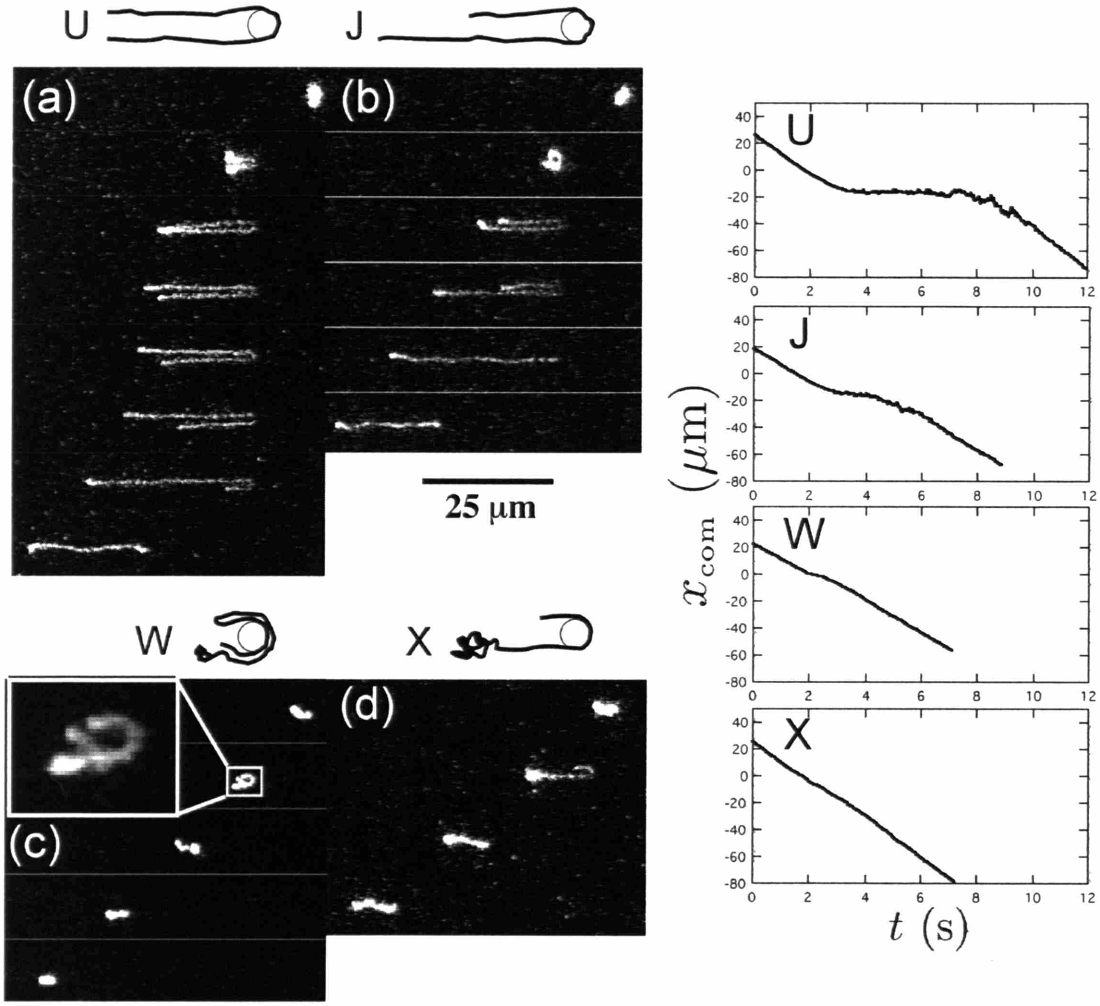

Figure 7-6: Types of hooking collisions (T4 DNA at Pe=8). (a) U symmetric hooks, (b) J asymmetric hooks, (c) entangled W hooks and (d) continuously extending X collisions. Images in each series are separated by 1.33 s. The plots to the right of the DNA images correspond to the x-component of each DNA's center of mass trajectory.

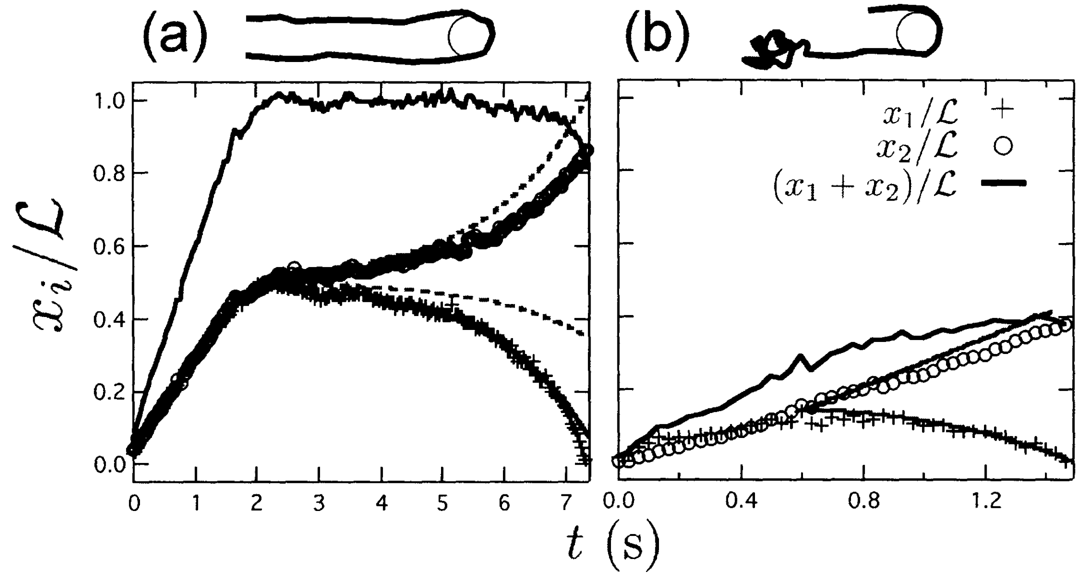

Figure 7-7: Comparison of U/J collisions to X collisions. Characteristic trajectories of x_1, x_2, and $x_{\mathrm{cx}} = x_1 + x_2$ scaled by the constant U/J extension $\mathcal{L}$ for (a) a U/J collision and (b) an X collision (T4 molecules at Pe=8; the same ones showed in Fig. 7-6 (a) and (d)). All red lines correspond to the model predictions for $x_1(t)$ and $x_2(t)$ ((a) J model (b) X model). In (a), the choice of the model initial condition was varied (dashed line at $x_1(t = 2.3 \text{ s})/\mathcal{L} = 0.492$ and solid line at $x_1(t = 4.4 \text{ s})/\mathcal{L} = 0.438$) .

anticipate these collision types to be highly dependent on the impacting DNA's initial configuration. However, as in extensional flows, classification of collision types is more powerful than a qualitative observation, as it can lead to quantitative conclusions. Specifically, the resulting collision times will be different for each class of collision types. The center of mass trajectories for each example collision in Fig. 7-6 give a feel for this, as U collisions tend to have very long collision times, while X collisions can have very short times. Knowledge of how long it takes these hooked configurations to unhook can lead to useful predictive models of a macroscale separation process.

7.4 Collision time models

In this section, we develop and test mathematical models for the unhooking process. These models will only be for U, J, and X collisions and will not consider the more unpredictable but rare W collisions. Three trapping time models will be presented: a deterministic model for constant extension chains (J model), a deterministic model for extending chains (X model), and a model for configurations fluctuating around constant extension (Fluctuation model). The goal will be able to predict the first two moments of the collision time distribution, though as we will show, the second moment will only be examined approximately.

In the following analysis, friction on the obstacle will be considered negligible because thermal

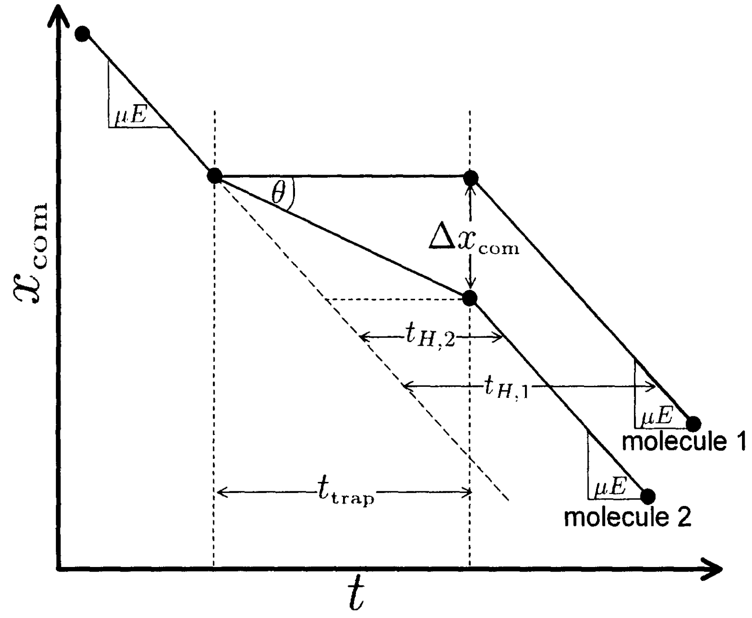

Figure 7-8: A schematic of typical center of mass traces for two molecules with the same time spent hooked on the obstacle t_{trap}. Molecule 1 has an immobile center of mass during t_{trap} whereas molecule 2's center of mass moves during t_{trap}. The center of mass hold-up times (as would be measured experimentally) are $t_{H,1}$ and $t_{H,2}$ respectively. Both before and after hooking on the obstacle, the molecules move at velocity μE.

fluctuations ensure the DNA thread is not pinned against the solid surface [184]. This is a well-accepted assumption [7]. Furthermore, we will initially assume the the total hold-up time for the center of mass t_H is dominated by the trapping time on the obstacle t_{trap}. This last approximation implies the DNA's center of mass is immobile during the unhooking process. This is a very good approximation for U/J collisions (see center of mass trajectories in Fig. 7-6 (a)-(b)) but not for X collisions (Fig. 7-6 (d)). This last point is most easily demonstrated graphically in Fig. 7-8. Here we show typical center of mass traces of two molecules, labeled "molecule 1" and "molecule 2", with the same trapping time t_{trap}, *i.e.* with the same time spent hooked on the obstacle. The center of mass of molecule 2 continues to move down field during t_{trap} whereas molecule 1 is immobilized. Consequently, the center of mass hold-up time for molecule 2 is less than that for molecule 1 ($t_{H,2} < t_{H,1}$). The difference in hold-up times can be computed geometrically as $t_{H,1} - t_{H,2} = \Delta x_{\text{com}}/(\mu E)$, where Δx_{com} is the distance the center of mass of molecule 2 moves during t_{trap}. X collisions have a large portion of DNA mass in a moving "ball" at the end of the long arm, and consequently they generally behave like molecule 2. The offset angle from horizontal (θ) of the center of mass trace during t_{trap} is generally nonzero. Conversely, U/J collisions generally show $\theta \sim 0$ so they behave like molecule 1. In the following unhooking modeling sections, we will keep in mind these differences.

Unhooking physics: Before we introduce unhooking models, we first ask what is the governing physics driving the unhooking. At first glance, it is clear that unhooking is driven by asymmetry in the arms; the longer arm will naturally pull the shorter arm around and off of the obstacle. One might first consider a quasi-steady equilibrium model where the force at the obstacle pivot point is a balance between the tension of two tethered chains in a uniform field at equilibrium. As mentioned earlier in this thesis, tethered DNA in a uniform field [46] or flow [45] has been studied previously. These studies confirm that the fractional extension of a tethered chain at equilibrium is a universal function of $\eta(\mu E)L^{\gamma}$ where η is viscosity and $0.54 < \gamma < 0.75$ [45, 52]. Consequently, for competing quasi-equilibrium tethered chains with different number of monomers N_i in each arm, we would expect two different fractional extensions on either side of the obstacle. The equilibrium tensions in these two arms would then be very different and discontinuous at the pivot point, as the worm-like chain force law is a nonlinear function of fractional extension. A schematic of this situation is presented in Fig. 7-9 (a). Furthermore, Fig. 7-9 (b) shows the anticipated theoretical tension distribution in a tethered worm-like chain in a uniform field, using Eqs. 7 and 23 from Ref. [44]. Along with a single tethered T4 configuration (solid black), three types of hooked configurations of T4 are presented (N_i=number of monomers in arm i, N_{T4} is total number of monomers in T4): $N_1 = N_2 = N_{T4}/2$ (red), $N_1 = N_{T4}/3$ (blue), $N_1 = N_{T4}/10$ (green dashed). It is clear that for asymmetric collisions, the tension at the pivot point ($n = j$) can be orders of magnitude different for *equilibrium* tethered arms. Such a drastic tension gradient at the pivot point is unlikely and an alternate viewpoint is needed.

We do know that a subset of hooking collisions achieve constant extension $\mathcal{L}$. However we must first ask, why do some of the DNA have a constant extension during unhooking? We can imagine a limit in which this is true. If the molecule unhooks on a time scale much shorter than the stress relaxation time, the tension profile in each arm can be thought of as frozen, and it would exhibit dynamics of a *constant extension rope* [11]. As a consequence, the location of maximum tension at the start of unhooking would move onto and then down the long arm over time. This is obviously an oversimplification, and in fact we know that trapping times are often longer than the longest stress relaxation time ($t_{\text{trap}} > \tau$). However this picture may capture the important physics of the chain release. In fact, the simulations of Sevick and Williams showed that the position of maximum stress does shift onto the long arm of the DNA during unhooking [11]. Furthermore, even if the tension distribution does shift during the unhooking process, bead-rod simulations show that because of non-linear elasticity, very large changes in stress can result from very small shifts in a stretched configuration [185]. Therefore, the first order model for an unhooking DNA is to consider an unhooking chain of constant length; we will consider both complete extension (L) and moderate extension ($\mathcal{L}$). We will term a model with constant extension the "J model" since it likely best describes J collisions. The J model is based on previously proposed full extension "rope-on-pulley" models [7, 11, 96].

J model: Previously, a collision model based on rope-on-pulley dynamics was used to model fully-stretched DNA unhooking at high fields [7, 96]. The unhooking driving force is $\lambda E x_o$ where λ is a phenomenological charge per length driving DNA unhooking and x_o is the difference in *contour length* of the two arms. Choosing a linear driving force may seem somewhat arbitrary at first glance given that DNA and other polymers have nonlinear elasticity at full extension. Consequently, we will go through a detailed derivation of the driving force using a bead-spring picture, and then more generally apply results to moderately extended chains.

Figure 7-9 (c) shows a schematic of the bead-spring polymer hooked on an obstacle. First, in agreement with previously proposed rope-on-pulley models, we will consider a chain stretched to its full contour length so that $x_1 + x_2 = L$. At the small length scale of a DNA persistence length, inertia is negligible so that the forces on a small piece of the DNA sum to zero. Consequently,

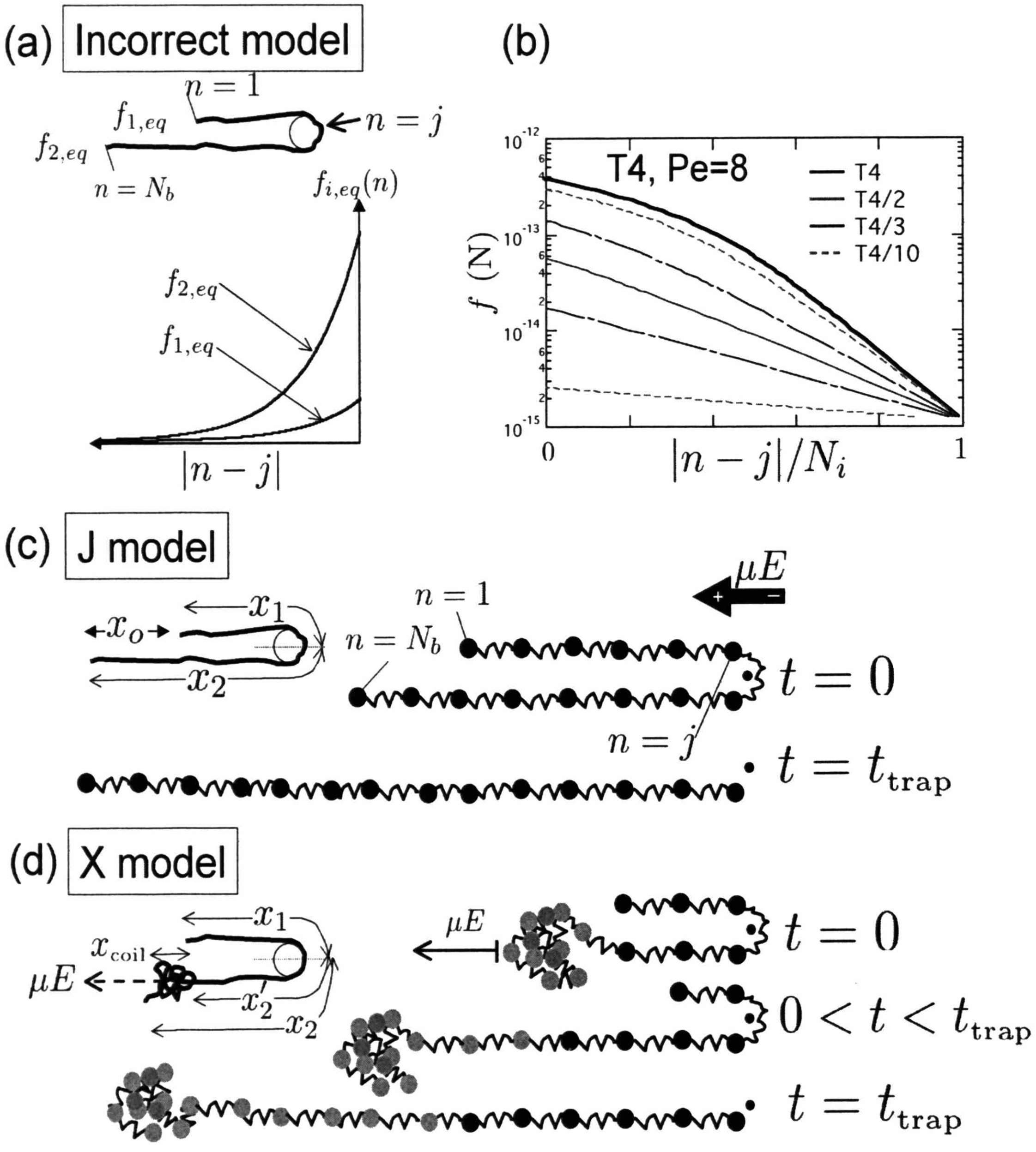

Figure 7-9: Model schematics at the onset of unhooking. (a) Diagram for an unhooking model based on competing arms at equilibrium fractional extension. Included is a schematic of the resulting tension distributions in this scenario with $n = j$ at the pivot spring. (b) Theoretical tension distribution in a tethered DNA chain at E=8.6 V/cm (corresponds to Pe=8 for T4 DNA) as a function of the dimensionless monomer number $|n - j|/N_i$, where N_i is the number of monomers in arm i. The lengths shown in the legend correspond to the number of monomers in a short arm of hooked T4 DNA. For each short arm, the corresponding long arm is shown in the same color/line type at a higher force. (c) Schematic for the constant-extension J model. (d) Schematic for the variable extension X model with an extending long arm.

in the bead-spring picture of polymer dynamics, the velocity of one bead of a tethered chain in a uniform electric field without intra-chain hydrodynamic interactions and without solvent-induced Brownian forces is:

$$\frac{d\mathbf{x}_n}{dt} = \frac{1}{\zeta_n}\mathbf{T}(\mathbf{x}_n) + \mu\mathbf{E} \tag{7.2}$$

where ζ_n is the bead drag coefficient, and for the n^{th} bead, $\mathbf{x}_n$ is the position vector, $\mathbf{T}(\mathbf{x}_n)$ is the force due to gradients in tension along the polymer, and $\mathbf{E}$ is the imposed electric field. See Eq. 6.1 for the more general situation. Neglecting long-range bead-bead hydrodynamic interactions is a good approximation for a stretched polymer in a thin slit [98], and ignoring Brownian forces is a good approximation for Pe≫1 for asymmetric hooked configurations. We will relax this last assumption later. The net spring force at bead n is $\mathbf{T}(\mathbf{x}_n) = \mathbf{T'}_n + \mathbf{T}_n$ where $\mathbf{T'}_n$ is the force from the spring connecting bead n to bead $n+1$ and $\mathbf{T}_n$ is the force from the spring connecting bead n to bead $n-1$. Note that $\mathbf{T'}_n = -\mathbf{T}_{n+1}$ except for the special case at the pivot spring j where $\mathbf{T'}_j = \mathbf{T}_{j+1}$. Also note that $\mathbf{T}_1 = \mathbf{T'}_{N_b} = 0$, where N_b is the total number of beads[2]. We can sum the force balance equations (Eq. 7.2) for the short arm and long arm of the hooked bead-spring chain. Assuming the the chain moves "rope-like", *i.e.* all sections move at the same velocity (dx_1/dt for the short arm and dx_2/dt for the long arm), we compute 1) for the short arm:

$$\begin{gathered}\sum_{n=1}^{j}\left[\zeta_n\left(\frac{d\mathbf{x}_n}{dt} - \mu\mathbf{E}\right) = \mathbf{T'}_n + \mathbf{T}_n\right] \\ j\zeta_n\left(\frac{dx_1}{dt} - \mu E\right) = -T'_j\end{gathered} \tag{7.3}$$

and 2) for the long arm:

$$\begin{gathered}\sum_{n=j+1}^{N_b}\left[\zeta_n\left(\frac{d\mathbf{x}_n}{dt} - \mu\mathbf{E}\right) = \mathbf{T'}_n + \mathbf{T}_n\right] \\ (N_b - j)\zeta_n\left(\frac{dx_2}{dt} - \mu E\right) = -T'_j\end{gathered} \tag{7.4}$$

We have moved to a 1D description where $\mathbf{T'}_j = \mathbf{T}_{j+1} = -T'_j\mathbf{e}_x$ and $\mathbf{e}_x = \mu\mathbf{E}/|\mu\mathbf{E}|$. Note that the details of the tension distribution in each arm are not important at this point because the only surviving tension terms in these above two equations are from the pivot point spring j. These equations (Eqs. 7.3 and 7.4) can be subtracted, and using $dx_1/dt = -dx_2/dt$ (constant velocity), they yield the governing equation for unhooking:

---

[2] Note the difference between N, the theoretical number of Kuhn lengths, and N_b, the number of beads in the bead-spring model. $N = L/l_k$ and $N_b = \mathcal{L}/l_s$, where l_s is the average spring length.

$$\frac{dx_1}{dt} = -\mu E\left(1 - \frac{2x_1}{L}\right) \tag{7.5}$$

The model trapping time is found simply by integrating from $t = 0$ to t_{trap} and $x_1 = x_1(0)$ to 0:

$$t_{\text{trap}}(x_1(0)) = -\frac{L}{2\mu E}\ln\left(1 - \frac{2x_1(0)}{L}\right) \tag{7.6}$$

Assuming a uniform distribution of $x_1(0)$, this model gives[3] $\langle t_{\text{trap}}\rangle = L/(2\mu E)$ which scales as N/E. At full extension, we also know that $x_2 - x_1 = x_o$ and $dx_o/dt = 2dx_1/dt$ [7]. By making this substitution in Eq. 7.5, one arrives with the governing equation used in Refs. [7, 11, 96] with a linear driving force: $\frac{dx_o}{dt} = 2\mu E x_o/L = 2\lambda E x_o/\zeta$ where λ is the phenomenological charge per length and ζ is the molecule's drag coefficient. We have shown here that $\lambda = \mu\zeta/L$ for a fully extended chain. We mentioned that previous work applied this model to Rouse simulations and ideal unhooking observations of U/J collisions at high fields, generally with good agreement. However it needs to be adjusted for our experiments because the DNA do not completely stretch, and some collisions (X collisions) do not have a constant extension. We will consider the modification of finite-Pe moderate stretching first.

The analysis for a constant-extension, *moderately* stretched DNA [11] is essentially the same as the fully stretched model derived above with an alternate average spring length l_s (so that $N_b l_s = \mathcal{L}$ and altered boundary limits $(0 < x_1 < \mathcal{L}/2)$. A sum of bead forces on each arm will give equations equivalent to Eqs. 7.3 and 7.4, yielding the governing equation:

$$\frac{dx_1}{dt} = -\mu E\left(1 - \frac{2x_1}{\mathcal{L}}\right) \tag{7.7}$$

To arrive at Eq. 7.7 we used the relation $j/N = x_1/\mathcal{L}$. The finite-Pe J model trapping time is then:

$$\begin{aligned} t_{\text{trap}}(x_1(0)) &= -\frac{\mathcal{L}}{2\mu E}\ln\left(1 - \frac{2x_1(0)}{\mathcal{L}}\right) \\ &= -\frac{\tau_c}{2}\ln\left(1 - \frac{2x_1(0)}{\mathcal{L}}\right) \end{aligned} \tag{7.8}$$

where $\tau_c = \mathcal{L}/(\mu E)$. Also note that $\langle t_{\text{trap}}\rangle = \tau_c/2$ for a uniform $x_1(0)$ distribution, so that the average trapping time scales as N^γ/E where γ is the empirical power-law exponent for stretching tethered chains at finite Pe $(0.54 < \gamma < 0.75)$ [45].

---

[3] The J model predicts an infinite trapping time for a symmetric hook with $x_1(0) = L/2$. This makes sense since unhooking is driven by asymmetry. However, this singularity is integrable and it can even be made finite by adding fluctuations.

Table 7.2: Summary of hooking collision parameters and results.

DNA, Pe	E (V/cm)	μE (μm/s)	$\mathcal{L}$ (μm)	$\tau_c = \mathcal{L}/(\mu E)$ (s)	$\tau_c^{\exp}$ (s)	$\langle t_H \rangle$ (s)
λ, Pe=2	5.2	8.8	6.6	0.75	0.93	1.2
λ, Pe=8	23.4	40	13	0.33	0.36	0.22
T4, Pe=8	8.7	14.7	45	3.1	3.0	1.8

Like a chain at full extension, this model also predicts that the long and short arms respectively grow and decay exponentially with time. The general solutions are $x_i(t) = \mathcal{L}/2 + (x_i(0) - \mathcal{L}/2)\exp(2t/\tau_c)$ for $i = 1, 2$. These model predictions are plotted in Fig. 7-7 (a) for two sets on initial conditions. The red dashed line begins when $x_1/\mathcal{L}$ achieves its maximum value, whereas the solid red line begins later in the unhooking process when the arms are clearly asymmetric. We see that the dashed line does not nicely fit the data, however the solid line does well at later times. The dashed line does a poor job because this configuration is unhooking from a highly symmetric configuration ($x_1/\mathcal{L}$=0.492 at maximum). The unhooking time becomes infinite as $x_1(0)/\mathcal{L} \to 1/2$ and arm length fluctuations are likely important to consider, thereby making the dynamics stochastic instead of deterministic. However, when applied to a clearly asymmetric starting configuration, *e.g.* the solid red line in Fig. 7-7 (a), the J model nicely predicts the arm length dynamics. We will return to this point later when we introduce fluctuations into the unhooking model.

We also note that the difference in arm lengths x_o grows exponentially during the unhooking process [7]:

$$x_o(t) = x_o(0)\exp\left(\frac{-2t}{\tau_c}\right) \tag{7.9}$$

and the time constant τ_c will depend on the extension.

This trapping model requires two experimentally observable parameters (μE and $\mathcal{L}$) (discussed in previous sections) and one parameter derived from these ($\tau_c = \mathcal{L}/(\mu E)$). However, our determination of τ_c can be *independently double-checked* using the experimental data. To check τ_c we track $x_o(t)$ for 5 symmetric U collisions, fit exponentials in the form of Eq. 7.9 to the data (after $x_1/\mathcal{L} < 0.45$, where we showed that the J model nicely describes arm dynamics), and then average the fitted time constants to get $\tau_c^{\exp}$. Table 7.2 summarizes our measurements as well as average hooking time results. The values of $\tau_c^{\exp}$ scale closely with $\mathcal{L}/(\mu E)$ (more so at higher Pe). We also note that the measured $\mathcal{L}$ values are very close to values derived from empirical master curves for tethered DNA in uniform flows and fields of Refs. [45] and [46]. Note that the J model of Eq. 7.8 is not expected to model collisions with variable extension during unhooking. The difference between $\langle t_H \rangle$ and the model prediction $\tau_c/2$ may then be expected at Pe=2 due to the importance of arm fluctuations at low Pe. However, the experimental $\langle t_H \rangle$ values are approximately $\tau_c/2$ for Pe=8, even though these ensembles contain many X collisions. The close agreement at Pe=8 suggests that X collisions and U/J collisions have similar characteristics to first order and may be why $P(t_H/\langle t_H \rangle)$ looks so similar to results of simple simulations. This similarity is further probed by comparing measured t_H values to model predictions.

We compare the J model to our experimental data in two ways: first plotting the measured hold-up time t_H versus $x_o(0)$, and second plotting t_H versus $x_1(0)$. We expect Eq. 7.8 to nicely describe U/J collision unhooking time as a function of $x_1(0)$. Similarly, using the relation $\mathcal{L} - 2x_1(0) = x_o(0)$ for a constant-extension unhooking chain, Eq. 7.8 can be rewritten as:

$$t_{\text{trap}}(x_o(0)) = -\frac{\tau_c}{2}\ln\left(\frac{x_o(0)}{\mathcal{L}}\right) \tag{7.10}$$

which would predict hold-up times for U/J collisions as a function of $x_o(0)$. For comparison of the model to our data, we have split our ensemble into U/J collisions (solid circles), X collisions (open boxes), and W collisions (crossed boxes). To obtain $x_o(0)$ and $x_1(0)$, we measure the distance between the two arms at the instant the short arm begins to retract and the short arm length respectively. Figure 7-10 (a)-(c), shows the experimental collision times versus $x_o(0)$ and Fig. 7-10 (d)-(f) shows the same data plotted against $x_1(0)$. Figure 7-10 (a)-(c) clearly shows that the J model for a moderately extended DNA (Eq. 7.10) does nicely predict the collision times of many observed constant-$\mathcal{L}$ U and J collisions. The observed collision times are dispersed around the model prediction, likely due to thermal fluctuations of the arms. However, as expected, it is obvious that the model cannot predict the collision time of the many X (and possibly W) collisions. Since W events are rare, we neglect them in the bulk of the remaining discussion. It is striking though that Fig. 7-10 (d)-(f) shows that the *constant extension* J model nicely describes *all the observed data* (except W's) when plotted against $x_1(0)$. The close agreement between the predicted unhooking time and all observed collision times indicates that the short arm mediates the unhooking process. We can explain this result by examining the anticipated tension distribution of the hooked DNA chain.

As mentioned above, we assume a U or J DNA molecule to have a constant extension while unhooking. This implies the the tension distribution is more or less frozen during the unhooking process. More likely there is a complex competition between stress relaxation and the electrical driving force. However, what is this tension distribution at the onset of unhooking? During the unraveling, the short arm will eventually reach quasi-equilibrium extension even if the long arm is still extending. Therefore we can imagine the short arm as an idealized tethered chain at equilibrium in a uniform field, however the long arm has a non-equilibrium tension profile. The slight imbalance in the growing tension of the long arm will then begin to pull the short arm around the obstacle. *Consequently, the magnitude of the "tethering force" T'_j during unhooking is set by the length of the short arm.* The main result is that a J collision and an X collision with the same short arm lengths can modeled to have approximately the same collision times.

X model: Because of this anticipated equivalence in X and J collisions with the same short arm length, we seek to model X collision trapping and hold up times to gain more insight. Our goal will be to show that an X collision model provides practical bounds on observed t_H values of X collisions as a function of $x_1(0)$ in the limit $x_1(0) \ll \mathcal{L}$, and conveniently, the J model bisects these bounds.

To model the unhooking time of an X collision, we adopt a new model that is only valid for collisions with small $x_1(0)$ and a large arm which continues to grow in length during a collision (Fig. 7-9 (d)). In these X collisions, we divide the chain into two idealized sections: 1) a freely electrophoresing

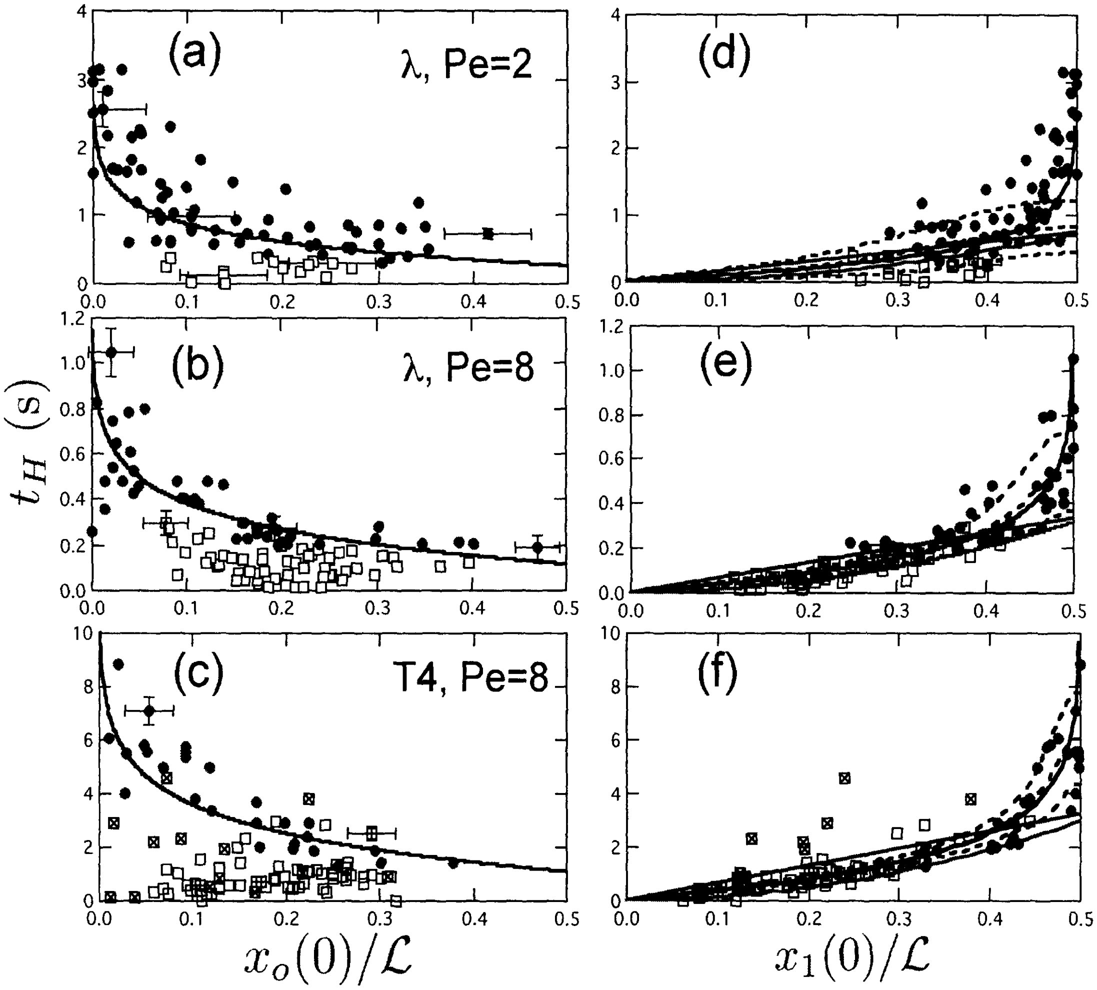

Figure 7-10: Experimental test of collision time models. (a)-(c) Plots of the collision time as a function of the difference in arm lengths x_o (scaled by the constant U/J extension value $\mathcal{L}$) at the onset of unhooking. U/J collisions are shown as solid circles and X or W collisions are shown as open squares. The black line on each plot is the J model for a chain at constant extension (Eq. 7.10). (d)-(f) Plots of the collision time as a function of the short arm length at the onset of unhooking (scaled by the constant U/J extension value $\mathcal{L}$). The black line in each plot is the rope-on-pulley model based on the short arm extension (Eq. 7.8), and the dashed lines are the predictions of the mean hooking time $\langle t_{\text{trap}} \rangle$ and standard deviation $\langle t_{\text{trap}} \rangle \pm \sigma$ from the diffusive fluctuation model with the first-passage time approximation (obtained from Eqs. 7.26 and 7.28). The red lines are the X model prediction for $t_{\text{trap}}(x_1(0))$ (Eq. 7.15) and the green lines are the X model prediction for $t_H(x_1(0))$.

chain and 2) a chain unhooking under tension. The end of the extending long arm can be thought of as a coil in free electrophoresis. We assume the coil to begin a distance $x_1(0)$ from the start of the long arm at $t = 0$ and x_{coil} is the size of the coil. This coil lays down contour length as it moves, thereby adding to the *time-dependent* length of the chain under tension; we denote the long arm length under tension as $x_2'(t)$ and $x_2(t) = x_2'(t) + x_{\text{coil}}(t)$. We have made this clear in Fig. 7-9 (d) by labeling beads that are initially in the coil with gray. We assume the long arm increases in length as fast as the field can move the coil so that $x_2(t) = x_1(0) + x_{\text{coil}}(0) + \mu E t$. The change in coil size will be much smaller than the change in the long arm length ($dx_{\text{coil}}/dt \ll dx_2/dt$), so that $dx_2/dt = dx_2'/dt$. Returning to Eqs. 7.3 and 7.4, we can sum the contribution from tension-bearing springs (all springs not in the leading coil). For the short arm:

$$j\zeta_n\left(\frac{dx_1}{dt} - \mu E\right) = -T_j' \tag{7.11}$$

and for the long arm:

$$\left(j(0) + \frac{\mu E t}{l_s}\right)\zeta_n\left(\frac{dx_2}{dt} - \mu E\right) = -T_j' \tag{7.12}$$

Recall l_s is the average spring length of the bead-spring model so $j(0) + \frac{\mu E t}{l_s}$ is the number of beads in the chain under tension if we assume $dx_{\text{coil}}/dt \ll dx_2/dt$. Using the constant arm velocity approximation ($dx_1/dt = -dx_2/dt$), the relations $j(0)l_s = x_1(0)$ and $jl_s = x_1$, and subtracting these two equations yields:

$$(x_1(0) + \mu E t + x_1)\frac{dx_1}{dt} = -\mu E(x_1(0) + \mu E t - x_1) \tag{7.13}$$

The governing equation of the X model (Eq. 7.13) is a nonlinear, nonautonomous differential equation. This equation can be nondimensionalized, using $\tilde{x}_1 = x_1/x_1(0)$ and $\tilde{t} = \mu E t/x_1(0)$:

$$\frac{d\tilde{x}_1}{d\tilde{t}} = \frac{-1 - \tilde{t} + \tilde{x}_1}{1 + \tilde{t} + \tilde{x}_1} \tag{7.14}$$

In this non-dimensional equation, all initial conditions map to $\tilde{x}_1(0) = 1$. $\tilde{x}_1(\tilde{t})$ falls as $\tilde{t}$ increases, from a slope of 0 to -1 until $\tilde{x}_1(\tilde{t}_{\text{trap}}) = 0$. Note that now the condition $\tilde{x}_1(\tilde{t}_{\text{trap}}) = 0$ is independent of the initial condition $x_1(0)$. Using Euler's method[4], we numerically solve for when $\tilde{x}_1(\tilde{t}_{\text{trap}}) = 0$ and find that $\tilde{t}_{\text{trap}} \sim 2.1$. This is a universal result for all initial conditions. Converting back to dimensional variables, we see that the trapping time is a linear function of the initial short arm length $x_1(0)$:

---

[4] A step size of $\Delta\tilde{t} = 0.001$ was used to obtain a convergent solution to Eq. 7.14.

$$t_{\text{trap}}(x_1(0)) \sim 2.1\frac{x_1(0)}{\mu E} \tag{7.15}$$

For this X model to be physically consistent, $x_1(0)/\mathcal{L} < 1/3.1$. If this condition fails, the coil completely unwinds during unhooking. We therefore stress that this model is most useful for small short arms.

The X model establishes that the short arm of the DNA governs the unhooking dynamics of X collisions. Observation of single DNA configurations during unhooking support this result. In all cases (except W's), even if the long arm is still extending, the short arm is clearly extended to a presumably quasi-equilibrium extension before the DNA begins to release. We can apply the numerical solution $x_1(t)$ for Eq. 7.13 to the observed T4 DNA X collision at Pe=8 in Fig. 7-7 (b). We plot this numerical solution, along with the X model prediction of $x_2(t) = x_1(0) + \mu Et$ in red in Fig. 7-7 (b) beginning at the maximum value of x_1 and using the same experimentally measured values of $\mathcal{L}$ and μE. The X model very nicely predicts the observed time dependence of both arms, though x_2 slightly drops below the idealized coil unwinding prediction of the model near the end of the unhooking time. Adding up the time from the maximum value of x_1 to when $x_1 = 0$, we extract an experimentally observed trapping time of 0.87 s. The X model predicts 0.9 s. However, the center of mass hold-up time was measured to be 0.43 s, a lower value than the observed trapping time because the leading coil moves the center of mass down field during unhooking (see Fig. 7-8 and refer to Fig. 7-6 (d)).

The anticipated center of mass hold-up time can be computed geometrically from Fig. 7-8 to be $t_H = t_{\text{trap}} - \Delta x_{\text{com}}/(\mu E)$, where Δx_{com} is the distance the center of mass moves down field during unhooking. We approximate the center of mass of the coil section of an X collision at the end of the long arm's rope section (x_2'). Consequently:

$$x_{\text{com}}(0) \simeq \frac{1}{N_b}\left(2j(0)\frac{x_1(0)}{2} + (N_b - 2j(0))x_1(0)\right) \tag{7.16}$$

and using $x_2'(t) = \mu Et + x_1(0)$ and Eq. 7.15:

$$x_{\text{com}}(t_{\text{trap}}) \simeq \frac{1}{N_b}\left(3.1j(0)\frac{3.1x_1(0)}{2} + (N_b - 3.1j(0))3.1x_1(0)\right) \tag{7.17}$$

Subtracting these two equations gives $\Delta x_{\text{com}} \simeq 2.1x_1(0) - 3.8x_1(0)j(0)/N$ where $j(0)/N (= x_1(0)/\mathcal{L})$ is the fraction of beads in the short arm at the onset of unhooking. Consequently, the X model center of mass hold up time is approximately $t_H \simeq 3.8\tau_c x_1(0)^2/\mathcal{L}^2$, which is 0.23 s for the T4 molecule in Fig. 7-7 (b). Thus by including the effect of the center of mass movement, the X model now underestimates the observed hold up time. We include both t_H and t_{trap} for the X model in Fig. 7-10 (d)-(f). Aside from the scattered W collisions, these model predictions appear to bound the experimental data. Consequently, the results for the X model t_H and t_{trap} provide empirical limits on hold up times. Looking at Fig. 7-10 (d)-(f), we can compare these X model results to the J model (Eq. 7.8). The J model nearly bisects the maximum time for a X collision (t_{trap}) and the predicted hold up time (t_H). Therefore, when formulated in terms of x_1, the constant extension J model can nicely predict t_H for even X collisions.

Fluctuation model: When evaluating the J model in Fig. 7-7 (a), it was clear that there is a transition from collisions that behave deterministically ("J", small-x_1) and collisions greatly affected by Brownian noise ("U", large-x_1). Motivated by the spread of data around the deterministic rope-on-pulley model predictions in Fig. 7-10, we now ask what is the difference between a U and a J collision? In the J-collision regime, one arm extends longer than the other does, so that the unhooking driving force ($\lambda E(\mathcal{L} - 2x_1)$) is much greater than the random forces from length fluctuations[5]. However, in the U-collision regime, the two arms extend to approximately the same length so that this driving force is of the same order as the thermal noise. Thus there exists a transition region where the unhooking driving force begins to dominate the random thermal fluctuations. To determine this region, we seek to investigate what happens when the chain hooks into a symmetric state. With no Brownian effects, the rope-on-pulley model predicts an infinite unhooking time, however, as we just saw, this singularity is integrable when determining $\langle t_H \rangle$. Obviously, at low Pe, Brownian effects may greatly influence collision time results. Hence it would be useful to develop a collision time model that includes the effect of DNA fluctuations on unhooking time. This method has already been attempted in Ref. [7] using diffusive fluctuation model and a rope-on-pulley first passage time approximation [186] for the unhooking time. We will continue along these lines and apply these ideas to the short arm model presented above.

We begin with the 1D Langevin equation governing unhooking of the DNA:

$$\zeta \frac{dx_1}{dt} = -\lambda E(\mathcal{L} - 2x_1) + f_R(t) \tag{7.18}$$

where $f_R(t)$ is a random white noise term satisfying $\langle f_R(t) \rangle = 0$ and $\langle f_R(t) f_R(t') \rangle = \sigma^2_{\text{noise}} \delta(t - t')$. We can then convert to the Fokker-Planck equation [187, 188], where $p(x_1, t|x_1(0), 0)$ is the probability the unhooking molecule has x_1 at time t, given that $x_1 = x_1(0)$ at $t = 0$:

$$\frac{\partial p(x_1, t|x_1(0), 0)}{\partial t} = \frac{\partial}{\partial x_1}\left(\frac{\nabla U}{\zeta} p\right) + 4D \frac{\partial^2 p}{\partial x_1^2} \tag{7.19}$$

where $\nabla U = \lambda E(\mathcal{L} - 2x_1)$ and $D = \sigma^2_{\text{noise}}/(2\zeta^2) \equiv kT/\zeta$ is the molecule's diffusion coefficient. With this approximation, we are modeling the fluctuations of the stretched DNA on the obstacle as diffusive noise. This is an obvious oversimplification and does not provide a physically meaningful scaling with E. A proper noise model would consider the dependence of the fluctuation distribution on Pe, for Ref. [45] clearly shows that the fluctuation magnitude for a tethered chain in a uniform flow decreases as E increases. However, this simple diffusive noise model will suffice as a first-order attempt to include the effect of fluctuations on unhooking time.

In order to see how the unhooking time depends on $x_1(0)$, Eq. 7.19 is written in the Adjoint Fokker-Planck form [186]:

---

[5] We will use the "driving force" notation here, recognizing that $\lambda = \mu\zeta/\mathcal{L}$ from the bead-spring derivation.

$$\frac{\partial p(x_1, t | x_1(0), 0)}{\partial t} = -\frac{\nabla U}{\zeta}\frac{\partial p}{\partial x_1(0)} + 4D\frac{\partial^2 p}{\partial x_1(0)^2} \tag{7.20}$$

Simplifying the notation in terms of a linear operator $L^+(x_1(0))$ gives:

$$\frac{\partial p}{\partial t} = L^+(x_1(0))p \tag{7.21}$$

with:

$$\begin{aligned} L^+(x_1(0)) &= -\frac{\nabla U}{\zeta}\frac{\partial}{\partial x_1(0)} + 4D\frac{\partial^2}{\partial x_1(0)^2} \\ &= 4D\mathrm{e}^{\frac{U}{4kT}}\frac{\partial}{\partial x_0(0)}\left(\mathrm{e}^{-\frac{U}{4kT}}\frac{\partial}{\partial x_0(0)}\right) \end{aligned} \tag{7.22}$$

The initial condition is that the molecule is hooked on the obstacle with some $x_1(0)$. The boundary conditions are reflective at $x_1(0) = \mathcal{L}/2$ (allows for switching of long and short arms of symmetric collisions), and infinitely reactive at $x_1(0) = 0$ (*i.e.* molecules are unhooked):

$$\begin{aligned} \text{initial condition: } & p(t=0) = 1 \\ \text{reflective b.c.: } & \frac{\partial p}{\partial x_1(0)}\,|_{x_1(0)=\mathcal{L}/2} = 0 \\ \text{reactive b.c.: } & p\,|_{x_1(0)=0} = 0 \end{aligned} \tag{7.23}$$

First passage solution: Knowledge of $p(x_1, t \mid x_1(0), 0)$ provides all the information required to study the fluctuating two-arm unhooking process. However, once $x_1 = 0$ for the first time, the molecule unhooks. Therefore first passage time analysis is relevant to simplify the solution. Note that $p(x_1, t \mid x_1(0), 0)$ is not conserved; we define $S(t, x_1(0))$ as the probability that a molecule initially on the obstacle with $x_1(0)$ is still on the obstacle at time t [189]:

$$S(t, x_1(0)) = \int_{\mathcal{L}/2}^{0} p(x_1, t \mid x_1(0), 0)dx_1 \tag{7.24}$$

The first passage time is defined as the time it takes to first reach $x_1 = 0$ when starting at $x_1(0)$. The first passage time distribution $f_{FPT}(t \mid x_1(0))$ can be related to both $p(x_1, t \mid x_1(0), 0)$ and $S(t, x_1(0))$:

$$\begin{aligned} f_{FPT}(t \mid x_1(0)) &= -\frac{\partial S(t, x_1(0))}{\partial t} \\ &= -\frac{\partial}{\partial t}\int_{\mathcal{L}/2}^{0} p(x_1, t \mid x_1(0), 0)dx_1 \end{aligned} \tag{7.25}$$

The average first passage time (first moment) can be found as:

$$\begin{aligned}\langle t_{\text{trap}}(x_1(0))\rangle &= \int_0^\infty t f_{FPT}(t \mid x_1(0))dt \\ &= \int_0^\infty S(t, x_1(0))dt\end{aligned} \tag{7.26}$$

The second moment is:

$$\begin{aligned}\langle t^2_{\text{trap}}(x_1(0))\rangle &= \int_0^\infty t^2 f_{FPT}(t \mid x_1(0))dt \\ &= -t^2 \int_t^\infty f_{FPT}(t' \mid x_1(0))dt' \mid_0^\infty + \int_0^\infty 2t\Big(\int_t^\infty f_{FPT}(t' \mid x_1(0))dt'\Big)dt \\ &= \int_0^\infty 2tS(t, x_1(0))dt\end{aligned} \tag{7.27}$$

So that the variance of the first passage time distribution is:

$$\begin{aligned}\sigma^2 &= \langle t^2_{\text{trap}}(x_1(0))\rangle - \langle t_{\text{trap}}(x_1(0))\rangle^2 \\ &= \int_0^\infty 2tS(t, x_1(0))dt - \Big(\int_0^\infty S(t, x_1(0))dt\Big)^2\end{aligned} \tag{7.28}$$

Solution: Directly calculating moments: Calculating the first passage time moments directly requires a solution for $S(t, x_1(0))$. Note an alternate method is presented in Appendix 7A. To obtain $S(t, x_1(0))$, we first integrate the adjoint Fokker-Planck equation (Eq. 7.20) over x_1, and using the definition of Eq. 7.24:

$$\begin{aligned}\int_{\mathcal{L}/2}^0 \frac{\partial p(x_1, t|x_1(0), 0)}{\partial t}dx_1 &= \int_{\mathcal{L}/2}^0 \Big[-\frac{\nabla U}{\zeta}\frac{\partial p}{\partial x_1(0)} + 4D\frac{\partial^2 p}{\partial x_1(0)^2}\Big]dx_1 \\ \frac{\partial S(t, x_1(0))}{\partial t} &= -\frac{\nabla U}{\zeta}\frac{\partial S}{\partial x_1(0)} + 4D\frac{\partial^2 S}{\partial x_1(0)^2}\end{aligned} \tag{7.29}$$

We then substitute $\nabla U = \lambda E(\mathcal{L} - 2x_1)$ and nondimensionalize using $\hat{t} = t/\tau_c$, and $\hat{x}_1 = x_1(0)/\mathcal{L}$ to obtain:

$$\frac{\partial S(\hat{x}_1,\hat{t})}{\partial \hat{t}} = (2\hat{x}_1 - 1)\frac{\partial S}{\partial \hat{x}_1} + 4\epsilon\frac{\partial^2 S}{\partial \hat{x}_1^2} \tag{7.30}$$

where $\epsilon = D\tau_c/\mathcal{L}^2$. In general, $\epsilon \ll 1$ so we are left with a singular perturbation problem[6]. By solving Eq. 7.30 numerically, and applying the solution of $S(\hat{x}_1,\hat{t})$ to Eqs. 7.26 and 7.28, we can solve for the first two moments of the first passage time distribution. Solutions for λ DNA at Pe=2 and 8 and T4 at Pe=8 are shown by dashed black lines in Fig. 7-10 (d)-(f). Except for the few W collisions for T4, the diffusive noise model captures the order of magnitude of the spread in collision time around the mean at Pe=8. Results are less ideal at Pe=2. Universal agreement is not expected because the model's fluctuation magnitude is independent of E. A more realistic model would account for both the N and E dependence of arm fluctuations, growing in strength with decreasing Pe. Despite this inadequacy, this noise model does provide insight into the transition from U to J collisions. The (boundary layer) region of U collisions grows as $\epsilon^{1/2} = \sqrt{D\tau_c}/\mathcal{L}$ in $x_1/\mathcal{L}$-space. When D is the molecule's diffusion coefficient, (though it is more generally a nonlinear function of N and E), the U region thickness scales as $N^{-\gamma}E^{-3/2}$ where γ is the empirical coefficient $0.54 < \gamma < 0.75$ to scale fractional extension of tethered DNA with N in uniform flows and fields [45, 52]. More realistic noise models should be pursued to obtain scalings for the second moment of $f_{FPT}(t \mid x_1(0))$, which enter into calculations of separation dispersion [181].

7.5 Conclusions and outlook

In this study, we systematically analyzed the dynamics of a uniform ensemble of DNA molecules hooking on a small post. We divided the ensemble into roll-offs and hooks and showed that obstacle-induced electric field gradients stretch DNA, so that in addition to two geometric parameters (R_{obs}/R_g and b/R_g), the hooking probability depends on a dynamic parameter (De). Hooking collisions can lead to size-dependent DNA separations, so we examined the unhooking dynamics which dominate the total hold-up time. We found that the unhooking distribution $P(t_H/\langle t_H\rangle)$ had a similar shape to the results of a simplified simulation of constant extension hooks. We classified the collisions and then developed models to predict the collision time. We found that the short arms governs the release dynamics and that X (extending) collisions and J collisions with the same short arm length have similar unhooking times. Consequently, we found that a rope-on-pulley model based on the short arm length dynamics of a constant extension chain can nicely predict the observed collision time data. By incorporating diffusive noise into this model, we saw that the U collision region, where fluctuations dominate unhooking, scales as $\sqrt{D\tau_c}/\mathcal{L}$ in $x_1/\mathcal{L}$-space.

Given the difficulty and labor required to perform these experiments, follow-up work would best be performed with simulations. Furthermore, simulations would allow researchers access to actual tension distributions in the hooked DNA arms. Finite element methods could be incorporated into a Brownian dynamics simulation of a bead-spring chain to investigate effects of obstacle size, geometry, and induced field gradients. Furthermore, more realistic noise models should be attempted with hopes of deriving analytical scalings for the dispersivity of macroscale separation models.

---

[6] This problem is characterized by a "thick" boundary layer, as its thickness scales as $\epsilon^{1/2}$, not ϵ [190, Sec. 9.4]. The boundary layer is essentially the thickness of parameter space where fluctuations dominate the unhooking dynamics.

Appendix 7A

In this section we briefly outline an alternate method to obtain the moments of the first passage time distribution.

Starting with the first moment:

$$\begin{aligned}\langle t_{\text{trap}}(x_1(0))\rangle &= \int_0^\infty t f_{FPT}(t \mid x_1(0))dt \\ &= \int_0^\infty S(t, x_1(0))dt\end{aligned} \tag{7.31}$$

we claim that all higher moments can be obtained from recurrence relations [189]. Define $\langle t^n(x_1(0))\rangle = \int_{\mathcal{L}/2}^{0} T_n(x_1, x_1(0))dx_1$ for $n > 0$ with $T_0 = \delta(x_1 - x_1(0))$. Then is is straightforward from Eqs. 7.25 and 7.26 to show:

$$T_n(x_1, x_1(0)) = \int_0^\infty t^{n-1} p(x_1, t \mid x_1(0), 0)dt \tag{7.32}$$

Because $\frac{\partial p}{\partial t} = L^+(x_1(0))p$, one can apply L^+ to both sides of Eq. 7.32 and simplify the right hand side to achieve a moment generating recurrence relation:

$$L^+(x_1(0))T_n(x_1, x_1(0)) = -nT_{n-1}(x_1, x_1(0)) \tag{7.33}$$

For $n = 1$, integration of both sides over x_1 gives:

$$L^+(x_1(0))\langle t_{\text{trap}}(x_1(0))\rangle = -1 \tag{7.34}$$

Returning to the moment recurrence relations, for $n = 2$:

$$L^+(x_1(0))\langle t^2_{\text{trap}}(x_1(0))\rangle = -2\langle t_{\text{trap}}(x_1(0))\rangle \tag{7.35}$$

Assuming these last two equations can be solved, analytical results for the first two moments of the first passage time distribution can be obtained. For our problem, an integral solution for the first moment may be obtained, however it must be solved numerically. Given that these recurrence relations lead to equations that require numerical solutions, we instead chose to numerically solve for $S(t, x_1(0))$ directly. However, this recurrence relation method would be more suited to obtaining analytical scalings for the second moment of the first passage time distribution.

Chapter 8

Uniform and Complete Stretching of DNA: entering an extensional field from a porous gel

Recall from Chapter 1 that the ability to controllably and continuously stretch large DNA molecules in a microfluidic format is important for gene mapping technologies such as Direct Linear Analysis (DLA) [25, 26]. We have already shown that electric field gradients can be readily generated in a microfluidic device and the resulting field is purely elongational. In addition, as we will show in this chapter, we are able to selectively pattern a porous crosslinked gel anywhere inside the microchannel. With an applied electric field, DNA molecules are entropically forced to reptate through the gel and they moderately stretch as they exit the gel. By placing a gel immediately in front of the hyperbolic contraction, we bypass "molecular individualism" and achieve highly uniform and complete stretching of T4 DNA. In this chapter, we present a single molecule fluorescence microscopy analysis of T4 DNA (169 kbp) stretching in the electric field gradients in a hyperbolic contraction with a porous gel placed at its entrance.

8.1 Linear mapping and engineering stretched DNA

Engineering DNA stretching processes and understanding the dynamics of DNA stretching are key steps in the development of the next generation of biological microfluidic (BioMEMs) devices.

Many current applications like criminal DNA "fingerprinting" and medical diagnostics rely on a very low resolution view of a DNA's gene map [2]. However, genetic information is inherently difficult to extract directly from DNA molecules because, in the size range of O[10 kbp] and above, they adopt "random coil" configurations. Thus, if certain gene locations can be tagged with a fluorescent probe, a detection device cannot accurately determine the linear distance between the respective genes along the DNA backbone. The coil must first be unraveled and stretched [25, 26]. Access to a long strand of stretched DNA has recently led to powerful applications for gene mapping [25, 26, 191–195].

Researchers have stretched tethered double-stranded DNA (dsDNA) with optical tweezers [54], uniform flows [45], and uniform electric fields [46]. However, tethering a DNA molecule is an involved and not easily integrated step in a process design. Consequently, research groups are trying to completely stretch free DNA in a microchannel. Some current techniques are flowing DNA through a channel contraction [25–27], forcing DNA into a nanochannel [195, 196], hydrodynamic focusing of multiple streams [197], dynamic combing onto a surface [191–194] , or applying an AC field to DNA in a gel [198, 199]. From an engineering perspective, it is most attractive to stretch DNA in a continuous process. One such promising application is direct linear analysis (DLA) [25–27], which entails binding probes to known sequences along the strand of DNA, stretching the molecule from a coiled to a linear conformation, and then directly measuring the distance between these probes continuously in-line. In current DLA designs, DNA is stretched by flow gradients as it moves through a channel contraction. However, more generally, a DNA macromolecule driven by any external field (e.g. a flow or an electric field) stretches in the presence of *strong field gradients*. These gradients may be induced by obstacles, channel contractions, or even surface modifications. Continuous stretching of DNA in field gradients has been studied in homogeneous hydrodynamic flows (like extensional flow [86, 89], shear [92], or mixed flow [93, 94]), and electric fields [152, 153, 169, 200][2]. As introduced in Chapter 6, the main problems to overcome in order to stretch DNA continuously are *shear* [26] and *"molecular individualism"* [86, 87].

Shear, which arises in fluid flows near any surface due the no slip condition, induces tumbling motion as opposed to strong extensional deformation [92]. In a pressure-driven flow microdevice with a high surface area to volume ratio, shear rates near walls can often be much higher than strain rates. As these DNA stretching devices move to the nanoscale it will be important to eliminate this surface induced shear, though as explained below, some "pre-shear" may actually be useful to aid stretching [91]. We showed previously [152, 153, 169] that *electrophoretic deformation* is purely elongational without any rotational components. Thus by using electric field gradients to stretch DNA, very high electrophoretic strain rates can be achieved in microdevices without any shear. Electric fields are also easily implemented by placing electrodes in reservoirs at the ends of the microchannel. Furthermore, they have the additional advantages over pressure driven flows at nanoscopic dimensions of avoiding high pressure-related channel failure and viscoelastic instabilities like corner vortex formation.

The other primary problem for continuous stretching of DNA is molecular individualism [86, 87], a term introduced earlier to describe the high sensitivity of DNA stretching dynamics in an extensional flow to its initial configuration. An ideal DLA device would be able to fully stretch every DNA molecule *uniformly*, but the highly configuration-sensitive dynamics makes this impossible

---

[2] We note that the value of the DNA mobility in the 30 cP buffer presented in Ref. [200] (-1.16 $\frac{\mu\mathrm{m}}{\mathrm{s}}/\frac{\mathrm{V}}{\mathrm{cm}}$) is an order of magnitude too high. Thus it is doubtful that the observed stretching was electrophoretically induced.

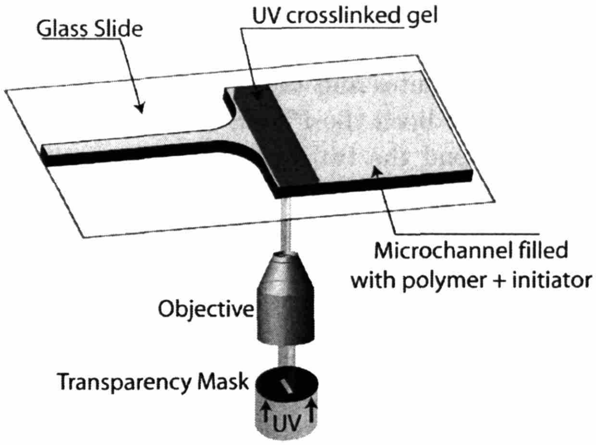

Figure 8-1: Schematic of the selective UV crosslinking procedure used to fabricate gels at the entrance to the hyperbolic contraction (not to scale).

when a molecule experiences a finite strain. Often a strain of at least 10 is needed for the majority of DNA in an ensemble to reach steady-state extension in extensional flows [170], and as we explain below, it is difficult to construct devices to yield such large strain. However, it is possible to control molecular individualism effects on the stretching dynamics. Larson [91] used Brownian dynamics simulations to show that shifting the initial configurational distribution before applying an extensional flow can increase average DNA stretching for finite strain. Specifically, he studied DNA stretching in a two-step process: first imposing shear flow and then immediately thereafter an extensional flow. At strong extensional flow conditions, he found that some pre-sheared ensembles achieved a near uniform fractional extension after a strain of 4, whereas molecules *simultaneously* sheared and extended (with shear rate $\leq$ strain rate) showed the characteristic broad extension distribution and lower mean extension resulting from molecular individualistic effects. We seek to employ this general methodology of *preconditioning* the initial configurational distribution in order to reliably and uniformly stretch DNA.

In this chapter, we use single molecule fluorescence microscopy to study electrically-driven T4 DNA (169 kbp) migrating through a porous gel, and extending in a hybrid gel/contraction channel where we pattern a porous UV crosslinked gel at the inlet of the contraction. The patterned gel causes the molecules to reptate and adopt extended configurations before entering the contraction. We will show that DNA can fully and uniformly stretch when the gel biases the DNA configurations before entering the extensional electrical field. Refer to Chapter 6 for a detailed background on DNA deformation in electric field gradients.

8.2 Experimental

In these experiments, we selectively crosslink a porous gel directly before the hyperbolic contraction channel used in Chapter 6. To do this we first soak the PDMS channel in an initiator solution of 10% 1-hydroxycyclohexyl phenyl ketone (Aldrich, 405612) in 70% ethanol and ultrapure water for

30 minutes. We then rinse the channel in ultrapure water, going through a cycle three times of rinsing in a water bath and then sonicating for 20 seconds. After rinsing, we let the PDMS soak in an ultrapure water bath for 30 minutes and then carefully dry the PDMS and a glass slide (as cleaned without gel). We then treat both the PDMS and glass in a RF plasma cleaner (Harrick, PDC-32G) for 5 s at 60 W and bond the two together. We speculate that this bonding step is necessary when patterning gels in these channels because the gel may swell in aqueous buffers and cause lift-off. The remaining gel patterning steps [201] are shown schematically in Fig. 8-1. Once bonded, we fill the channel with 5 μL of a solution of 2.5% poly(ethylene glycol) 1000 dimethacrylate ("PEG-DM 1000", Polysciences, 15178), 2% poly(ethylene glycol) 400 diacrylate ("PEG-DA 400", Polysciences, 01871), 1% 2-hydroxy-2-methyl-propiophenone ("Darocur-1173", Aldrich, 405655) in 50% ethanol and 50% 5 $\times$TBE. The PEG-DM 1000 and PEG-DA 400 monomers crosslink when in the presence of the Darocur initiator and UV light. After filling, we expose the intended gel region with $\sim$ 365 nm UV light obtained with a UV excitation filter set (11000v2:UV, Chroma, Rockingham, VT) through a transparency mask (placed in the microscope's field stop aperture, CAD/Art Services Inc., Bandon, OR) and a 40$\times$ 0.75 numerical aperature objective. The mask has an 8 mm-long by 2 mm-wide transparent region which creates a gel approximately 150 μm-wide after focussing through the objective. Exposure is performed in two steps: first a 3-s exposure, followed by a 10-s cooling time, and then a 2-s exposure. This two-step process is required to prevent the transparency mask from melting. Following exposure, we then remove the monomer solution from the loading reservoir and then fill both reservoirs with 0.5 $\times$TBE. We then overfill the outlet reservoir and apply a potential of 50 V across the reservoirs to force a combined pressure-driven and electroosmotic rinse flow from the outlet to the inlet of the microchannel for 30 minutes. Following the rinse, we empty the reservoirs and then fill both reservoirs with the DNA solution. We allow for a 15 minute equilibration period with an applied voltage of 130 V to load DNA and buffer into the microchannel and to allow for quenching of the electroosmotic flow. The DNA observation and analysis then proceeded as in the experiments without gels (Chapter 6).

8.3 Results

8.3.1 UV crosslinked gel and uniform electric fields

In order to more uniformly stretch DNA, we seek to preconfigure the configuration ensemble to more dumbbell-like open configurations before they enter the contraction as in Fig. 6-16 (e). The method we choose is to force the DNA into a crosslinked porous gel which we are able to pattern anywhere inside a microchannel [201]. Before we do that, we first investigate the DNA deformation dynamics in a 150 μm-wide gel in a *straightwalled* channel with a uniform applied electric field ($E = 10$ V/cm, equivalent to the inlet field E_1 in De=14 experiments).

The gel has pores sizes of O[l_p] which will force each molecule to adopt more extended configurations in order to reptate through. Figure 8-2 (a) shows a time series of images of a T4 DNA moving through the gel. We immediately see that on average, the DNA adopt extended so-called "I-shape" configurations and traverse the pores in the same manner as observed in concentrated agarose or polyacrylamide solutions [198, 202, 203]. This is best seen by observing the third, fourth, and fifth images. The leading end of the T4 DNA in the third frame hits a narrow pore and halts so that

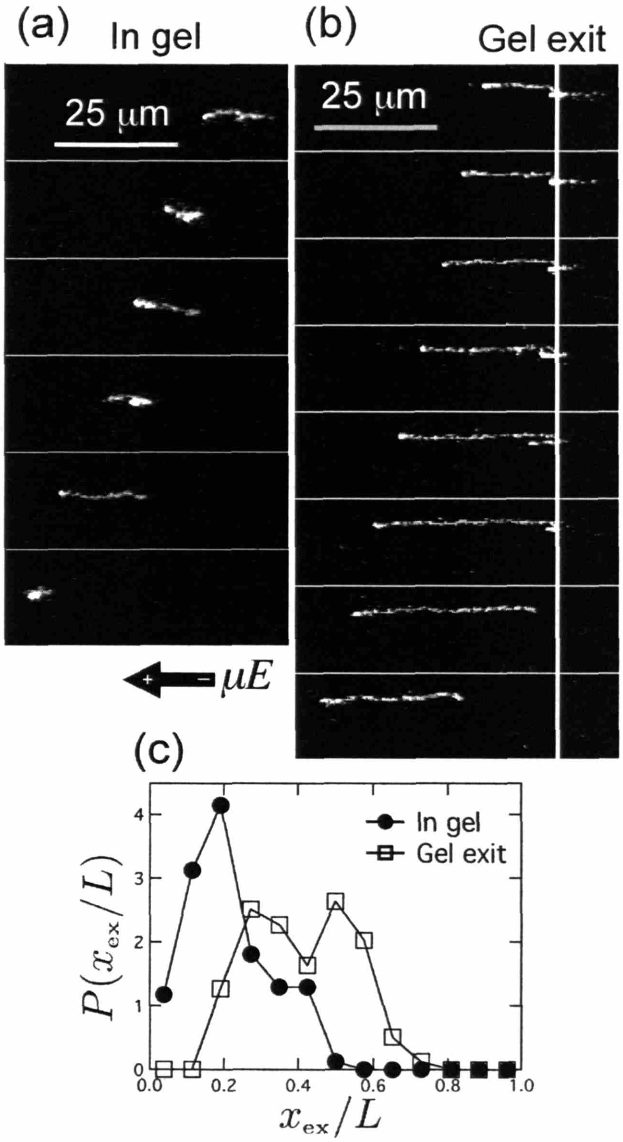

Figure 8-2: Images and data for a T4 DNA in the UV crosslinked gel in a straightwalled microchannel (uniform electric field) and exiting the UV crosslinked gel in the same channel (different molecule). The channel has dimensions of height=2 μm, width=200 μm, length=4.9 mm and E=10 V/cm. (a) Images (spaced 6.7 s apart) of DNA moving through the gel. (b) Images (spaced 0.6 s apart) of DNA exiting the gel. The vertical white line marks the end of the gel. (c) Probability distributions (n=100) of T4 DNA fractional extension within and exiting this UV crosslinked gel at E=10 V/cm.

the trailing arm can catch up and then pass it through the pore.

Though the DNA do adopt extended configurations while reptating in the gel, they stretch even more as they leave. In a uniform field, DNA stretching is induced by imposing a tethering force. The gel provides the tethering effect, much like the large "drag tags" of end-labeled free solution electrophoresis (ELFSE) [204, 205] or by driving DNA into a porous matrix [206]. The stretching at the exit occurs because the average mobility in the gel (at E=10 V/cm) is less than the mobility in buffer. However, the instantaneous mobility difference may vary significantly depending on the DNA's configuration. In an extreme example, some molecules act like they are tethered at the back due to formation of hairpin hooks around pieces of the gel. Figure 8-2 (b) shows an example of a T4 DNA exiting the gel in the uniform field, where the back end of the molecule becomes hooked on a piece of the gel and forms a hairpin. Many other exiting configurations are possible, *e.g.* dumbbells, half-dumbbells, or leading folds [86, 89]. Figure 8-2 (c) shows the fractional extension probability distribution of an ensemble of 100 T4 DNA molecules both inside the gel and as its back end exits the gel at E=10 V/cm. Note that the configuration distribution has shifted to moderately extended states ($\langle x_{\text{ex}}/L \rangle = 0.21 \pm 0.11$ standard deviation) inside the gel (versus $\langle x_{\text{ex}}/L \rangle = 0.07 \pm 0.01$ in a channel without the gel). Furthermore, the DNA stretch even more as they leave the gel ($\langle x_{\text{ex}}/L \rangle = 0.44 \pm 0.13$). These DNA do not completely stretch, though it may be possible to achieve high stretching by increasing the field. However, the gel exit stretching distribution is still qualitatively *broad*, indicating that the details of an individual exiting DNA's configuration are still greatly influencing the stretching dynamics. A more attractive method to complete and uniform stretching is to introduce these prestretched DNA to an extensional field.

8.3.2 Hybrid gel / contraction

In the following experiments we selectively UV crosslink a 150 μm-wide gel before the entrance to the hyperbolic contraction as in Fig. 8-1 (gel ends at $\hat{x} = -0.13$). Figure 8-3 (a)-(d) show a comparison of T4 DNA fractional extension without the gel and with the gel at De=2 and 14. Note that for both De, the gel causes a large majority of the ensemble to strongly stretch before the hyperbolic exit. This is seen more clearly in Fig. 8-3 (e) which shows the fractional extensional probability distributions at $\hat{x}_f = 1$. The very broad extension distributions without the gel have shifted to narrow spikes with the gel ($\langle x_{\text{ex}}/L \rangle = 0.71 \pm 0.13$ at De=2 and $\langle x_{\text{ex}}/L \rangle = 0.95 \pm 0.08$ at De=14). The stretching results at De=14 had particularly excellent uniformity, as 80% of the ensemble stretched over $x_{\text{ex}}/L = 0.96$ and only 7% of the ensemble stretched less than $x_{\text{ex}}/L = 0.80$. We confirmed that these outliers corresponded to molecules that had a leading fold in their configuration as they exited the gel. Figure 8-3 (f) shows a series of snapshots of a T4 molecule stretching as it exits the gel and enters the hyperbolic contraction at De=14.

8.4 Discussion

By adding a short gel region before a contraction we are able to continuously obtain highly uniform DNA stretching using electric fields. This uniformity is not possible without the gel in a device that limits molecular strain to moderate values, *e.g.* $\epsilon < 10$, because of conformational molecular

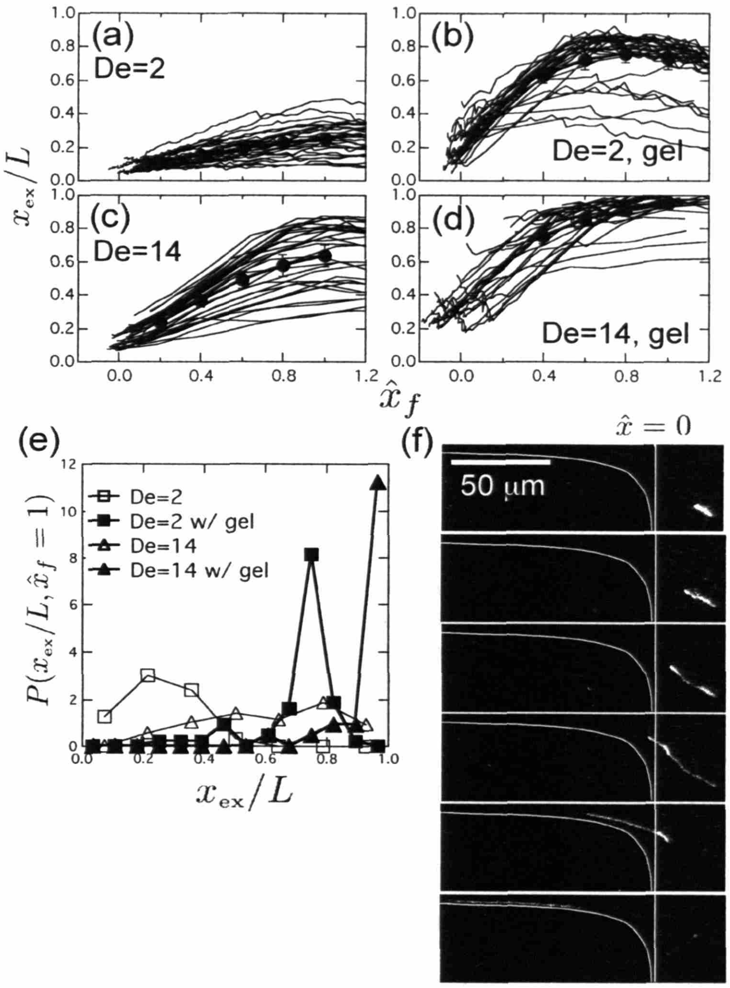

Figure 8-3: Fractional extension of T4 DNA extending at (a) De=2 in the hyperbolic contraction (b) De=2 in the contraction / gel hybrid channel (c) De=14 in the hyperbolic contraction (d) De=14 in the contraction / gel hybrid channel. Ensemble sizes of n=30 are shown. Ensemble averages and standard error are given by filled circles. (e) Comparision of the fractional extension probability distributions (n=60) at $\hat{x}_f = 1$ for cases with and without the UV gel in front of the contraction. (f) Sample images of T4 DNA exiting the gel (its left edge is at $\hat{x} = -0.13$) and entering the hyperbolic contraction at De=14. All frames are spaced by 0.67 s except the last two are separated by 0.23 s.

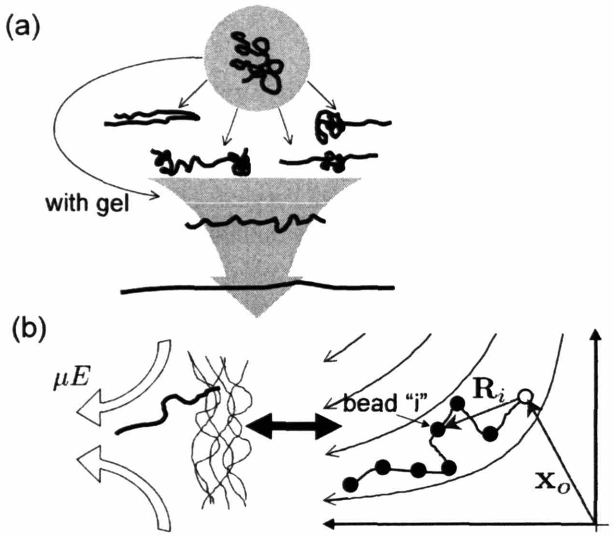

Figure 8-4: (a) Schematic representation of the configuration manifold of a polymer coil transitioning to high extension (with and without pre-conditioning). (b) Sketch of a DNA molecule exiting a gel into an extensional field and the "pseudo-tethered" chain model.

individualism. However, because $\epsilon \sim \ln(w_1/w_2)$, it is extremely difficult to construct devices with $\epsilon > 10$. For example, decreasing the width of w_2 by a factor of 10 to 380 nm would only increase the strain to $\epsilon \sim 6$. The hybrid gel/contraction is able to uniformly stretch DNA at moderate strain because 1) the gel shifts the entering configuration to mostly untangled stretched states (*i.e.* controlling molecular individualism) and 2) it acts as a pseudo-tether for the back of the molecule. Figure 8-4 (a)-(b) shows a schematic of each of these effects.

8.4.1 Controlling molecular individualism

Molecular individualism is an example of the general phenomenon of transient chaos [207], which causes a complex system's dynamics to be unpredictable even though the system eventually achieves a stable fixed point at long time. An example of transient chaos is a coin toss without catching; the coin may bounce around on the floor unpredictably before the eventual heads or tails. Stretching a long polymer in an extensional field is similar because chain connectivity leads to multiple kinks or folds that make the transient stretching dynamics unpredictable. Hence, molecules that move to dumbbell-like configurations deform much differently than those that move to folded configurations [86, 89]. With Brownian motion and infinite strain, the kinks eventually unkink and all chains achieve a final extended state. However, by adjusting system parameters, transient chaos can be stabilized [208]. For the coin-toss problem, an example may be to always toss it like a frisbee which would greatly diminish the unpredictable dynamics of it hitting the floor off-angle. Similarly for a stretching polymer, one might preconfigure the configuration to an adequately unkinked and hence moderately stretched state. Larson's simulations proved that a sequential shear and then extension can shift the extension distribution to higher stretching [91]. His results clearly showed that the shearing must occur *before* the extension in order to increase stretching efficiency. The UV crosslinked gel serves the same purpose, as it unravels and moderately stretches the DNA molecules as they leave the gel before the hyperbolic contraction (Fig. 8-2 (c)). More generally, any porous structure will serve this purpose, and given the great advancements in microfabrication, it may be more desirable to use a nano-scale microfabricated obstacle course [206] before the contraction because of the ability to control the obstacle course layout and pore spacing. Attractive studies would be to determine how much the initial configuration distribution must be adjusted to still yield uniform stretching results and how the obstacle course structure can be designed to optimize the stretching efficiency.

One may also attempt to tackle these configurational control issues theoretically. The non-equilibrium statistical mechanics of the molecular individualism problem has been examined by Gorban and Karlin [209] by first developing a closure method for the dynamics of a stretching FENE-P dumbbell and then applying it to model the highly-configuration sensitive deformation dynamics of a large bead-spring chain. They provide a nice qualitative view of what may be happening to the configurational manifold, however the full chain problem is currently fairly intractable analytically without approximations.

8.4.2 Pseudo-tethered chain model

In addition to biasing the DNA configurations, the gel aids stretching by slowing down the back of the molecule while the front is leaving, acting as a pseudo-tether (Fig. 8-4 (b)). A simple model of DNA stretching at the gel exit is a quasi-equilibrium tethered DNA, *i.e.* a piece of DNA tethered at the gel exit and having a contour length that increases with time. Throughout this discussion we will model the DNA as if it is tethered at the gel, but we stress that there is nothing causing the DNA to stick to the gel; it is simply moving at an average lower mobility. Often the back end of the DNA forms a hairpin hook around a piece of the gel (*cf.* the third and fifth frames of Fig. 8-3 (f)) which directly provides a tethering force. Because of the average mobility differential and hairpin snags at the rear of the DNA, strong stretching can occur as the DNA exits the gel, even in a uniform electric field (*cf.* Fig. 8-2 (b)).

For a tethered chain in a uniform flow (or field), the governing dimensionless group is a Peclet number, defined as Pe=Ul_p/D where U is the uniform flow velocity (or $U = \mu E$ for stretching in a uniform electric field). At equivalent Pe, two different DNA chains will stretch to the same fractional extension in the linear elasticity force regime. Experimental studies of tethered DNA strongly stretching in a uniform flow have shown a collapse of fractional extension data with the parameter $\eta U L^{\gamma}$ where $0.54 \leq \gamma \leq 0.75$ is the contour-length dependent scaling of the Stokes drag coefficient [45]. Given that D scales as $\eta^{-1} N^{-b_2}$ where $0.58 \leq b_2 \leq 1$ depending on the importance of intrachain hydrodynamic interactions, Pe may closely collapse stretching data at even high extension. Though named differently, this dimensionless group has been shown in literature to collapse collision time results of a Rouse model for unhooking hairpin DNA from obstacles (a version of the tethered chain problem) [15]. For Pe$\sim$ 1, tethered chains will only slightly extend, whereas for Pe$\gg$ 1 they will completely extend. The data in Fig. 8-2 (c) corresponds to Pe dynamically ramping up to Pe=7 from the time when the front of the DNA first exits the gel until the back finally leaves. The resulting stretching yields many DNA about 60% extended, and in theory one may be able to fully stretch DNA with a high enough applied field. However the resulting stretching distribution is fairly broad. Efficient stretching of DNA may be difficult in a uniform field gel for two reasons. First, the tethering effect relies on a difference in DNA mobility in the gel versus in the buffer, but this difference decreases with increasing field. Secondly, at high enough fields, leading folds in the DNA configuration may be able to pass through the entropic barrier of the gel pore. In order to maximize stretching efficiency, it would be more desirable to place an extensional field at the exit of the gel.

Consequently, we ask what happens to a polymer chain in an ideal, homogeneous extensional field when the position of one of its ends is fixed. Figure 8-4 (b) shows a schematic of a bead-spring polymer tethered at a position $\mathbf{x}_o$. The vectors connecting the tethered bead (unfilled) to a bead i (filled) are $\mathbf{R}_i$. By tethering the polymer we break the symmetry of the ideal homogeneous extensional field so that the chain stretching will depend on where we tether the molecule. We can easily see this by examining the electrophoretic kinematics in the lab frame. For the tethered chain, the electrophoretic velocity field at each bead $\mathbf{v}_i$ is $\mathbf{v}_i = (\mathbf{x}_o + \mathbf{R}_i) \cdot \nabla(\mu \mathbf{E})$, where we assume $\nabla(\mu \mathbf{E})$ is uniform. Breaking this velocity field up in parts, we see that it is a superposition of a chain tethered at the origin in an extensional field and a chain tethered in a uniform field (since $\mathbf{x}_o \cdot \nabla(\mu \mathbf{E})$ is a constant vector equal to $\mu \mathbf{E}(\mathbf{x}_o)$). As previously described, De governs the extensional field behavior while Pe governs the uniform field stretching.

The strength of uniform stretching part of the field interestingly depends on the coordinates of the DNA leaving the gel. This additional stretching component is low wherever the electrophoretic velocity is low, *i.e.* near ($\hat{x} = 0, \hat{y} = 0$), however it may dominate the extensional stretching component at large $\hat{y}$ or $\hat{x}$. Also, in the limit of an abrupt contraction ($L/l_c \gg 1$) with a patterned gel at the entrance, the uniform field tethering effect will be the dominating stretching mechanism. In our problem $L/l_c = 0.88$ and the gel is located near $\hat{x} = 0$ so the dominant stretching mechanism is the pseudo-tethered molecule in the extensional field.

For a free chain stretching in an extensional field, the tension is on average maximum at the middle of the chain and falls off to zero at both chain ends. Conversely, for a tethered chain, the tension is maximum at the tether point and then falls to zero at the free end [45]. Because we model the DNA exiting the gel as tethered in the extensional field, it will behave qualitatively like a free chain twice its contour length in an extensional field at steady state. Since τ scales as $N^{3\nu}$ (or even more strongly considering confinement), the effective De for a tethered chain in an extensional field is about four times De for the free chain. Hence, extensions leaving the gel may be larger than the expected steady-state extension for a free chain at a given De. We see evidence of this additional tethering force by looking at the De=2 gel data (Fig. 8-4 (b)). Note that the stretched molecules contract slightly from $\hat{x}_f = 0.5 - 1$, meaning that they were initially stretched beyond the steady-state extension at De=2 ($\langle x_{\mathrm{ex}}/L \rangle_{\mathrm{De=2,\ SS}} \sim 0.75$). The same holds at De=14 with the gel, but this chain relaxation is not observable because the molecules nearly completely stretch and it takes only 0.02τ for DNA to traverse the region $0.88 < \hat{x}_f < 1.2$.

8.4.3 High fields

There are a few issues that must be dealt with if device designers seek to use very high field strengths to stretch DNA (or similarly, higher viscosity). First, one must use fields low enough so tensions greater than O[100 pN] do not develop and cause the double-stranded DNA to "overstretch" [27, 54, 210]. This transition value is about an order of magnitude larger than the O[1-10 pN] tension in a completely stretched dsDNA. This leaves room to design stretching devices, though researchers must be wary of operating at extremely large De or Pe, as others have observed overstretching in microcontractions operating at high pressure driven flow rates [27].

Additionally, high electric fields and velocities can induce nonlinear electrokinetic effects [72, 79–81], *i.e.* forces or flows not directly proportional to **E**. The two primary nonlinear electrokinetic effects in DC fields are dielectrophoretic forces [70] and induced charge fields and flows [81]. Both of these phenomena result from polarization of the O[nm] electrical double layer around the DNA molecule which in turn results from large ionic currents in the double layer. A polarized object in an electric field gradient experiences a dielectrophoretic force $\mathbf{F}_{\mathrm{DEP}} = \alpha|\mathbf{E}|\nabla\mathbf{E}$, where α may depend on frequency for an AC field, and we have taken the low frequency limit. Not much quantitative work has been done to study the polarizability of DNA, especially in DC fields, and it remains a difficult problem because of DNA's coiled configuration and elasticity. We do know that DNA can positively polarize, meaning that in a field gradient a dielectrophoretic force would tend to pull it toward the maximum of $|\mathbf{E}|\nabla\mathbf{E}$ (and potentially enhance stretching in our device) [157–159]. However, the low frequency polarizability of 12 kbp plasmid DNA at room temperature has been measured to be $\alpha \sim$O[10^{-29} Fm^2] [211]. Using this rough estimate for α, $\mathbf{F}_{\mathrm{DEP}} \sim 0.001$ pN at the outlet of the hyperbolic contraction at De=23, which is two orders of magnitude smaller than $kT/l_p \sim 0.1$ pN and 3-4 orders of magnitude smaller than the tensions expected in stretched DNA. Hence dielectrophoretic forces are not believed to be important in this DC device.

The other possible nonlinear effect is an induced field or flow from charge polarization. A polarized double layer has recently been shown in some cases to induce long range ionic concentration gradients *outside of the double layer* [81]. Hence, polarization may induce long range induced electroosmotic flows from diffusiophoresis [82], *i.e.* the flow induced by an ionic species concentration gradient. These nonlinear flows have not been studied in conjunction with single DNA electrophoresis, but given previous observations of DNA's polarizability and aggregation [83–85], they are bound to arise at high enough fields. Our observations indicate that De=23 may be close to where a nonlinear electrokinetic flow becomes important for T4 DNA. The strength of this flow would depend on the DNA shape and size, the ionic components of the buffer, and would presumably grow with increasing η, increasing **E**, and decreasing ionic strength.

8.5 Conclusions and outlook

We have analyzed electrophoretic stretching of DNA at the exit of a porous gel and in the hybrid contraction with a gel at its entrance. By placing a gel directly before the channel contraction, we preconfigured DNA to moderately extended configurations. Consequently, as the DNA exited the gel and entered the contraction, they strongly and uniformly stretched after only $\epsilon = 4$. The gel additionally supplied a tethering force at the back of the DNA so that at a given De, it is possible to extend DNA greater than the steady state extension of a free molecule. The high stretching uniformity we achieve has not been observed in any other continuous stretching device.

Chapter 9

Conclusions and Outlook

In this thesis, we presented a single molecule experimental study of the fundamental physical processes in modern DNA mapping designs. Specifically, we investigated DNA dynamics in confinement, DNA deformation in electric field gradients, and DNA hooking collisions on a small post. As an aside, we additionally studied background flows in these devices. Using knowledge gained from this work, we also showed a proof-of-principle application to completely and uniformly stretch DNA. Here we will review a few highlights of this work and comment on future directions.

In our examination of background flows in thin PDMS channels, we discovered a permeation-driven flow. We were able to model and extinguish this converging flow profile, a very important task required for the viability of the next generation of PDMS-based devices. However, we foresee future applications that may advantageously use this flow, *e.g.* to stack colloids or form crystals in a thin microchannel. After we achieved a stagnant fluid environment in these microchannels, our first work with DNA was to experimentally determine how polymer dynamics (diffusion coefficient D and relaxation time τ) are affected by confinement on the order of the radius of gyration R_g. Our results pointed towards DeGennes' blob model scalings, though future work in thinner channels is required to confirm this hypothesis. Furthermore, we studied the electrophoretic collision of a DNA molecule with a *small obstacle.* This is the first study that fully decomposed the collision problem into a hooking probability and an unhooking time distribution at arbitrary electric field strengths, and it is the first to quantitatively show how populations of collision types affect the the overall collision time probability distribution. Though the experimental results provided insight into what types of collisions result from a hooking event and how these collisions affect the overall unhooking time distribution, the next step of this study is more suitable to simulation work. Simulations would be able to generate more statistics and more importantly, they would give access to the tension distributions in the unhooking arms that drive the release.

The main impact of this thesis is the notion that complex microfluidic geometries can strongly deform DNA during electrophoresis, even near surfaces. Not only did this thesis show this in principle, but it also quantitatively examined the deformation dynamics, specifically at the stagnation point of a large obstacle and in a hyperbolic contraction. The electric field gradients generated by the obstacle or in the contraction induce conformation changes in DNA similar to those produced by hydrodynamic flows. The effect of "molecular individualism" was apparent as deformation results were not predictable from molecule to molecule. However, we showed that "molecular individualism" could be bypassed by combining deformation processes in series so that the DNA enters an extensional field in a moderately extended configuration.

The geometries discussed may have typically been studied in the context of *solutions of many polymers* in mixed-flow simulations. However these experiments are unique because 1) the geometries have been scaled down to the length scale of a *single polymer molecule* and 2) *purely extensional deformation* results from the electric field gradients. The various case studies treated here (deformation at the front and rear stagnation points of a large obstacle, deformation in a hyperbolic contraction, DNA hooking and unhooking off of a small post, and DNA exiting a gel) can be incorporated into much more complex microfluidic designs for custom manipulation of DNA and other macromolecule conformations. Examples of such custom macromolecule manipulations are sorting, stretching, or compression unit operations.

Bibliography

[1] P. André, D. Long, and A. Ajdari, Eur. Phys. J. B **4**, 307 (1998).

[2] D. M. Olive and P. Bean, J. Clin. Microbiol. **37**, 1661 (1999).

[3] J.-L. Viovy, Rev. Mod. Phys. **72**, 813 (2000).

[4] T. Ove, Pittsburgh Post-Gazette, (Sept. 21, 2004).

[5] M. A. Burns, B. N. Johnson, S. N. Brahmasandra, K. Handique, J. R. Webster, M. Krishnan, T. S. Sammarco, P. M. Man, D. Jones, D. Heldsinger, et al., Science **282**, 484 (1998).

[6] R. H. Austin and W. D. Volkmuth, Analusis **21**, 235 (1993).

[7] W. D. Volkmuth, T. Duke, M. C. Wu, R. H. Austin, and A. Szabo, Phys. Rev. Lett. **72**, 2117 (1994).

[8] M. Tabuchi, M. Ueda, N. Kaji, Y. Yamasaki, Y. Nagasaki, K. Yoshikawa, K. Kataoka, and Y. Baba, Nature Biotech. **22**, 337 (2004).

[9] M.-F. Huang, Y.-C. Kuo, C.-C. Huang, and H.-T. Chang, Anal. Chem. **76**, 192 (2004).

[10] G. I. Nixon and G. W. Slater, Phys. Rev. E. **50**, 5033 (1994).

[11] E. M. Sevick and D. R. M. Williams, Phys. Rev. E **50**, R3357 (1994).

[12] E. M. Sevick and D. R. M. Williams, Phys. Rev. Lett. **76**, 2595 (1996).

[13] P. M. Saville and E. M. Sevick, Macromolecules **32**, 892 (1999).

[14] P. S. Doyle, J. Bibette, A. Bancaud, and J.-L. Viovy, Science **295**, 2237 (2002).

[15] P. D. Patel and E. S. G. Shaqfeh, J. Chem. Phys. **118**, 2941 (2003).

[16] N. Minc, C. Fütterer, K. D. Dorfman, A. Bancaud, C. Gosse, C. Goubault, and J.-L. Viovy, Anal. Chem. **76**, 3770 (2004).

[17] O. Bakajin, T. A. J. Duke, J. Tegenfeldt, C.-F. Chou, S. S. Chan, R. H. Austin, and E. C. Cox, Anal. Chem. **73**, 6053 (2001).

[18] T. A. J. Duke and R. H. Austin, Phys. Rev. Lett. **80**, 1552 (1998).

[19] L. R. Huang, P. Silberzan, J. O. Tegenfeldt, E. C. Cox, J. C. Sturm, R. H. Austin, and H. Craighead, Phys. Rev. Lett. **89**, 178301 (2002).

[20] M. Baba, T. Sano, N. Iguchi, K. Iida, T. Sakamoto, and H. Kawaura, App. Phys. Lett. **83**, 1468 (2003).

[21] J. Han and H. G. Craighead, Science **288**, 1026 (2000).

[22] M. Streek, F. Schmid, T. T. Duong, and A. Ros, J. Biotech. **112**, 79 (2004).

[23] T. T. Duong et al., Microelectronic Engineering **67-68**, 905 (2000).

[24] M. Streek, F. Schmid, T. T. Duong, D. Anselmetti, and A. Ros, Phys. Rev. E **71**, 011905 (2005).

[25] J. O. Tegenfeldt, O. Bakajin, C.-F. Chou, S. S. Chan, R. Austin, W. Fann, L. Liou, E. Chan, T. Duke, and E. C. Cox, Phys. Rev. Lett. **86**, 1378 (2001).

[26] E. Y. Chan, N. M. Goncalves, R. A. Haeusler, A. J. Hatch, J. W. Larson, A. M. Maletta, G. R. Yantz, E. D. Carstea, M. Fuchs, G. G. Wang, et al., Genome Research **14**, 1137 (2004).

[27] J. W. Larson, G. R. Yantz, R. Charnas, C. M. D'Antoni, M. V. Gallo, K. A. Gillis, L. A. Neely, K. M. Phillips, G. G. Wong, S. R. Gullans, et al., (submitted).

[28] H. Lodish, A. Berk, S. L. Zipursky, P. Matsudaira, D. Baltimore, and J. Darnell, *Molecular Cell Biology* (W. H. Freeman: New York, 2000).

[29] K. F. Freed, Adv. Chem. Phys. **22**, 1 (1972).

[30] E. Helfland, J. Chem. Phys. **62**, 999 (1975).

[31] R. K. Pathria, *Statistical Mechanics* (Butterworth Heinemann: Oxford,, 1996).

[32] D. Keller, D. Swigon, and C. Bustamante, Biophys. J. **84**, 733 (2003).

[33] P. T. Underhill and P. S. Doyle, J. Non-Newtonian Fluid Mech. **122**, 3 (2004).

[34] M. Doi and S. F. Edwards, *The Theory of Polymer Dynamics* (Clarendon Press: Oxford, UK,, 1988).

[35] H. Yamakawa, *Modern Theory of Polymer Solutions* (Harper & Row: New York, 2001).

[36] H. Kleinert, *Path Integrals in Quantum Mechanics, Statistics, Polymer Physics, and Financial Markets* (World Scientific: New Jersey, 2004).

[37] W. M. Sunada and H. W. Blanch, Biotechnol. Prog. **14**, 766 (1998).

[38] M. Fixman, J. Chem. Phys. **36**, 306 (1962).

[39] H. Fujita and T. Norisuye, J. Chem. Phys. **52**, 1115 (1970).

[40] B. Söderberg, arXiv:chem-ph/9608004 v2 (1996).

[41] O. Kratky and G. Porod, Rec. Trav. Chim. **68**, 1106 (1949).

[42] N. Saito, K. Takahashi, and Y. Yuniki, J. Phys. Soc. Japan **22**, 219 (1967).

[43] C. G. Baumann, S. B. Smith, V. A. Bloomfield, and C. Bustamante, Proc. Natl. Acad. Sci. USA **94**, 6185 (1997).

[44] J. F. Marko and E. D. Siggia, Macromolecules **28**, 8759 (1995).

[45] T. T. Perkins, D. E. Smith, R. G. Larson, and S. Chu, Science **268**, 83 (1995).

[46] S. Ferree and H. W. Blanch, Biophys. J. **85**, 2539 (2003).

[47] F. Brochard, Europhys. Lett. **23**, 105 (1993).

[48] Y. Marciano and F. Brochard-Wyart, Macromolecules **28**, 985 (1995).

[49] F. Brochard-Wyart, A. Burguin, and P. G. de Gennes, Europhys. Lett. **47**, 171 (1999).

[50] R. Rzehak, W. Kromen, T. Kawakatsu, and W. Zimmermann, Eur. Phys. J. E **2**, 3 (2000).

[51] B. H. Zimm, Macromolecules **31**, 6089 (1998).

[52] R. G. Larson, T. T. Perkins, D. E. Smith, and S. Chu, Phys. Rev. E **55**, 1794 (1997).

[53] A. Y. Grosberg and A. R. Khokhlov, *Statistical Physics of Macromolecules* (AIP Press, 1994).

[54] S. B. Smith, Y. Cui, and C. Bustamante, Science **271**, 795 (1996).

[55] C. Bouchiat, M. D. Wang, J.-F. Allemand, T. Strick, S. M. Block, and V. Croquette, Biophys. J. **76**, 409 (1999).

[56] S. F. Edwards, Proc. Phys. Soc. **85**, 613 (1965).

[57] F. Schmid, J. Phys.: Condens. Matter **10**, 8105 (1998).

[58] G. H. Fredrickson, V. Ganesan, and F. Drolet, Macromolecules **35**, 16 (2002).

[59] P. G. de Gennes, Phys. Lett. **38A**, 339 (1972).

[60] R. G. Larson, J. Rheol. **39**, 1 (2005).

[61] D. E. Smith, T. T. Perkins, and S. Chu, Macromolecules **29**, 1372 (1996).

[62] J.-L. Barrat and J.-F. Joanny, Adv. Chem. Phys. **94**, 1 (1996).

[63] P. E. Rouse, J. Chem. Phys. **21**, 1272 (1953).

[64] M. Rubinstein and R. H. Colby, *Polymer Physics* (Oxford University Press: New York, 2003).

[65] T. T. Perkins, Ph.D. thesis, Stanford University (1997).

[66] W. M. Deen, *Analysis of Transport Phenomena* (Oxford University Press: New York, 1998).

[67] B. H. Zimm, J. Chem. Phys. **24**, 269 (1956).

[68] Y. Oono and M. Kohmoto, J. Chem. Phys. **78**, 520 (1983).

[69] J. Lyklema, *Fundamentals of Interface and Colloid Science* (Academic Press: London, 1995).

[70] J. D. Jackson, *Classical Electrodynamics* (Wiley: New York, 1999).

[71] W. B. Russel, D. A. Saville, and W. R. Schowalter, *Colloidal Dispersions* (Cambridge University Press: London, 1999).

[72] T. M. Squires and M. Z. Bazant, J. Fluid Mech. **509**, 217 (2004).

[73] K. Chu, Ph.D. thesis, MIT (2005).

[74] D. Stigter, J. Phys. Chem. **82**, 1417 (1978).

[75] D. Stigter, J. Phys. Chem. **82**, 1424 (1978).

[76] D. Stigter and C. Bustamante, Biophys. J. **75**, 1197 (1998).

[77] N. C. Stellwagen, C. Gelfi, and P. G. Righetti, Biopolymers **42**, 687 (1997).

[78] E. Stellwagen and N. C. Stellwagen, Biophys. J. **84**, 1855 (2003).

[79] S. S. Dukhin, Adv. Colloid Inter. Sci. **44**, 1 (1993).

[80] N. A. Mishchuk and S. S. Dukhin, Electrophoresis **23**, 2012 (2002).

[81] M. Z. Bazant, K. Thornton, and A. Ajdari, Phys. Rev. E **70**, 021506 (2004).

[82] D. C. Prieve, J. L. Anderson, J. P. Ebel, and M. E. Lowell, J. Fluid Mech. **148**, 247 (1984).

[83] H. Isambert, A. Ajdari, J.-L. Viovy, and J. Prost, Phys. Rev. Lett. **78**, 971 (1997).

[84] H. Isambert, A. Ajdari, J.-L. Viovy, and J. Prost, Phys. Rev. E **56**, 5688 (1997).

[85] S. Magnusdottir, H. Isambert, C. Heller, and J.-L. Viovy, Biopolymers **49**, 385 (1999).

[86] T. T. Perkins, D. E. Smith, and S. Chu, Science **276**, 2016 (1997).

[87] P. G. de Gennes, Science **276**, 1999 (1997).

[88] R. G. Larson and J. J. Magda, Macromolecules **22**, 3004 (1989).

[89] D. E. Smith and S. Chu, Science **281**, 1335 (1998).

[90] C. M. Schroeder, H. P. Babcock, E. S. G. Shaqfeh, and S. Chu, Science **301**, 1515 (2003).

[91] R. G. Larson, J. Non-Newt. Fluid Mech. **94**, 37 (2000).

[92] D. E. Smith, H. P. Babcock, and S. Chu, Science **283**, 1724 (1999).

[93] H. P. Babcock, R. E. Teixeira, J. S. Hur, E. S. G. Shaqfeh, and S. Chu, Macromolecules **36**, 4544 (2003).

[94] J. S. Hur, E. S. G. Shaqfeh, H. P. Babcock, and S. Chu, Phys. Rev. E **66**, 011915 (2002).

[95] M. Yanagida, Y. Hiraoka, and I. Katsura, Cold Spring Harbor Symposia on Quantitative Biology **47**, 177 (1982).

[96] L. Song and M. F. Maestre, J. Biomol. Str. and Dyn. **9**, 87 (1991).

[97] C. Carlsson, Ph.D. thesis, Chalmers University of Technology (1997).

[98] O. B. Bakajin, T. A. J. Duke, C. F. Chou, S. S. Chan, R. H. Austin, and E. C. Cox, Phys. Rev. Lett. **80**, 2737 (1998).

[99] M. Petersen and J. P. Jacobsen, Bioconjugate Chem. **9**, 331 (1998).

[100] S. Inoué and K. R. Spring, *Video Microscopy* (Plenum Press: New York,, 1997).

[101] B. Ladoux, J.-P. Quivy, P. S. Doyle, G. Almouzni, and J.-L. Viovy, Science Progress **84**, 267 (2001).

[102] R. S. Bodannes and P. C. Chan, Febs Lett. **105**, 195 (1979).

[103] L. J. Marnett, Carcinogenesis **21**, 361 (2000).

[104] Y. Yoshikawa, M. Suzuki, N. Chen, A. A. Zinchenko, S. Murata, T. Kanbe, T. Nakai, H. Oana, and K. Yoshikawa, Eur. J. Biochem. **270**, 3101 (2003).

[105] D. E. Smith, Ph.D. thesis, Stanford University (1999).

[106] D. J. Beebe, G. A. Mensing, and G. M. Walker, Annu. Rev. Biomed. Eng. **4**, 261 (2002).

[107] C. S. Effenhauser, G. J. M. Bruin, A. Paulus, and M. Ehrat, Anal. Chem. **69**, 3451 (1997).

[108] Y. Xia and G. M. Whitesides, Angew. Chem. Int. Ed. **37**, 550 (1998).

[109] J. C. McDonald, D. C. Duffy, J. R. Anderson, D. T. Chiu, H. Wu, O. J. Schueller, and G. M. Whitesides, Electrophoresis **21**, 27 (2000).

[110] S. R. Quake and A. Scherer, Science **290**, 1536 (2000).

[111] J. C. McDonald and G. M. Whitesides, **35**, 491 (2002).

[112] W. L. Robb, Ann. NY Acad. Sci. **146**, 119 (1968).

[113] J. Lee, C. Park, and G. Whitesides, Anal. Chem. **75**, 6544 (2004).

[114] H. P. Chou, C. Spence, A. Scherer, and S. Quake, Proc Natl Acad Sci U S A **96**, 11 (1999).

[115] B. Zhang, S. Roach, and R. Ismagilov, J. Am. Chem. Soc. **125**, 11170 (2003).

[116] N. Goedecke, J. Eijkel, and A. Manz, Lab on a Chip **2**, 219 (2002).

[117] E. Kim, Y. N. Xia, and G. M. Whitesides, Adv. Mater. **8**, 245 (1996).

[118] G. M. Walker and D. J. Beebe, Lab on a Chip **2**, 57 (2002).

[119] G. M. Walker and D. J. Beebe, Lab on a Chip **2**, 131 (2002).

[120] J. M. Watson and M. G. Baron, J. Membr. Sci. **110**, 47 (1996).

[121] G. I. Barenblatt, V. M. Entov, and V. M. Ryzhik, *Theory of Fluid Flows Through Natural Rocks* (Kluwer: Boston, 1990).

[122] R. Schinzinger and P. A. A. Laura, *Conformal Mapping: Methods and Applications* (Dover Publications, 2003).

[123] Y. S. Shin, K. Cho, S. H. Lim, S. Chung, S. J. Park, C. Chung, D. C. Han, and J. K. Chang, Journal of Micromechanics and Microengineering **13**, 768 (2003).

[124] K. K. S. Lau and K. K. Gleason, J. Fluorine Chem. **2000**, 119 (2000).

[125] G. Seong and R. Crooks, J. Am. Chem. Soc. **124**, 13360 (2002).

[126] B. J. Kirby and E. F. Hasselbrink, Electrophoresis **25**, 203 (2004).

[127] A. M. Spehar, S. Koster, V. Linder, S. Kulmala, N. F. de Rooij, E. Verpoorte, H. Sigrist, and W. Thormann, Electrophoresis **24**, 3674 (2003).

[128] X. Ren, M. Bachman, C. Sims, G. P. Li, and N. Allbritton, J. Chromatogr. B **762**, 117 (2001).

[129] J. Zheng, H.-W. Li, and E. S. Yeung, J. Phys. Chem. B **108**, 10357 (2004).

[130] J. L. Harden, D. Long, and A. Ajdari, Langmuir **17**, 705 (2001).

[131] F. Tessier and G. W. Slater, Macromolecules **38**, 6752 (2005).

[132] H. Makamba, J. H. Kim, K. Lim, N. Park, and J. H. Hahn, Electrophoresis **24**, 3607 (2003).

[133] D. Wu, Y. Luo, X. Zhou, Z. Dai, and B. Lin, Electrophoresis **26**, 211 (2005).

[134] Q. Gao and E. S. Yeung, Anal. Chem. **70**, 1382 (1998).

[135] E. A. S. Doherty, K. D. Berglund, B. A. Buchholz, I. V. Kourkine, T. M. Przybycien, R. D. Tilton, and A. E. Barron, Electrophoresis **23**, 2766 (2002).

[136] P. G. Righetti, *Capillary Electrophoresis in Analytical Biotechnology* (CRC Press: Boca Raton, FL, 1996).

[137] Y.-L. Chen, M. D. Graham, J. J. de Pablo, G. C. Randall, M. Gupta, and P. S. Doyle, Phys. Rev. E **70**, 060901 (2004).

[138] M. Daoud and P. G. deGennes, J. Phys. (Paris) **38**, 85 (1977).

[139] F. Brochard and P. G. deGennes, J. Chem. Phys. **67**, 52 (1977).

[140] R. M. Jendrejack, E. T. Dimalanta, D. C. Schwartz, M. D. Graham, and J. J. de Pablo, Phys. Rev. Lett. **91**, 038102 (2003).

[141] R. M. Jendrejack, D. C. Schwartz, M. D. Graham, and J. J. de Pablo, J. Chem. Phys. **119**, 1165 (2003).

[142] A. Milchev and K. Binder, J. Phys. II France **6**, 21 (1996).

[143] K. Hagita and H. Takano, J. Phys. IV France **10**, 305 (2000).

[144] J. L. Harden and M. Doi, J. Phys. Chem. **96**, 4046 (1992).

[145] P. G. de Gennes, *Scaling Concepts in Polymer Physics* (Cornell University Press: Ithaca, NY, 1979).

[146] J. Happel and H. Brenner, *Low Reynolds number hydrodynamics* (Kluwer: Boston, 1983).

[147] L. P. Faucheux and A. J. Libchaber, Phys. Rev. E **49**, 5158 (1994).

[148] E. R. Dufresne, D. Altman, and D. G. Grier, Europhys. Lett. **53**, 264 (2001).

[149] B. Dunweg and K. Kremer, J. Chem. Phys. **99**, 6983 (1993).

[150] A. Meller, L. Nivon, and D. Branton, Phys. Rev. Lett. **86**, 3435 (2001).

[151] K. Inatomi, S. Izuo, S. Lee, H. Ohji, and S. Shiono, Microelectronic Engineering **70**, 13 (2003).

[152] G. C. Randall and P. S. Doyle, Phys. Rev. Lett. **93**, 058102 (2004).

[153] G. C. Randall and P. S. Doyle, Mater. Res. Soc. Symp. Proc. **790**, P3.3 (2004).

[154] F. Tessier, L. J., and G. W. Slater, Macromolecules **35**, 4791 (2002).

[155] B. M. Olivera, P. Baine, and N. Davidson, Biopolymers **2**, 245 (1964).

[156] D. Long, A. V. Dobrynin, M. Rubinstein, and A. Ajdari, J. Chem. Phys. **108**, 1234 (1998).

[157] C. L. Asbury and G. van der Engh, Biophys. J. **74**, 1024 (1998).

[158] C. L. Asbury, A. H. Diercks, and G. van der Engh, Electrophoresis **23**, 2658 (2002).

[159] C.-F. Chou, J. O. Tegenfeldt, O. Bakajin, S. S. Chan, E. C. Cox, N. Darnton, T. Duke, and R. H. Austin, Biophys. J. **83**, 2170 (2002).

[160] M. U. Nollert and W. L. Olbricht, Rheol. Acta **24**, 3 (1985).

[161] A. J. Szeri, S. Wiggins, and L. G. Leal, J. Fluid Mech. **228**, 207 (1991).

[162] J. Feng and L. G. Leal, J. Non-Newt. Fluid Mech. **72**, 187 (1997).

[163] S. P. Carrington, J. P. Tatham, and J. P. Odell, Polymer **38**, 4595 (1997).

[164] A. S. Panwar and S. Kumar, J. Chem. Phys. **118**, 925 (2003).

[165] G. C. Randall and P. S. Doyle, Proc. Natl. Acd. Sci. **102**, 10813 (2005).

[166] J. C. Crocker and D. G. Grier, J. Colloid Interface Sci. **179**, 298 (1996).

[167] M. Gutman, E. Nachliel, and S. Kiryati, Biophys. J. **63**, 274 (1992).

[168] B. Maier and J. O. R´adler, Macromolecules **33**, 7185 (2000).

[169] G. C. Randall and P. S. Doyle, Macromolecules **38**, 2410 (2005).

[170] R. G. Larson, H. Hu, D. E. Smith, and S. Chu, J. Rheol. **43**, 267 (1999).

[171] R. G. Larson, Rheol. Acta **29**, 371 (1990).

[172] F. C. MacKintosh, J. Käs, and P. A. Janmey, Phys. Rev. Lett. **75**, 4425 (1995).

[173] G. Marrucci, J. Non-Newt. Fluid Mech. **62**, 279 (1996).

[174] W. D. Volkmuth and R. H. Austin, Nature **358**, 600 (1992).

[175] D. J. Olson, J. M. Johnson, P. D. Patel, E. S. G. Shaqfeh, S. G. Boxer, and G. G. Fuller, Langmuir **17**, 7396 (2001).

[176] P. S. Doyle, B. Ladoux, and J.-L. Viovy, Phys. Rev. Lett. **84**, 4769 (2000).

[177] N. Kaji, Y. Tezuka, Y. Takamura, M. Ueda, T. Nishimoto, H. Nakanishi, Y. Horiike, and Y. Baba, Anal. Chem. **76**, 15 (2004).

[178] K. D. Dorfman and J.-L. Viovy, Phys. Rev. E **69**, 011901 (2004).

[179] N. Minc, P. Bokov, K. B. Zeldovich, C. Fütterer, J.-L. Viovy, and K. D. Dorfman, Electrophoresis **26**, 362 (2005).

[180] N. Minc, J.-L. Viovy, and K. D. Dorfman, Phys. Rev. Lett. **94**, 198105 (2005).

[181] B. H. Hughes, *Random Walks in Random Environments* (Oxford University Press: New York, 1995).

[182] D. Long, J.-L. Viovy, and A. Ajdari, J. Chem. Phys. **118**, 2941 (2003).

[183] S. M. Bhattacharjee and G. H. Fredrickson, Phys. Rev. A **41**, 3372 (1990).

[184] J.-L. Viovy, Science **264**, 112 (1994).

[185] P. S. Doyle, E. S. G. Shaqfeh, G. H. McKinley, and S. H. Spiegelberg, J. Non-Newt. Fluid Mech. **76**, 79 (1998).

[186] A. Szabo, K. Schulten, and Z. Schulten, J. Chem. Phys. **72**, 4350 (1980).

[187] R. Kubo, M. Toda, and N. Hashitsume, *Statistical Physics II, Nonequilibrium Statistical Mechanics* (Springer: Berlin, 1985).

[188] H. C. Öttinger, *Stochastic Processes in Polymeric Fluids* (Springer: Berlin, 1996).

[189] S. Redner, *A Guide to First-Passage Processes* (Cambridge University Press: Cambridge, UK, 2001).

[190] C. M. Bender and S. A. Orszag, *Advanced Mathematical Methods for Scientists and Engineers* (Springer: Berlin, 1999).

[191] D. C. Schwartz, X. Li, L. Hernandez, S. P. Ramnarain, E. J. Huff, and Y. K. Wang, Science **262**, 110 (1993).

[192] X. Michalet, R. Ekong, F. Fougerousse, R. S, C. Schurra, N. Hornigold, M. van Slegtenhorst, J. Wolfe, S. Povey, J. S. Beckmann, et al., Science **277**, 1518 (1997).

[193] C. A. P. Petit and J. D. Carbeck, Nano Letters **3**, 1141 (2003).

[194] E. T. Dimalanta, A. Lim, R. Runnheim, C. Lamers, C. Churas, D. K. Forrest, J. J. de Pablo, M. D. Graham, S. N. Coppersmith, S. Goldstein, et al., Anal. Chem. **76**, 5293 (2004).

[195] R. Riehn, M. Lu, Y.-M. Wang, S. F. Lim, E. C. Cox, and R. H. Austin, Proc. Natl. Acad. Sci. **102**, 10012 (2005).

[196] J. O. Tegenfeldt, C. Prinz, H. Cao, S. Chou, W. W. Reisner, R. Riehn, Y. M. Wang, E. C. Cox, J. C. Sturm, , et al., Proc. Natl. Acad. Sci. **101**, 10979 (2004).

[197] P. K. Wong, Y.-K. Lee, and C.-M. Ho, J. Fluid Mech. **497**, 55 (2003).

[198] M. Ueda, J. Biochem. Biophys. Methods **41**, 153 (1999).

[199] N. Kaji, M. Ueda, and Y. Baba, Biophys. J. **82**, 335 (2003).

[200] Y.-J. Juang, S. Wang, X. Hu, and L. J. Lee, Phys. Rev. Lett. **93**, 268105 (2004).

[201] J. C. Love, D. B. Wolfe, H. O. Jacobs, and G. M. Whitesides, Langmuir **17**, 6005 (2001).

[202] C. Carlsson, A. Larsson, M. Jonsson, and B. Nordén, J. Am. Chem. Soc. **117**, 3871 (1995).

[203] M. Ueda, H. Ono, Y. Baba, M. Doi, and K. Yoshikawa, Biophys. Chem. **71**, 113 (1998).

[204] P. Mayer, G. W. Slater, and G. Drouln, Anal. Chem. **66**, 1777 (1994).

[205] W. N. Vreeland, R. J. Meagher, and A. E. Barron, Anal. Chem. **74**, 4328 (2002).

[206] S. W. P. Turner, M. Cabodi, and H. G. Craighead, Phys. Rev. Lett. **88**, 128103 (2002).

[207] S. H. Strogatz, *Nonlinear Dynamics and Chaos* (Addison-Wesley: Reading, MA, 1994).

[208] Y.-C. Lai, T. Tél, and C. Grebogi, Phys. Rev. E **48**, 709 (1993).

[209] A. N. Gorban and I. V. Karlin, Physica A **336**, 391 (2004).

[210] P. Cluzel, A. LeBrun, C. Heller, R. Lavery, J.-L. Viovy, D. Chatenay, and F. Caron, Science **271**, 792 (1996).

[211] D. J. Blakewell, I. Ermolina, H. Morgan, J. Milner, and Y. Feldman, Biochemica et Biophysica Acta **1493**, 151 (2000).